FACULTY OF SCIENCE
UNIVERSITY OF COPENHAGEN

NIELS BOHR INSTITUTE

PhD thesis

Kamilla Nørregaard

Physics based investigations

of DNA supercoiling

&

of plasmonic nanoparticles for photothermal cancer therapy

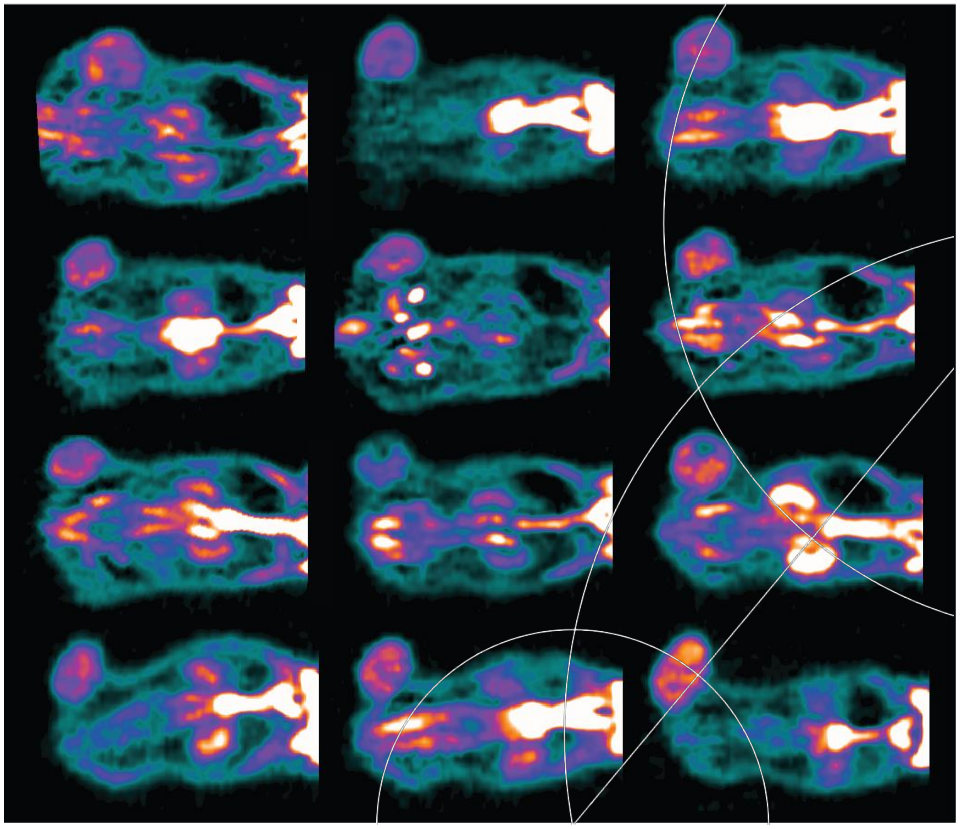

This thesis has been submitted to the PhD School at the Faculty of Science, University of Copenhagen

Academic advisor: Lene Broeng Oddershede, NBI, KU
Academic co-advisors: Pól Martin Bendix, NBI, KU and Andreas Kjær, BMI, KU

Submitted: March 6, 2015

Abstract

Hyperthermia has great potential as a cancer therapy as it weakens or causes irreversible damage to cancer cells. However, available heat sources are poor in discriminating between healthy and cancerous tissue. In this thesis work, the application of plasmonic nanoparticles as photo-induced strong, localized thermal transducers was investigated for cancer therapy.

Gold nanoparticles exhibit surface plasmon resonance that greatly enhances their photoabsorption properties. When irradiated with resonant light, they efficiently absorb the light and convert it into extremely local and well-controlled heating with temperature increases that easily exceed 100 ℃. Due to these unique optical properties and their biocompatibility, gold nanoparticles are promising candidates for selective photothermal cancer therapy. Light with wavelengths in the near-infrared (NIR) region has low absorption and high penetration through biological material. Hence, the combination of these two non-destructive moieties can inflict irreversible damage to the tumor tissue by strong localized hyperthermia, without harming the surrounding healthy tissue. However in the literature, the optimal choice of plasmonic nanoparticles for this therapy remains an open question.

Using positron emission tomography/computed tomography (PET/CT) imaging as a treatment evaluation tool it was found that NIR irradiated resonant silica-gold nanoshells had a higher therapeutic efficacy than non-resonant colloidal gold nanoparticles, when delivered directly into subcutaneous tumor xenografts in mice. To better understand the photo-physical properties, the plasmonic heating of the resonant and non-resonant nanoparticles was also compared using an *in vitro* temperature sensitive assay. This assay enabled measurements of the heat generation of single NIR irradiated nanoparticles and confirmed that the resonant silica-gold nanoshells were superior to the non-resonant nanoparticles. These findings were in agreement with numerical photo-absorption calculations. The presented comparative study is a novel strategy to quantify the photothermal effect at a single particle level as well as in a therapeutic context. It is proposed that this strategy can be used to evaluate any type of nanostructure as well as different tumor models.

The thesis work also contains a study of the epigenetic switch in the model system of Bacteriophage λ. A novel assay for single particle analysis on naturally supercoiled DNA was developed, and used to investigate the effect of supercoiling on a regulatory protein-mediated DNA loop that is the basis of the epigenetic λ switch. It was found that supercoiling greatly enhanced DNA looping probability, thus rendering the transition between epigenetic states an efficient and robust process. This part of the thesis project is described in three published papers that are included in this dissertation.

Dansk resumé

Hypertermi har stort potentiale som kræftbehandling, da det enten svækker eller forårsager uoprettelige skader på kræftceller. Desværre er de tilgængelige varmekilder dårlige til at skelne mellem sundt og kræftsygt væv. I denne afhandling blev anvendelsen af plasmoniske nanopartikler som lokalt fotoinducerede termiske kilder undersøgt til kræftbehandling.

Guld nanopartikler udviser overflade-plasmon-resonans, der i høj grad forbedrer deres fotoabsorptionsegenskaber. Ved bestråling med resonant lys, omdanner de effektivt det absorberede lys til ekstrem lokal og velkontrolleret opvarmning med temperaturstigninger, der let overstiger 100 ℃. På grund af disse unikke optiske egenskaber og deres biokompatibilitet er guld nanopartikler derfor lovende kandidater til selektiv fototermisk kræftterapi. Lys med bølgelængder i den nær-infrarøde (NIR) region har lav absorption og høj penetreringsevne gennem biologisk materiale. Kombinationen af disse to ikke-destruktive egenskaber kan dermed påføre tumorvæv irreversibel skade ved hjælp af stærk lokal hypertermi, uden at det omkringliggende raske væv påvirkes. Det optimale valg af plasmoniske nanopartikler til denne terapi er dog stadig et åbent spørgsmål i litteraturen.

Ved at bruge positronemissionstomografi/computertomografi-billeddannelse (PET/CT) til at evaluere behandlingen, fandt vi at NIR bestrålet resonante silica-guld nanoshells havde en højere terapeutisk virkning end ikke-resonante kolloide guld nanopartikler, når de leveredes direkte ind i subkutane tumorxenoplantater i mus. For bedre at forstå de foto-fysiske egenskaber blev plasmonisk opvarmning af de resonante og ikke-resonante nanopartikler derudover sammenlignet ved hjælp af et *in vitro* temperaturfølsomt assay. Dette assay tillod målinger af varmegenereringen af de enkelte NIR bestrålede nanopartikler der bekræftede, at de resonante silica-guld nanoshells var overlegne i forhold til de ikke-resonante guld nanopartikler. Dette var i overenstemmelse med numeriske beregninger af deres foto-absorption. Disse sammenligningstudier præsenterer en ny strategi, der kan bruges til at kvantificere den fototermiske effekt af en enkelt partikel såvel som i en terapeutisk sammenhæng. Vi vurderer at denne strategi kan anvendes til at bedømme enhver type nanostruktur og forskellige tumormodeller.

Afhandlingen indeholder også en undersøgelse af den såkaldte epigenetiske switch i modelsystemet Bakteriofag λ. Vi har udviklet et nyt assay, der kan bruges til enkeltpartikelanalyser på naturligt supercoilet DNA.
Ved hjælp af assayet undersøgte vi virkningen af supercoiling på et regulatorisk protein-medieret DNA-loop der er grundlaget for den epigenetiske λ-switch. Vi fandt frem til, at supercoiling markant øger sandsyligheden for DNA looping, hvilket gør overgangen mellem de epigenetiske tilstande til en effektiv og robust proces. Denne del af PhD studiet er beskrevet i tre publicerede artikler, der er inkluderet i denne afhandling.

Acknowledgments

This PhD project is the product of my work during the last three years in the Optical Tweezers Group at the Niels Bohr Institute (NBI). First, I would like to thank my supervisor, Lene B. Oddershede, for excellent support and engagement during this project. Her enthusiasm and commitment to science is truly inspiring.

The photothermal cancer therapy project was a collaboration with Cluster for Molecular Imaging, Department of Biomedical Sciences (BMI), Copenhagen. I would like to give special thanks Jesper Tranekjær Jørgensen, who is my close collaborator from BMI and the central person in everything related to PET/CT imaging and *in vivo* experimental work. Without him and his great expertise, the project would have looked completely different.
Thanks to my co-supervisors, Poul Martin Bendix for always being willing to help in the lab or discuss possible interpretations of the data, and Andreas Kjær, who is the driving force of Cluster for Molecular Imaging. I would like to thank Thomas Andersen for his enormous and unremitting effort in helping me with the GUV assay. I would also like to thank Ann-Katrine Vransø West for her work on the microRNA assay, Pengfei Tian for simulating the absorption cross-sections, and Natascha Leijnse for her help with proof-reading this thesis.

For the supercoiling project, I would like to thank Stanley Brown who was the central person in the design of the DNA plasmids. I want to thank him for being an indispensable helping hand when my biological expertise and knowledge came short. Thanks to Magnus Anderson, Peter Nielsen, and Kim Sneppen who all contributed to the work. The CI protein was generously provided by Dale Lewis and Sankar Adhya, (Laboratory of Molecular Biology, Center for Cancer Research, National Cancer Institute, National Institutes of Health, Bethesda, MD 20892-4264, USA). The thermodynamic model was provided by Carlo Manzo and Laura Finzi (Department of Physics, Computational and Life Science (CLS) Core Faculty, Emory University, Atlanta, GA 30322, USA).

Thanks to all my colleagues in the K-building at NBI and at Cluster for Molecular Imaging at BMI for making the workplace a fun place to be. I would also like to thank Naomi Halas and my colleagues in the Halas group at Rice University, Texas, for making Houston my second home and for teaching me about plasmonic nanoparticles. A special thanks to Christine O. Rasmussen, Kristian Moss Bendtsen, and Dino Ott for their indispensable support both scientifically and privately, and for proof-reading this thesis.

Thanks to my family, for always helping me when I am short-handed, proof-reading my thesis, and for keeping my spirits up.

Finally I would like to thank the Lundbeck Foundation and the PhD school at NBI for funding.

Publication List

2014 **Nat. Protoc.**

K. Norregaard, M. Anderson, P. Nielsen, S. Brown, and L.B. Oddershede

Tethered particle analysis of supercoiled circular DNA using PNA handles, vol. 9 pp.:2206–2223

2014 **Phys. Chem. Chem. Phys.**

K. Norregaard, L. Jauffred, K. Berg-Sorensen, and L.B. Oddershede

Optical manipulation of single molecules in the living cell, vol. 16(25) pp.:12614-12624

2014 **IEEE J. of Sel. Top. Quantum Electron.**

P.M. Bendix, L. Jauffred, K. Norregaard, and L.B. Oddershede

Optical trapping of nanoparticles and Quantum Dots, vol. 20(3)

2014 **Bacteriophage**

K. Norregaard, M. Anderson, K. Sneppen, P. Nielsen, S. Brown, and L.B. Oddershede

Effect of supercoiling on the λ switch, vol. 4(1) pp.: e27517-(1-5)

2013 **Proc. Natl. Acad. Sci. U. S. A.**

K. Norregaard, M. Anderson, K. Sneppen, P. Nielsen, S. Brown, and L.B. Oddershede

DNA supercoiling enhances cooperativity and efficiency of an epigenetic switch, vol. 110(43) pp. :17386-17391

Contents

Chapter 1

Introduction

This thesis work consists of two parts, where the first part addresses epigentics studied in the model system of Bacteriophage λ, and the second part contains a study of plasmonic nanoparticle for photothermal cancer therapy.

1.1 Epigentics studied in the model system of Bacteriophage λ

The first part of this thesis is a study on epigenetic regulation in Bacteriophage λ, that is a model on the basis of which epigenetic switch regulation is understood. Using a novel single molecule assay we investigated the gene regulatory effect of a protein-mediated DNA loop on a naturally supercoiled DNA plasmid. Bacteriophage λ is a virus that infects bacterium *Escherichia coli* whereupon it enters either of two very distinct developmental pathways inherent to the Bacteriophage λ life cycle. The lytic state is a virulent state where the Bacteriophage λ hijacks the bacterium's replication machinery and within an hour produces $\sim$ 100 copies of itself and lyses the cell. The lysogenic state is a dormant state where the Bacteriophage λ incorporates its DNA into the bacterium's and is passed on into the daughter cells.

The lysogenic state of Bacteriophage λ is exceptionally stable, still, it is capable of responding to DNA damage and rapidly enter the lytic state to escape the dying cell. The mediator of the lysogenic state is the λ repressor protein, CI. Dimers of CI interact with the λ operators, OR and OL, located $\sim$ 2.3 kbp apart on the λ DNA, and facilitate long-range cooperative interactions that arrange the intervening DNA in a loop (see Fig. 1.1A).

We have invented an assay where positions adjacent to the λ operators on a naturally super-

coiled plasmid are marked with peptide nucleic acids (PNA) handles. These handles mediate tethering of the plasmid between a surface and a submicron sized reporter bead (see Fig. 1.1B) [1, 2].

Monitoring the movement of the reporter bead by tethered particle tracking allows for single molecule investigations of the effect of supercoiling on the DNA plasmid dynamics, and the efficiency of the CI-mediated DNA loop that constitutes the epigenetic λ switch. Compared with relaxed DNA [1, 3], the presence of supercoils enhanced the juxtaposition probability, thereby overall increased the CI mediated DNA looping probability (see Fig. 1.1C).

Using a thermodynamic model that describes the probability of DNA looping for a given CI concentration, we found free energies for the looping transition on supercoiled DNA that is in better agreement with *in vivo* observations than those obtained on linear relaxed DNA [1, 3]. The transition between the looped and unlooped states was found to be steeper with the supercoiled DNA, thus rendering the process a more cooperative one confirmed by an increased Hill coefficient ($h = 2.5$ for the supercoiled DNA compared to $h = 1.2$ on linear relaxed DNA) [1]. Interestingly, the transition occurs exactly at the CI concentration corresponding to the minimum number of CI molecules capable of maintaining the lysogenic promotor-repressed state (see bottom configuration in Fig. 1.1A and *grey box* in C) [4]. Our results showed that the λ switch is finely tuned to have an optimal, fast and efficient response to lytic induction and that supercoiling is essential.

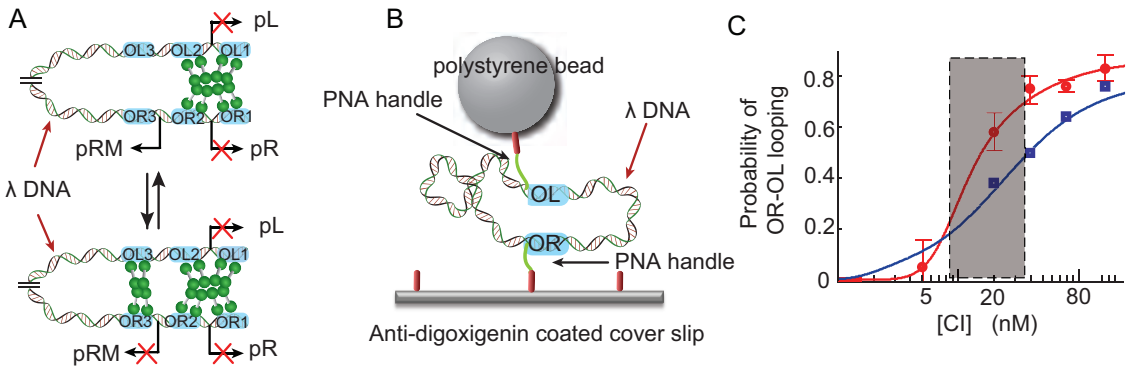

Figure 1.1: Epigenetic switch regulation by Bacteriophage λ. **(A)** CI dimers (green dumbbells) bind cooperatively at the λ operators, OR and OL, and facilitate DNA looping and regulation of the lysogenic (pRM) and lytic (pR and pL) promoters (marked by bent arrows). Red cross indicates that the promoter is repressed. **(B)** The PNA-based tethered particle motion assay. A supercoiled DNA plasmid is tethered between a glass surface and a polystyrene bead via PNA handles. The PNA handles are flanking the λ operators, OR and OL, which limit the λ DNA (marked with red arrow). **(C)** Probability of CI-mediated looping as function of CI concentration for supercoiled DNA (red circles) and for linear DNA (blue squared; published by Zurla et al. [3]). The curves show corresponding thermodynamical models. Supercoiling enhances the binary response to changes in CI concentration and lowers the CI concentration necessary for pRM repression. The dashed box highlights the narrow sigmoidal transition interval for the supercoiled DNA.

These results are to our knowledge the first single molecule studies showing the regulatory

importance of DNA supercoiling. As DNA in its natural state is supercoiled, we believe that this novel assay can improve single molecule studies of the physical properties of supercoiled DNA in itself, as well as other regulatory systems involving interactions between DNA and DNA associating proteins. This part of the thesis project is described in detail in three published papers that are included in this dissertation [1, 2, 4].

1.2 Plasmonic nanoparticles for photothermal cancer therapy

While the major part of this work was performed at the Niels Bohr Institute and Cluster for Molecular Imaging, during my time as a PhD student I also visited Naomi Halas' lab at Rice University in Houston, Texas, for three months. The Halas group has great expertise in materials that possess surface plasmon properties, and were the inventors of the so-called silica-gold nanoshells. These are the first and heaviest used plasmonic nanoparticles in the field of photothermal cancer therapy, why we decided to also include them in this thesis work. My time in the Halas group was therefore well spent, learning about how the nanoshells are synthesized, their chemical and physical characteristics, as well as how they can be conjugated with biomolecules for biological applications.

Cancer research and development of therapeutic strategies have become a multidisciplinary challenge, joining forces across fields in modern science. The main part of this thesis dissertation is devoted to our results regarding the use of gold nanoparticles in cancer medicine. Gold nanoparticles are promising candidates for photothermal cancer therapy due to their unique optical properties. Light excitation of gold nanoparticles induces collective oscillations of the conduction band electrons, resulting in strong absorption of resonant light and significant heating of the nanoparticle and its local surroundings. The phenomenon of collective oscillations of the conduction electrons in metallic nanoparticles is known as surface plasmon resonance, and particles that possess such optical properties are popularly called plasmonic nanoparticles.

Gold in itself is inert, at least when the dimension of the material is larger than $\sim$ 10 nm, making gold nanoparticles biocompatible. In addition, gold nanoparticles are easily functionalized via Au-thiol chemistry paving the way for designing multi-functional nanoparticles that possess synergistic effects by combining their therapeutic, targeting and/or imaging capabilities.

The principle in photothermal cancer therapy is that plasmonic nanoparticles are administered to the tumor site and irradiated with resonant light. The light is rapidly absorbed by the plasmonic nanoparticles and converted into heat that dissipates into the local environ-

ment. The temperatures generated are so extreme that the cancer cells immediately ablate or obtain irreversible damage. For this treatment to be efficient and superior to conventional strategies, three conditions are particularly important: 1) the wavelength of the light used to irradiate the nanoparticles must have low absorption in biological material to penetrate deep into the tissue and to provide minimal damage to healthy tissue, 2) the nanoparticles must be biologically inert and small enough for systemic delivery, and 3) the nanoparticles should be efficient in converting the irradiated light into heat, i.e., the particles should be resonant with the wavelength of the irradiated light.

The research on plasmonic nanoparticle mediated photothermal therapy has so far mostly focused on the synthesis of plasmonic nanoparticles that meets the above mentioned conditions. The literature contains an extensive amount of different types of plasmonic nanoparticles spanning geometries such as stars, cubes, and rods [5], to multi-layered compositions such as the nanomatryoshkas [6], all aiming at being the best possible cancer cell killer. In these papers, pre-clinical proof-of-concept is most commonly evaluated by measuring if the tumor volume shrinks over the course of weeks using a simple mechanical caliper, which clinically is an impractical and irrelevant evaluation method.
For clinical evaluation of the tumor volume after a treatment, computed tomography (CT) has successfully been used as it provides detailed information about the anatomical development of the tumor. However, the response time is, similar to caliper-based evaluation, limited by an actual change in tumor volume that can take days before being detectable.
Positron emission tomography (PET) is a diagnostic imaging tool based on nuclear medicine, that provides feedback of the functional state of the tumor as early as an hour after a treatment. PET thereby greatly improves the timescale of tumor evaluation in contrast to CT/caliper-based assessment, that can take up to weeks.

An outstanding question in the literature regards which nanoparticle is the optimal for photothermal therapy. Importantly, the best light-to-heat converter on a single particle level might not be the best in a therapeutic context. In this thesis I compare the ability of different types of plasmonic nanoparticles to convert light into heat upon excitation, through rigorous comparison studies both *in vivo* using human tumor xenografts in mice and *in vitro* at a single particle level. The aim is to develop a protocol that can help finding the best candidate for photothermal cancer therapy.

Using CT/PET imaging as a treatment evaluation tool we compared the photothermal efficiency of silica-gold nanoshells, that are known to be near-infrared (NIR) resonant, with solid gold nanoparticles of similar diameter (= 150 nm) that are non-resonant at NIR wavelengths and thus should generate less heat upon NIR irradiation. We used NIR light as it represents a wavelength region with low absorption in tissue and deep penetration depth. The size of the nanoparticles might have a large impact on the photothermal effect as tumor

accumulation upon systemic administration increases for smaller nanoparticles (< 100 nm). Therefore we included a class of smaller solid gold nanoparticles (diameter = 80 nm) that are also not NIR resonant but might possess the same photothermal capabilities as the larger silica-gold nanoshells simply because they accumulate better at the tumor site.

We also conducted *in vitro* investigations focusing on the temperature increase of the individual nanoparticles as the *in vivo* studies "only" give information about the heating capabilities of a cluster of nanoparticles. *In vitro* we used an assay based on a temperature sensitive biological matrix to assess the surface temperature of a single irradiated nanoparticle.

The presented comparative study is a novel strategy to quantify the photothermal effect at a single particle level as well as in a therapeutic context and can be used to evaluate any type of nanostructure and different tumor models.

Chapter 2

Light and plasmonic nanoparticles

Gold in bulk form has always been highly valuable and a source of fascination for mankind. Its popularity is evident in its abundant use for jewelry, coinage, ancient treasures, and electrical devices for over thousands of years. Gold's low reactivity prevents it from oxidation and corrosion which is why it retains its beautiful appearance and luster for a very long time. However, on the nanoscale gold exhibits very different properties than in bulk giving gold colloids the most beautiful colors when interacting with light. Whether or not the physical properties were actually understood, craftsmen back in ancient time used metallic colloidal nanoparticles to stain glasses. One example is the Lycurgus cup from the 4th century that changes color dependent on which side the light is coming from. Later on the techniques were refined and the beautiful windows seen in middle Age churches all over Europe are great examples of how skilled the craftsmen were.

The first documented physical description of the unique, colorful properties of metallic nanoparticles was introduced by Faraday in 1857 [7]. A little more than 50 years later these properties were explained theoretically by Mie, who formulated the scattering and absorption properties of irradiated spherical nanoparticles by solving Maxwell's equations [8]. It should be mentioned, that despite the great theoretical work, the optical properties of metallic nanoparticles are not yet fully understood.

Utilizing the unique optical properties, modern nanomedincine has vastly expanded the scope of biomedical applications of metallic nanoparticles. Amongst others, their strong scattering properties are used for light imaging-based diagnostics and their strong absorption properties make them efficient light-to-heat converters for photothermal therapy.

2.1 The biological transparency window

Light is electromagnetic radiation that carries energy in packages of photons. The energy of a photon, $E = hc/\lambda$, is a function of the wavelength λ, where h is Plancks constant and c the speed of light. The inverse relation between energy and wavelengths means that ultraviolet light (λ = 200 - 400 nm) carries a lot of energy compared to NIR light (λ = 700 - 1100 nm). The width of biomedical applications that can take advantage of the unique interactions between light and plasmonic nanoparticles is fully dependent on the choice of the wavelength. Figure 2.1 shows the absorption spectrum as a function of wavelength of some of the most abundant molecules in tissue. Deoxyhemoglobin (Hb) and oxyhemoglobin (HbO_2), and the natural skin pigment melanin absorb strongly in the ultraviolet and visible (UV-VIS) region whereas water (H_2O) starts absorbing significantly beyond 2000 nm.

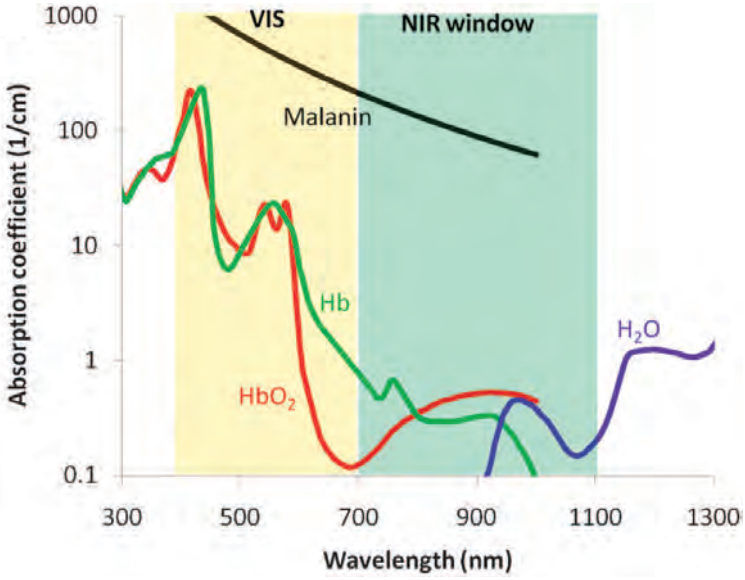

Figure 2.1: The biological transparency window. The graph shows absorption of biological materials as a function of wavelength. The components of biological tissue that are known to have highest absorption and abundance are shown. The region where the absorption spectra dip (marked by a green box) is known as the biological transparency window. Reproduced from Ref. [9].

As is seen in the absorption spectra (Fig. 2.1), there is a dip from around 700 - 1100 nm. This is the region known as the biological transparency window and represents wavelengths where light can penetrate as deep as up to several centimeters through the tissue [10]. Besides deep penetration, low tissue absorption also means that photo-induced damage is minimal. Unspecific tissue absorption can have severe consequences as in the case of radiation therapy where photo toxicity in healthy tissue is an inherent problem (radiation therapy uses wavelengths in the picometer range). Taking together the penetration depth and low photo toxicity, the NIR region has become the preferred wavelength range of light for plasmonic nanoparticle applications.

2.2 Surface plasmons

The emergence of surface plasmons in metallic nanoparticles

Metallic nanoparticles exhibit unique optical properties that are absent in bulk materials. These unique optical properties arise as a consequence of the collective oscillations of the free electrons in the conduction band; a phenomenon know as plasmons [11]. When the length scale of the free electrons, i.e., the mean free path, is of the same order as the dimension of the material structure, surface effects dominate resulting in surface plasmons [12].

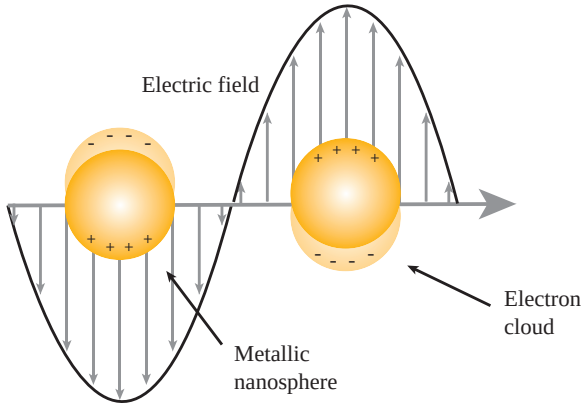

Figure 2.2: Light resonant with the surface plasmon resonance leads to collective oscillations of the free electrons in the conduction band.

When a wavefront of an electric field interacts with a plasmonic nanoparticle the free electron cloud is polarized to one side of the particle (see Fig. 2.2). The polarizability of the particle's surface causes uncompensated charges on the opposite side of the particle resulting in a restoring force, that sets up standing oscillations of the surface plasmons. If the frequency of the incident light is resonant with the particle's surface plasmons, this will cause standing resonance conditions resulting in a strong enhancement of the optical properties. Changing the boundary of a nanoparticle that possesses surface plasmons, such as its geometry or size, will alter the electron density on the surface, and thereby induce a shift in the surface plasmon resonance.

In the simplest form, the optical response of plasmonic nanoparticles to an electric field is characterized by a harmonic oscillator. In this formulation the interactions between the surface plasmons in the nanoparticle and an incoming electric field can be described by a linear local approximation given by [11]:

$$\mathbf{D}(\mathbf{r},\omega) = \epsilon(\omega)\mathbf{E}(\mathbf{r},\omega) \ , \tag{2.1}$$

where $\mathbf{D}(\mathbf{r},\omega)$ is the electric displacement at position $\mathbf{r}$ and at the frequency of the incoming

field, ω. $\mathbf{E}(\mathbf{r},\omega)$ is the electric field and $\epsilon(\omega)$ is the dielectric function. By solving Maxwell's equations, using appropriate boundary conditions and the dielectric function, the linear optical response of the nanoparticle can be derived.

Surface plasmon resonance

In practice, it is not as simple as that. However, for particle sizes comparable to the electron mean free path, it is sufficient to solve the Maxwell equations using a combination of the dipole approximation, formulated by Rayleigh, and the Drude model [13]. Within the Rayleigh approximation, the extinction cross-section gives the amount of scattering and absorption of a particle embedded in a dielectric medium with permittivity ϵ_m at a wavelength λ. The extinction cross-section is written as the sum of the scattering and absorption cross-sections:

$$C_{ext} = C_{scat} + C_{abs} = \frac{k^4}{6\pi}|\alpha|^2 + k\mathrm{Im}(\alpha) \ , \tag{2.2}$$

where k is the wavenumber, $k = 2\pi\sqrt{\epsilon_m}/\lambda$. α is the polarizability of the particle and describes how much charge separation can be obtained within the particle when exposed to an external electric field. The polarizability of a nanoparticle, with a radius of a and volume of $V = 4\pi a^3/3$, is extracted from the Clausius-Mossotti relation:

$$\alpha = 3V\frac{\epsilon(\omega) - \epsilon_m}{\epsilon(\omega) + \varphi\epsilon_m} \ . \tag{2.3}$$

Here, φ is a shape dependent parameter. The dielectric function, $\epsilon(\omega)$, contains the electronic structure of the particle. For metallic nanoparticles the dielectric function is complex, $\epsilon(\omega) = \epsilon_1(\omega) + i\epsilon_2(\omega)$ [14], and can be expressed by the Drude approximation [11]:

$$\epsilon(\omega) = \epsilon_{ib} - \frac{\omega_p^2}{\omega(\omega + i\gamma_b)} \ . \tag{2.4}$$

ϵ_{ib} is the electronic interband transitions contribution, and ω_p is the plasmon frequency of bulk gold. $\gamma_b = l_b/v_F$ is the damping of the conduction electrons in bulk gold, where l_b is the electron mean free path and v_F the Fermi velocity.

Surface plasmon resonance is obtained when the absorption and scattering cross-sections are at their maximum. From eq. 2.2 we can extract that resonance conditions are met when α is at its maximum, i.e., $\epsilon(\omega_{max}) = -\varphi\epsilon_m$ (see eq. 2.3) [15]. Inserting this into eq. 2.4 and using $\gamma_b \ll \omega_p$, gives the plasmon frequency resonance and the corresponding resonance

wavelength [15, 16]:

$$\omega_{max} = \frac{\omega_p}{\sqrt{\epsilon_{ib} + \varphi\epsilon_m}} , \quad \lambda_{max} = \lambda_p\sqrt{\epsilon_{ib} + \varphi\epsilon_m} . \tag{2.5}$$

$\lambda_p = 2\pi c/\omega_p$ is the plasmon wavelength in bulk gold. The shape dependent parameter for spheres is $\varphi = 2$. For thin metallic shells (total radius of a) with a dielectric core (radius of a_c) φ takes the form [11]:

$$\varphi = \frac{3}{f_s}(1 + \epsilon_c/2\epsilon_m) . \tag{2.6}$$

f_s is the volume fraction of the shell given by $f_s = 1 - (a_c/a)^3$, and ϵ_c the dielectric permittivity of the core. As eq. 2.6 is dependent on the fraction between the core and the shell radius, it directly explains why the plasmon resonance (eq. 2.5) for nanoshells can be tuned (unlike for spheres where $\varphi = 2$). The tunability of the resonance will be discussed further in the next section.

The resonance equations are valid only for the dipole resonances. For multipole resonances ($n > 1$), equation 2.5 is corrected to:

$$\omega_n = \frac{\omega_p}{\sqrt{\epsilon_{ib} + \epsilon_m((n+1)/n)}} . \tag{2.7}$$

Multipoles are primarily of consideration when the particle size becomes bigger. For example, for spherical gold nanoparticles the quadropole peaks emerge when the diameter exceeds $\approx$ 100 nm [11].

It should be mentioned that the derivations above in principle only apply to particles that are smaller than the mean free path of plasmon electrons in gold ($l_b \sim$ 40 - 50 nm). For larger particles the dielectric function becomes size dependent, $\epsilon(\omega, a)$, and should correctly be expressed by the size-corrected Drude model to account for enhanced electron-scattering events [11, 12].

Designing the surface plasmon resonance

The optical properties near the surface plasmon resonance are significantly enhanced compared to off-resonance. This is because the scattering and absorption cross-sections of the plasmonic nanoparticles are enhanced by orders of magnitude. As just discussed, the scattering and absorption cross-sections are functions of the polarizability, that depends on factors including size, shape and material composition of the plasmonic nanoparticles. Hence, by changing any of these parameters, the surface plasmon resonance described by eq. 2.5 can be shifted, enabling us to design "the optimal" NIR resonant plasmonic nanoparticle for

biomedical applications.

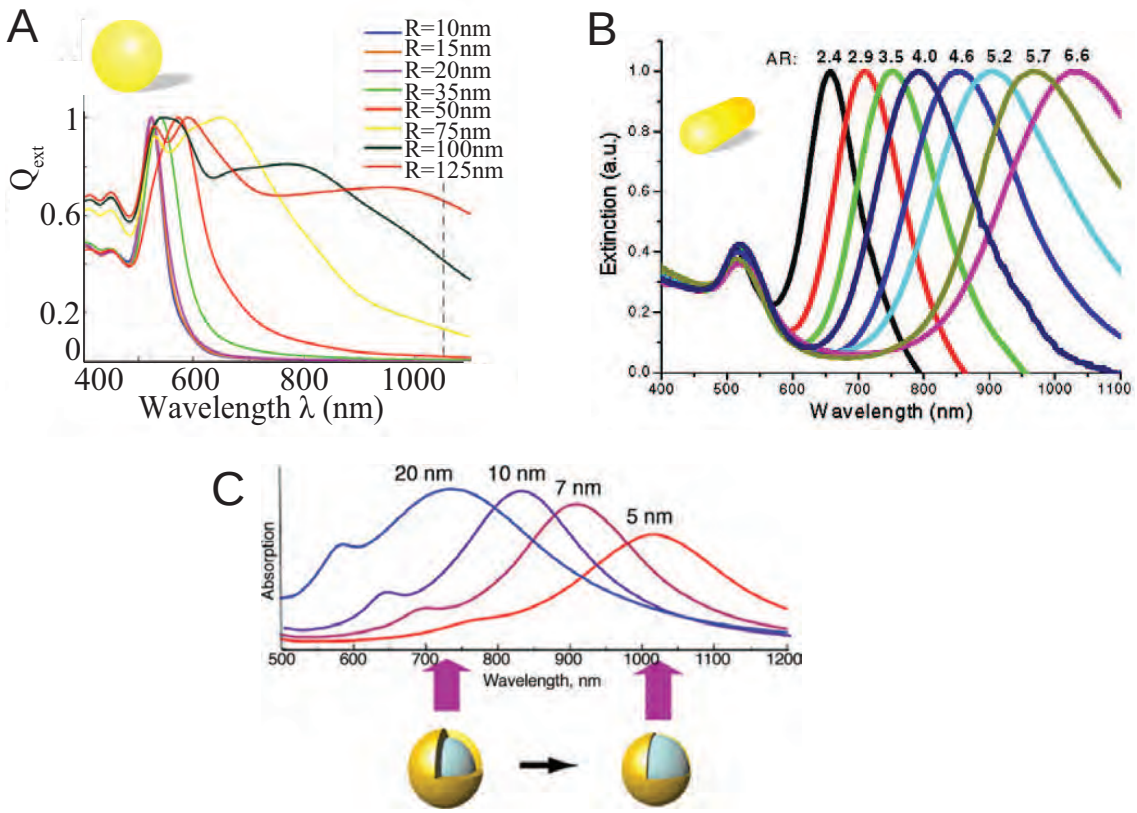

Figure 2.3: Extinction spectra of different types of gold nanoparticles. **(A)** Spectra of different sizes of colloidal gold nanoparticles calculated using Mie's equations. The surface plasmon resonance is only slightly red-shifted but broadened substantially due to increased scattering contributions. The dashed line indicates the laser wavelength of 1064 nm that we use in our *in vitro* studies. Reproduced from our review in Ref. [14]. **(B)** Spectra of gold nanorods. The longitudinal plasmon resonance red-shifts with increasing aspect ratio (AR). Reproduced from Ref. [17]. **(C)** Absorption spectra of silica-gold nanoshells. The plasmon resonance red-shifts when the gold shell is made thinner indicated by an arrow. Reproduced from Ref. [18].

Colloidal gold nanoparticles are simple spherical structures with a solid gold core. They have a surface plasmon resonance in the visible region, shown for various sizes of colloidal gold nanoparticles in Figure 2.3A. When increasing the diameter of the colloidal gold nanoparticles, the resonance peak is red-shifted accordingly and broadened, due to phase retardation and size-dependent increased scattering effects [19]. Phase retardation comes from the increasing amplitude of the free electron oscillations as the particle size increases. Larger amplitudes extend the period of the plasmon oscillations which means that the plasmon frequency becomes red-shifted. The magnitude of the red-shifts for colloidal gold nanoparticles is minimal, meaning that even for the largest colloidal gold nanoparticles a resonance in the NIR region is unachievable [14, 20].

What does change when increasing the particle size, is the relative contribution from scattering and absorption to the extinction cross-section. The scattering cross-section scales

quadratically with the polarizability (see eq. 2.2), which is proportional to the volume (see eq. 2.3). This means that smaller nanoparticles mainly absorb whereas for larger nanoparticles the scattering contribution dominates. The turnover point at which the contributions of absorption and scattering are equal is 80 nm for colloidal gold nanoparticles [11].

The resonance is also highly dependent on the shape of the gold nanoparticle via the shape parameter φ in eq. 2.5. A good example of the shape-dependence is given in the case of gold nanorods where the optical properties can be changed dramatically simply by elongating the rod. Gold nanorods exhibit two well-separated plasmon peaks; one corresponding to the short axis and one corresponding to the long axis (see Fig. 2.3B). The short resonance peak is due to the dipole plasmon resonance similar to the resonance of colloidal nanoparticles (around 528 nm) [20]. The longer resonance peak emerges from the plasmon oscillations along the longitudinal axis of the rod and can be shifted by changing the aspect ratio of the gold nanorod. Due to this tunability, NIR-resonance can be achieved simply by changing the length of the rod while keeping the width fixed.

Plasmonic nanoparticles that are composite structures, such as silica-gold nanoshells, also exhibit a high degree of plasmon resonance tunability (see Fig. 2.3C). The shape dependent parameter for thin metallic shells (φ in eq. 2.6) is inversely proportional to the volume fraction, $f_s = 1 - (a_c/a)^3$, for thin metallic shells with core radius a_c and a total radius a. As the shell becomes thinner, φ becomes larger leading to an increase of λ_{max} (see eq. 2.5). In total, this means that the plasmon resonance can be tuned by changing the ratio of the core to the shell radius; red-shifting when decreasing the shell thickness and blue-shifting when increasing the shell thickness.

Effect of plasmon hybridization

When nanoparticles are injected into living subjects and accumulate in the tumor tissue, they are most often not present as single nanoparticles but as clusters of nanoparticles. The plasmon resonance of a nanoparticle is sensitive to the vicinity of another nanoparticle and alters significantly when the plasmonic nanoparticles are close enough to interact.

If we consider two identical spherical particles approaching each other, their individual surface plasmons can couple and start oscillating in phase. When the interparticle separation is short enough, multipole resonances emerge that are well-separated from the dipole resonance of the individual single particles [21]. Hence, the short-wavelength plasmon resonance corresponds to that of a single particle and the long-wavelength plasmon resonance to that of the electrodynamic coupling between the two spheres.

The effect of plasmon hybridization is well-explained by considering metallic spheres arranged in a chain. The long-wavelength resonance is dependent on the number of particles in the

chain, similarly to the length dependence for nanorods. In addition, it is also highly senstive to the strength of the plasmon coupling which is a function of the interparticle distance. As the length and plasmon coupling increases, the long-wavelength resonance red-shifts. However, the coupling effect saturates as the number of particles in the chain increases because the effective electrodynamic interactions are finite. For metallic spheres with a diameter of 40 nm this saturation happens at around 10 particles [22].

Mechanism of heat generation

In photothermal cancer therapy, the absorption of a strong light source by plasmonic nanoparticles and the corresponding abrupt temperature increase on the nanoparticles' surfaces is exploited to kill cancer cells in the vicinity. The underlying process of this extreme temperature increase can be explained by non-linear optical effects (shown in Figure 2.4) [19, 21].

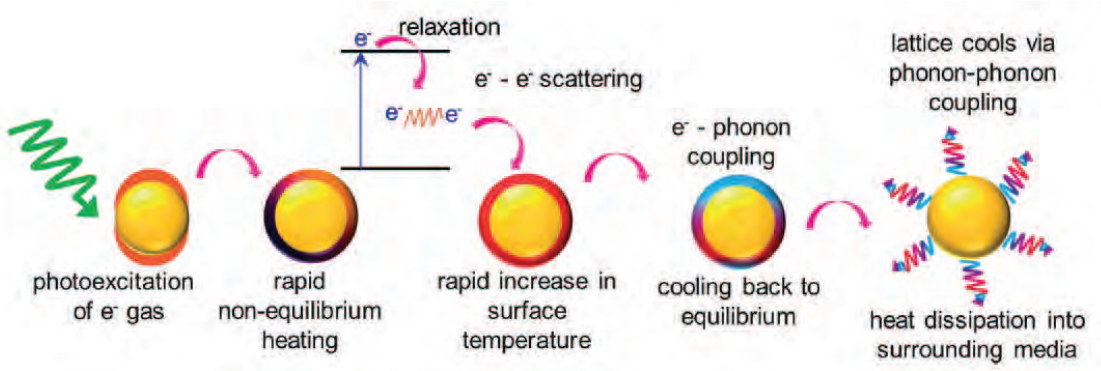

Figure 2.4: Schematic illustration of the light-to-heat conversion upon photon absorption of a plasmonic nanoparticle. This whole process takes on the order of a couple of hundreds of picoseconds. Reproduced from Ref. [19].

When resonant light is absorbed by the nanoparticle, the plasmons are rapidly excited into a non-equilibrium thermal state creating hot electrons [23]. Because hot electrons have an energy level above the thermal state, they rapidly redistribute their energy amongst lower-level electrons via electron-electron scattering and relax into a thermal distribution. This process effectively increases the surface temperature of the nanoparticle on a time scale of picoseconds. The hot surface cools to equilibrium by heat exchange with the lattice phonons through electron-phonon scattering. Finally, the lattice cools via heat exchange with the local environment through phonon-phonon coupling on a timescale that depends on the heat capacity of the environment, and the material and size of the particle ($\approx$ hundreds of nanoseconds for a 80 nm gold nanoparticle embedded in water [24]).

The temperature increase of irradiated plasmonic nanoparticles is very high, but the corresponding heating profile is narrow compared to the dimensions of a cell. Bendix et al. found that even though gold nanoparticles in the size range of 200 nm reached temperature

elevations of 250 K when irradiated with a 1064 nm continuous wave laser, the size of the temperature profile was only on the order of ≈ 10 μm (power = 100 mW) [25]. In addition, it was found that the temperature elevation was already at 50% only 200 nm away from the surface of the nanoparticle and at 10 K at a distance of ≈ 2 μm. This means that regardless of how much the temperature of the nanoparticle increases, the effect is so local that only cell within a couple of microns from the nanoparticles are affected.

2.3 Synthesis and optical properties of different plasmonic nanoparticles

Colloidal gold nanoparticles

Colloidal gold nanoparticles are typically produced by either the citrate reduction method or a seeding technique [26, 27]. Following the citrate reduction method, also known as the Turkevitch method (1951), tetrachloroauric acid ($HAuCl_4$) is stirred while adding citrate. Citrate is working both as a reducing and as a capping agent. This method only applies for fabrication of smaller sizes of gold nanoparticles (10-20 nm) as the monodispersity and shape are compromised by risk of aggregation when the particles are grown larger (producing elongated nanoparticles).

To synthesize larger colloidal nanoparticles, the seeding technique can be used instead. First the seeds are produced by generating very small gold nanoparticles. These work as nucleation sites and facilitate the reduction of the remaining gold ions from a growth solution consisting again of gold salt and a reducing agent. For both methods, the growth continues until all of the reducing agents or gold ions are depleted.

Figure 2.5 shows the quality and optical properties of the colloidal gold nanoparticles used in this study. We have taken transmission electron microscopy (TEM) images of the 80 nm and 150 nm nanoparticles, shown in Figure 2.5A-B, respectively. This was done to validate that they are fairly uniform in size and shape. The suppliers reported a diameter for the 80 nm of 81.7 nm $\pm$14% (Nanocomposix, CA USA) and a diameter for the 150 nm of 150 nm $\pm$4% (Nanopartz, CO USA), both measured by TEM.

I have also calculated the extinction spectra for these two particle sizes using Mie equations, shown in Figure 2.5C. The calculated spectrum for the 80 nm nanoparticles has a plasmon resonance of $\approx$ 548 nm. This is in good agreement with the plasmon resonance that the suppliers have measured to be 550 nm, using a UV/VIS spectrometer. The nanoparticles with a diameter of 150 nm have a calculated plasmon resonance of $\approx$ 650 nm, that compared to that the suppliers measured of 615 nm, also is in good agreement. In the calculated spectrum

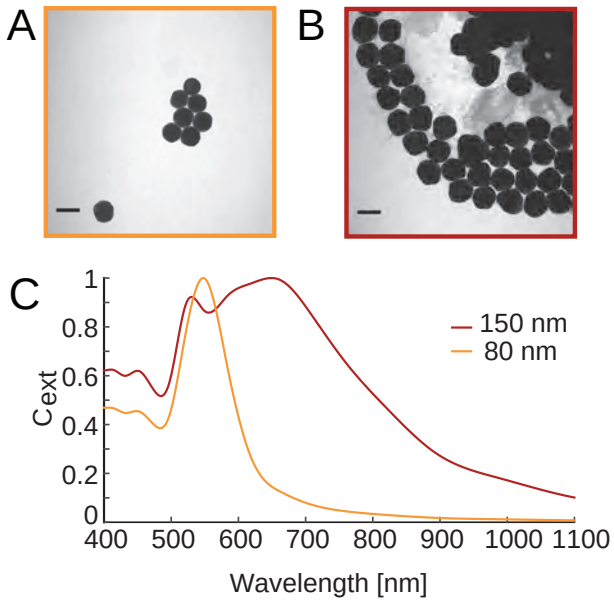

Figure 2.5: Characteristics of the colloidal gold nanoparticles used in this study. TEM images of **(A)** 80 nm and **(B)** 150 nm colloidal gold nanoparticles. Scale bar is 100 nm. **(C)** Extinction cross-sections calculated using Mie's theory; it can be seen that the plasmonic resonance is at 548 nm and 650 nm for the 80 and 150 nm colloidal gold nanoparticles, respectively. The spectra have been normalized.

for the 150 nm nanoparticles, the quadropole peak described by eq. 2.7, emerges around 530 nm and spectral broadening that stems from increased scattering effects is observed. In contrast, the calculated spectrum for the 80 nm nanoparticles exhibits only a narrow resonance peak (the dipole peak).

The nanoparticles used in this study are conjugated with a polymer, poly(ethylene glycol) (PEG), to protect them from aggregation in physiological conditions and prevent them from *in vivo* degradation. The polymer conjugation does not affect the plasmon resonance (if it does it is only a shift on the order of 5 - 10 nm), however, it serves to stabilize the particles and to minimize aggregation. The quality of the polymer conjugation can be assessed by the particle's zeta potential that is a measure of the surface charge of the particle. A good polymer conjugation is screening the particle's surface charges, thereby making it more neutral. These nanoparticles have zeta potentials around -20 mV which is within a reasonable range for biological systems.

Silica-gold nanoshells

In 1998 Naomi Halas and her group at Rice University, Texas, developed silica-gold (core/shell) nanoshells to overcome the resonance limitations of colloidal gold nanoparticles [18]. They showed that the plasmonic resonance for these particles could be tuned across the NIR range

by changing the core/shell ratio. At my stay in the Halas group, I first learned how to synthesize these particles. Briefly, the nanoshells consist of a dielectric core (silica) grown as monodispersed spheres by the Stöber method [28]. The spheres are functionalized by coating them with aminopropyltriethoxysilane (APTES). After their amination, gold seeds (1-2 nm) are added which attach to the amine groups. A complete gold shell is formed by reduction of $HAuCl_4$ using the gold seed-decorated silica sphere as nucleation site. Using this method, both the size of the core and the shell can be controlled (however, the size range is limited to between 80 and 400 nm [16]). Smaller cores give plasmon resonances in the visible region, but by increasing the size of the core, and decreasing the thickness of the shell, the plasmon resonance can be shifted to wavelengths deep into the infrared [29].

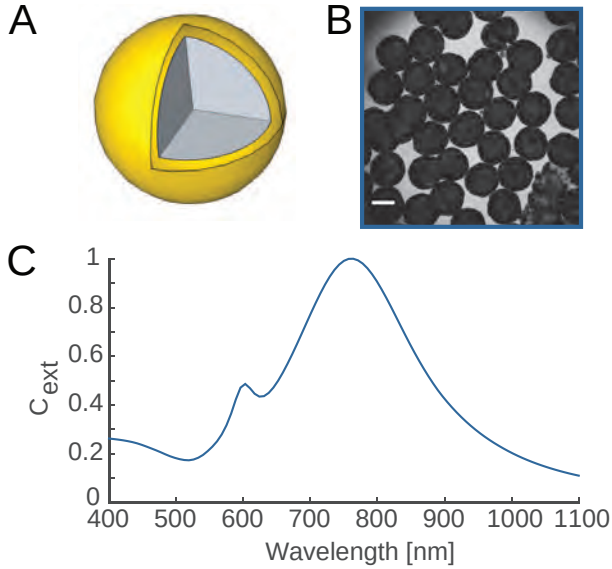

Figure 2.6: Characteristics of the silica-gold nanoshells used in this study. **(A)** Graphic showing the silica core with the thin gold shell. **(B)** TEM image of 150 nm silica-gold nanoshells. Scale bar is 100 nm. **(C)** Extinction cross-sections of 150 nm silica-gold nanoshells calculated using Mie's theory (Online Mie Theory Simulator, NanoComposix). From the spectrum it can be seen that the plasmonic resonance for the nanoshells is at 760 nm. The spectrum has been normalized.

Figure 2.6A shows a graphic of a silica-gold nanoshell. In this study we use nanoshells obtained commercially as we do not have the wet-lab facilities necessary for their fabrication. The nanoshells we use have a core consisting of a 120 nm silica sphere, upon which a thin gold shell (15 nm) has been grown, giving a total diameter of the complex of 150 nm (Nanocomposix, CA USA). We have taken TEM images of the nanoshells that are shown in Fig. 2.6B. Most particles appear uniform in size and mostly the shells are complete (no larger "holes" in the shells). The suppliers reported a diameter of 151.3 nm ±5.1%, where the core was 119.7 ± 8.9 nm assessed by TEM images (Nanocomposix, CA, USA).

Using the Online Mie Theory Simulator (NanoComposix, CA, US), I have calculated the extinction spectrum of silica-gold nanoshells with a core diameter of 120 nm and a gold shell

of 15 nm, shown in Figure 2.6C . In the calculated spectrum, the plasmon spectral band is broad with a resonance at $\approx$ 760 nm and the quadropole peak is emerging around 600 nm. The experimental spectrum that is measured by the suppliers using a UV-VIS spectrometer, have a plasmon resonance of 802 nm. The measured resonance deviates somewhat from the calculated one, but is within the biological transparency window.
Like the colloidal gold nanoparticles, the nanoshells are conjugated with PEG. The zeta potential is -27.3 mV indicating an acceptable conjugation for biological applications. The silica-gold nanoshells are very strong scatterers. In fact, the ratio between scattering and absorption efficiencies is seven. It would be advantageous to use silica-gold nanoshells with a higher absorption contribution for photothermal therapy, however these are, for the time being, the only commercially available silica-gold nanoshells.

2.4 Summary

Due to the NIR optical properties of the silica-gold nanoshells we anticipate them to be the best NIR photothermal transducers out of the nanoparticles included in this study. After this chapter it should be clear to the reader, that both of the 80 nm and the 150 nm colloidal gold nanoparticles have resonances in the visible region and their geometry supports only little tunability.

To conduct a rigorous comparison study we chose to use colloidal gold nanoparticles with an identical diameter (150 nm) as the NIR resonant silica-gold nanoshells. This was to investigate the optical advantages of NIR resonance for plasmonic nanoparticle mediated photothermal cancer therapy. The 80 nm colloidal gold nanoparticles are interesting for reasons that are connected to the biology of tumors. Tumor uptake upon systemic administration has been shown to be higher for particle sizes below 100 nm [30, 31]. Using these 80 nm gold nanoparticles, we investigate if a higher accumulation in the tumor compared to 150 nm silica-gold nanoshells could compensate for the lack of NIR resonance properties. Furthermore, studies have shown that nanoparticles accumulate in clusters in the tumor microenvironment. We investigate if the collective behavior of the 80 nm gold nanoparticles potentially can enhance the NIR optical properties, due to plasmon hybridization, such that they become relevant for photothermal therapy.

Chapter 3

Nanoparticle assisted cancer therapy and diagnosis

The expanding field of nanomedicine goes hand in hand with the advancement of synthesis techniques, allowing for design and control of nanoparticles that possess the desired properties for the aimed biomedical application. In this chapter an introduction to a tumor delivery route of nanomedicine based on intravenous injection is given, that shows great clinical potential. Gold nanoparticles are particularly interesting owing to their biocompatibility and straight-forward surface modification, making the nanoparticles promising candidates as drug and gene delivery vehicles, targeted heat transducers, or imaging based diagnostic agents [32].
Some of these strategies using gold nanoparticles directly or as carrier platforms are discussed to highlight the diversity of gold nanoparticle applications in nanomedicine. It naturally follows to discuss possible pitfalls that would prevent the approval of gold nanoparticles for clinical use. One major concern is that it still remains unclear whether the gold nanoparticles are cleared from the body on longer time scales, or if there could be any long-term toxic effects.

3.1 Progress in cancer research

Cancer is a disease where the cells have mutated such that they have abnormal growth and potentially can spread and invade other parts of the body (metastasis). Some common characteristics of cancers are that they have mutations in their anti-growth and self-destruct (apoptosis) signal pathways. They have uncontrollable and limitless replication potential, and they possess the ability to induce self-sustainment (oxygen and nutrient supply) by the

formation of new blood vessels.

In the western world, cancer is one of the most common causes of death only exceeded by heart diseases. In the US, cancer is responsible for almost one of every four deaths, and The American Cancer Society predicts that there will be about 1.7 million new cancer cases in 2015 alone [33].

As a consequence of the extensive research in cancer and development of new therapeutic/-diagnostic strategies, the 5-year survival rate has increased from 49% in the years 1975-1977 to 68% in the years 2004-2010 [33]. These numbers are evidence of great advancement in cancer research, but there is still a pressing need for improving screening for early detection, diagnosis, and treatment of cancer. New strategies should be aimed at improving clinical outcome and decreasing side effects. Standard strategies include surgical removal, chemotherapy, and radiation therapy. Even though these strategies have shown remarkable enhancement of survival rates, they all still suffer from limitations; surgery from the limited accessibility of tumors, chemotherapy is associated with severe side effects and illness for the patient, and radiation therapy is extremely invasive to healthy tissue in the path of the radiation.

NIR laser-mediated photothermal therapy using plasmonic nanoparticles has emerged as a potential treatment strategy within the last decade. This technique offers a high selectivity and kills cancer cells by localized hyperthermia, overall decreasing side effects.

3.2 Delivery of nanoparticles to the tumor

Once a tumor reaches a certain volume, there is an increased demand for nutrient and oxygen supply. This triggers angiogenesis, the formation of new blood vessels, a process that plays a key role in the delivery of nanoparticles to tumors (see Fig. 3.1). The ability to trigger angiogenesis is vital for tumor progression and metastasis.

Enhanced permability and rentention effect

The formation of new vasculature allows the tumor to grow and metastasize but it also gives the tumor a "kink in its amour". The enhanced permeability and retention (EPR) effect arises as a consequence of excessive growth rate where the newly formed blood vessels are leaky and abnormal in form (see Fig. 3.2). Small holes in the vasculature enable extravasation of small particles from the blood to the tumor tissue [31]. Effectively, the tumor and its leaky vasculature functions as a sieve for nanoparticles circulating with the blood flow.

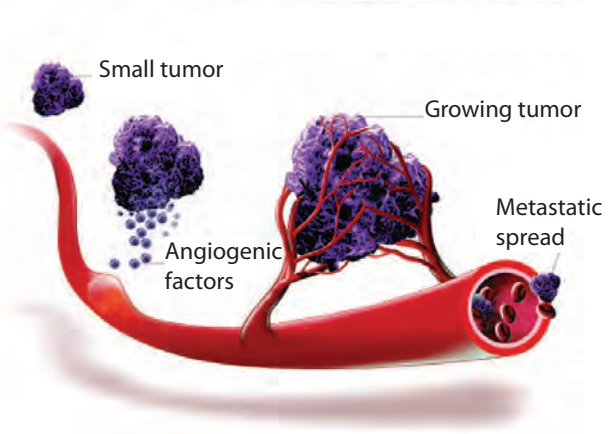

Figure 3.1: Tumor angiogenesis. As the growing tumor reaches a certain size it requires nutrients and oxygen supply. By releasing angiogenic growth factors the tumor can promote sprouting from existing blood vessels, building a scaffold of new vessels that support the tumor and allow metastatic spread. Downloaded from http://medicalart-work.co.uk.

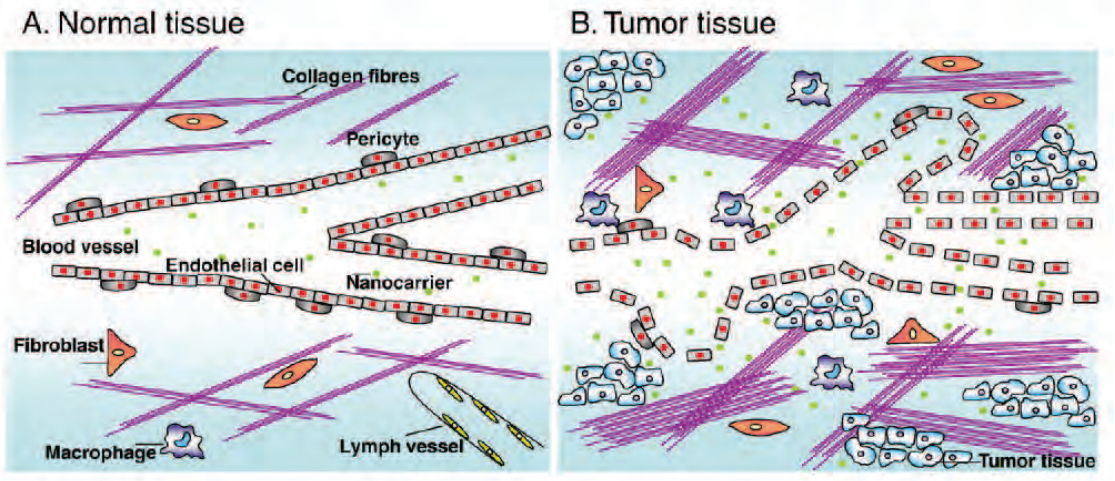

Figure 3.2: Illustration of the enhanced permeability and retention (EPR) effect. Normal tissue has well-structured blood vessels with the endothelial cells tightly connected. The normal vasculature provides a prohibitive barrier between the tissue and the blood. In the tumor tissue, the blood vessels are malformed leading to changes in the blood flow. There are large junctions between the endothelial cells allowing nanoparticles to diffuse into the tumor. A lack of lymphatic vessels prevents drainage of internalized nanoparticles. Reproduced from Ref. [19]

Even if the particles are small enough to diffuse throughout the tissue, effective uniform delivery of nanoparticles to the tumor microenvironment is complicated. Rapidly proliferating tumor cells and poor lymphatic drainage create interstitial hypertension and hypo-perfused regions mostly in the center of the tumor, eventually leading to hypoxic and necrotic regions when the tumor gets large enough. These conditions usually lead to a non-uniform distribution of the nanoparticles in the tumor, and especially for large tumors the nanoparticles are mostly found in the periphery or around the vasculature [34].

Biodistribution

When assessing the delivery of nanoparticles to the tumor after systemic administration it is common to perform a biodistribution study. The goal is to optimize the characteristics of the nanoparticles (i.e., the size, surface modifications, and charge) so that upon systemic administration, nanoparticle accumulation is enhanced in the tumor while avoided in healthy tissue. In normal vasculature the endothelial cell layer lining the blood vessels act as a barrier between the blood and the tissue (see Fig. 3.2). This prevents undesired penetration of potentially malicious molecules in the blood from entering healthy tissue.

In a typical biodistribution study in mice, the nanoparticles are injected via a tail vein and allowed to distribute throughout the body. After a certain time period (typically ≈ 24 hours) the animals are euthanized and their organs harvested. The gold content in the tissue is often measured with inductively-coupled plasma mass spectrometry (ICP-MS). ICP-MS has very low detection limits for gold (18 parts per trillion), permitting very rigorous quantification in biological specimens.
In the literature, it is consistently proven via ICP-MS studies that the liver and spleen have the highest uptake of gold nanoparticles in the size range from $\sim$ 20 - 150 nm [30, 35, 36]. Considering the biological function of the liver and spleen this is no surprise as they basically "rinse" the blood from antigens and foreign intruders by mechanical filtration. Subsequent to the liver and spleen, the tumor shows a much higher gold content than any other organ. Finally tissues such as brain, muscle, heart and lung show essentially no uptake of gold. As systemic administration is a clinically favorable method, the low uptake in vital organs and high tumor accumulation is promising for the therapeutic use of gold nanoparticles.

Optimizing tumor accumulation

The tumor accumulation and the tissue depth that the nanoparticles can achieve by diffusion depends primarily on three parameters; size, shape, and charge. The permeability of the tumor vasculature is inverse to the particle size, as it essentially is the pore size in the endothelial layer that constitutes the limitations [37]. Plasmonic nanoparticles in the size

range of 20 - 100 nm can easily diffuse through the vascular pores. Particles as large as 200 nm can also slip through the pores although with a much smaller probability [38]. Intuitively, inside the tumor smaller particles should give a more uniform distribution as they diffuse better. However, in tumors with high interstitial pressure, large particles are retained better, though closer to the vasculature [31, 39].

In general, tumor accumulation increases with prolonged circulation time in the blood. The key to prolonging the circulation time is to protect the nanoparticle from degradation and clearance by the reticuloendothelial system (RES) in the liver and spleen. The RES system is a part of the immune system, responsible for trapping and removing foreign particles. The RES system consists of macrophages that are cells responding to serum proteins adsorbing to the nanoparticles, known as opzonization, and are capable of removing the particles from the blood. Serum protein adsorption will begin immediately after the nanoparticles are injected into the blood but can be circumvented or delayed by "stealthening" the particles. PEG is a polymer known for its ability to stabilize nanoparticles *in vivo* [30, 31]. PEG neutralizes the charged surface of gold nanoparticles and prevents aggregation of the particles in physiological conditions. In addition, PEG reduces opsonization by sterically hindering serum protein adsorption, hence masking the particles from the RES system. Because of its ability to prolong circulation times, PEG is widely used in the pharmaceutical industry to protect small molecules and drugs.

The surface chemistry of gold shows strong binding affinity for thiols, disulfides, and amines allowing easy functionalization with targeting or therapeutic biomolecules, such as peptides, DNA, and proteins [35]. The most common conjugation scheme is through thiolation (Au-S bond), where the molecule that needs to be attached either naturally holds a thiol group or has a synthetic thiol group incorporated. Thiolated PEG molecules are easily conjugated to the gold nanoparticles, a process known as PEGylation. In the next section I will go through some conjugation schemes, in addition to PEGylation, that enable synergestic therapeutic strategies.

3.3 Gold nanoparticles as a multi-strategy platform

As illustrated in Figure 3.3 gold nanoparticles have unique physical and chemical properties that make them applicable both in therapeutics and diagnostics relations (or the combination of the two known as "theranostics"). The great potential in using gold nanoparticles as carrier platforms for therapeutic molecules is due to their easy surface modification, as well as their high tumor accumulation and intracellular uptake. In addition, release of ther-

apeutics from plasmonic nanoparticle carriers can be achieved using an external source such as NIR light, with high spatiotemporal control within the tumor or even inside cancerous cells. For some therapeutics, such as chemotherapeutics, combining the drug with a plasmonic nanoparticle carrier could promote the applicability of a drug that would otherwise be discarded due to a too high toxicity or a too low tumor delivery, which is the case for many water insoluble drugs and nucleic acids.

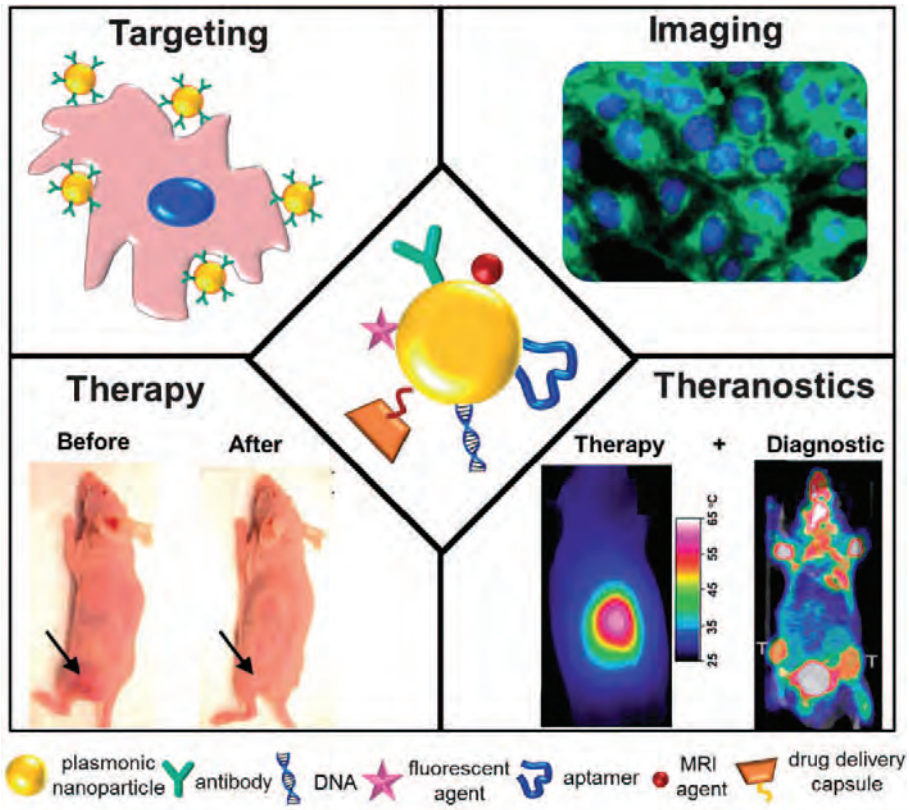

Figure 3.3: Illustration of different types of conjugation schemes and applications. Reprinted from Ref. [19]

Passive and active targeting

Before going into the different applications shown in Figure 3.3, I will first elaborate a little further on the subject of tumor delivery and methods used to increase the tumor accumulation. As stated before it is essential to optimize the accumulation in the tumor site to lower the long-term side effects and to increase the photothermal efficiency. Passive targeting simply means to inject the passivated (PEGylated, etc.) nanoparticles intravenously and allow them to accumulate at the tumor site via the EPR effect. Because of the PEGylation, the recognition of the RES system in blood, liver, and spleen is decreased, which ultimately increases the blood circulation time and thereby the accumulation in tumor tissue.

Passive targeting through the EPR effect has become the standard delivery method in nanomedicine for cancer therapy. Moreover, to get higher specificity it is common to attempt to actively target the nanoparticles against cancer specific proteins. Especially for cancer, immunotargeting has been widely used because many cancer cells show a different surface receptor profile compared to healthy cells [37, 40–43]. Nanoparticles conjugated with antibodies, peptides or aptamers that recognize receptors overexpressed in cancer cells, on the tumor vasculature, or other components of the tumor microenvironment have been widely exploited for selective targeting.

One way of benefiting from active targeting is through endocytosis-related receptors that promotes cellular uptake [37, 43]. Endocytosis is a mechanism a cell uses for uptake of nutrients and other large molecules, such as signaling proteins and receptors. The cell engulfs the molecules when in contact with the cell membrane, by budding and forming a large vesicle that is internalized. The uptake rate varies from cell type to cell type, but there is a general trend that smaller nanoparticles (20-50 nm) are taken up faster than larger nanoparticles (up to $\approx$ 100 nm) [44, 45].

El-Sayed et al. used anti-EGFR antibody conjugated gold nanoparticles to show specific uptake in oral cancer cell cultures expressing EGFR receptors that enhanced the photothermal laser ablation in comparison to non-cancerous cells [40, 42]. Loo et al. used anti-HER2 antibody conjugated nanoshells for scattering based imaging and photothermal ablation of HER2-expressing breast cancer cell cultures [41]. In these studies it was also shown that cancerous cell lines incubated with non-conjugated nanoparticles, suffered a much lower degree of photo-induced damage, demonstrating the great advantage in active targeting.

Imaging agent

Plasmonic nanoparticles are great contrast agents for scattering-based imaging and show promising potential for diagnostic applications, such as optical coherence tomography, x-ray based computed tomography, and two-photon-induced photoluminescence [46–48]. Because of their enhanced scattering properties at their resonance wavelengths, plasmonic nanoparticles have a superior optical signal that exceeds that of conventional dyes by orders of magnitude. Unlike conventional contrast agents based on fluorescent dyes or endogenous chromophores, plasmonic nanoparticles also do not photobleach.

The diagnostic capabilities can in the same plasmonic nanoparticle be combined with a therapeutic approach, a concept known as theranostics. The multifunctionality of theranostic nanoparticles was demonstrated by Bardhan et al. using a nanoshell-based complex doped with iron oxide and NIR fluorophores. The novel theranostic nanoparticles enabled deep tissue imaging with magnetic resonance imaging (MRI) and NIR fluorescence imaging

meanwhile performing photothermal therapy [43, 49]. Following active targeting, achieved by antibody conjugation, the nanoparticle complexes could be tracked with high resolution before, during, and after photothermal treatment.

More relevant for our comparative studies is that the gold nanoparticles can be conjugated with PET isotopes [5] and aimed at stratified therapy. This is a personalized medical approach trying to predict which treatment the patient's cancer responds best to by identifying its genetic properties, e.g., its receptor profile that can be targeted. All in all, multifunctional plasmonic nanoparticles can provide important information that in clinic can ease translation and allow immediate response to the diagnosis.

Gene therapy

Successfully delivered oligonucleotide therapeutics such as singlestranded DNA, antisense DNA, short interfering RNA, and micro RNA (miRNA) have the ability to silence or destruct their targeted pathogenic genes and consequently down-regulate their encoded proteins. Unfortunately, the applicability of gene therapy using oligonucleotides has been limited by their low stability *in vivo* due to enzymatic digestion and low cellular uptake. To obtain a gene regulatory effect of oligonucleotides, they must be safely routed to their target site, pass the cell membrane barrier, and reach their intracellular target while still being functional.

As mentioned earlier, gold nanoparticles are exactly in the size range suitable for cellular uptake via endocytosis and therefore show great potential as a carrier platform of oligonucleotide therapeutics to the interior of cells [50,51]. Oligonucleotides are easily modified with thiols and conjugated to gold nanoparticles, which protect them from degradation.

Endocytosed gold nanoparticles are trafficked in endocytic vesicles to different compartments inside the cell. The lysosomes are considered to be the terminal compartment of the endocytotic pathway and have a highly aggressive environment responsible for degrading the content delivered by the endosomes. Figure 3.4 shows a study we conducted on neuroendocrine cancer cells confirming that over time, endocytosed 60 nm colloidal gold nanoparticles co-localized with the lysosomes [52].

Because of the dismal future if delivered to the lysosomes, gold nanoparticles carrying a therapeutic payload must escape the endosomes to prevent enzymatic degradation of the payload. Furthermore, the functionality of most therapeutic molecules requires release from the surface of the gold nanoparticles. Irradiating the nanoparticles with resonant laser light triggers photothermal release of the therapeutic oligonucleotides and endosomal rupture letting the oligonucleotides into the cytosol where they have their therapeutic effect [53].

The opportunity of combining photothermal cancer therapy with a therapeutic release is

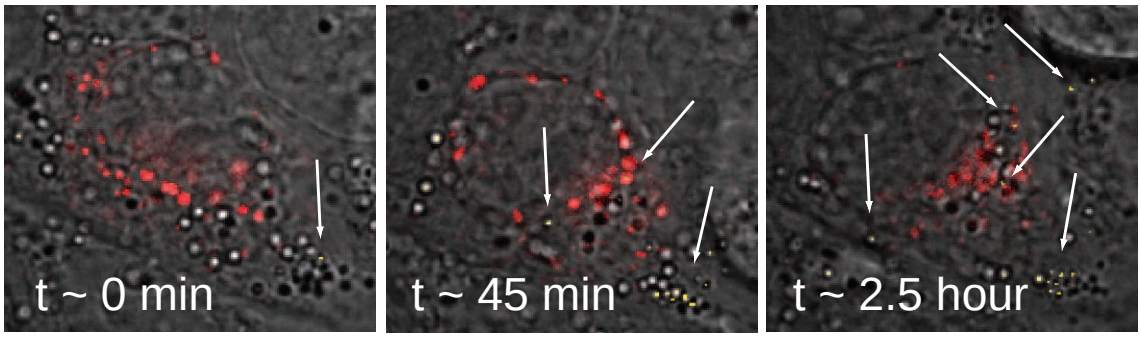

Figure 3.4: Endocytosis of gold nanoparticles. Confocal images of H727 neuroendocrine cancer cells incubated with 60 nm colloidal gold nanoparticles (marked by arrows). If the signal from the lysosomes (marked in red) overlap with the gold nanoparticles, it indicates that they are co-localized. Over time more and more nanoparticles are transported to the lysosomes. The data is published in Ref. [52].

very attractive, therefore we are conducting a project aiming at performing remote light triggered miRNA release from gold nanoparticles. Under my co-supervision, Ann-Katrine V. West developed an assay consisting of doublestranded miRNA; one strand was attached to the gold surface by thiol modification, and the complimentary strand was modified with a fluorescent Cy-5 molecule (see Fig. 3.5A). The loading of the miRNA onto gold nanoparticles was measured by the intensity of Cy-5 using confocal microscopy. We found that the miRNA was loading onto the nanoparticles in a size dependent manner: 60 nm colloidal gold nanoparticles had the highest loading rate per surface area compared to that of 80, 100 and 200 nm colloidal gold nanoparticles (see Fig. 3.5B). These findings suggest that because of the high surface curvature of the smaller nanoparticles, miRNA can be loaded at a higher density while stabilized by PEGylation [54].
We anticipate that upon irradiation of the miRNA conjugated gold nanoparticles, the double-stranded miRNA will undergo de-hybridization that releases the Cy-5 modified strand. Hence, we can assess the release properties by observing the Cy-5 signal before and after laser irradiation (work in progress).

Drug delivery

Most drugs are small molecules that are systemically distributed in the body, and potentially can lead to side effects. In addition, many drugs have poor solubility and hence low performance by systemic delivery. Utilizing gold nanoparticles as delivery vesicles, the drug efficacy can be increased as the effective dose at the target site is significantly enhanced. Drugs conjugated to a gold nanoparticle do not dissociate upon systemic administration meanwhile target-specific release of the drug can be remotely controlled by an external light source: This means that exposure to healthy tissue of drugs that are highly toxic can be decreased. Doxorubicin and Rituximab are amongst the commercially available chemotherapeutic drugs

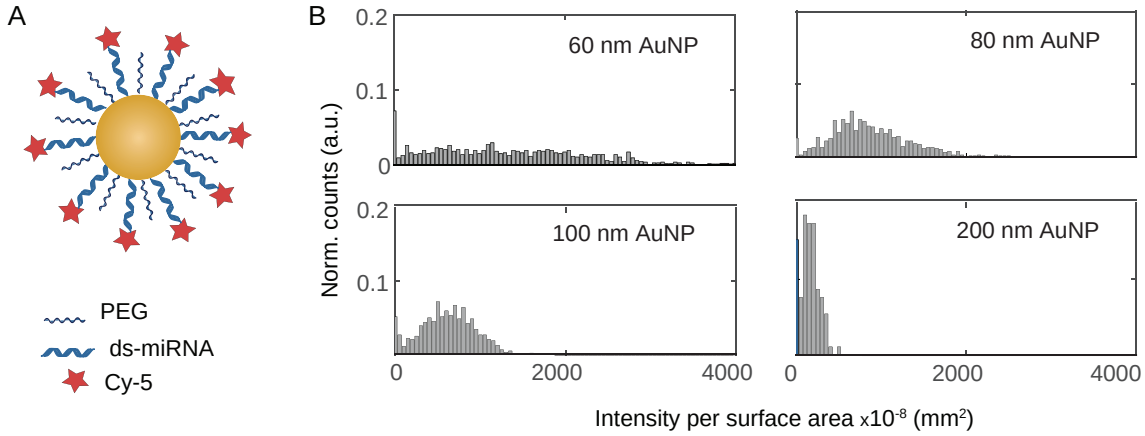

Figure 3.5: Gold nanoparticles as carrier vesicles for miRNA. **(A)** The doublestranded (ds) miRNA-Cy-5 molecules were loaded onto the gold nanoparticles by Au-thiol conjugation. The complex was stabilized with PEG. **(B)** The miRNA loading onto the gold nanoparticles was assessed by the intensity of Cy-5. The intensity distributions showed that miRNA loading increased with higher surface curvature (i.e., particles with smaller diameters have a higher Cy-5 intensity per surface area).

that have been shown to induce cancerous cell death upon nanoparticle assisted delivery and light triggered release [55, 56]. Drugs are conjugated to the surface of a gold nanoparticle via, e.g., thiolated aptamers or oligonucleotides and stabilized by PEGylation.

3.4 Toxicity

The clinical transition of nanoparticle-mediated photothermal cancer therapy is crucially dependent on the toxicology profile of the nanoparticles. As the most common route of administration of nanoparticles is via intravenous injection the exposure and possible uptake of the vital organs must be considered.

One of the major reasons for gold nanoparticles' great success in biological applications is that they in general are believed to be non-toxic in contrast to, e.g., silver nanoparticles. However, there is a consensus that the toxicity of gold nanoparticles is both size and coating dependent, which is why these parameters should be taken into account. Gold nanoparticles are believed to be biologically inert until they get below a certain size (< 2 nm) where they become catalytically active and hence toxic (can induce oxidative stress and mitochondrial damage) [57].

Gold nanorods stabilized using CTAB as the capping agent have been found to be toxic, unless CTAB desorption is prevented or replaced by exposure to serum proteins [36, 57]. Also leftover chemicals and poor purification can induce toxicity. Goodman et al. showed that hollow gold nanoshells, synthesized by galvanic replacement of Ag with Au^{3+}, displayed fragmentation and remnants of the sacrificial Ag core *in vivo*, which led to accumulation of

toxic silver nanoparticles in various organs [58].

To date, most toxicology studies of gold nanoparticles have been performed *in vitro* using experimental evaluation in cell cultures based on cell viability assays, reactive oxygen species analysis, gene expression, and cell morphology studies [35]. These *in vitro* studies are both faster and cheaper, but inadequate for a whole body assessment of the fate of the nanoparticles. Before the treatment can be allowed in clinic, whole body response to the metallic nanoparticles and the pharmacokinetic parameters (absorption, distribution, metabolism, and elimination) must be assessed. Chronic inflammation and immunological responses are of great concern as these can be lethal. In animal studies, the toxicology profile has been studied by tracking body weight, food consumption, hematological parameters, organ weights, and mortality rates [57].

Despite the requirement for long circulation times of the nanoparticles to enhance tumor delivery, after the treatment, clearance of the nanoparticles from the whole body is desirable. Clearance by the kidney (renal excretion) is only efficient in the size range $<$ 6-8 nm as it requires the nanoparticles to cross filtration barriers that exclude larger particles from passing through [57]. Biodistribution studies show that the main retention of nanoparticles is in the liver and spleen where they remain even after six months [36]. As of now, no acute toxic effects have been observed after gold nanoparticle administration to animals. However, the long-term effects ($>$ 6 months) of gold nanoparticle retention in liver and spleen and whether they eventually clear from the body remain unclear. As for any other drug, the long-term retention of nanoparticles must be elucidated before they can be clinically approved regardless of the apparent biocompatibility.

Nanoshells have been used in clinical trials for therapy in head and neck cancers. 11 patients were enrolled and followed for six months after PEGylated nanoshell were administered and irradiated with a 808 nm laser at different doses. The study was completed August 2014 (FDA trial: NCT00848042). Furthermore, a study on primary or metastatic lung tumors was initiated October 2012 where patients (estimated enrollment of 25 patients) will be given systemic intravenous infusion of nanoshells and escalating doses of irradiation. The study follows patients for 6 months and is set to end in 2016 (FDA trial: NCT01679470). Other types of plasmonic gold nanoshells (silica-gold shells with iron oxide) have been used in clinical trials of photothermal treatment of Atherosclerosis following the patients up to 12 months (FDA trial: NCT01436123,NCT01270139). Gad et al. [59] published a study on silica-gold nanoshell toxicity in different animal models that were followed for about 400 days without observing any systemic toxicity.
In addition, there has been no indication of fragmentation of silica-gold nanoshells for the range of laser-energies used in photothermal therapy so the safety profile is expected to rely on the gold surface characteristics and morphology alone. Considering that gold nanopar-

ticles have been used for rheumatoid arthritis since the 1920s, they are believed to be safe. However, there is still a lack of studies on excretion of the nanoparticles, that remains the major barrier for FDA clinical approval.

3.5 Summary

In this chapter, some of the biomedical applications of gold nanoparticles have been introduced. Notably this introduction only covers a small fraction of the versatility found in the literature. These capabilities were highlighted as they are easily combined and together they can provide synergistic effects for cancer treatment. Cancer can be a complex and rapidly adapting disease, why development of multi-functional strategies might be necessary for improving cancer diagnosis and therapy. Gold nanoparticles are, despite of what people might think, not very expensive, and the fabrication is straightforward, keeping the cost of clinical implementation down. The first FDA clinical trials exploiting plasmonic nanoparticles for photothermal therapy have already been conducted showing promising results (see FDA trials described in the section on toxicity). Gold is generally considered to be biologically inert, but the clinical safety is still an open question. Hence, thorough pharmacokinetic assessment is the bottleneck for clinical approval of gold nanoparticles in cancer therapy.

Chapter 4

In vitro comparative study of the photothermal efficiency of colloidal gold nanoparticles and silica-gold nanoshells

Plasmonic nanoparticles experience severe heating upon irradiation, in particular when the irradiation wavelength is close to their plasmon resonance wavelength. For photothermal cancer therapy hyperthermia is a necessity, however in other biological applications where plasmonic nanoparticles are used for optical manipulation inside or outside organisms such as living cells, the temperature increase is a concern (see our reviews on optical trapping of nanoparticles [14, 52]).
For these reasons a huge effort has been made to develop methods for quantifying how much an individual nanoparticle actually heats upon irradiation. Optical tweezers provide a unique nano-tool capable of trapping nanoparticles at a laser intensity focus.
In this chapter we combine optical trapping of plasmonic nanoparticles with a temperature-sensitive biological assay developed in our group (Optical Tweezers Group, NBI, DK) to give us a direct measurement of the increased surface temperature of irradiated plasmonic nanoparticles. The strength of *in vitro* experiments is that mostly all parameters can be controlled thereby isolating the characteristics of the single particle under investigation, including its absorption properties.

This chapter will start with an introduction to the physics behind an optical trap and the experimental setup we use to assess the photothermal properties of each of the nanoparticles. As the plasmonic nanoparticles are compared one-to-one, their theoretical absorption

properties are presented to get a hint of how they are anticipated to perform with respect to each other. After this the biological assay and the experimentally measured temperature profiles are introduced. From the experiment the surface temperatures is calculated and discussed in relation to the theoretically expected absorption properties. Finally the particles' trapping position is measured as it has been shown, that dependent on size and material, particles can exhibit different aberrated axial trapping potentials that will influence on the exact position of the particle within the laser focus.

4.1 Optical trapping

Optical trapping is a way to optically confine and manipulate micron-and nano-sized particles. Arthur Ashkin demonstrated in 1970 trapping of microscopic particles with a focused continuous wave (CW) laser beam [60]. Since his groundbreaking work the field of optical manipulation and its applications has increased tremendously. One field that in particular has benefited from the invention of optical tweezers is single-molecule biophysics. The strength of optical tweezers in biophysics is that the technique is capable of measuring well-calibrated forces and distances that coincide with the range where many biological processes and biomolecules function (typically in the pico-Newton and nanometer range [61]). Furthermore, since optical trapping is a single-molecule technique it can reveal dynamic properties of a system that are hidden in ensemble studies.
In biological force spectroscopy measurements optically trapped particles have been used as force transducing handles. Thus, providing insight into the cellular machinery, such as the mechanical and dynamical properties of single molecular motors as well as micro-rheological properties of living cells (see our review on optical manipulation inside living cells [52]).

Optical tweezers are formed by tightly focusing a laser beam to a diffraction limited spot (spot size $\approx \lambda/2$)(see Fig. 4.1).

The optical forces acting on a nanoparticle can be described by Maxwell's equations and depend on the size and dielectric function of the nanoparticle as well as the electric field. Therefore, to solve Maxwell's equations these parameters must be taken into account which is evoked using the Rayleigh or the Mie approximations for nanoparticles [62]. The Rayleigh regime applies for particles much smaller than the wavelength of light where we consider the particle as an oscillating dipole in a time varying electric field [63]. The Mie regime accounts for larger particles where multipole effects are no longer negligible.

For a so-called Rayleigh particle the incoming electric field induces a uniform dipole polarization, $\mathbf{p}$, of the particle given by $\mathbf{p} = \alpha\mathbf{E}$, where α is the polarizability of the particle given by eq. 2.3, and $\mathbf{E}$ is the electromagnetic field. The total optical force acting on the dipole

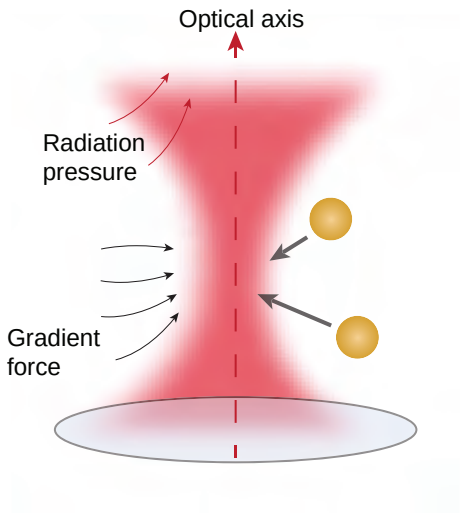

Figure 4.1: A laser beam can be focused via appropriate optical lenses. The intensity gradient generates an optical force pointing towards the highest intensity region. When the radiation pressure exceeds that of the gradient force (e.g., for large and highly reflective particles) the particles will be pushed out of the focus in the direction of the light.

can be calculated by combining the expression for the dipole polarization and the Lorentz optical force [62]. We write the total optical force as the sum of two parts: the gradient force F_{grad} and the radiation force F_{rad}. The gradient force causes the particles to be attracted to the high intensity region of the field (see Fig. 4.1) and is given by:

$$\mathbf{F}_{grad} = \frac{1}{2}|\alpha|\nabla\langle\mathbf{E}^2\rangle \ , \tag{4.1}$$

where the brackets denote time averaging. From this expression it is seen that the gradient force is proportional in size to the intensity of the field and points in the direction of the intensity gradient (i.e., towards the focal point).

The radiation force relates to the momentum transfer or loss from the electric field to the particle that causes scattering or absorption of the photons. The radiation force can be written as a function of the scattering and absorption cross-sections and the time averaged Poynting vector, $\langle \boldsymbol{P} \rangle$, describing the intensity of the light:

$$\mathbf{F}_{rad} = \frac{n_m}{c}\langle \boldsymbol{P} \rangle C_{scat} + \frac{n_m}{c}\langle \boldsymbol{P} \rangle C_{abs} \ . \tag{4.2}$$

Here, n_m is the index of refraction of the surrounding medium and c is the speed of light. In chapter 2 we saw that the scattering cross-section for very small nanoparticles scales quadratically with α, which is proportional to the volume. In contrast, the gradient force only scales linearly with α. This means that when the particle becomes larger, the radiation pressure arising from the scattering force overcomes the gradient force and pushes the particle out of the trapping focus in the direction of the light (see Fig. 4.1).

The stability of the optical trap is also dependent on the particles' material and shape and reduces for particles with lower relative refractive index (i.e., the refractive index of the particle with respect to that of the surrounding medium). The refractive index is a function of the dielectric permittivity of the particle, $n_p^2 = \epsilon(\omega)$. For dielectric particles, where the relative refractive index is low, nano-sized particles are almost impossible to trap [63]. In comparison, metallic nanoparticles have a high refractive index, enabling trapping of particles with diameters down to $\sim$ 20 nm [64]. For more details and comparison between dielectric and metallic nanoparticles, see our review on Optical Trapping of Nanoparticles and Quantum Dots [14].

Most commonly optical traps are generated with laser beams having a Gaussian intensity profile. The first order expansion of the beam profile results in a harmonic potential, U. Hence, for small particle displacements, $(x-x_0)$, the optical trap exerts a restoring harmonic force on the trapped nanoparticle given by $U' = F_{trap} = k_{trap}(x - x_0)$, where k_{trap} is the trap stiffness characterizing the strength of the trapping potential [14]. The actual force in an experiment can be obtained by performing calibrations of the particles' Brownian fluctuations within the trapping potential [14, 52].
A so-called power spectrum force calibration, is performed by considering the power spectral densities of the particle's Brownian fluctuations in the harmonic trapping potential. The motion of the particle is well-described by the power spectrum of the Langevin equation, that has a Lorentzian form [65]:

$$P(f) = \frac{k_B T}{\gamma} \frac{1}{f^2 + f_c^2} \ . \tag{4.3}$$

Here, $k_B T$ is the thermal energy, γ is the Stokes drag coefficient, and is f the frequency. f_c is the corner frequency that is related to the trap stiffness as, $f_c = k_{trap}/2\pi\gamma$. An example of a power spectrum force calibration is shown in Figure 4.2A, where I acquired the time series of silica-gold nanoshells' positions in an optical trap and plotted their power spectral densities [14]. The inset in Figure 4.2A shows that the position histogram has a Gaussian shape confirming that the nanoshells in fact were trapped in a harmonic potential. By fitting the data with eq. 4.3, I could extract the corner frequency and infer the trap stiffness [66], which is plotted as a function of laser power in Figure 4.2B.

4.2 Optical setup

The optical setup used in this part of the project is based on a NIR optical tweezers implemented in a confocal microscope (see Fig. 4.3). The optical tweezers are formed by tightly focusing a 1064 nm Nd:YVO_4 continuous wave (CW) laser (5 W) to a diffraction limited

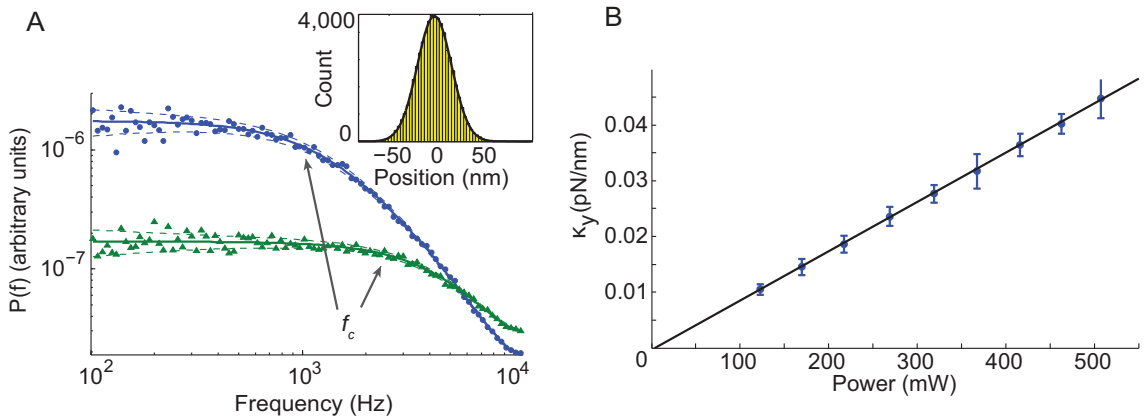

Figure 4.2: Power spectrum force calibration of optically trapped silica-gold nanoshells. **(A)** Power spectra of the trapped silica-gold nanoshells fitted with the Lorentzian function, eq. 4.3. The laser power at the sample was $P = 508$ mW (green triangles) or $P = 123$ mW (blue circles). The corner frequency, f_c, from which the trap stiffness can be inferred is marked by arrows. Inset shows the Gaussian position distribution of a silica-gold nanoshell trapped at $P = 123$ mW. **(B)** Trap stiffness as a function of laser power for silica-gold nanoshells (n = 12), the full line denotes a linear fit to data. The data is published in Ref. [14].

spot through a high nummerical aperture (NA=1.2) 63x apochromatic water immersion obejctive (Leica, No. 11506279). The collimated laser beam goes into a beam expander and an optical telescope to slightly overfill the infinitely corrected objective. A beam steering telescope further ensures that the trapping position can be translated in the sample plane in the axial direction. A quadrant photo diode (QPD) collects the interference pattern of the optical signal of the trapped particle at the back focal plane and converts it into voltage. The output yields the position of the trapped particle in a time series with nanometer resolution. By performing Brownian motion calibration and calculating the power spectrum it is possible to obtain the spring constant, k_{spring}, for the harmonic potential which confines the nanoparticle (see Fig. 4.2).

The confocal scanning microscope used is a Leica SP5 with an Argon laser (458, 477, 488, 496, 514 nm), and a HeNe 494- and 633 nm laser. By implementing point illumination and inserting a pinhole in front of the detector, the out-of-focus illuminated part of the sample is eliminated and only light from within the focal plane is detected. Illumination and detection separation allows for imaging of multiple fluorescent markers simultaneously and is achieved by Acousto Optical Beam Splitters (AOBS) and rotating photomultiplier tubes (PMT). Conveniently, a confocal microscope operated in reflection mode allows for visualization of trapped metallic nanoparticles. The signal strongly depends on the particles' ability to reflect light and the illumination intensity. As the scattering cross-section of metallic nanoparticles is wavelength dependent, some wavelengths result in a better visualization than others.

This optical setup, combining a confocal system with optical tweezers, enables simultane-

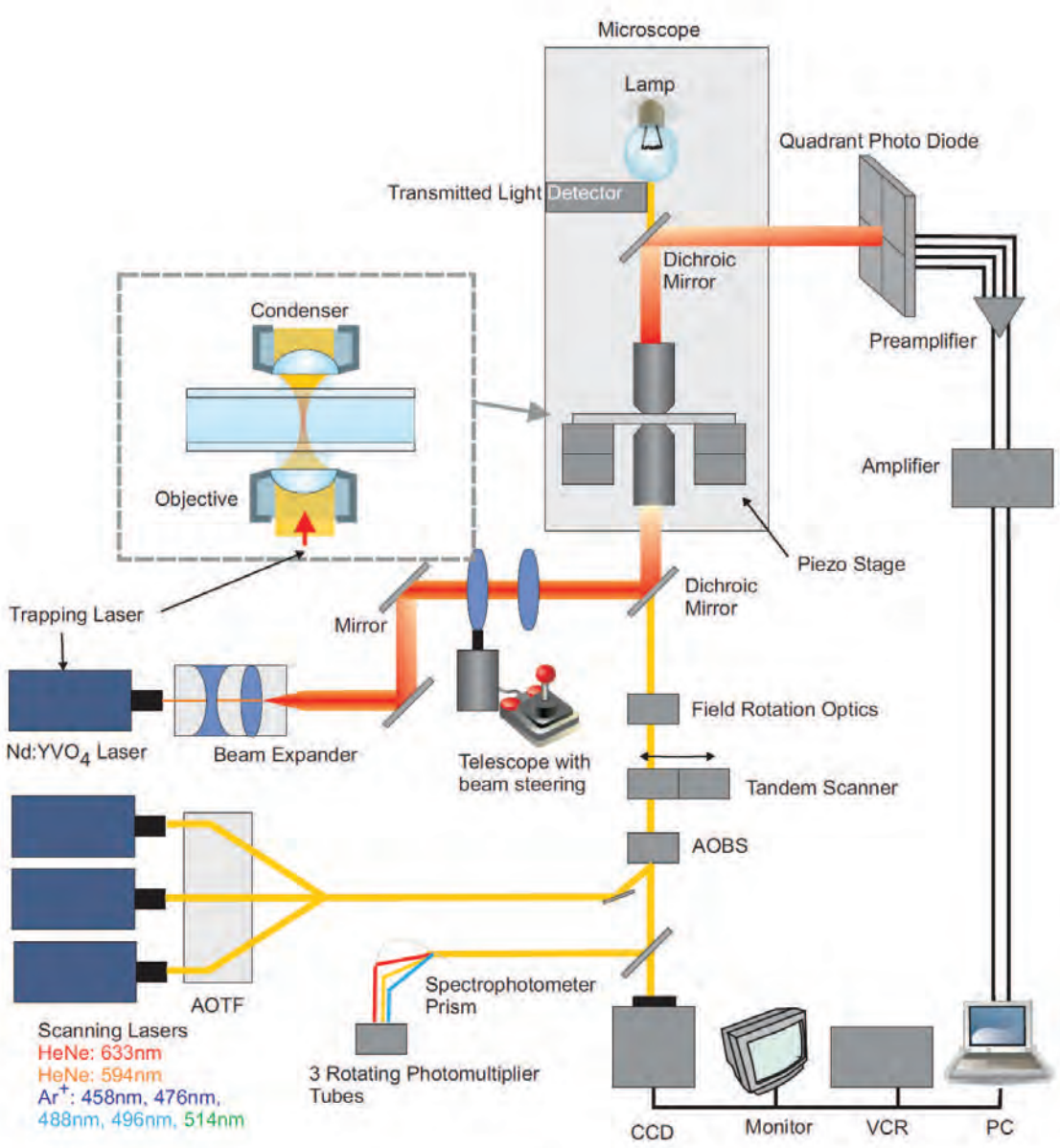

Figure 4.3: Illustration of the optical setup. A 1064 nm Nd:YVO_4 laser is implemented into a confocal microscope for simultaneous fluorescent/reflection based imaging and force measurements of optically trapped nanoparticles. Particle position detection with nanometer resolution is achieved with an interferometric position detection scheme based on a quadrant photo diode. Reproduced from Ref. [67].

ous imaging of fluorescently labelled biomolecules and the reflection of trapped metallic nanoparticles.

4.3 Calculated absorption cross-sections

For clinical application it is important to select the nanoparticle that is the best light-to-heat converter. The absorption cross-section is a very important parameter as it provides a theoretical framework of the optical properties on the basis of which the different types of plasmonic nanoparticles can be compared directly.

The calculated absorption cross-section can be determined by building a mathematical model describing the electric field of the plasmonic nanoparticle and solving it. For plasmonic nanoparticles with simple geometries, e.g., colloidal gold nanoparticles, the plasmonic model is readily solved using numerical methods such as the discrete dipole approximation, and the boundary element method [11]. However for composite structures such as silica-gold nanoshells or complex geometries such as triangles, the Finite Element Method (FEM) has been used successfully [68, 69]. Pengfei Tian contributed to this project with simulations (FEM Multiphysics, COMSOL) of the absorption cross-sections for all three nanoparticles that are shown in Figure 4.4 as a function of wavelength.

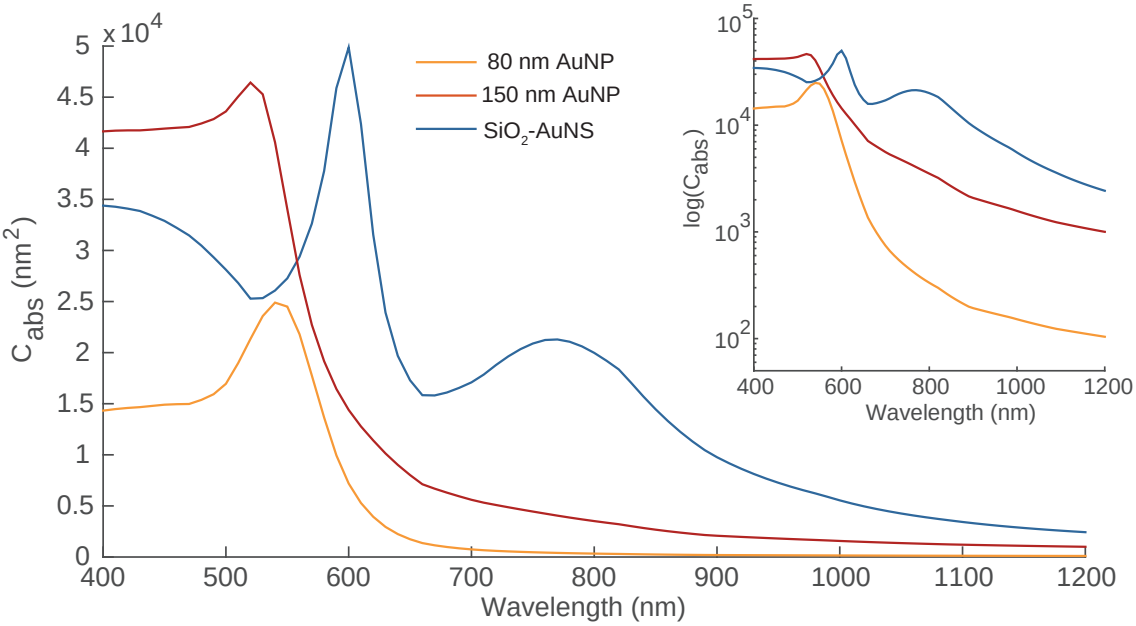

Figure 4.4: FEM simulations of the absorption cross-sections for all three plasmonic nanoparticles. At all NIR wavelengths the silica-gold nanoshells have a significantly higher absorption cross-section compared to that of 80 and 150 nm gold nanoparticles. *Inset*: The absorption cross-sections are plotted on a semilog scale to better resolve the simulated values around 1064 nm (the wavelength of our *in vitro* implemented laser). The simulations were performed by Pengfei Tian for this project.

Without doubt, the silica-gold nanoshells have superior absorption properties throughout the entire NIR region. Jain et al. [20] showed, using Mie theory and discrete dipole approximation, that smaller gold nanoparticles (20 - 80 nm) primarily are absorbers with negligible scattering properties. Consistent with these findings we can see that the absorption spectrum of the 80 nm gold nanoparticles in Fig. 4.4 resembles the extinction spectrum in Fig. 2.5C. In spite of the dominating absorption contribution for small gold nanoparticles, the cross-section scales linearly with particle volume which is why 150 nm gold nanoparticles have a substantially larger absorption compared to that of 80 nm gold nanoparticles (see Fig. 4.4).

If the FEM calculations shown in Fig. 4.4 are compared directly at $\lambda = 810$ nm (the wavelength of the *in vivo* laser), we find an absorption cross-section of 316 nm^2 for the 80 nm colloidal gold nanoparticles, 3357 nm^2 for the 150 nm colloidal gold nanoparticles, and 19219 nm^2 for the 150 nm silica-gold nanoshells. At this wavelength the absorption for the silica-gold nanoshells is almost six times higher than that of the 150 nm gold nanoparticles with equal diameter underpinning the significance of plasmon resonance.

In the *in vitro* comparative study, a 1064 nm laser was used to optically trap and irradiate the plasmonic nanoparticles. In this end of the NIR region the silica-gold nanoshells are still superior in terms of optical properties (see inset in Fig. 4.4). The absorption cross-section derived from the FEM calculations at $\lambda = 1064$ nm is 132 nm^2 for the 80 nm colloidal gold nanoparticles, 1326 nm^2 for the 150 nm colloidal gold nanoparticles, and 4066 nm^2 for the nanoshells.

Hence, a priori we expect the silica-gold nanoshells to exhibit substantially higher temperature increases in the NIR region compared to both 80 and 150 nm gold nanoparticles, followed by the 150 nm gold nanoparticles and lastly the 80 nm gold nanoparticles.

4.4 Photothermal heat generation by resonant and non-resonant nanoparticles

In the literature, several different assays have been proposed to assess the heating capability of irradiated nanoparticles (these different techniques are discussed in our review on optical trapping of nanoparticles and quantum dots [14]). One approach is based on the change of the nanoparticle's Brownian fluctuations upon heating due to a decrease in the surrounding medium's viscosity [70]. As both the particle and the medium gain energy upon heating, it is necessary to correct the Brownian fluctuations for the temperature-dependence in the viscosity to extract the actual surface temperature of the nanoparticles.
Other approaches are based on embedding the nanoparticles in a phase sensitive matrix,

such as ice, to measure the heating of the irradiated nanoparticles [24,71]. As ice might be a very difficult matrix to work with, more recent studies have utilized phospholipid membranes with a well-defined phase transition where the temperature assessments are based on, e.g., the heat-induced velocity of melted lipid regions and phase preferential fluorescent lipid molecules [72,73].

In our group, Bendix et al. developed a 2D assay based on a surface lipid bilayer, where phase sensitive fluorescent dyes were incorporated and used to measure the heating footprint of irradiated gold nanoparticles stuck on the bilayer [25]. The temperature profiles of different sizes of irradiated gold nanoparticles were measured revealing a temperature increase of several hundreds degrees that was proportional to the particle volume.

Kyrsting et al. refined this assay to study the heating capability of 3D optically trapped nanoparticles by exchanging the lipid bilayer with lipid vesicles [74]. The temperature profile was acquired by measuring the distance between the trapped nanoparticle and the lipid vesicle at the point where the vesicle became leaky (e.g., to large fluorescent molecules trapped in the lumen of the vesicle). They found the same proportionality between temperature increase and volume as Bendix et al. [25], but only for particles smaller than $\sim$ 100 nm. For larger nanoparticles the thermal response was reversed. Interestingly, it was found that for these larger nanoparticles there existed trapping minima axially displaced in front of the laser focus, leading to an overall lower irradiation intensity compared to the smaller nanoparticles trapped close to the focus, thus explaining the lower heating [75].

3D lipid vesicle assay utilized as a temperature sensor

In this study we used an assay similar to Kyrsting et al. [74] based on Giant Unilamellar Vesicles (GUV) combined with membrane incorporating fluorescent molecules that enable detection of the local temperature [76]. The GUV consists of a bilayer of $DC_{15}PC$ phospholipids that at atmospheric pressure, dependent on the temperature, can exist in two states; at temperatures lower than the melting temperature (T_m), the membrane exists in an ordered gel phase resembling a frozen membrane, whereas at temperatures higher than T_m the membrane transitions into a disorganized fluid state.

GUVs consisting of $DC_{15}PC$ phospholipids are ideal for sensing a local temperature change as they have their phase transition, i.e., the temperature at which the membrane goes from the gel phase to the fluid phase, above room temperature ($T_m = 33$ ℃, according to Avanti Polar Lipids). Consequently, in absence of a heat source such as an irradiated nanoparticle, GUVs kept at room temperature only occur in their frozen gel phase. When a trapped nanoparticle approaches the GUV, it undergoes local phase transition exactly at the point where the temperature profile of the particle is equal to the phase transition of the GUV (i.e., $T = T_m$;

see Fig. 4.5). Because the temperature profile is dependent on the absorption properties, different types of nanoparticles will be able to induce local phase transition of the GUV at different distances. Since, the temperature is known to decay with the inverse distance to the nanoparticle [77] we can infer the temperature of the nanoparticle by quantifying the distance to the melting point on the GUV.

The experimental protocol

In practice, using confocal microscopy, we cannot determine the phase state of the GUV so instead we used a fluorescent marker (di-4-ANEPPDHQ) that preferentially partitions into melted regions (see Fig. 4.5) [76].

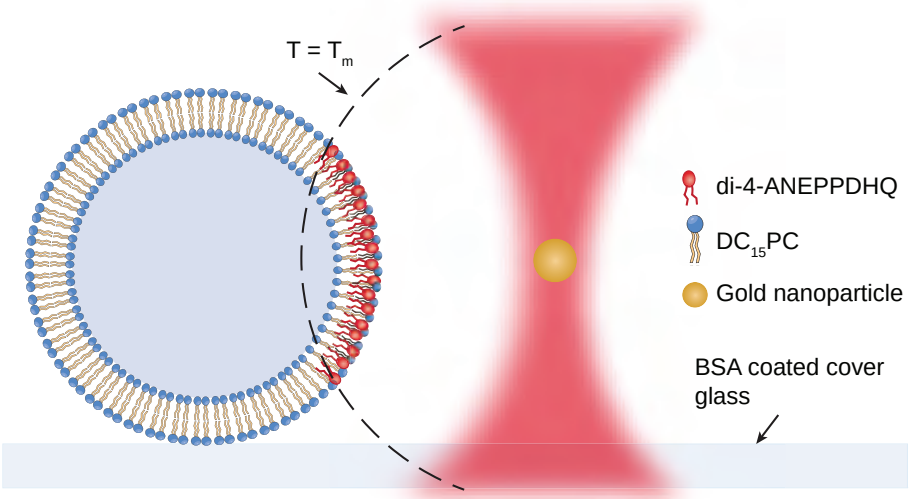

Figure 4.5: 3D heating assay used to compare the light-to-heat conversion of different sizes and compositions of plasmonic nanoparticles. The 3D assay consists of an immobilized giant unilamellar vesicle (GUV) with a well-characterized melting transition and a phase-sensitive dye (di-4-ANEPPDHQ). The temperature (T) of the trapped gold nanoparticle can be calculated by measuring the distance between the gold nanoparticle and the membrane at the point where the membrane starts melting ($T = T_m$). This is directly observed by a strong local partitioning of the phase sensitive dye into the melted region.

The GUVs were prepared by electroformation of 2 μmoles of saturated lipids (1,2-dipentadecanyol-*sn-glycero*-3-phosphicholine, Avanti Polar lipids), mixed with 1 mol% of di-4-ANEPPDHQ (Invitrogen) and chloroform. On clean indium tin oxide (ITO) slides a thin film of the lipid-dye mixture was carefully placed and left in vacuum for 90 minutes. A rubber ring enclosing the lipid film and 300 mM sucrose was "sandwiched" between two ITO slides in the electroformation chamber that was run for 130 minutes.

On a clean microscope coverslide (no. 1.5, Menzel-Gläser) 1 mg/ml of Bovine Serum Albumin (BSA) in DI water was incubated for 10 minutes in a sample container to passivate the surface. Excess BSA was removed by washing at least 5 times with 150 mM Phosphate Buffered Saline (PBS) buffer. A small volume of the freshly prepared GUVs was added to the sample chamber containing 300 μl of PBS buffer. The plasmonic nanoparticles were diluted to an appropriate concentration, sonicated and vortexed to ensure their monodispersity, and added to the sample chamber.
The confocal microscope and a stage heater were turned on at least two hours prior to the experiment to allow equilibration of thermally induced drift and laser stability. The prepared sample was placed on the microscope stage for at least 15 minutes to allow the GUVs to sink to the bottom of the sample and to ensure it was equilibrated with its surroundings.

The background temperature is experimentally important both to secure that the GUVs are in the gel phase, but also with regards to the experimental error related to the day-to-day variation in ambient temperature. The further the temperature of the membrane is from its phase transition the more heat is needed to raise the local temperature of the membrane above the phase transition. Consequently, the background temperature has a huge impact on how close the trapped nanoparticle needs to go to the membrane to induce phase transition. To eliminate, or at least minimize, this primary source of experimental error, the room temperature was kept around 21 ℃ and the stage heater was set to 47 ℃ . The sample temperature was closer to 28 ℃ since there is a heat loss over the heat leading tubes from the water bath to the stage heater and because the objective is a huge heat sink.

The microscope was equipped with a piezoelectric stage (Physik Instrumente, Germany) so that a surface immobilzed GUV could be moved laterally in small increments towards the trapped nanoparticle until it locally melted (as in Fig. 4.5). Because of the large scattering cross-section of plasmonic nanoparticles the position of the trapped nanoparticle could be visualized, within the diffraction limit of $\sim \lambda/2$, using the confocal microscope in reflection mode (excited by $\lambda = 594$ nm). The fluorescent molecule, di-4-ANEPPDHQ, was excited by $\lambda = 488$ nm and emission collected with a bandwidth from 605 - 750 nm. Image acquisition was performed with 1.2 frames per second. Each position was imaged for 10 seconds before moving the sample with the piezo stage. The laser power was through all experiments fixed to 433 mW at the sample.

Melting distance

An example of an experiment conducted with a silica-gold nanoshell is seen in Figure 4.6A. Before the trapped nanoparticle is close enough to the membrane to induce local melting the GUV appears very dim (Fig. 4.6A, see region I). Suddenly there is an abrupt and

strong increase of the fluorescence from di-4-ANEPPDHQ, indicating that the temperature has reached the phase transition causing the fluorescent lipid molecules to partition into the melted region (Fig. 4.6A, see region II). This distance between the trapped nanoparticle and the GUV corresponds to the distance at which the temperature profile has decayed to $T = T_m = 33$ ℃ and is defined as the melting distance. Bringing the trapped nanoparticle even closer to the GUV has only little effect on the intensity of di-4-ANEPPDHQ (Fig. 4.6A, see region III).

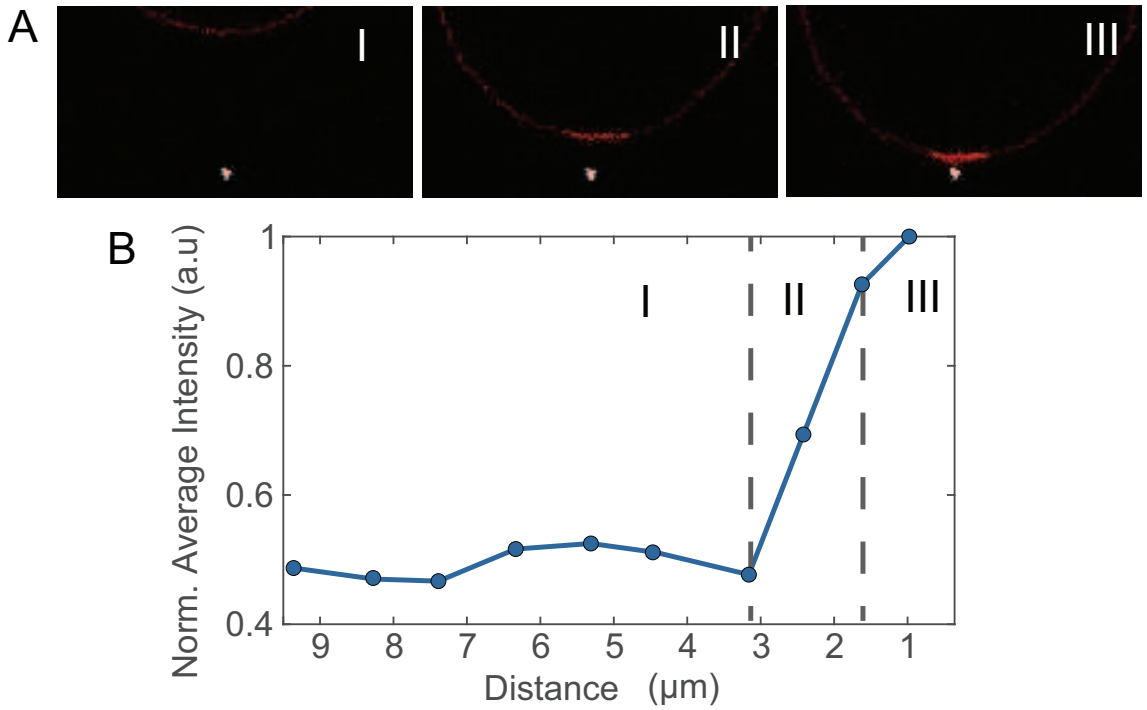

Figure 4.6: The experimental temperature profile of an optically trapped silica-gold nanoshell using a GUV as temperature sensor. **(A)** The frozen GUV (red curve) is moved closer to the trapped nanoparticle (white dot) in discrete steps (from I to III) until it undergoes local phase transition. **(B)** The melting curve relates the distance between the GUV and the trapped nanoparticle to the average intensity (normalized) of the membrane partitioning dye, di-4-ANEPPDHQ. Each point in the curve is the average intensity of at least two consecutive images. The images in **(A)** are representatives of a region in the melting curve (the regions are marked by numbers and divided by dashed lines). Image (I) is taken before the membrane starts melting which is why the intensity of di-4-ANEPPDHQ is only about 50 %. Image (II) is taken just at the phase transition seen by the abrupt increase in the intensity of di-4-ANEPPDHQ. Image (III) is taken after the initiation of the local phase transition. The intensity of di-4-ANEPPDHQ only increases about 5 % compared to that at the phase transition in (II).

The melting distance was quantified by image analysis as the distance where the intensity of di-4-ANEPPDHQ became substantially higher than the background intensity (see Fig. 4.6B). Each consecutive image was analyzed using Matlab producing a melting curve, that related the distance to an intensity. In detail, first the image was rotated such that the shortest distance between the nanoparticle and the GUV was horizontally aligned. The cen-

troid position of the nanoparticle was found by fitting a 2D Gaussian curve to the diffraction limited point spread function of the nanoparticle. The position of the locally melted region on the GUV was defined as the point on the curved membrane where the intensity was highest and likewise closest to the nanoparticle. By vertically collapsing the pixel values from the GUV image and plotting the 1D intensity distribution, the peak could be estimated and related to a pixel coordinate.

In the data sets, each distance versus intensity data point is the average of at least two images. Averaging the distance and the intensity is a precaution taken to ensure correct distance acquisition, as: 1) membrane fluctuations can occur close to the phase transition as it becomes softer. 2) We sometimes observed a lag in the response time of fluorescent partitioning after moving the GUV closer to the trapped particle. It should be noted, that the nanoparticle also fluctuates about 100 nm laterally within the trap. However, these fluctuations occur on a millisecond timescale whereas acquisition of one image takes ~ 1 second.

Figure 4.6B shows the melting curve that corresponds to the images in Figure 4.6A. In the step going from ~ 3 μm to ~ 2 μm (i.e., from region I to II), the intensity increases to almost double the value. Hence, in this experiment the melting distance was measured to be $D_m = 2419$ nm.

For each of the plasmonic nanoparticles the melting distance, D_m, was measured and the result is shown in Figure 4.7. The average melting distance ($\pm$ std) is 933 $\pm$ 295 nm for the 80 nm colloidal gold nanoparticles, 1539 $\pm$ 405 nm for the 150 nm colloidal gold nanoparticles, and 2141 $\pm$ 885 nm for the silica-gold nanoshells. In this *in vitro* experiment we used a trapping laser with a wavelength of 1064 nm. This is close to the surface plasmon resonance of the nanoshells that indeed have the largest melting profile compared to that of the non-NIR resonant 80 and 150 nm colloidal gold nanoparticles.

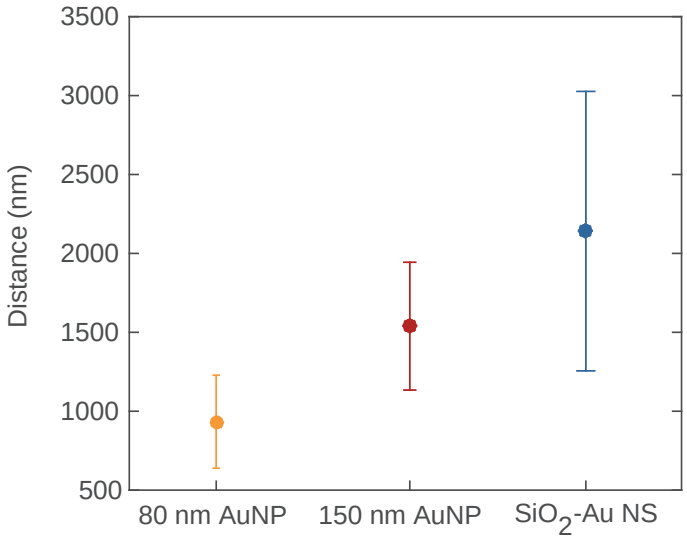

Figure 4.7: The melting distance for all three types of plasmonic nanoparticles. The 80 nm colloidal gold nanoparticles have the smallest melting distance (n =9), followed by the 150 nm colloidal gold nanoparticles (n =18). Silica-gold nanoshells have the largest melting distance (n =14) that is in agreement with the photoabsorption-dependence on the temperature profile. Error bars represent STD. The large standard deviation could be explained by the natural spread in the particle size populations coming from the synthesis, and/or experimental error from day-to-day variation in the background temperature.

Surface temperature increase

From the melting distance we can infer the temperature at the surface of the irradiated nanoparticle. The Goldenberg relation can be used to calculate the temperature increase of a point-like or nanoscopic particle embedded in an infinite medium as a function of the distance from the particle center [77]:

$$\Delta T(D) = \frac{Aa^3}{3K_w D} \ , \tag{4.4}$$

where a is the radius of the particle, K_w is the thermal conductivity of the medium, and D is the distance from the particle center. A is the heating rate per unit volume given by:

$$A = IC_{abs}/V \ . \tag{4.5}$$

Here, I is the power density of the laser ($I = 433$ mW), C_{abs} is the absorption cross-section of the particle given by eq. 2.2, and V is the volume of the particle. As the distance D is the only variable in this experiment (both intensity and particle radius are fixed), eq. 4.4 can be rewritten as:

$$\Delta T(D) = \frac{C}{D}, \quad \text{where} \quad C = IC_{abs}/4\pi K_w \ . \tag{4.6}$$

C is a constant containing all the physical parameters in the experiment. By calculating the experimental value for C for each of the nanoparticles we can back-calculate the temperature increase at any distance from the particle center, including at the surface of the nanoparticles, using the inverse relation from eq. 4.6.

The experimental value for C is calculated using $\Delta T(D_m) = C/D_m$, were the melting distance D_m is obtained in Fig. 4.7. The temperature increase at the phase transition, $\Delta T(D_m)$, is a bit more difficult to determine exactly as it relies on the correct determination of the background temperature, T_0, in the sample chamber (influenced by the heat flux from the equipment, day-to-day variation in the room temperature, etc.).

In practice, we estimated T_0 using an electric temperature probe placed in the sample chamber under the same conditions as for the experiments (incl. the same room temperature). To get a good estimate, it was measured every half hours over 90 minutes, but it was found to saturate already after 30 minutes. The background temperature was therefore found to be $T_0 = (28.2 + 29 + 28.8)$ ℃/ $3 = 28.7$ ℃.

Using this T_0 and $T_m = 33$ ℃ we get a temperature increase at the phase transition of $\Delta T(D_m) = T_m - T_0 = 4.3$ ℃ . The calculated values of the constant C for the three different nanoparticles are given in table 4.1. To calculate the experimental temperature increase at the particle's surface, $\Delta T(a)$, it is sufficient to insert C and the particle radius a into eq. 4.6; the values for each nanoparticle are given in table 4.1.

	80 nm AuNP	150 nm AuNP	150 nm SiO_2/Au NS
C	4.2 μmK	6.9 μmK	9.5 μmK
$\Delta T(a)$	105 K	92 K	127 K

Table 4.1: The experimentally estimated surface temperature increase of different types of plasmonic nanoparticles as a function of their radius, a. The nanoparticles were irradiated with a 1064 nm CW laser using a power of $P = 433$ mW in the sample.

At a laser power of 433 mW the surface of the particles reaches a temperature of about hundred Kelvin above the ambient temperature. The silica-gold nanoshells have the largest temperature profile as well as surface temperature increase, leaving them the best experimental light-to-heat converters at a wavelength of 1064 nm. This is in agreement with the strongly enhanced absorption and scattering properties that silica-gold nanoshells exhibit at NIR wavelengths due to resonance conditions.
It is surprising though, that the surface temperature increase of the silica-gold nanoshells does not differ more from that of the colloidal gold nanoparticles, considering that the absorption cross-section is $\geq$ four times higher (see Fig. 4.4). However, there is also a fairly large standard deviation on the melting distance for the nanoshells (see. Fig 4.7), which could indicate that either the nanoshells in the sample had fragmented or had incomplete

shells. The large deviation could also be due to fluctuations in the background temperature when performing the experiment, which would have a huge impact on the melting distance of the particle and is difficult to control or measure during the experiment.

We would expect the 150 nm gold nanoparticles to reach higher surface temperatures than the 80 nm gold nanoparticles owing to their higher absorption properties and larger melting distance. In contrary, we find the reverse relation; the 80 nm gold nanoparticles actually reach a slightly higher surface temperature.
From this result we can see how the volume of the nanoparticle affects the size of the temperature profile. Intuitively, we expect that a particle with a larger temperature profile also exhibits a higher temperature on the surface than a particle with a smaller temperature profile. However, this is clearly not the case. The temperature profile from large nanoparticles simply decays slower than the temperature profile from small nanoparticles.

Consistent with this contradicting result, Kyrsting et al. [74] found, using the same 3D temperature sensitive assay, that larger gold nanoparticles (> 100 nm) obtain a much smaller surface temperature increase when irradiated compared to that of smaller nanoparticles. In contrast, Bendix et al. [25] found, using a 2D temperature sensitive assay where the irradiated gold nanoparticles were confined on a lipid bilayer, that the surface temperature increase is proportional to particle size. The difference in the results was assigned to the difference in trapping volume between the two assays. The classical view is that larger gold nanoparticles experience substantial radiation pressure due to increased scattering properties, that can destabilize the 3D trapped nanoparticle and "push" it out of the focus, in the direction of the propagating laser light. Effectively at the particle's position, the local laser power is reduced compared to at the focus leading to a decreased photo absorption and heating.

This classical view of particle positions within optical traps applies to an optical focus which only contains one energy minimum. However, as will be explained in the next section, optical traps do indeed exhibit a complex potential energy landscape which can be sensed by the nanoparticles.

Trapping volume of nanoparticles

Interestingly, Kyrsting et al. [75] found by examining the 3D trapping volume of gold nanoparticles, that there existed local trapping minima for larger gold nanoparticles ($>$ 100 nm) in front of the laser focus. Hence, the reduced heating capabilities as a function of particle size reported in Ref. [74] was due to the fact that the particles were located in these additional trapping minima. To examine if we observe the same effect, that could explain the heating capability discrepancy between the 80 and 150 nm gold nanoparticles, we investigated the trapping position for each of the three plasmonic nanoparticles using the

same experimental approach as Kyrsting et al. [75].

The trapping position of a nanoparticle can be found by moving the trapping focus through the confocal focus and assessing where the two foci coincide. When the two foci coincide, the imaged intensity of the nanoparticle will be maximal. Using a steerable telescope lens, the position of the trapping focus can be controlled in the axial direction and translated in discrete steps. For each position of the trapping focus, the reflection of the trapped nanoparticle is imaged using the confocal microscope. Figure 4.8A shows an example of a data set where a trapped 150 nm gold nanoparticle is displaced axially in discrete steps through the confocal focus. It is clearly seen, that in the beginning the trapped nanoparticle is out of the confocal focus since it has a very low intensity. Towards the center of the series the intensity of the trapped nanoparticle becomes much brighter indicating that the trapping position coincides with the confocal focus. When the trapped nanoparticle is moved further into the sample the intensity drops again as it moves out of the confocal focus.

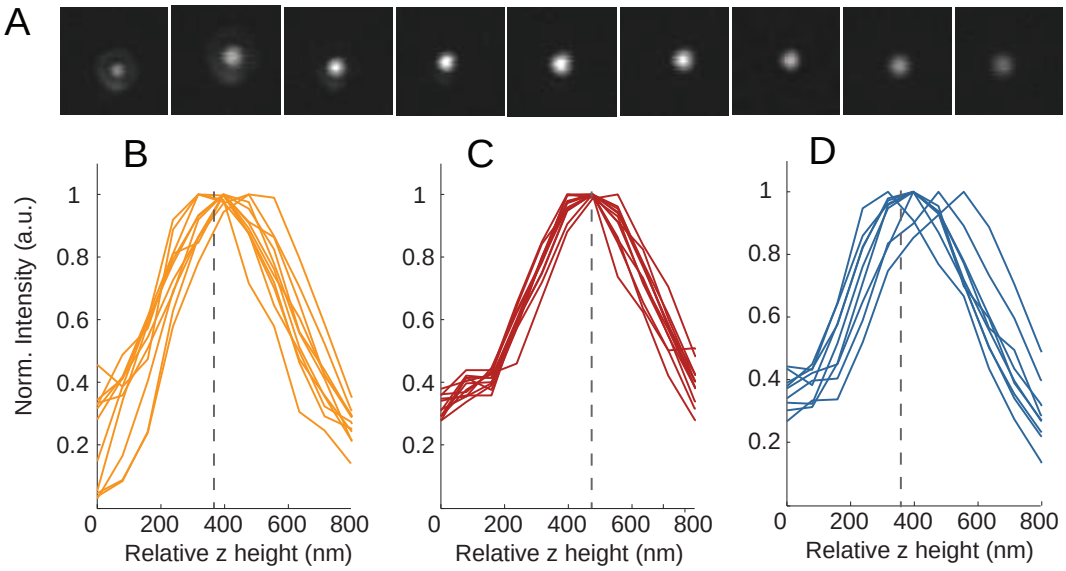

Figure 4.8: The relative trapping position of the three different types of nanoparticles. **(A)** Example of a trapped 150 nm gold nanoparticle moved through the confocal focus by displacing the trapping focus via a telescope. Analyzing the intensity of the nanoparticle at each of the trapping heights produces the axial intensity distributions shown for 80 nm gold nanoparticles in **(B)**, 150 nm gold nanoparticles in **(C)**, and 150 nm silica-gold nanoshells in **(D)**. The 80 nm gold nanoparticles and the silica-gold nanoshells trap in the same axial position, whereas the 150 nm gold nanoparticles trap in an axial position about 100 nm in front of the other two (average axial position is marked by a dashed line). $n = 11$ for (B), $n = 12$ for (C), and $n = 10$ for (D).

The experimental protocol

To prepare for the experiment all three types of nanoparticles were briefly sonicated and vortexed to obtain a homogeneous monodisperse sample. The nanoparticles were diluted in

PBS buffer to ensure single particle trapping (in a highly diluted sample the probability of trapping two particles simultaneously is considerably lower) and added to a flow chamber by capillary forces. Briefly, the flow chamber was made of a clean coverglas slide (no. 1.5, Menzel-Gläser) where two strips of parafilm were used as spacers and a smaller coverglas slide on the top was used as a lid. After adding the sample to the chamber, it was sealed with vacuum grease to prevent evaporation and placed on the microscope stage.
The laser power used in all experiments was fixed to 433 mW and the nanoparticles were imaged in reflection mode with the confocal microscope using an excitation wavelength of λ = 594 nm.

For particles smaller than the optical resolution limit, it is not straightforward to conclude the number of particles that are imaged. Consequently, there could be two particles in the trap instead of just one. To confirm that there was only one particle in the trap, the power spectrum of the trapped particle's position was measured simultaneously (data not shown). From the power spectrum we obtained the spring constant, that changes if multiple particles are in the trap. Thus, we could validate appropriate single particle trapping simply by checking the power spectrum for each measurement.

The intensity in each consecutive image was found by a Matlab based image analysis. The point spread function of the imaged particle was fitted by a 2D Gaussian function and the intensity defined as the Gaussian amplitude. The telescope lens was displaced in units of the dial (increments of 0.2) so it was necessary to find the conversion factor to produce the axial intensity distribution in terms of nanometers. The conversion factor of the 63x water immersion objective used in this experiment has previously been measured by Anders Kyrsting and found to be 396 nm per unit [75].

Measured trapping positions

The axial intensity distributions for each of the nanoparticles are shown in Figure 4.8. It should be noted that the axial distance is relative as we did not map out where the "true" trapping focus is with respect to the confocal focus as was done in the work by Kyrsting et al. [75]. In practice this means that we cannot conclude how close the trapping position of a particle is to the laser focus, but we can compare where the nanoparticles are trapping relative to each other. By doing so, we find that the average axial position corresponding to the maximum of the intensity distribution is 475 $\pm$ 36 nm for the 150 nm gold nanoparticles compared to that of 356 $\pm$ 119 nm and 356 $\pm$ 238 nm for the 80 nm gold nanoparticles and the silica-gold nanoshells, respectively (see Fig. 4.8(B-D)). Hence, the 150 nm gold nanoparticles trap more than 100 nm in front of the other two nanoparticles.
The reason for this local trapping position of the 150 nm gold nanoparticles outside the

main focus is not entirely understood but is most likely related to local intensity maixma that were also observed in the study by Kyrsting et al. [75].

From this result it follows that the 80 nm gold nanoparticles experience the same laser intensity as the silica-gold nanoshells, whereas the 150 nm gold nanoparticles either experience a lower, or higher, laser intensity. A lower laser irradiance due to axial trapping displacement can explain why the surface temperature of the 150 nm gold nanoparticles is lower than that of the 80 nm gold nanoparticles even though the opposite was expected based on their individual absorption cross-sections.

4.5 Summary

The *in vitro* comparative study focuses on the optical response of a single irradiated plasmonic nanoparticle. Using an experimental setup that combines a 3D temperature sensitive lipid assay with a confocal system implemented with a NIR optical trap, we showed that the silica-gold nanoshells are the best light-to-heat converters supported by theoretical photoabsorption calculations.

The performance relation between the 80 and 150 nm gold nanoparticles is a little harder to interpret due to the inconsistency between the calculated absorption properties and the experimentally measured heating capabilities. According to the absorption properties of the gold nanoparticles (see Fig. 4.4), the 150 nm gold nanoparticles should perform better than the 80 nm gold nanoparticles, which is in agreement with the results by Bendix et al. [25]. However, in the presented experiments the results are reversed. To address this, as well as the surprisingly little deviation in surface temperatures between the silica-gold nanoshells and the colloidal gold nanoparticles, additional experiments should be performed. The 2D lipid assay developed by Bendix et al. [25] is a great candidate as it is independent of the trapping position of the nanoparticles and thereby eliminates that experimental error.

Chapter 5

In vivo comparative study of the photothermal effect of colloidal gold nanoparticles and silica-gold nanoshells

Traditionally, clinical evaluation of cancer therapy has relied on changes in the tumor burden as a readout for the therapeutic effect [78, 79]. As the survival time to a great extent is related to the tumor growth this is a valid assessment tool, however, it is solely based on anatomical changes (shrinkage or progression) that can be fairly slow processes. Imaging techniques that can reveal immediate biological changes in the tumor are very attractive, as they can improve the ability to predict and modify the forward going therapy at an early stage. In recent years, positron emission tomography (PET) using the radioisotope labelled glucose analogue, 2-deoxy-2-[F-18]fluoro-D-glucose (^{18}FDG), has been acknowledged as one of the most important assessment tools in early cancer diagnosis and therapy response evaluation.

To date, there has been significant focus on developing plasmonic nanoparticles that possess effective NIR photothermal properties, as well as meet the size range optimal for passive EPR-based tumor delivery. As more and more NIR plasmonic nanoparticles are presented, there is an increasing need for further optimization of the strategy, in particular related to clinical translation. PET imaging has already been validated as a reliable treatment evaluation tool both with radiation therapy and chemotherapy [80–82]. We therefore anticipate that it will also be applicable for evaluation of nanoparticle mediated photothermal therapy, and that it can be used to develop personalized treatment protocols.

In this part og the comparative study we use PET/computed tomography (CT) imaging to benchmark the photothermal capabilities of NIR resonant nanoparticles to that of non-resonant nanoparticles in tumor bearing mice. This study is conducted in collaboration with Cluster for Molecular Imaging, KU, that has animal and PET/CT facilities, as well as access to the cyclotron at Rigshospitalet, KU. The chapter starts with a brief introduction to the prior studies on nanoparticle mediated photothermal therapy, with particular emphasis on silica-gold nanoshells that are the first and heaviest utilized plasmonic nanoparticles in the field. Thereafter, PET in cancer imaging will be introduced followed by the experimental procedure. At last the results will be given and the best photothermal transducer in this *in vivo* study identified.

5.1 Photothermal cancer therapy using NIR-resonant plasmonic nanoparticles

The first demonstration of photothermal therapy using NIR irradiated plasmonic nanoparticles was published by Hirsch et al. in 2003 [83]. They investigated the temperature profile as a function of tissue depth of the newly developed silica-gold nanoshells [18]. The nanoshells were injected directly ≈ 5 mm into subcutaneous tumors in mice and the thermal increase upon NIR irradiation was followed in real time using magnetic resonance thermal imaging (MRTI). They observed a maximal temperature increase of ~ 35 ℃ approximately 1 mm beneath the skin surface for the longest applied exposure time (6 minutes). The deepest temperature induced tumor damages could be detected 4-6 mm beneath the skin surface. This length-scale was attributed to be restricted by the depth-dependent reduction of the laser intensity, due to tissue scattering and photoabsotion of upper lying nanoshells.

The studies that followed that of Hirsch et al., focused on examining the efficacy of nanoshell-mediated photothermal therapy by animal survival times. A survival time study is commonly based on how long an animal lives without breaching some predefined human endpoints to avoid the animals suffer pain or distress. This also includes a predetermined tumor volume, at which the animal is euthanized. In this way, if the photothermal ablation is efficient enough to make the tumor growth abate, treated mice will have a longer survival time than untreated mice.

Studies have been conducted on mice, bearing different subcutaneous tumor models (colon, prostate, glioma, and breast amongst others), that received nanoshells by intravenous injection (systemic administration), and were assessed by caliper measurements of the tumor volume [43, 84–86]. The general trend for these studies was that mice receiving both nanoshells and NIR laser treatment survived for at least 90 days (at which point the study was ter-

minated). In contrast, mice that did not receive nanoshells were euthanized within 14 days post-treatment, the longest survival time being 24 days [86]. It is worth noting that the effective evaluation time in these studies, i.e., from the treatment until a discrepancy in the response could be detected, was on the order of two weeks.

As discussed in chapter 3, the degree of tumor accumulation of nanoparticles is believed to have a huge impact on the efficacy of the photothermal therapy. Therefore, Stern et al. [85] investigated the optimal dose of systemic administered nanoshells in a subcutaneous prostate tumor model. For the highest implemented dose, complete tumor regression was observed 21 days post-treatment in 14 out of the 15 treated mice. In comparison, only partial necrosis was observed in the mice in the low dose group [85]. In addition, mice that received the highest dose developed scabs, indicating a rather extreme temperature increase.
Day et al. [86] improved the evaluation protocol by combining the caliper based survival time studies with tumor luminescence imaging that provides a surrogate for cancer cell viability. This was achieved by innoculating the mice with firefly luciferase expressing cancer cells and monitoring the cellular development on a daily basis post-treatment. Ayala-Orozco et al. [34] used the exact same firefly luciferase expressing cell line and showed that tumor relapse occurs, in particular in larger tumors, because the cancer cells at the periphery of the tumor remain viable after treatment. Bioluminescence is a great tool to obtain detailed information about tumor regression or relapse in *in vivo* studies, but cannot be used as a clinical assessment tool as natural cancer cells are not luminescent.

In the recent years, theranostic (therapy and diagnostic) nanocomplexes have been developed with the aim of combining NIR laser therapy with imaging modalities. Bardhan et al. [43,49] presented nanoshells, that were modified to include MRI contrast and NIR fluorescent dyes. Via these imaging modalities, they showed that tumor accumulation of anti-body conjuagted nanoshells was much higher in tumors expressing the targeted receptors in comparison to tumors that did not. In addition, tracking the nanoshells in real-time allowed for temporal optimization of the NIR laser therapy [43].

In the wake of the theranostic nanoparticles developed by Bardhan et al. [49], a new class of NIR plasmonic nanoparticles called nanomatryoshkas was developed in the group of Prof. Halas. Nanomatryoshkas consist of a silica layered gold core upon which a thin gold shell is grown (i.e., gold/silica/gold). They are superior to silica-gold nanoshells in that they have a higher absorption to scattering ratio, and that their diameter can be made sub-100 nanometer while maintaining NIR resonance [69]. Ayala-Orozco et al. [6,34] conducted a photothermal comparative study of silica-gold nanoshells and nanomatryoshkas, and found that nanomatryoshka-treated mice had substantially higher survival rates, relative to nanoshell-treated mice [6]. In particular in larger tumor volumes, where nanoparticle accumulation is more complicated due to the poor perfusion and high interstitial fluid pressure, the nanoma-

tryoshkas greatly outperformed the larger nanoshells by a 4-5 times higher tumor accumulation [34].

Since the first demonstration of nanoparticle-mediated photothermal therapy, gold nanorods have probably been the most challenging candidates to the nanoshells. Nanorods can be produced with smaller dimensions than nanoshells and exhibit higher absorption cross-sections [20]. However, their photo-absorption properties are highly sensitive to their orientation with regards to the polarization of the incoming light and they easily fragment upon high irradiation intensities [73]. Furthermore, safety concerns are associated with the use of gold nanorods *in vivo* due to the toxic surfactants involved in their synthesis and this is an issue that needs to be solved before further clinical implementation.
In addition to Halas group that developed the nanomatryoshkas and the nanoshells, many other groups have aimed at developing plasmonic nanoparticles with NIR resonance, meanwhile improving the dimensions to sub-100 nanometer for efficient EPR-mediated tumor uptake. There is ample room for improvement as clinical implementation of nanoshells is challenged by their dimensions, and nanomatryoshkas so far have been by the difficulty in large-scale production.
For an broader introduction to the different types of plasmonic nanoparticles used for photothermal cancer therapy the review by Dreaden et al. [57] is highly recommended.

5.2 PET-based cancer imaging

PET is a nuclear imaging technique that uses the unique decay characteristics of positron emitting radioisotopes. It is a highly sensitive and nearly non-invasive technique, that allows for three-dimensional imaging of physiological processes in living animals. The concept of PET is built on injecting radioisotope labelled molecules (or tracers) intravenously and tracking where they locate.
When the radioisotope decays it emits a positron that travels for a short distance in the tissue until it loses energy (path length of $\sim 10^{-1}$ - 10^{-2} cm) and collides with an electron [87]. Upon annihilation of the positron and the electron, two gamma rays with energies of 511 keV are created and emitted in opposite directions (see Fig. 5.1A). The gamma rays are registered by the PET scanner that consists of a ring of multiple detectors. The detectors are made of solid scintillator crystals that create a burst of light when a gamma ray is deposited inside of it, with an energy proportional to that of the gamma ray. The light burst is collected in a photomultiplier tube and translated into an electric signal. Since the detectors are coupled, selected detection for gamma rays that arrive in pairs and in approximately opposite directions can be introduced. This means that gamma rays that are probably not stemming from the same annihilation process are excluded from the data set. In a typical

PET scan, 10^6 - 10^9 events are detected.

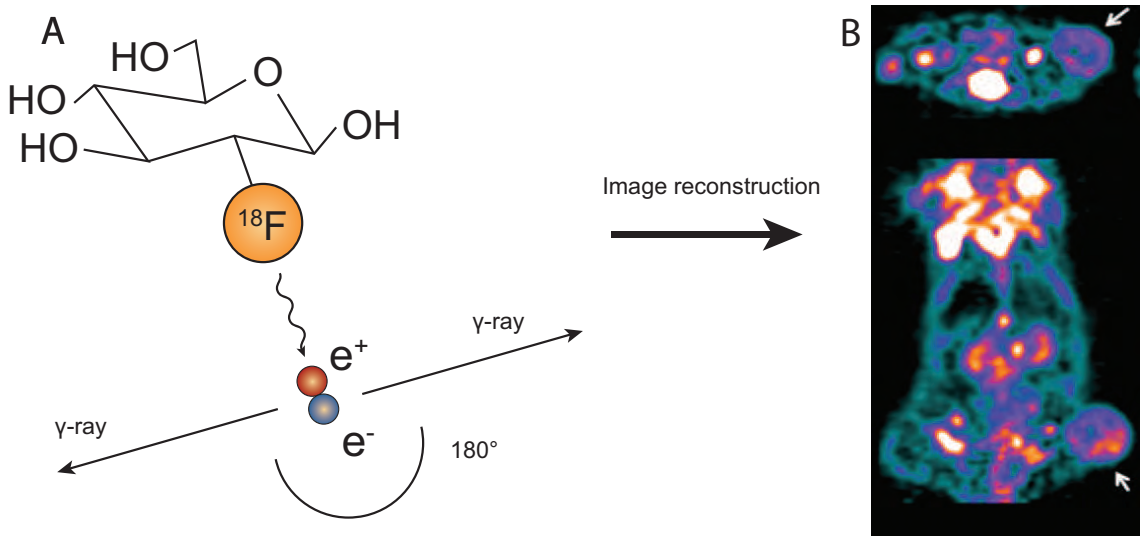

Figure 5.1: (A) The radioisotope tracer ^{18}FDG, that is a glucose analogue, decays by emitting a positron. After a short distance the positron looses energy and annihilates with a electron by which a pair of gamma rays are emitted in opposite directions. The gamma rays are collected by a scanner and the image providing the whole-body distribution of the tracer is reconstructed. **(B)** Reconstructed image showing transverse (upper) and coronal (lower) accumulation of ^{18}FDG in a mouse. The arrows mark the tumor site where there is a high uptake of ^{18}FDG.

The electric output signal is reconstructed as a 3D image by a line of response analysis, that identifies the location of the annihilation process based on a straight line connecting the positions where the pair of gamma rays is detected (see Fig. 5.1B) [87]. The signal intensity in the image volume is proportional to the concentration of the radioisotope, and therefore the spatial distribution of the tracer in the whole body is obtained. There are small experimental errors related with the PET technique as it is the location of the annihilation process that can be reconstructed and not the point of positron emission. In addition, the gamma rays are not exactly emitted with an angle of 180°, but with a distribution of angles around 180°.

The temporal resolution in PET scanners is given by the so-called dead time, that is the detectors ability to temporarily distinguish arriving gamma rays ($\sim$ 2 - 6 ns) [87]. The spatial resolution in whole-body human PET scanners is on the order of (6 - 8)^3 mm^3 and the sensitivity of 10^{-11} - 10^{-12} moles/litre [88]. In small animal PET scanners the spatial resolution is $\approx$ 1 mm^3. It should be noted that in general, the resolution depends on the tracer [89].

^{18}FDG

The glucose analogue, ^{18}FDG, is the most applied PET tracer in cancer diagnostic due to the increased glucose metabolism found in cancer cells. After being taken up by the cells, ^{18}FDG is phosphorylated to FDG-6-PO_4, that cannot be metabolized further in the glycolytic pathway. Therefore ^{18}FDG remains intact inside the cell until it decays ($\tau_{1/2} \approx$ 110 min [87]). Glucose and ^{18}FDG are completely cleared from the blood after about an hour which enable accurate PET detection of the whole-body ^{18}FDG distribution before the tracer decays (see Fig. 5.1B). In non-viable cancer cells the glucose uptake is diminished which results in a reduction of the ^{18}FDG signal within the tumor volume.
Essentially this means that the treatment response can be assessed by a ^{18}FDG PET scan as early as an hour after the therapeutic intervention. The recurrence or regression of the cancer cells can be evaluated by subsequent ^{18}FDG PET scans in a time frame that is only restricted by the biological processes and outperforms anatomical based evaluation methods (e.g., assessment by mechanical calipers, CT, or MRI).
Anatomical information for cancer diagnosis and evaluation is highly relevant, and therefore PET and CT imaging are often integrated. CT is a technique based on the tissues' ability to block X-rays and provides high resolution 3D anatomical information, that also improves accuracy of image interpretation.

5.3 *In vivo* heating capabilities of resonant and non-resonant nanoparticles

In this part of the comparative study we aim at strictly comparing the NIR photothermal capabilities of resonant nanoshells to those of non-resonant colloidal gold nanoparticles in tumor bearing mice. To acquire as unbiased data as possible, all other experimental parameters than the optical properties are kept constant throughout a comparison study, by using the same laser power and exposure time, and same number of nanoparticles delivered to the tumor. Tumor delivery via tail vein injection and passive accumulation largely depends on the particle size (i.e., the EPR-effect, see chapter 3), so to circumvent this factor we instead deliver the nanoparticles by intratumoral injection.

Experimental protocol

The time line for the *in vivo* photothermal therapy study is shown in Figure 5.2. In the following sections each step will be outlined in details.

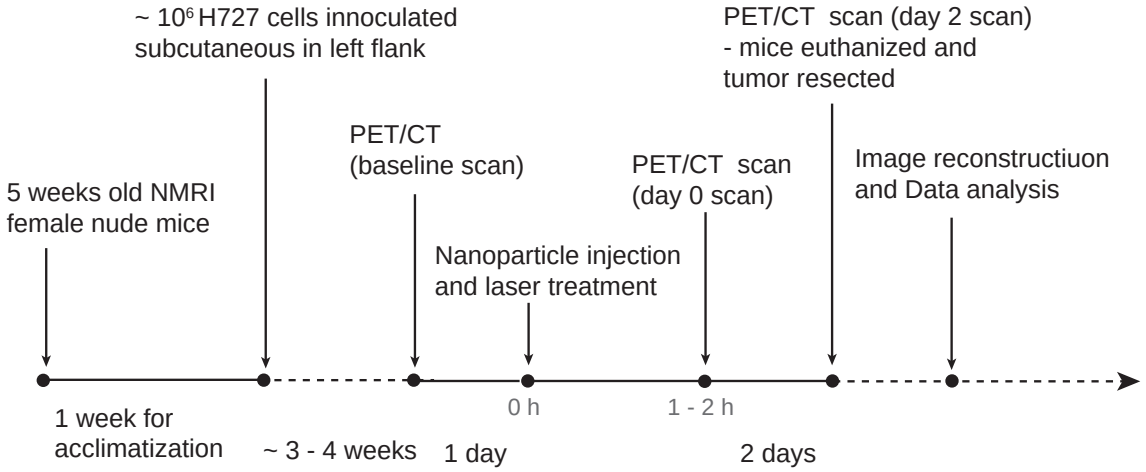

Figure 5.2: Time line for the *in vivo* photothermal therapy study.

Briefly, the tumor bearing mice were divided into four groups constituting the three different types of plasmonic nanoparticles and a control group. The mice were PET/CT scanned one day prior to the nanoparticle-laser treatment for a baseline level of ^{18}FDG uptake. After the treatment, the mice were PET/CT scanned again using ^{18}FDG at an early ($\sim$ 1 hour) and a late (2 days) time point for assessment of the treatment response.

Animals

The mice used for this study were female NMRI nude mice (5 weeks old) obtained from Taconic Europe (Lille Skensved, Denmark)(see Fig. 5.3). Due to a genetic mutation they lack the thymus; the organ associated with the adaptive immune system and T cell maturation. T cells recognize foreign intruders (such as cancer cells) and with a small population of T cells the mice are effectively immune deficient and hence it is easy to establish a human tumor xenograft in them.

Neuroendocrine cancer cells

The cell line we used was a human neuroendocrine lung carcinoid (H727) from the European Collection of Cell Cultures (ECCAC, Salibury, UK). The cells were cultured in standard cell culture medium (RPMI medium 1640+ GlutaMAX) supplemented with 10% fetal calf serum and 1% penicillin-streptomycin (Invitrogen Co., CA, USA) at 37 ℃ and in 5 % CO_2.

Neuroendocrine tumors belong to a heterogenous group of neoplasms that arise from cells of the diffuse hormonal (endocrine) and nervous system [90]. Carcinoid is a slow-growing tumor that is most commonly found in the intestines. However, as in the case of the H727 cell line, carcinoid tumors also occur in the lungs.

Figure 5.3: Picture of a female NMRI nude mouse.

Establishing tumor xenografts

All animal care and experiments have been approved by the Danish Animal Welfare Council, Ministry of Justice. Upon arrival the mice were allowed to acclimatize for one week before $\sim 10^6$ H727 cells were inoculated into the left flank of the 6 weeks old female NMRI nude mice. Up to the age of 6 weeks, mice gain about 5 grams per week and afterwards the growth rate slows down. The mice were held in an animal facility, maintaining the availability of water, chow and the general standard of living for the mice. The tumors were allowed to grow for a few weeks until they reached a volume of 593 $\pm$ 221 mm^3 (never bigger than 1000 mm^3). The tumor dimensions were measured with a mechanical caliper and the tumor volume calculated as: $volume = \frac{1}{2}(length \cdot width^2)$.
The mice were divided into four subgroups receiving 80 nm gold nanoparticles, 150 nm gold nanoparticles, silica-gold nanoshells, or saline (control group). The groups were matched such that the total tumor volume in all groups was comparable.

PET/CT baseline scan

The day before the photothermal therapy, each mouse underwent a baseline ^{18}FDG PET/CT scan to be used as a reference point for the PET tracer signal post-treatment.

The mice were administered approximately 10 MBq ^{18}FDG via the tail vein while being anesthetized by breathing sevoflurane (see Fig. 5.4A). ^{18}FDG was obtained from the daily production at Rigshospitalet, KU.
One hour after ^{18}FDG injection, the mice were static PET scanned for 10 minutes using a dedicated small animal PET scanner (see Fig. 5.4B) (microPET Focus 120, Siemens Medical

Solutions, Malvern, PA, USA). The energy window of the PET detectors were set to 350 - 650 keV and the time resolution to 6 ns.
The PET scan was subsequently followed by a CT scan (360°; 220 projections) using a MicroCAT II tomograph (Siemens Medical Solutions). The x-ray tube has a 0.5 mm aluminum filter and was set at 60 mV in tube voltage and 430 μA in tube current with an exposure time of 680 ms per projection.

During all scans the mice were placed on a scan bed and were anesthetized by breathing sevoflurane. Their body temperature was kept stable using a heating pad (see Fig. 5.4C). The mice were injected with ^{18}FDG with a time gab of approx. 12 - 15 minutes such that it matched the scan period of each mouse (incl. an extra few minutes for preparation).

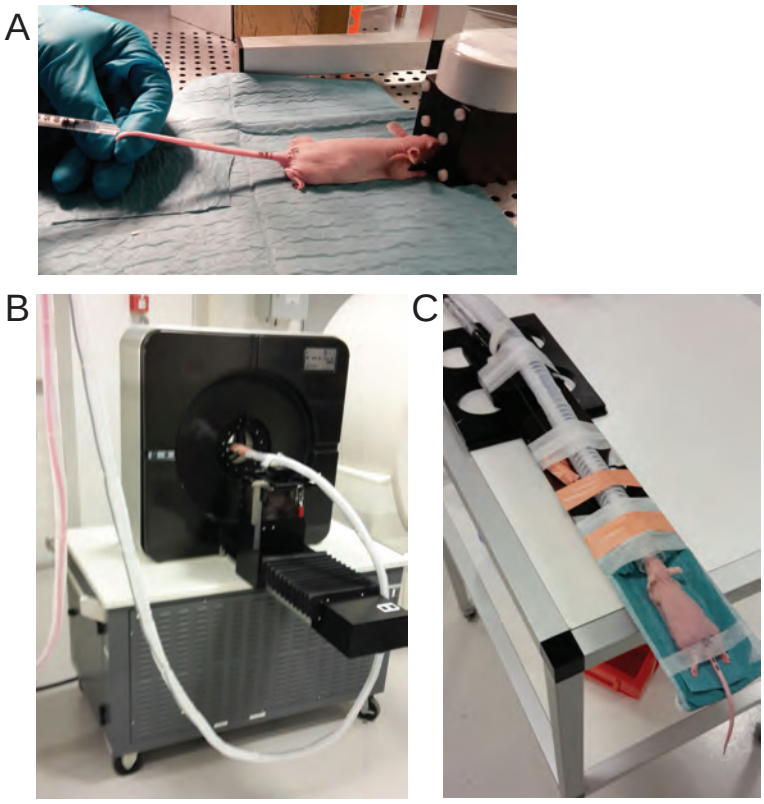

Figure 5.4: PET protocol. **(A)** ^{18}FDG was injected into the blood via a tail vein. **(B)** and **(C)** An hour after ^{18}FDG injection, the PET scan was performed. The mouse was placed on a bed with a heating pad and anesthesia incorporated, that fits into the small animal PET scanner.

Nanoparticle injection

On the next day, the mice were weighted and their tumor volume was measured (with a mechanical caliper). The nanoparticles were sonicated for 5 min. and vortexed to ensure they were homogeneous and monodisperse. They were diluted to a final concentration of 5x10^{10} nanoparticles/ml in buffered saline water (saline) and sonicated for 30 s.

The mice were anesthetized by breathing sevoflurane and injected intratumorally with 50 μl of nanoparticles using a programmable syringe pump (Harvard Apparatus) with a flow rate of 5 μl/min. (1 ml syringe, 25G needle) (see Fig. 5.5). The control group received 50 μl of saline instead of nanoparticles. The needle was inserted approx. 3 mm into the tumor. After injection the needle was left in the tumor for about 10 minutes to equalize the interstitial pressure and prevent back flow of blood and nanoparticles when the needle was pulled out.

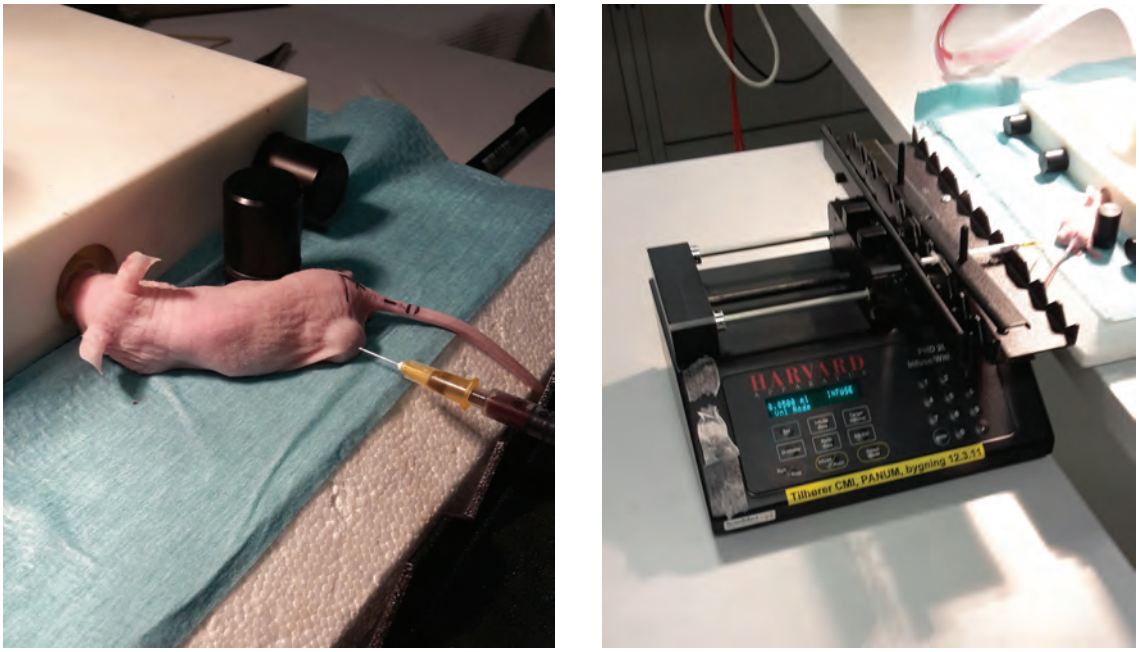

Figure 5.5: Intratumoral injection of nanoparticles. The mouse was anesthetized while a syringe was inserted into the tumor. The Harvard pump injected the particle with a infusion rate slow enough to prevent pressure induced damage.

In the majority of *in vivo* studies using photothermal therapy, the treatment was initiated when the tumor volumes were around $\approx$ 200 mm^3 [6] (in comparison to $\approx$ 600 mm^3 in this study). The motivation for using relatively smaller tumor volumes is that the studies are terminated if the tumors breach the predetermined volume ($\approx$ 1500 mm^3) [6] and therefore the initial tumor volume is a limiting factor for how long the study can be conducted.

In this study we are not investigating if the therapy can lead to tumor remission, but instead we are comparing the photothermal effect of different types of plasmonic nanoparticles directly. To do this, we inject the same number of nanoparticles into the tumor volume which is much easier to do accurately in larger volumes. In addition, for PET/CT based comparison it is sufficient to follow the tumor progression for two days post-treatment to evaluate if there is a treatment response.

Laser treatment

Immediately after the nanoparticle injection (or saline injection), the mice were irradiated for 5 min. with a laser power of 300 or 500 mW. The optical setup used in the *in vivo* study is based on an 807 nm diode laser (Highlight FAP DUO 30/810, Coherent) that produces a maximum output of 30 W. The diode laser is coupled via a fiber to a fixed focus collimator (F220SMA-780, Thorlabs) and is set to have a beam diameter of 1 cm. The mice were placed on a height-adjustable table in a way that the tumor coincided with the laser spot, and on a heating pad in order to avoid temperature fluctuations (see Fig. 5.6). The mice were anesthetized by breathing sevoflurane and observed during the entire exposure time to ensure they did not suffer if burn blisters appeared.

If the mice developed burn blisters after the laser treatment they were euthanized at this point. Otherwise they were kept alive, under observation for the next two days.

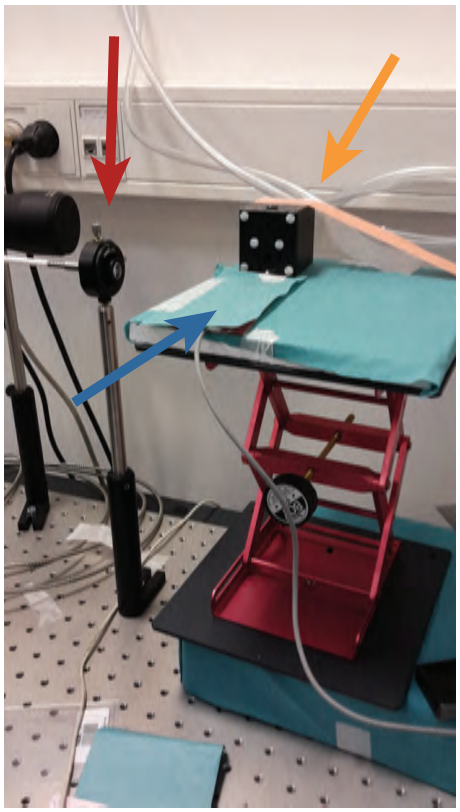

Figure 5.6: Picture of the optical setup. In front of the laser port (marked by the red arrow), there was a height adjustable table where the mouse was lying during the laser treatment. The mouse was placed with its nose in the black nosecone (marked by the yellow arrow) that provided anesthesia during the entire exposure period. The mouse was lying on a heating pad (marked by the blue arrow).

Post-treatment PET/CT scan

30 - 60 minutes after the laser treatment the mice were again anesthetized and injected with approximately 10 MBq of ^{18}FDG via a tail vein. One hour later they were PET/CT scanned to assess the immediate effect of the treatment.

Two days after the treatment, the mice were weighted and their tumor volume measured (with a mechanical caliper). Thereafter they were ^{18}FDG PET/CT scanned following the same protocol as in the previous scans.

PET/CT scanning on two days post-treatment is serving as a control of the signal measured immediately after the treatment. If a blood vessel ruptures, either caused by the injection or the laser treatment, proper perfusion of the tumor can be prevented which will cause a decrease in the ^{18}FDG signal that is unrelated to the photothermal treatment. The ^{18}FDG uptake two days after may not be as pronounced as immediately after the treatment, but if it remains we can conclude that it is in fact a result of the photothermal treatment (tumor angiogenesis is faster than this timescale).

After the PET/CT scan on day 2, the mice were euthanized and the tumors resected for visual inspections. Leakage of the nanoparticles appeared as large dark spots in the periphery of the tumor or on the outer dermal surface. Hence, by looking at the tumor tissue and the skin surrounding it we could validate if the nanoparticle injection was deposited correctly and did not leak out of the tumor after the needle was pulled out.

PET/CT evaluation of photothermal therapy

Images of ^{18}FDG PET scans (Fig. 5.7) are displayed as projection images showing the coronal planes and the uptake is given as the injected dose (MBq) per body weight (%ID/g) (Inveon software). PET scans are taken the day before the treatment (baseline scan), immediately after (day 0), and two days post-treatment (day 2). The baseline scans show that the tumors have a high ^{18}FDG uptake (the tumors are the ball-like structure at the upper-left corner on the mouse). The location in the tumor where the nanoparticles have been injected, and subsequently irradiated with the NIR laser, is marked by white arrows.

By simple visual inspection of the images it is clearly seen that the mouse that received silica-gold nanoshells, shows a tumor subvolume with limited ^{18}FDG uptake, both immediately and two days after the treatment (marked by red arrows in Fig. 5.7). However, the effect is less pronounced two days after. This signal loss occurring post-treatment is a strong indication that the cancer cells in this region have reduced metabolism (or are ablated) as a consequence of the treatment. Another factor that can be deduced from these images,

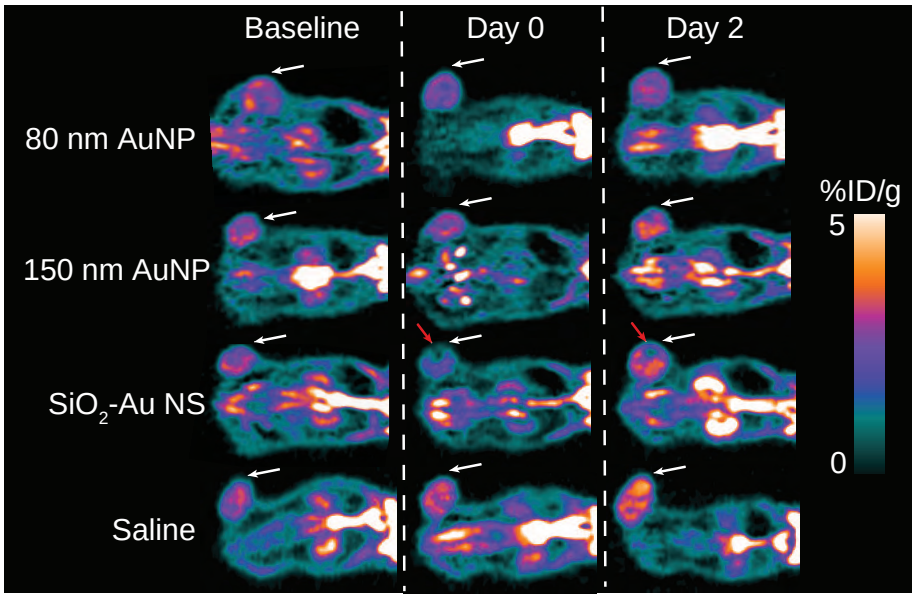

Figure 5.7: PET evaluation of the treatment response. The images show the coronal planes of the ^{18}FDG body distributions of mice from each nanoparticle group. The first column shows the baseline PET scan, the second the PET scan just after the laser treatment, and the last show the PET scan two days post-treatment. White arrows mark where the nanoparticles were intratumorally injected and subsequently irradiated with the NIR laser. In the images of mice receiving 80 and 150 nm gold nanoparticles, there are no clear indications of a treatment response, however in the silica-gold nanoshell group there is a region with high loss of activity, that remains after 2 days (marked by red arrows). Notably, from the images it seems that the saline group is the only one where the metabolic activity increases.

is that the fraction of the tumor volume that is affected is very small, meaning that the nanoparticles only induce cell ablation in their local environment.

Mean and maximum ^{18}FDG uptake

The treatment effect can be analyzed semiquantitatively by considering the %ID/g within a volume of interest (VOI). The VOIs are generated by free-hand drawing so that the tumor volume is covered. From the VOI, the average ^{18}FDG signal intensity within the tumor can be obtained as well as the maximum signal intensity. These measures are indications of the metabolic activity and are commonly used for clinical evaluation. The mean and maximum ^{18}FDG uptake in the tumor for the three subgroups (silica-gold nanoshells ($n = 4$), 80 nm gold nanoparticles ($n = 3$), and 150 nm gold nanoparticles ($n = 3$)) are shown in Figure 5.8 for a laser power of $P = 300$ mW.

The mean ^{18}FDG uptake (see Fig. 5.8A) does not change significantly over the time course of the study, neither does the maximum ^{18}FDG uptake (see Fig. 5.8B). This result can be explained by either of two scenarios: The cells are unaffected by the treatment or the treated volume is too small to affect the mean activity. As it was clear from visual inspection of the PET scans in Fig. 5.7 that there is in fact a signal loss, however highly localized, we assume that the fraction of the tumor volume that can be affected using this setup is too small to influence the mean value. That the maximum activity is unchanged, is not a big surprise as a change would require that the nanoparticles were deposited exactly on the spot where the highest pixel value of FDG uptake is obtained. By means of intratumoral delivery the chance of this is very low.
Importantly, in the data set shown in Fig. 5.8 the uptake levels are very similar meaning that the groups can easily be compared in terms of treatment response.

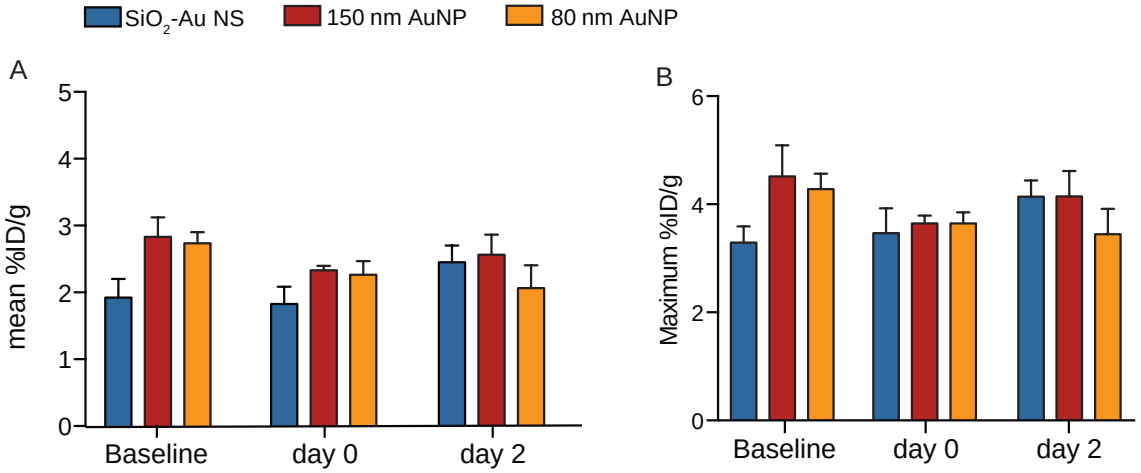

Figure 5.8: Analysis of the ^{18}FDG uptake in the tumors. **(A)** Mean ^{18}FDG uptake over the time course of the study for each of the three subgroups: silica-gold nanoshells ($n = 4$), 80 nm gold nanoparticles ($n = 3$), and 150 nm gold nanoparticles ($n = 3$). **(B)** The maximum ^{18}FDG uptake for the same data as shown in **(A)**. We do not observe any development in the mean or in the maximum uptake over time indicating that either the therapeutic response is absent or restricted to a very local region within the tumor volume. As we have seen indications of a treatment response, at least in the silica-gold nanoshell receiving group, we assume that the latter explanation is the reason. Error bars represent SEM.

Thresholded volume based on reduced ^{18}FDG uptake

Since the therapy is so local, the fraction of the tumor volume that has lost activity because of the treatment might carry more information about the treatment response than the mean metabolic activity. The affected volume can be quantified by generating an additional VOI. The VOI is set by the assumption that tissue that has been irreversibly damaged by the therapy has a lower ^{18}FDG uptake due to loss of metabolism. The threshold value is set to 30% of the maximum ^{18}FDG uptake and hence returns the volume where cells have a metabolic activity reduced to 0 - 30 % of the maximum (see Fig. 5.9A).

From this analysis we clearly see a treatment response in the group that receives silica-gold nanoshells as the thresholded volume increases substantially from the baseline PET scan to after the treatment. The other two groups, receiving the 80 and 150 nm gold nanoparticles, show no sign of treatment response. As this thresholded volume could be influenced by necrosis, in particular in larger tumor volumes, the volume fraction (thresholded volume per total volume) is also calculated to exclude such effects (see Fig. 5.9B). The largest volume with reduced activity is observed in the silica-gold nanoshell group with a volume fraction of $\sim$ 17 %. Based on this small overall percentage, we can conclude that the treatment is indeed confined to the local environment surrounding the nanoparticles and that it makes sense that we cannot see a change in the mean ^{18}FDG tumor uptake (see Fig. 5.8).

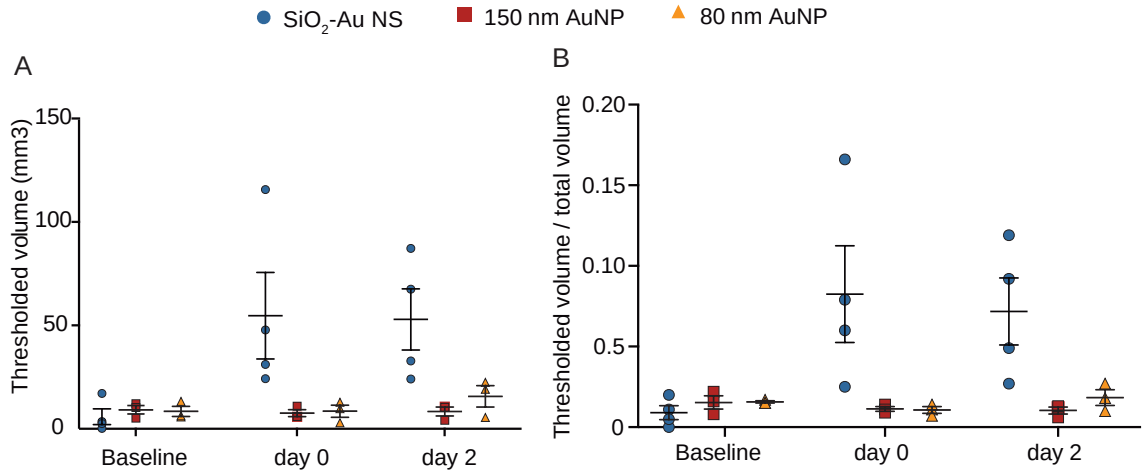

Figure 5.9: Analysis of the tumor volume affected by the treatment. **(A)** The volume of the tumor showing 0 - 30 % metabolic activity of the maximum. The silica-gold nanoshell group has a substantial increase in the thresholded volume post-treatment indicating therapeutic induced cell ablation. The other two groups, receiving the 80 and 150 nm gold nanoparticles, show no sign of therapeutic response. **(B)** The volume fraction of the tumor showing 0 - 30 % metabolic activity of the maximum, follows the same tendency as in **(A)**. The percentage of the total volume having a therapeutic response is < 20 %, indicating that the treatment is highly localized. Error bars represent SEM.

High laser group

As the 80 and 150 nm gold nanoparticles showed no effect in the study, we were motivated to conduct a new experiment where the laser power was increased from $P = 300$ mW to $P = 500$ mW. In this study we included the control group with mice receiving saline and laser irradiation, as we expect that if there is no therapeutic effect at the high laser power, there should neither be any effect at lower laser powers.
We did not observe any scabs in the initial study, but we did see mild flushing on the skin covering the treated area in the group receiving silica-gold nanoshells. As the mice must not suffer pain or distress we have to euthanize them if they develop burn blister. Therefore, the silica-gold nanoshells were left out of this study. Hence, we had three groups with mice receiving 80 nm gold nanoparticles ($n = 3$), 150 nm gold nanoparticles ($n = 2$), or saline (control group; $n = 3$). Unfortunately one of the mice was omitted from the 150 nm gold nanoparticle group due to technical difficulties with the PET scanner.

Mean and maximum ^{18}FDG uptake

The mean and maximum ^{18}FDG uptake in the tumors are shown in Figure 5.10. As in the first photothermal study (see Fig. 5.8), the mean and the maximum ^{18}FDG uptake in all groups are not significantly different, even after the laser treatment. Interestingly

there is a small increase in the saline receiving group (the observation is not statistical significant).

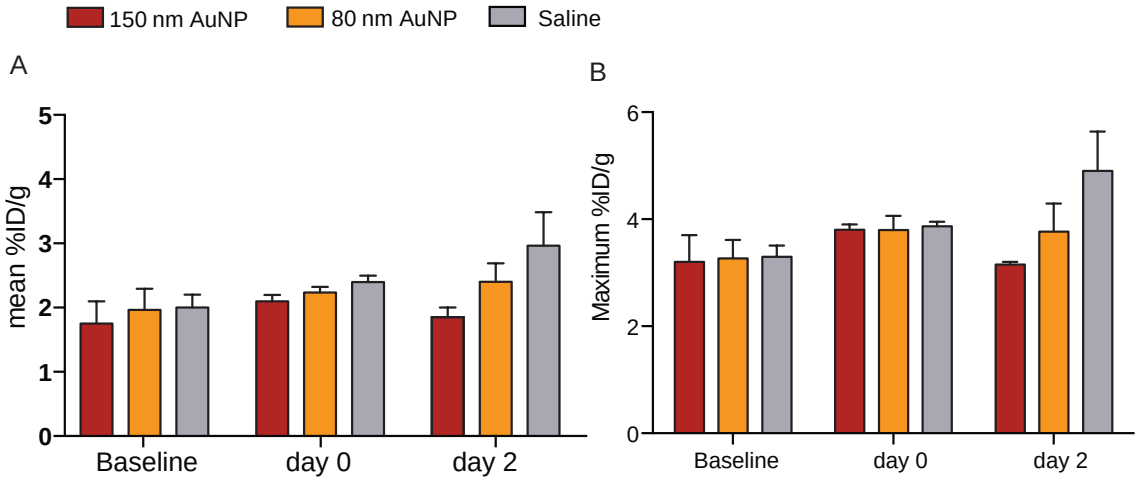

Figure 5.10: Analysis of the ^{18}FDG uptake in the tumors. **(A)** Mean ^{18}FDG uptake over the time course of the study for each of the three subgroups: 150 nm gold nanoparticles ($n = 2$), 80 nm gold nanoparticles ($n = 3$), saline (control group; $n = 3$). **(B)** Maximum ^{18}FDG uptake for the same data as shown in **(A)**. We do not observe any development in the mean or the maximum uptake over time indicating that either the therapeutic response is absent or restricted to a very local region within the tumor volume. Error bars represent SEM.

Thresholded volume based on reduced ^{18}FDG uptake

The lack of metabolic change in the groups receiving both nanoparticles and laser treatment could be due to either no effect of the therapy, or because the treated volume is too small to enable a detectable change in the mean ^{18}FDG uptake. Hence, we threshold the ^{18}FDG uptake, in a similar fashion as done in the low laser power study, and obtain both the thresholded volume and the volume fraction, that has a metabolic activity reduced to 0 - 30 % of the maximum. The results are shown in Figure 5.11.

One mouse in the 150 nm gold nanoparticle group has an increased threshold volume after the treatment that remains for the next two days. However, as this data set only contains two data points, where one of them is non-responsive, it is difficult to make any conclusion. The group receiving 80 nm gold nanoparticles has no significant increase in the thresholded volume.

The saline receiving group serves as a control to confirm that the NIR laser alone does not induce tissue damage. In addition, we also did a control study to confirm that the intratumorally injected nanoparticles also do not possess any toxic effects within the time course of this study. This control study was conducted according to the experimental protocol but without irradiating the nanoparticle-laden tumors. We did not observe any tissue damage

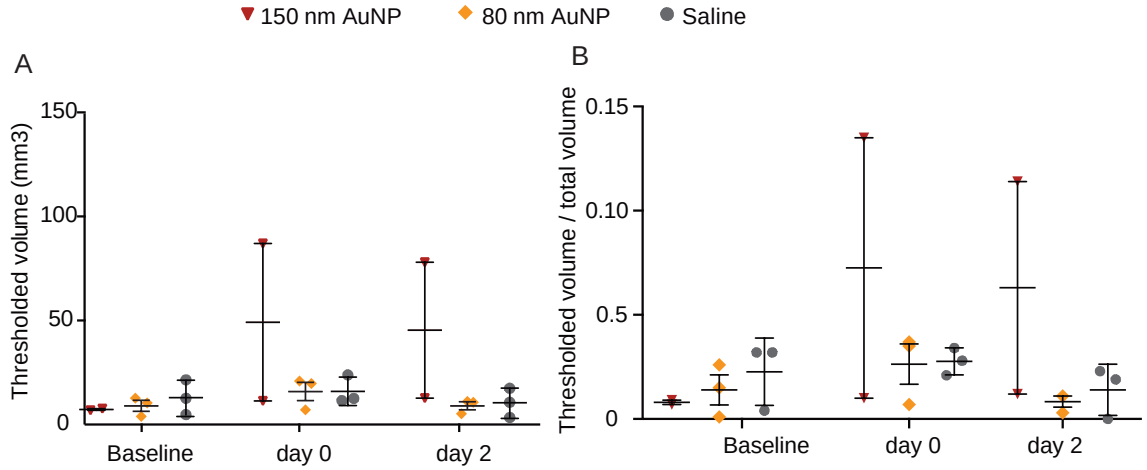

Figure 5.11: Analysis of the tumor volume affected by the treatment. **(A)** The volume of the tumor showing 0 - 30 % metabolic activity of the maximum. **(B)** The volume fraction of the tumor showing 0 - 30 % metabolic activity of the maximum, shows the same tendency as in **(A)**. In the group receiving 150 nm gold nanoparticles there is one mouse that show a response to the treatment with a thresholded volume fraction of $\sim$ 15 % of the total volume. The group receiving 80 nm nanoparticles, has no therapeutic response. The lack of response in the saline group serves as a positive control for the therapy. Error bars represent SEM.

(the data is not analyzed quantitatively; only visually inspected by reconstructed PET images and the resected tumor tissue). In conclusion, the therapeutic intervention requires the presence of both nanoparticles and laser irradiation.

Statistics

At the different time points in the data containing the thresholded volumes (Fig. 5.8) groups were compared using one-way ANOVA with Tukeys post hoc test. Using this test the mean is compared with every other mean under the assumption that the data is normally distributed.

All multiple comparison tests for the 80 and 150 nm gold nanoparticle groups showed no statistical significance (all p-values were > 0.9). However, when comparing the silica-gold nanoshells group on day 0 and day 2 to the other groups (including the saline group), the p-values were < 0.18. If comparing the silica-gold nanoshell group at day 2 with the 150 nm gold nanoparticles and the saline groups, the data in fact represented a statistical significance, i.e. $p < 0.05$.

Clearly the statistics are fairly poor. It reflects that the number of subjects in these compared experiments is very low and we expect that the statistics become better if we include more animals in each group.

High nanoparticle dose

The treatment efficacy is also dependent on the dose of delivered nanoparticles [85]. Hence, we conducted a single experiment where the concentration of 80 nm gold nanoparticles was increased by a factor four (i.e., 50 μl of 2x10^{11} nanoparticles/ml are injected intratumorally; $P = 100$ mW). The whole-body ^{18}FDG uptake is shown Figure 5.12.

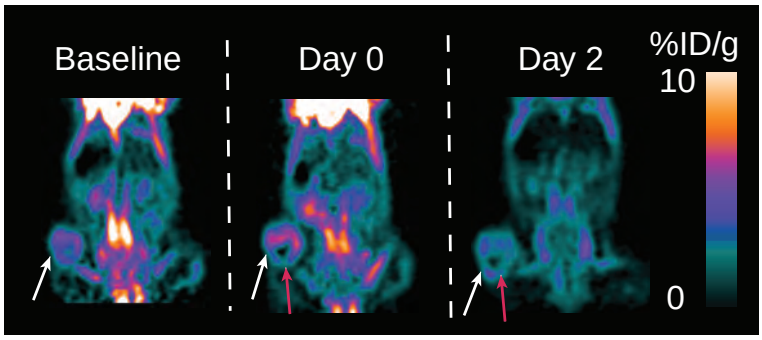

Figure 5.12: PET evaluation of the treatment response. The images show the coronal planes of the ^{18}FDG body distributions of a mouse receiving a higher dose of 80 nm gold nanoparticles and a laser power of $P = 100$ mW. White arrows mark where the nanoparticles were intratumorally injected and subsequently irradiated with the NIR laser. By increasing the dose of nanoparticles a treatment response can be achieved, that remains after 2 days (marked by red arrows).

By visual inspection of the PET scans, it is clear that there is a region in the tumor where the ^{18}FDG uptake is reduced after the treatment (marked by red arrows in Fig. 5.12; effect is not quantified). It should be mentioned that these images are scaled differently than those shown in Fig. 5.7 and therefore cannot be compared directly. However, the point was to prove that a photothermal response can be achieved with the 80 nm gold nanoparticles as well, by tuning the experimental parameters, e.g., the delivered nanoparticle dose.

5.4 Discussion

In this *in vivo* study we used PET/CT imaging to benchmark the photothermal capabilities of NIR resonant silica-gold nanoshells to those of non-resonant gold nanopaticles in tumor bearing mice. To control the number of nanoparticles in the tumor directly, we used intratumoral injection for delivery of the nanoparticles as opposed to systemic administration where nanoparticle tumor accumulation is size dependent.

We found that intratumorally delivered silica-gold nanoshells have a strong, but very localized, treatment response upon NIR irradiation. In this study we could detect any significant therapeutic difference between the 80 and 150 nm gold nanoparticles. However, by increasing the concentration of the nanoparticles or the laser power, our results indicate that photothermal ablation is also achievable with non-resonant nanoparticles. The treatment

response observed in the silica-gold nanoshell receiving group, was found to be effective only in the local environment of the nanoparticles. In addition, we found that neither NIR laser irradiation alone nor the intratumoral presence of nanoparticles in itself, pose any harm to the tissue. These are promising results for the applicability of this photothermal strategy as it is aimed at being specific to only cancerous tissue and at having minimized invasiveness compared to traditional cancer therapies (e.g., radiation and chemotherapy).

Interestingly, there is a small tendency in the saline receiving group that the ^{18}FDG uptake increases through the time course of the study (see Fig. 5.10; this is not statistically proven). In contrast, all the nanoparticle and laser receiving groups have unchanged ^{18}FDG uptake levels (see Fig 5.8 and Fig. 5.10). Cells that receive damage by, e.g., mild hyperthermia, tend to go into a state where division is arrested while the cells attempt to repair the damages. We propose, that even though we cannot detect any therapeutic effect in the groups receiving 80 or 150 nm gold nanoparticles, the cancer cells might still be in a stressed state induced by, e.g., mild hyperthermia. Using ^{18}FDG we only obtain information about the metabolic state, that is maintained as long as the cells are still alive. Therefore, cell proliferation would be a good complimentary measure of the physiological state of the cells. The PET tracer, 3´-deoxy-3´-[18-F]fluorothymedine (^{18}FLT), is a thymidine analogue, that is needed for DNA replication. Hence, we propose that ^{18}FLT should be investigated in combination with ^{18}FDG to obtain more detailed information of the functional state of the tumor upon photothermal therapy [80].

Due to the relative low numbers of mice investigated in each group, the results in this comparative study are accompanied with fairly large uncertainties. We believe that the treatment response is highly dependent on how well the intratumoral injection was executed: If the nanoparticles were injected too deeply into the tissue, the effective radiation power could be substantially reduced because of tissue attenuation. Furthermore, if the nanoparticles leaked out when the needle was withdrawn, the effective nanoparticle dose in the tumor volume would be reduced.

It is clear that we need to include more subjects in each group to make any valid quantitative conclusions. However, we have proven that PET/CT imaging can be used to evaluate treatment responses as early as an hour after the therapeutic intervention. In addition, we have shown that in an *in vivo* context, where the number of particles are kept constant by delivering them via intratumoral injection, the silica-gold nanoshells are the best NIR light-to-heat converters. Our results show qualitative indications that the 80 nm gold nanoparticles, in high doses, can induce cell ablation (see Fig. 5.12). In a study where the particles are delivered by intravenous injection, we expect the 80 nm gold nanoparticles to have a higher passive tumor accumulation than the larger nanoparticles examined in this study, that accordingly would enhance their effective photothermal capabilities.

Chapter 6

Conclusion

6.1 Conclusion on plasmonic nanoparticles for photothermal cancer therapy

This part of the thesis work contains a comparative study of the capabilities of NIR resonant silica-gold nanoshells as photothermal transducers to those of non-resonant colloidal gold nanoparticles with two different sizes. We use these particular nanoparticles as they are commercially available and because they represent three distinct classes: The 150 nm silica-gold nanoshells have optimal NIR optical properties, the 80 nm gold nanoparticles have an optimal size for tumor accumulation by systemic administration, and the 150 nm gold nanoparticles represent the a group that neither have NIR resonance nor are optimal in size. The aim of this project was to develop a strategy that can help answering the question in the literature regarding which nanoparticle is the optimal for photothermal cancer therapy. Our long-term goal is to develop a clinical protocol for photothermal cancer therapy, that based on PET/CT evaluation can be used to tailor the best treatment strategy for the individual patient, and that can be used regardless of which plasmonic nanoparticle is utilized.

The heating capability of each of the plasmonic nanoparticles was assessed *in vitro* using a 3D assay based on a lipid membrane vesicle. The vesicles had a well-characterized phase transition incorporated with phase sensitive fluorescent dyes [74, 76]. The assay directly returned the distance at which the heating of a trapped nanoparticle induced local melting of the membrane that via the Goldenberg relation [77], was used to calculate the temperature increase at the surface of the nanoparticle. We found that the surface temperature increase of the silica-gold nanoshells was highest as anticipated. Surprisingly, we found that the 80 nm gold nanoparticles obtained a slightly higher surface temperature than the 150 nm gold

nanoparticles, contradicting the linear relationship between the absorption cross-section and the volume of the particle.
It has previously been shown that larger 3D optically trapped nanoparticles (> 100 nm) exhibit reduced heating compared to smaller nanoparticles as they stably trap in front of the laser focus, effectively reducing the radiance power [74, 75]. By mapping the trapping position of each of the nanoparticles we found that the 150 nm gold nanoparticles indeed did trap about 100 nm in front of the other two nanoparticles. This can explain the discrepancy between the measured heat generations and the calculated absorption cross-sections of the 80 and 150 nm gold nanoparticles.
In the light of these results, the next step could be to examine the heat generation properties of the three nanoparticles in the 2D lipid assay developed by Bendix et al. [25], where the particles are immobilized, and see if the heating tendencies prevail in this assay.

According to the theoretical FEM-based calculations provided by Pengfei Tian, the absorption cross-section of the silica-gold nanoshells was orders of magnitude larger throughout the entire NIR region compared to the other two nanoparticles. Therefore, they should be the obvious choice as the best photothermal transducers of the three we have examined (which is also confirmed in our *in vitro* experiments). However, as stated in the beginning, the best light-to-heat converter on a single particle level might not be the best in a therapeutic context. Factors such as the nanoparticle accumulation and plasmon hybridization, that in particular become significant in the tumor microenvironment, are unaccounted for in the theoretical calculations and single particle experiments. We therefore also investigated the photothermal capabilities of the three nanoparticles in tumor human xenografts in mice using intratumoral delivery of the nanoparticles and PET/CT treatment evaluation.

Mice were divided into four groups with comparable total tumor volume and received either silica-gold nanoshells, 80 nm gold nanoparticles, 150 nm gold nanoparticles, or saline (control). A constant number of nanoparticles was injected intratumorally and irradiated with NIR light. PET imaging, using a glucose analogue as tracer (^{18}FDG), was used to evaluate the treatment response, immediately after the therapy, and two days post-treatment.

The treatment evaluation showed that the silica-gold nanoshell receiving group, achieved the biggest treatment response as expected. In addition, we found that the treatment was only effective in the local environment of the nanoparticles, which is in agreement with the sizes of the melting profiles that were found in the *in vitro* studies. These results highlight the high spatial control and minimized invasiveness of the therapy.

In the experiments using a low nanoparticle dose and a low laser power, we could not detect any quantitative treatment response in the 80 and 150 nm gold nanoparticle groups. Based on this study, we must conclude that the effect of plasmon hybridization, if it is present, is not enough to enhance the colloidal gold nanoparticles' NIR optical properties so they

become comparable with the resonant silica-gold nanoshells. However, for higher nanoparticle doses we saw that photothermal ablation can also be achieved with these non-resonant nanoparticles. These findings are highly relevant as the tumor accumulation upon systemic administration most likely favors smaller nanoparticles (i.e., sub-100 nm dimension), that potentially can counterbalance the lack of optical resonance in clinical implementation.

As the FDG uptake level remained unchanged during the study course for all the groups except for the control that received laser treatment alone, we suggest that the non-resonant nanoparticles potentially can generate sufficient heating to induce tumor growth arrest.

In conclusion, we have developed a strategy that can be used to quantify the photothermal effect at a single particle level as well as in a therapeutic context. We propose that the strategy can be used to evaluate any type of nanostructure and different tumor models, and that it applies to systemic administered nanoparticles as well. Based on the broad applicability, we anticipate that this strategy has great potential for clinical evaluation of plasmonic nanoparticle-mediated photothermal cancer therapy, and that it can be used as a tool to develop a personalized therapy.

The long-term effect of gold nanoparticles in the body remains an open question and is the bottleneck for clinical approval of nanoparticle-mediated photothermal therapy. However, innovative strategies can in some cases be the only option for a patient with poor prognosis therefore the risk/benefit ratio should be considered for such therapies.

6.2 Outlook

In this study we aimed at strictly comparing the optical properties of the different types of promising plasmonic nanoparticles and at finding out if PET/CT imaging could be used as a reliable method for treatment evaluation. Therefore, all other experimental parameters were kept constant. For future studies, we aim at transitioning to systemic administration of the nanoparticles by intravenous injection and passive tumor accumulation, that is a more clinically relevant delivery method. For proper assessment of the nanoparticles' ability to actually accumulate in the tumor (the EPR effect is particle size dependent) we are currently conducting biodistribution studies on all three nanoparticles using ICP-MS. We are anticipating that the number of tumor-delivered nanoparticles will vary between the groups, the 80 nm nanoparticles having the highest uptake.
The first and most essential study, after obtaining the biodistributions, will be to examine the effect of laser power and exposure time over longer study periods. We have already seen indications in this study that these parameters can tune the treatment response (see Fig. 5.11 and 5.12).

A lot of previous studies report development of scabs in the high-responsive groups after laser treatment [86]. In contrast, mice that only responded partially showed reappearance of tumor cells after $\approx$ 20 days [6, 86]. In radiotherapy, multiple smaller doses can be more effective than one big dose. Motivated by this we will examine the effect of multiple laser treatments to nanoparticle-laden tumors with more conservative laser powers. We anticipate that this strategy can increase the tumor regression and minimize invasiveness, e.g., occurrence of scabs, that comprise a risk of infection and is unpleasant for the patient.
For better execution of multiple laser treatments, information about where the particles are located inside the body or even in the tumor microenvironment at any time point after initial administration is crucial. We aim at combining PET/CT-based evaluation with an imaging modality such as MRI, that would enable us to follow the tumor accumulation of nanoparticles in real-time as well assess if they remain in the tumor for subsequent laser treatments [43].
For a more thorough evaluation, we are also planning on including ^{18}FLT for PET evaluation, to include assessment of cell proliferation after the photothermal therapy.

The maximal penetration depth is both wavelength and tissue specific as scattering and absorption, perfusion, and pigmentation vary between tissues [91]. It would be highly relevant to investigate the tissue photo-diffusion and heat dissipation as a function of wavelength in biologically relevant phantoms [92]. We anticipate that the therapy, in particular in larger tumors, would benefit of higher irradiation doses or exposure times. There could also be an advantage in delivering the laser from several directions that would distribute the deposited energy over a larger region (in contrast to a irradiating from only one direction where the near region of the tumor might be overheating while the rear region is unaffected).
The size of the tumor potentially plays a large role in: 1) how well the particles are accumulating in the tumor, and 2) how the particles distribute inside the tumor microenvironment. The relation between the tumor volume and the efficiency of photothermal therapy can be investigated both in tumor bearing mice and in phantoms where the nanoparticles are deposited differently (e.g., a large fraction of nanoparticles in the periphery versus a uniform distribution).
In conjunction with optimizing laser delivery and investigating the role of the tumor size, we are also aiming at implementing orthotopic tumor models as was done in a brain tumor study in hound dogs [93]. Orthotopic models are tumors that are implanted into their normal occurring place in the body and therefore mimic natural tumors better than subcutaneous xenografts. They are considered to be more clinically relevant and a better predictive tool of therapeutic interventions.

Finally, other plasmonic nanoparticles could be investigated for photothermal therapy using the strategy developed in this project. We have shown that nanoshells are good photothermal transducers both at the single particle level (*in vitro*), and upon intratumoral injection

in tumor bearing mice (*in vivo*). However, their applicability is somewhat limited by their relatively large scattering to absortion efficiency [69] and their synthesis limitations to diameters larger than 100 nm. The size and low absorption issues have been solved with the nanomatryoshkas that are the next generation of multi-layered NIR plasmonic nanoparticles. These are unfortunately still not commercially available and have until recently been difficult to fabricate in large-scale [6]. Alternatively, Ma et al. [68] showed that titanium, that is also biocompatible, and has a high photothermal conversion in the NIR region. Hence, it would be interesting to include titanium nanoparticles in a future comparative study.

6.3 Conclusion on epigentics studied in the model system of Bacteriophage λ

Using a novel single molecule assay we investigated the regulatory effect of DNA supercoiling on the CI-mediated DNA loop that constitutes the epigenetic λ switch [1, 2, 4]. We found that the internal DNA dynamics were greatly enhanced in supercoiled plasmids compared to relaxed plasmids. We examined the DNA looping probability as a function of CI concentration on the supercoiled DNA and found that it was increased for lower concentrations of CI in comparison to what was reported in a study on linear relaxed DNA [3]. The transition between looped and unlooped states was found to be a cooperative process, confirmed by a Hill Coefficient of 2.5. Using a thermodynamic model, free energies for the looping transition on supercoiled DNA were extracted that were in better agreement with *in vivo* observations than those obtained on linear relaxed DNA [1]. In conclusion, our single molecule analysis showed that DNA supercoiling enhanced the switch-like nature of Bacteriophage λ and that the lysogenic state is robust to transcriptional noise.

Bibliography

[1] K. Norregaard, M. Andersson, K. Sneppen, P. E. Nielsen, S. Brown, and L. B. Oddershede, "DNA supercoiling enhances cooperativity and efficiency of an epigenetic switch," *Proc. Natl. Acad. Sci. U. S. A.*, vol. 110, no. 43, pp. 17386–91, 2013.

[2] K. Norregaard, M. Andersson, P. E. Nielsen, S. Brown, and L. B. Oddershede, "Tethered particle analysis of supercoiled circular DNA using peptide nucleic acid handles," *Nat. Protoc.*, vol. 9, pp. 2206–23, Sept. 2014.

[3] C. Zurla, C. Manzo, D. Dunlap, D. E. A. Lewis, S. Adhya, and L. Finzi, "Direct demonstration and quantification of long-range DNA looping by the lambda bacteriophage repressor," *Nucleic Acids Res.*, vol. 37, pp. 2789–2795, 2009.

[4] K. Norregaard, M. Andersson, K. Sneppen, P. E. Nielsen, S. Brown, and L. B. Oddershede, "Effect of supercoiling on the λ switch," *Bacteriophage*, vol. 4, no. 1, p. e27517, 2014.

[5] Y. Wang, K. C. L. Black, H. Luehmann, W. Li, Y. Zhang, X. Cai, D. Wan, S. Y. Liu, M. Li, P. Kim, Z. Y. Li, L. V. Wang, Y. Liu, and Y. Xia, "Comparison study of gold nanohexapods, nanorods, and nanocages for photothermal cancer treatment," *ACS Nano*, vol. 7, pp. 2068–2077, 2013.

[6] C. Ayala-Orozco, C. Urban, M. W. Knight, A. S. Urban, O. Neumann, S. W. Bishnoi, S. Mukherjee, A. M. Goodman, H. Charron, T. Mitchell, M. Shea, R. Roy, S. Nanda, R. Schiff, N. J. Halas, and A. Joshi, "Au Nanomatryoshkas as Efficient Transducers for Cancer Treatment: Benchmarking against Nanoshells," *ACS Nano*, vol. 8, no. 6, pp. 6372–6381, 2014.

[7] M. Faraday, "The Bakerian Lecture: Experimental Relations of Gold (and Other Metals) to Light," *Philos. Trans. R. Soc. London*, vol. 147, no. January, pp. 145–181, 1857.

[8] G. Mie, "Contributions to the optics of turbid media, particularly of colloidal metal solutions," *Ann. Phys.*, vol. 25, pp. 377–445, 1908.

[9] Z. Qin and J. C. Bischof, "Thermophysical and biological responses of gold nanoparticle laser heating," 2012.

[10] R. Weissleder, "A clearer vision for in vivo imaging progress continues in the development of smaller, more penetrable probes for biological imaging. Toward the phosphoproteome," *Nat. Biotechnol.*, vol. 19, pp. 316–317, 2001.

[11] N. G. Khlebtsov and L. A. Dykman, "Optical properties and biomedical applications of plasmonic nanoparticles," *J. Quant. Spectrosc. Radiat. Transf.*, vol. 111, no. 1, pp. 1–35, 2010.

[12] S. Link and M. A. El-Sayed, "Optical properties and ultrafast dynamics of metallic nanocrystals," *Annu. Rev. Phys. Chem.*, vol. 54, pp. 331–66, Jan. 2003.

[13] C. F. Bohren and D. R. Huffman, *Absorption and scattering of light by small particles*, vol. 1. New York: Wiley Interscience, 1983.

[14] P. M. Bendix, L. Jauffred, K. Norregaard, and L. B. Oddershede, "Optical trapping of nanoparticles and quantum dots," *IEEE J. Sel. Top. Quantum Electron.*, vol. 20, no. 3, 2014.

[15] B. N. Khlebtsov and N. G. Khlebtsov, "Biosensing potential of silica/gold nanoshells: Sensitivity of plasmon resonance to the local dielectric environment," vol. 106, pp. 154–169, 2007.

[16] N. G. Khlebtsov, "Optics and biophotonics of nanoparticles with a plasmon resonance," *Quantum Electron.*, vol. 38, pp. 504–529, June 2008.

[17] X. Huang and M. A. El-Sayed, "Gold nanoparticles: Optical properties and implementations in cancer diagnosis and photothermal therapy," *J. Adv. Res.*, vol. 1, pp. 13–28, Jan. 2010.

[18] S. Oldenburg, R. Averitt, S. Westcott, and N. Halas, "Nanoengineering of optical resonances," *Chem. Phys. Lett.*, vol. 288, pp. 243–247, May 1998.

[19] J. A. Webb and R. Bardhan, "Emerging advances in nanomedicine with engineered gold nanostructures," *Nanoscale*, vol. 6, pp. 2502–30, Mar. 2014.

[20] P. K. Jain, K. S. Lee, I. H. El-Sayed, and M. A. El-Sayed, "Calculated absorption and scattering properties of gold nanoparticles of different size, shape, and composition: Applications in biological imaging and biomedicine," *J. Phys. Chem. B*, vol. 110, pp. 7238–48, Apr. 2006.

[21] M. Pelton, J. Aizpurua, and G. Bryant, "Metal-nanoparticle plasmonics," *Laser Photonics Rev.*, vol. 2, pp. 136–159, July 2008.

[22] B. Khlebtsov, V. Zharov, A. Melnikov, V. Tuchin, and N. Khlebtsov, "Optical amplification of photothermal therapy with gold nanoparticles and nanoclusters," *Nanotechnology*, vol. 17, pp. 5167–5179, Oct. 2006.

[23] M. L. Brongersma, N. J. Halas, and P. Nordlander, "Plasmon-induced hot carrier science and technology," *Nat. Nanotecnology*, vol. 10, no. 1, pp. 25–34, 2015.

[24] A. O. Govorov, W. Zhang, T. Skeini, H. Richardson, J. Lee, and N. A. Kotov, "Gold nanoparticle ensembles as heaters and actuators: Melting and collective plasmon resonances," *Nanoscale Res. Lett.*, vol. 1, pp. 84–90, 2006.

[25] P. M. Bendix, S. N. Reihani, and L. B. Oddershede, "Direct measurements of heating by electromagnetically trapped gold nanoparticles on supported lipid bilayers," *ACS Nano*, vol. 4, no. 4, pp. 2256–2262, 2010.

[26] J. Turkevich, P. C. Stevenson, and J. Hillier, "A study of the nucleation and growth processes in the synthesis of Colloidal Gold," *Discuss. Faraday Soc.*, vol. 11, no. c, pp. 55–75, 1951.

[27] G. Frens, "Controlled Nucleation for the Regulation of the Particle Size in Monodisperse Gold Suspensions," *Nat. Phys. Sci.*, vol. 241, pp. 20–22, 1973.

[28] W. Stober, A. Fink, and E. Bohn, "Controlled Growth of Monodisperse Silica Spheres in the Micron Size Range," *J. Colloid Interf. Sci.*, vol. 26, pp. 62–69, 1968.

[29] S. J. Oldenburg, J. B. Jackson, S. L. Westcott, and N. J. Halas, "Infrared extinction properties of gold nanoshells," *Appl. Phys. Lett.*, vol. 75, pp. 2897–2899, 1999.

[30] R. A. Petros and J. M. DeSimone, "Strategies in the design of nanoparticles for therapeutic applications," *Nat. Rev. Drug Discov.*, vol. 9, pp. 615–627, 2010.

[31] R. K. Jain and T. Stylianopoulos, "Delivering nanomedicine to solid tumors," *Nat. Rev. Clin. Oncol.*, vol. 7, pp. 653–664, 2010.

[32] P. K. Jain, I. H. El-Sayed, and M. A. El-Sayed, "Au nanoparticles target cancer," *Nanotoday*, vol. 2, no. 1, pp. 18–29, 2007.

[33] "Cancer Facts & Figures 2015," tech. rep., American Cancer Society, Atlanta, 2015.

[34] C. Ayala-Orozco, C. Urban, S. Bishnoi, A. Urban, H. Charron, T. Mitchell, M. Shea, S. Nanda, R. Schiff, N. Halas, and A. Joshi, "Sub-100nm gold nanomatryoshkas improve photo-thermal therapy efficacy in large and highly aggressive triple negative breast tumors," *J. Control. Release*, vol. 191, pp. 90–7, Oct. 2014.

[35] I. Fratoddi, I. Venditti, C. Cametti, and M. V. Russo, "Gold nanoparticles and gold nanoparticle-conjugates for delivery of therapeutic molecules. Progress and challenges," *J. Mater. Chem. B*, vol. 2, no. 27, p. 4204, 2014.

[36] L. C. Kennedy, L. R. Bickford, N. A. Lewinski, A. J. Coughlin, Y. Hu, E. S. Day, J. L. West, and R. A. Drezek, "A new era for cancer treatment: Gold-nanoparticle-mediated thermal therapies," *Small*, vol. 7, pp. 169–83, Jan. 2011.

[37] E. A. Sykes, J. Chen, G. Zheng, and W. C. W. Chan, "Investigating the impact of nanoparticle size on active and passive tumor targeting efficiency," *ACS Nano*, vol. 8, pp. 5696–5706, 2014.

[38] F. Danhier, O. Feron, and V. Préat, "To exploit the tumor microenvironment: Passive and active tumor targeting of nanocarriers for anti-cancer drug delivery," *J. Control. Release*, vol. 148, pp. 135–46, Dec. 2010.

[39] S. D. Perrault, C. Walkey, T. Jennings, H. C. Fischer, and W. C. W. Chan, "Mediating tumor targeting efficiency of nanoparticles through design," *Nano Lett.*, vol. 9, pp. 1909–15, May 2009.

[40] I. H. El-Sayed, X. Huang, and M. A. El-Sayed, "Surface plasmon resonance scattering and absorption of anti-EGFR antibody conjugated gold nanoparticles in cancer diagnostics: Applications in oral cancer," *Nano Lett.*, vol. 5, pp. 829–34, May 2005.

[41] C. Loo, A. Lowery, N. Halas, J. West, and R. Drezek, "Immunotargeted nanoshells for integrated cancer imaging and therapy.," *Nano Lett.*, vol. 5, pp. 709–11, Apr. 2005.

[42] I. H. El-Sayed, X. Huang, and M. a. El-Sayed, "Selective laser photo-thermal therapy of epithelial carcinoma using anti-EGFR antibody conjugated gold nanoparticles.," *Cancer Lett.*, vol. 239, pp. 129–35, July 2006.

[43] R. Bardhan, W. Chen, M. Bartels, C. Perez-Torres, M. F. Botero, R. W. McAninch, A. Contreras, R. Schiff, R. G. Pautler, N. J. Halas, and A. Joshi, "Tracking of multimodal therapeutic nanocomplexes targeting breast cancer in vivo," *Nano Lett.*, vol. 10, pp. 4920–4928, 2010.

[44] S.-H. Wang, C.-W. Lee, A. Chiou, and P.-K. Wei, "Size-dependent endocytosis of gold nanoparticles studied by three-dimensional mapping of plasmonic scattering images," *J. Nanobiotechnology*, vol. 8, p. 33, Jan. 2010.

[45] T. G. Iversen, T. Skotland, and K. Sandvig, "Endocytosis and intracellular transport of nanoparticles: Present knowledge and need for future studies," *Nano Today*, vol. 6, pp. 176–185, 2011.

[46] C. Loo, A. Lin, L. Hirsch, M. Lee, J. Barton, N. Halas, J. West, and R. Drezek, "Nanoshell-enabled photonics-based imaging and therapy of cancer," *Technol Cancer Res*, vol. 3, no. 1, pp. 33–40, 2004.

[47] J. Park, A. Estrada, K. Sharp, K. Sang, J. A. Schwartz, D. K. Smith, C. Coleman, J. D. Payne, B. a. Korgel, A. K. Dunn, and J. W. Tunnell, "Imaging of Tumors Using Near-Infrared Excited Gold Nanoshells," *Opt. Express*, vol. 16, no. 3, pp. 214–221, 2008.

[48] R. Popovtzer, A. Agrawal, N. A. Kotov, A. Popovtzer, J. Balter, T. E. Carey, and R. Kopelman, "Targeted Gold Nanoparticles Enable Molecular CT Imaging of Cancer," *Nano Lett.*, vol. 8, pp. 4593–4596, 2008.

[49] R. Bardhan, W. Chen, C. Perez-Torres, M. Bartels, R. M. Huschka, L. L. Zhao, E. Morosan, R. G. Pautler, A. Joshi, and N. J. Halas, "Nanoshells with targeted simultaneous enhancement of magnetic and optical imaging and photothermal therapeutic response," *Adv. Funct. Mater.*, vol. 19, pp. 3901–3909, 2009.

[50] N. L. Rosi, D. A. Giljohann, C. S. Thaxton, A. K. R. Lytton-Jean, M. S. Han, and C. A. Mirkin, "Oligonucleotide-modified gold nanoparticles for intracellular gene regulation," *Science*, vol. 312, pp. 1027–1030, 2006.

[51] A. K. R. Lytton-Jean, R. Langer, and D. G. Anderson, "Five years of siRNA delivery: Spotlight on gold nanoparticles," *Small*, vol. 7, pp. 1932–1937, 2011.

[52] K. Norregaard, L. Jauffred, K. Berg-Sø rensen, and L. B. Oddershede, "Optical manipulation of single molecules in the living cell," *Phys. Chem. Chem. Phys.*, vol. 16, pp. 12614–24, 2014.

[53] R. Huschka, A. Barhoumi, Q. Liu, J. A. Roth, L. Ji, and N. J. Halas, "Gene silencing by gold nanoshell-mediated delivery and laser-triggered release of antisense oligonucleotide and siRNA," *ACS Nano*, vol. 6, pp. 7681–7691, 2012.

[54] S. J. Hurst, A. K. R. Lytton-Jean, and C. A. Mirkin, "Maximizing DNA loading on a range of gold nanoparticle sizes," *Anal. Chem.*, vol. 78, pp. 8313–8318, 2006.

[55] G. Bisker, D. Yeheskely-Hayon, L. Minai, and D. Yelin, "Controlled release of Rituximab from gold nanoparticles for phototherapy of malignant cells," *J. Control. Release*, vol. 162, pp. 303–309, 2012.

[56] Y.-S. Shiao, H.-H. Chiu, P.-H. Wu, and Y.-F. Huang, "Aptamer-Functionalized Gold Nanoparticles As Photoresponsive Nanoplatform for Co-Drug Delivery," *ACS Appl. Mater. Interfaces*, vol. 6, no. 24, pp. 21832–21841, 2014.

[57] E. C. Dreaden, A. M. Alkilany, X. Huang, C. J. Murphy, and M. A. El-Sayed, "The golden age: gold nanoparticles for biomedicine," *Chem. Soc. Rev.*, vol. 41, pp. 2740–79, Apr. 2012.

[58] A. M. Goodman, Y. Cao, C. Urban, O. Neumann, C. Ayala-Orozco, M. W. Knight, A. Joshi, P. Nordlander, and N. J. Halas, "The Surprising in Vivo Instability of Near-IR-Absorbing Hollow Au-Ag Nanoshells," *ACS Nano*, vol. 8, no. 4, pp. 3222–3231, 2014.

[59] S. C. Gad, K. L. Sharp, C. Montgomery, J. D. Payne, and G. P. Goodrich, "Evaluation of the toxicity of intravenous delivery of auroshell particles (gold-silica nanoshells)," *Int. J. Toxicol.*, vol. 31, pp. 584–594, 2012.

[60] A. Ashkin, "Acceleration and Trapping of Particles by Radiation Pressure," *Phys. Rev. Lett.*, vol. 24, pp. 156–159, Jan. 1970.

[61] L. B. Oddershede, "Force probing of individual molecules inside the living cell is now a reality," *Nat. Chem. Biol.*, vol. 8, pp. 879–886, 2012.

[62] M. Dienerowitz, M. Mazilu, and K. Dholakia, "Optical manipulation of nanoparticles: A review," *J. Nanophotonics*, vol. 2, no. 1, pp. 21832–21875, 2008.

[63] K. Svoboda and S. M. Block, "Optical trapping of metallic Rayleigh particles," *Opt. Lett.*, vol. 19, pp. 930–932, 1994.

[64] P. M. Hansen, V. K. l. Bhatia, N. Harrit, and L. Oddershede, "Expanding the optical trapping range of gold nanoparticles," *Nano Lett.*, vol. 5, pp. 1937–1942, 2005.

[65] F. Gittes and C. F. Schmidt, "Signals and noise in micromechanical measurements," *Methods Cell Biol.*, vol. 55, pp. 129–156, 1998.

[66] P. M. Hansen, I. M. Tolic-Nø rrelykke, H. Flyvbjerg, and K. Berg-Sø rensen, "tweezercalib 2.1: Faster version of MatLab package for precise calibration of optical tweezers," *Comput. Phys. Commun.*, vol. 175, pp. 572–573, 2006.

[67] A. C. Richardson, N. Reihani, and L. B. Oddershede, "Combining confocal microscopy with precise force-scope optical tweezers," 2006.

[68] H. Ma, P. Tian, J. Pello, P. M. Bendix, and L. B. Oddershede, "Heat generation by irradiated complex composite nanostructures," *Nano Lett.*, vol. 14, pp. 612–9, Feb. 2014.

[69] N. J. Hogan, A. S. Urban, C. Ayala-Orozco, A. Pimpinelli, P. Nordlander, and N. J. Halas, "Nanoparticles heat through light localization," *Nano Lett.*, vol. 14, pp. 4640–5, Aug. 2014.

[70] Y. Seol, A. E. Carpenter, and T. T. Perkins, "Gold nanoparticles: Enhanced optical trapping and sensitivity coupled with significant heating," *Opt. Lett.*, vol. 31, pp. 2429–2431, 2006.

[71] H. H. Richardson, Z. N. Hickman, A. C. Thomas, M. E. Kordesch, and A. O. Govorov, "Thermo-optical Properties of Nanoparticles and Nanoparticle Complexes Embedded in Ice: Characterization of Heat Generation and Actuation of Larger-scale Effects," *MRS Proc.*, vol. 964, 2006.

[72] A. S. Urban, M. Fedoruk, S. Wimmer, F. D. Stefani, and J. Feldmann, "Nanometric Phase Transitions on Phospholipid Membranes Using Plasmonic Heating of Single Gold Nanoparticles," *Biophys. J.*, vol. 98, p. 219a, 2010.

[73] H. Ma, P. M. Bendix, and L. B. Oddershede, "Large-scale orientation dependent heating from a single irradiated gold nanorod," *Nano Lett.*, vol. 12, pp. 3954–60, Aug. 2012.

[74] A. Kyrsting, P. M. Bendix, D. G. Stamou, and L. B. Oddershede, "Heat profiling of three-dimensionally optically trapped gold nanoparticles using vesicle cargo release," *Nano Lett.*, vol. 11, pp. 888–892, 2011.

[75] A. Kyrsting, P. M. Bendix, and L. B. Oddershede, "Mapping 3D focal intensity exposes the stable trapping positions of single nanoparticles," *Nano Lett.*, vol. 13, pp. 31–35, 2013.

[76] T. Andersen, A. Kyrsting, and P. M. Bendix, "Local and Transient Permeation Events are Associated with Local Melting of Giant Liposomes," *Soft Matter*, vol. 10, pp. 4268–74, 2014.

[77] H. Goldenberg and C. J. Tranter, "Heat flow in an infinite medium heated by a sphere," *Br. J. Appl. Phys.*, vol. 3, pp. 296–298, 1952.

[78] E. A. Eisenhauer, P. Therasse, J. Bogaerts, L. H. Schwartz, D. Sargent, R. Ford, J. Dancey, S. Arbuck, S. Gwyther, M. Mooney, L. Rubinstein, L. Shankar, L. Dodd, R. Kaplan, D. Lacombe, and J. Verweij, "New response evaluation criteria in solid tumours: Revised RECIST guideline (version 1.1)," *Eur. J. Cancer*, vol. 45, no. 2, pp. 228–247, 2009.

[79] M. Buyse, P. Thirion, R. W. Carlson, T. Burzykowski, G. Molenberghs, and P. Piedbois, "Relation between tumour response to first-line chemotherapy and survival in advanced colorectal cancer: a meta-analysis," *Lancet*, vol. 356, pp. 373–378, 2000.

[80] M. Munk Jensen, K. D. Erichsen, F. Björkling, J. Madsen, P. B. Jensen, M. Sehested, L. Hø jgaard, and A. Kjæ r, "Imaging of treatment response to the combination of

carboplatin and paclitaxel in human ovarian cancer xenograft tumors in mice using FDG and FLT PET," *PLoS One*, vol. 8, p. e85126, Jan. 2013.

[81] A. Debucquoy, E. Devos, P. Vermaelen, W. Landuyt, S. De Weer, F. Van Den Heuvel, and K. Haustermans, "18F-FLT and 18F-FDG PET to measure response to radiotherapy combined with celecoxib in two colorectal xenograft models," *Int. J. Radiat. Biol.*, vol. 85, no. 9, pp. 763–771, 2009.

[82] R. L. Wahl, H. Jacene, Y. Kasamon, and M. A. Lodge, "Response Criteria in Solid Tumors," *J. Nucl. Med.*, vol. 50, no. Suppl 1, pp. 122–150, 2009.

[83] L. R. Hirsch, R. J. Stafford, J. a. Bankson, S. R. Sershen, B. Rivera, R. E. Price, J. D. Hazle, N. J. Halas, and J. L. West, "Nanoshell-mediated near-infrared thermal therapy of tumors under magnetic resonance guidance," *Proc. Natl. Acad. Sci. U. S. A.*, vol. 100, pp. 13549–54, Nov. 2003.

[84] D. P. O'Neal, L. R. Hirsch, N. J. Halas, J. D. Payne, and J. L. West, "Photo-thermal tumor ablation in mice using near infrared-absorbing nanoparticles," *Cancer Lett.*, vol. 209, pp. 171–6, June 2004.

[85] J. M. Stern, J. Stanfield, W. Kabbani, J. T. Hsieh, and J. A. Cadeddu, "Selective prostate cancer thermal ablation with laser activated gold nanoshells," *J. Urol.*, vol. 179, pp. 748–753, 2008.

[86] E. S. Day, P. A. Thompson, L. Zhang, N. A. Lewinski, N. Ahmed, R. A. Drezek, S. M. Blaney, and J. L. West, "Nanoshell-mediated photothermal therapy improves survival in a murine glioma model," *J. Neurooncol.*, vol. 104, pp. 55–63, 2011.

[87] M. E. Phelps, *PET: molecular imaging and its biological applications*. New York: Springer Science & Business Media, 2004.

[88] S. S. Gambhir, "Molecular imaging of cancer with positron emission tomography," *Nat. Rev. Cancer*, vol. 2, pp. 683–93, Sept. 2002.

[89] A. F. Chatziioannou, "Molecular imaging Molecular imaging of small animals with dedicated PET tomographs," *Eur J Nucl Med*, vol. 29, no. 1, pp. 98–114, 2002.

[90] M. Sorschag, P. Malle, and H. J. Gallowitsch, "Nuclear medicine in NET," *Wiener Medizinische Wochenschrift*, vol. 162, pp. 416–422, 2012.

[91] S. Stolik, J. A. Delgado, A. Pérez, and L. Anasagasti, "Measurement of the penetration depths of red and near infrared light in human ex vivo tissues," *J. Photochem. Photobiol. B Biol.*, vol. 57, pp. 90–93, 2000.

[92] A. M. Elliott, R. J. Stafford, J. Schwartz, J. Wang, A. M. Shetty, C. Bourgoyne, P. O'Neal, and J. D. Hazle, "Laser-induced thermal response and characterization of nanoparticles for cancer treatment using magnetic resonance thermal imaging," *Med Phys*, vol. 34, pp. 3102–3108, 2007.

[93] J. A. Schwartz, A. M. Shetty, R. E. Price, R. J. Stafford, J. C. Wang, R. K. Uthamanthil, K. Pham, R. J. McNichols, C. L. Coleman, and J. D. Payne, "Feasibility study of particle-assisted laser ablation of brain tumors in orthotopic canine model," *Cancer Res.*, vol. 69, pp. 1659–1667, 2009.

Publications enclosed in the thesis

PROTOCOL

Tethered particle analysis of supercoiled circular DNA using peptide nucleic acid handles

Kamilla Norregaard[1], Magnus Andersson[1,3], Peter Eigil Nielsen[2], Stanley Brown[1] & Lene B Oddershede[1]

[1]The Niels Bohr Institute, University of Copenhagen, Copenhagen, Denmark. [2]Department of Cellular and Molecular Medicine, Faculty of Health and Sciences, University of Copenhagen, Copenhagen, Denmark. [3]Present address: Department of Physics, Umeå University, Umeå, Sweden. Correspondence should be addressed to L.B.O. (oddershede@nbi.dk).

Published online 21 August 2014; doi:10.1038/nprot.2014.152

This protocol describes how to monitor individual naturally supercoiled circular DNA plasmids bound via peptide nucleic acid (PNA) handles between a bead and a surface. The protocol was developed for single-molecule investigation of the dynamics of supercoiled DNA, and it allows the investigation of both the dynamics of the molecule itself and of its interactions with a regulatory protein. Two bis-PNA clamps designed to bind with extremely high affinity to predetermined homopurine sequence sites in supercoiled DNA are prepared: one conjugated with digoxigenin for attachment to an anti-digoxigenin-coated glass cover slide, and one conjugated with biotin for attachment to a submicron-sized streptavidin-coated polystyrene bead. Plasmids are constructed, purified and incubated with the PNA handles. The dynamics of the construct is analyzed by tracking the tethered bead using video microscopy: less supercoiling results in more movement, and more supercoiling results in less movement. In contrast to other single-molecule methodologies, the current methodology allows for studying DNA in its naturally supercoiled state with constant linking number and constant writhe. The protocol has potential for use in studying the influence of supercoils on the dynamics of DNA and its associated proteins, e.g., topoisomerase. The procedure takes ~4 weeks.

INTRODUCTION

Single-molecule investigations have proven to be successful for unraveling spatial and temporal information hidden in classical ensemble studies, for instance, the typical stepping size of a single molecular motor and its instantaneous velocities[1]. By using force-manipulation techniques[2], the force required to stall a molecular motor, as well as the mechanical properties of a biopolymer undergoing rupture, stretching or twisting[3], have also been investigated.

Despite the fact that the natural state of DNA inside a living cell is supercoiled, single-molecule investigations of DNA are typically carried out on linear DNA; that is, on a DNA tether with two ends that can be free or attached to a bead or a molecule, or on linear DNA on which supercoils were externally imposed using magnetic tweezers. This is true, e.g., for investigations of DNA's elasticity[4,5] and interaction with DNA-associating proteins[6–11], as well as of the DNA looping caused by regulatory proteins[12–15]. Before regulatory proteins, such as λ repressor protein (CI), attach to their specific DNA sites, they search the DNA to find the attachment sequence. The search mechanisms of proteins along the DNA may differ between linear and supercoiled DNA: on a supercoiled DNA the juxtaposition of any two sites markedly further apart than the dsDNA persistence length (which is defined as the length over which the polymer appears straight with respect to thermal fluctuations) is more frequent than on relaxed DNA[16,17]. This is because the dsDNA appears floppy and easily folds on length scales larger than the dsDNA persistence length. At a juxtaposition site, a protein bound to the DNA backbone can jump more quickly to the juxtaposed site than if the protein had to stroll along the entire backbone[18]. As the natural state of DNA is the supercoiled state, this is the most relevant state to study when probing the physical, chemical and dynamical properties of DNA itself, as well as its interaction with associated molecules.

Development of the protocol

Nielsen and co-workers[19,20] developed a method to attach supercoiled circular DNA to a streptavidin-coated polystyrene bead via a biotin-PNA conjugate. Recently, we exploited this method to analyze supercoiled circular DNA by tethered particle motion (TPM; see an overview of the main steps involved in **Fig. 1**). In our approach, the DNA is tethered with two PNA handles: one site of the plasmid was bound via the biotin-PNA to a streptavidin-coated polystyrene bead, and another site of the plasmid was bound via digoxigenin-PNA to an anti-digoxigenin-coated surface[16] (**Fig. 2**). The PNA handles bound specifically at their designated targets on the circular DNA, as determined by both electrophoretic mobility shift and single-molecule analysis. By using this construct and recording the thermal fluctuations of a reporter bead, we compared naturally supercoiled circular DNA with circular relaxed DNA (DNA with the identical sequence, which had been 'relaxed' by treatment with a nicking enzyme). The internal dynamics of the two forms of DNA plasmids were determined by calculating the autocorrelation between the positions visited by the reporter bead in the TPM time series. The supercoiled DNA showed a faster juxtaposition rate (the frequency with which two sites on the DNA are in vicinity of each other) than the relaxed DNA. We interpret the faster juxtaposition rate as the supercoiled form having a smaller number of accessible states; hence, two separated sites along the DNA contour are more often juxtaposed.

By using this assay, we determined the probability of λ repressor CI–mediated looping in the model system of bacteriophage λ, in which CI binds cooperatively to the λ operators and clamps them together. The plasmid contained the entire λ immunity region (~2.3 kbp) flanked by the λ operators (**Fig. 3**). The PNA target sites were placed as closely as possible to the two λ operators to enhance the ability to observe CI clamping. We found that the

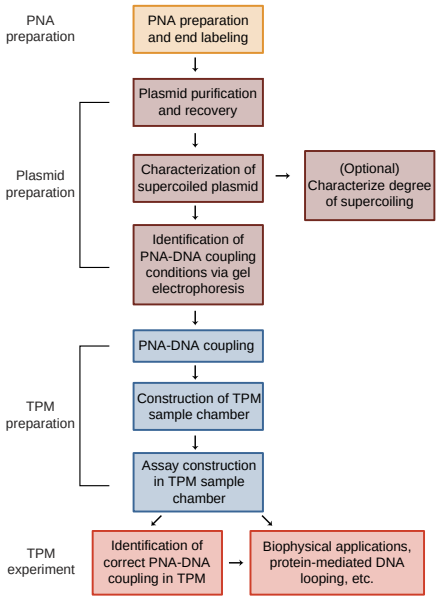

Figure 1 | Flowchart of the entire procedure providing an overview of the main steps involved in developing the assay and performing tethered particle motion experiments.

efficiency of the so-called λ switch substantially increases and the Hill coefficient rises on supercoiled DNA as compared with linear DNA or relaxed plasmids[16]. These findings infer that the transition between the CI-mediated looped and unlooped states occurs exactly at the CI concentration corresponding to the minimum number of CI molecules capable of maintaining repression of *cI* transcription[21]. Hence, as CI concentration declines during induction, the supercoiled state prevents autoregulation of *cI* from interfering with induction[21].

Future applications

This method is immediately applicable to examine the interactions between DNA in its natural supercoiled state and proteins that associate with DNA. So far, essentially all single-molecule DNA-protein studies have characterized protein interactions with linear DNA molecules or with linear DNA molecules that were mechanically twisted to impose supercoils[12–15,22,23]. Similar studies could be conducted using naturally supercoiled DNA. There is reason to believe that the topology and tertiary structure of the DNA in itself has a role in regulating protein interactions. Hence, the behavior observed with supercoiled DNA may differ from the behavior observed with linear DNA. One interesting possibility could be to address the effective nonspecific DNA binding by site-specific DNA-binding molecules. To this end, DNA lacking the binding site could be introduced into the prepared sample chambers together with the binding protein; the nonspecific DNA could be random linear fragments or purified supercoiled DNA, and the results could be compared with an experiment in which the nonspecific DNA was omitted. Similarly, the effect of potential cofactors such as general DNA-binding proteins and metabolites could be examined[23]. In addition, with few modifications, the assay could examine the behavior of topoisomerases on single molecules of circular DNA[24]. The assay can also be used to explore the physical properties of the supercoiled plasmid itself, e.g., the stiffness of the system[25]. As PNAs can also bind to plasmid DNA that can be transported into the cytoplasm and even into the nucleus[26], it is also possible to bring the PNA handles into the cytoplasm. Furthermore, micro- or nanoparticles can be brought inside the cell[27], and via the PNA handles they can be attached to chromosomal DNA. By such a construct one can use, e.g., optical or magnetic tweezers to study the forces acting on chromosomal DNA during cell division.

Comparison with other methods

The most commonly used geometry for studying DNA elasticity, protein association, supercoiling or protein-mediated looping at the single molecule level has been the linear assay, in which a linear DNA tether has been attached at one end to a surface and at the other end to a bead. The bead is then manipulated by optical or magnetic tweezers[15,24], or its thermal fluctuations are studied by TPM[12,28]. In such tethered linear DNA assays, the dynamics of the molecule are found by monitoring the position of the bead with a camera. TPM, in which supercoiling has been introduced on a linear tether using magnetic tweezers, presents a challenge in that it can be difficult to distinguish two different events, e.g., change in writhe and protein-mediated DNA looping, which both cause an overall change in the length of the tether. The assay described in the current protocol has the advantage that the linking number of the circular plasmid is 'locked,' as there are no free ends to rotate. In addition, we never observed a writhe change of the plasmid alone, possibly owing to the fact that the bead is too large to go through the plasmid circle. Hence, the plasmid stays in its natural supercoiled conformation during the experiment. As the writhe number remains constant, any changes in measured tether length can be attributed to protein-DNA interactions rather than to changes in supercoiled state. Of course, if one studies a catalytic protein such as topoisomerase with the plasmid assay,

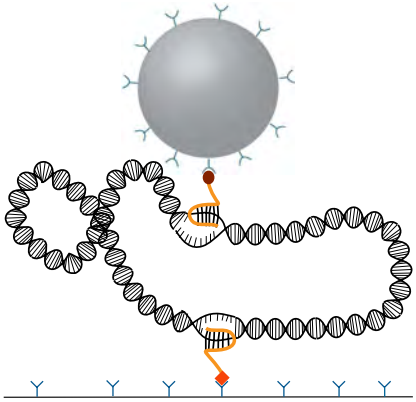

Figure 2 | Sketch of the naturally supercoiled DNA to which two PNA handles (yellow) are specifically attached. One PNA is biotinylated (red oval) and it can specifically attach to a streptavidin (blue cups)-coated bead. The other PNA is digoxigenin-labeled (orange square) and it specifically attaches to an anti-digoxigenin (blue Y)-coated surface.

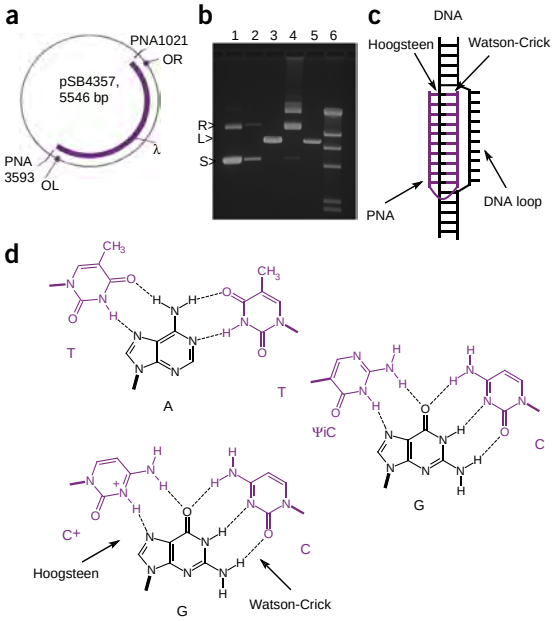

Figure 3 | Constructed plasmids. (**a**) 117 base pairs reside between the edges of the target of PNA1021 (biotin-labeled) and OR. 79 base pairs reside between the edges of the target of PNA3593 (digoxigenin-labeled) and OL. The purple part corresponds to the λ immunity region. The operators OL and OR can be clamped by the CI protein. (**b**) Illustration of the need to make the plasmid in a *recA*⁻ strain. Shown is an ethidium bromide–stained agarose gel of DNA electrophoresed in TAE buffer. Lane 1: a 7.6-kb plasmid prepared from a *recA*⁻ strain. Lane 2: same as Lane 1, but diluted tenfold. Lane 3: The 7.6-kb plasmid used in lanes 1 and 2 linearized with a restriction enzyme that cuts the plasmid once. Lane 4: A 7.6-kb plasmid >99.9% identical in sequence to the plasmid used in lanes 1–3 but prepared from a *recA*⁺ strain. Lane 5: The 7.6-kb plasmid used in lane 4 linearized with a restriction enzyme that cut the plasmid once. Lane 6: 0.5 μg of λ DNA cut with HindIII. R and S indicate, respectively, the mobility of relaxed and supercoiled plasmid in lanes 1 and 2. L indicates the mobility of linearized DNA in lanes 3 and 5. The plasmid preparations had been stored at 4 °C for 5 years. (**c**) Schematic drawing of the bis-PNA dsDNA triplex invasion complex (purple), showing how one PNA (Watson-Crick) strand replaces the sequence identical DNA strand (now forming a single-stranded loop), whereas the other (Hoogsteen) PNA strand stabilizes the internally formed PNA-DNA duplex via binding the major groove of this, forming a very stable PNA-DNA-PNA triplex. (**d**) The base triplets that are responsible for this binding (purple). Because such stable triplexes are only formed with adenine and guanine in the DNA, this type of PNA triplex invasive binding requires a homopurine DNA target. Furthermore, the C-G-C triplet requires an N-3 protonated cytosine, and because the pKa of cytosine is 4.5 (in solution) a triplex with cytosine has markedly reduced the stability at neutral pH. However, by using the pseudoisocytosine isomer, the pH dependence is minimized.

the linking number, as well as twist and writhe, would be expected to change upon enzymatic action. Furthermore, the assay allows for investigation of circular DNA, as the attachment of the PNA handles does not require single-stranded overhangs at the end of the tether. TPM studies on linear relaxed DNA have provided great insights into processes such as protein-mediated DNA looping. However, the thermodynamic parameters identified in these studies found that additional features must have a role (possibly tertiary structures as caused by supercoiling) in order for the interactions to be as efficient as those observed *in vivo*[12,14].

Experimental design

Plasmid design. The plasmids used in the study presented in Norregaard *et al.*[16] were designed to contain the λ operators, OR and OL (operator right and operator left), and the entire immunity region of bacteriophage λ of ~2.3 kbp. The target sites for the PNAs flanked the λ operator sites. The total length of the plasmid was 5,546 bp (**Fig. 3a**). A chloroquine gel (shown in **Fig. 4**) examination of the purified supercoiled plasmid found that the preparation was composed of a population of supercoiled species varying in at least ten states of supercoiling. This variation was reflected in our TPM experiments, in which many different overall lengths of the supercoiled plasmid were observed. In addition to the naturally supercoiled DNA plasmid, we prepared a plasmid that was relaxed by nicking with a single-stranded endonuclease.

Strain choice. As the plasmids must be monomer circles for simple interpretation of the TPM data, the host strain must be recombination-deficient (*recA*⁻). We chose a strain bearing a reporter that would allow us to genetically characterize our constructs[16], but any *recA*⁻ strain repressing any toxic genes on the plasmid and producing the desired DNA modifications should be suitable[29]. Once introduced into a *recA*⁻ strain, the multimeric state of the plasmid is 'locked'. That is, if introduced as a monomer, it propagates as a monomer. If introduced as a dimer, it propagates as a dimer and so on. In a *Rec*⁺ strain, the plasmid exists in an array of multimeric states (**Fig. 3b**). If the plasmid after purification is not a monomer, it can easily be converted to a monomer by digestion with a restriction endonuclease that cuts only once in the plasmid, ligation under dilute conditions to favor intramolecular ligation and transformation into a *recA*⁻ strain. The multimeric state of the plasmid can be determined by partial digestion with the same restriction endonuclease, followed by agarose gel electrophoresis and staining with ethidium bromide.

Although plasmids will not recombine in a *recA*⁻ strain, they can form catenates. That is, two circles can be interlocked. As much as 1% of our plasmids appear to be catenates, as determined by agarose gel electrophoresis after relaxing the plasmid preparation with a single-strand nicking endonuclease. The anisotropic and diminished diffusion of the tethered bead (as detailed in the PROCEDURE) permits elimination of catenates with appropriate selection criteria.

Choice of PNA targets and design of bis-PNAs. Binding of bis-PNAs[30] to double-stranded DNA via PNA triplex invasion requires opening of the DNA duplex and formation of a PNA-DNA:PNA triplex clamp on the homopurine strand[31]. In this triplex, one PNA strand binds the DNA in an antiparallel orientation (PNA C terminus facing the 5′-DNA end) target by Watson-Crick base pairing, whereas the other PNA strand binds the thus-formed PNA-DNA duplex in a parallel orientation by Hoogsteen base pairing. A homopurine target is necessary for the formation of Hoogsteen base pairing in the PNA_2DNA triplex (**Fig. 3c**). PNA targets must be homopurine tracts of no fewer than eight and optimally ten bases to allow effective and stable triplex invasion with optimal stability and sequence discrimination. Furthermore, the target should not be too G-rich (maximum 50–60%), and the

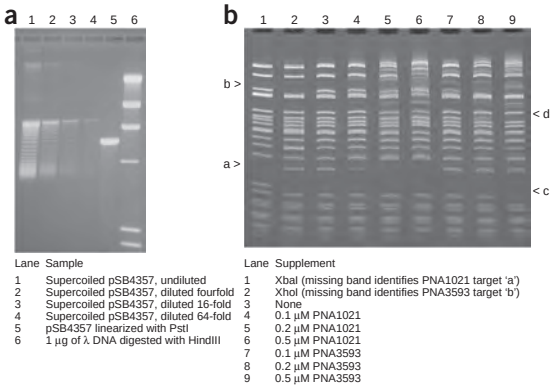

Figure 4 | Electrophoretic analysis of materials. (**a**) Distribution of supercoils assessed by a chloroquine gel. Lanes 1–4 are serial fourfold dilutions of the plasmid preparation pSB4357. Lane 5 is linearized plasmid DNA, and lane 6 contains size standards. A simple gel band quantification analysis using ImageJ of lane 2 shows that there are at least ten different supercoiled conformations in our sample. This gel is reproduced from Norregaard *et al.*[16] with permission. (**b**) Initial identification of PNA concentrations. The target of PNA1021, AAGAAGAAAA, is adjacent to an XbaI restriction recognition site and resides in the 188-bp HinfI fragment. This fragment migrates as the band marked a, and it is present in lane 3 but absent in lane 1. Lane 4 shows that the lowest concentration of PNA1021, 0.1 µM, reduces the amount of target fragment migrating at the same mobility as the naked DNA. The target of PNA3593, AGAGAAAGAA, is adjacent to an XhoI restriction recognition site. It resides within the band marked b and is present in lane 3 but absent in lane 2. Lane 7 shows that the lowest concentration of PNA3593, 0.1 µM, reduces the concentration of this fragment migrating at the same mobility as the naked DNA. At higher concentrations of PNA3593, the mobility of other fragments is altered. It can be seen in lane 9 that the bands marked c and d are depleted compared with lane 7. This gel is reproduced from Norregaard *et al.*[16] with permission.

two or more targets required should both differ from each other and any other sequence in the plasmid by at least two bases. The bis-PNA is designed with Watson-Crick binding and a Hoogsteen PNA oligomer connected with a flexible linker typically composed of three (or four) 8-amino-3,6-dioxaoctanoyl (ethylene glycol) units. The bis-PNA is synthesized by continuous solid-phase peptide synthesis and designed such that the Watson-Crick PNA strand is antiparallel to the purine DNA target and the Hoogsteen strand is parallel to the purine target (the N terminus of the PNA corresponds to the 5′-end of the DNA). Although standard thymine and cytosine bases are used in the Watson-Crick strand, cytosine (recognizing guanine) should be replaced by pseudoisocytosine (ψiC: J base) in the Hoogsteen strand, as this relieves most of the pH dependence of the DNA binding[30]: Cytosine (in contrast with pseudoisocytosine) must be sufficiently protonated at N3 for Hoogsteen recognition of guanine, and this requires a pH of <6. Finally, it is recommended to include three or four lysine (or ε-N,N-dimethyllysine, if postsynthetic, solution-phase N-conjugation is required) residues to accelerate binding kinetics of PNA to the double-stranded plasmid DNA[32].

Binding of PNA to dsDNA. The slow rate of formation of the bis-PNA–dsDNA triplex invasion complex is due to the slow rate of DNA helix opening. However, once formed, the triplex invasion complex is extremely stable. For 10-mer PNAs, the half-life is many days, even at physiological ionic strength conditions. If possible, binding should be performed at low ionic strength (<10 mM) in the absence of Mg^{2+} and other multivalent cations (including polyamines such as spermine or spermidine), as these stabilize the DNA helix, thus reducing DNA breathing and consequently slowing down PNA invasion kinetics. Subsequently, the medium can be changed for further manipulations (e.g., restriction enzyme cleavage) without substantial PNA-DNA complex dissociation. Furthermore, as negative supercoiling facilitates DNA helix unwinding and helix opening, the natural negative supercoiling of a plasmid can accelerate PNA invasion up to two orders of magnitude[20]. Thus, any studies conducted on plasmids relaxed by nicking should be free of residual supercoiled DNA. We have observed that isopycnic centrifugation in CsCl with ethidium bromide yields DNA that binds PNA more efficiently than the commercial cartridge or column purification systems. We suspect that some constituents of the initial plasmid lysate such as polyamines, which inhibit PNA invasion, are more efficiently removed by CsCl-ethidium bromide purification.

Tethering of the biological construct. One of the PNA handles is labeled with biotin and the other is labeled with digoxigenin at the N terminus. By surface functionalization of a cover glass with anti-digoxigenin and a sub-micrometer-sized bead with streptavidin, the circular DNA molecule with PNA handles can be tethered between the surface and a bead (**Fig. 2**). As a polystyrene bead of ~500 nm is too big to rotate through the circular DNA, the geometry of the circular DNA will remain constrained by the point of the tethers. Before starting experiments with the designed assay, a control TPM experiment should be conducted with three control plasmids to ensure efficient and correct binding of the PNA to the DNA: one control plasmid lacking the digoxigenin-PNA target, the second lacking the biotin-PNA target and the third with both targets intact. Our controls showed that tethers only formed correctly with the plasmid containing both PNA targets[16].

The tethered plasmid is subjected to TPM analysis[33]. This type of analysis monitors the *x* and *y* positions of a particle (in this case the polystyrene bead) tethered to an *x*-*y* plane and performing Brownian motion. TPM does not directly yield information on the overall length of the tether, but the overall length is reflected in the distribution of positions visited by the bead (the longer the tether, the larger the excursions of the bead). If the tether is linear, a calibration curve can be made that relates a certain lateral motion to an overall tether length[33]. For the naturally supercoiled plasmids, the spread in linking number and writhe give rise to a broad distribution of overall tether lengths of the plasmid (as further detailed in ANTICIPATED RESULTS). This is even without any clamping proteins present, and therefore it is not straightforward to make a calibration curve for the construct. Our linear control DNA had the same length as the shorter arc of the supercoiled plasmid, and for this linear tether we know the relation between its overall length and the observed Brownian motion[28] (as further detailed in the ANTICIPATED RESULTS section). The symmetry of the positions visited by the tethered particle gives information on whether the plasmid is catenated or whether multiple DNA tethers could be attached on one bead. Both such artifacts give rise to an anisotropic diffusion of the tethered bead. In our experiment, the TPM analysis gave information

on the kinetics of the plasmids and on the stability of CI-mediated DNA looping as a function of CI concentration.

Limitations

If one of the PNA handles is attached to a bead that is larger than a typical opening of the supercoiled DNA (as sketched in **Figure 2**), the plasmid geometry is locked and the supercoils are not able to 'slide' freely along the structure, as they probably do *in vivo*. This could be resolved by using a smaller marker, possibly a fluorophore instead of a bead. In conventional TPM studies using linear tethers, it is possible to establish a well-defined relation between the tether length and the magnitude of Brownian fluctuations of the bead and use this as a calibration curve[28]. For a linear assay, this calibration curve can give direct information on, e.g., whether a DNA molecule has been looped by a protein. In the assay described here, there is a large natural variation in the degree of supercoiling among the individual plasmids, and the distance between the bead and the surface will depend on the degree of supercoiling of the individual plasmid. Hence, a universal calibration curve cannot be established. A possible protein-mediated DNA looping is visible through a change in the bead's thermal fluctuations, as shown in Norregaard *et al.*[16], and not solely by the size of the fluctuations at any given instant. In addition, kinetic rates of protein-DNA interactions may be affected by the degree of supercoiling in the DNA molecule and on the exact location of supercoiled domains within the molecule. A final limitation regards the time scales resolvable by the methodology: at very short time scales (milliseconds) the motion of a tethered bead will be autocorrelated[16]; hence, it is advisable to use this methodology to investigate biological processes that appear on time scales larger than a millisecond.

MATERIALS

REAGENTS

▲ CRITICAL For the preparation of all growth media, do not tighten the cap of the bottle until it has cooled to room temperature (RT, 20–25 °C). If the cap is tightened while the contents are still hot, the cooling will create a vacuum. Any dust that falls on the shoulder of the bottle may be drawn in and may contaminate the medium on opening.

- M63 salts, 5× (see Reagent Setup)
- Acetic acid (glacial; Fluka, cat. no. 45731)
- Activated charcoal (powder; Merck)
- Agar (Becton, Dickinson, cat. no. 214010)
- α-Casein from bovine milk (Sigma-Aldrich, cat. no. C6780)
- α-Casein solutions (see Reagent Setup)
- Ammonium sulfate (ICN Biomedicals, cat. no. 808211)
- Ampicillin, sodium salt (Sigma-Aldrich, cat. no. A9518)
- Ampicillin solution (see Reagent Setup)
- Anti-digoxigenin (Roche, cat. no. 11 333 062 910)
- Anti-digoxigenin solution (see Reagent Setup)
- B1 stock solution (see Reagent Setup)
- Bromophenol blue (Serva, cat. no. 15375)
- Casamino acids (CAAs; Becton, Dickinson, cat. no. 228820)
- Cesium chloride (Cabot Specialty Fluids, 99.99%)
- Citric acid (Sigma-Aldrich, cat. no. C-1909)
- Decolorized CAA solution (see Reagent Setup)
- DIEA (*N*,*N*-diisopropylethylamine)
- Digoxigenin *N*-hydroxysuccinimide (NHS) ester (Sigma-Aldrich)
- Distilled H_2O
- DTT
- Dimethylformamide
- Dimethylsulfoxide (DMSO)
- DNA (see PROCEDURE)
- Ethanol (absolute)
- EDTA, disodium salt (Sigma-Aldrich, cat. no. E-1644)
- EDTA stock solution (see Reagent Setup)
- Ethidium bromide (Sigma-Aldrich, cat. no. E-7637)
- Ethidium bromide solution (see Reagent Setup)
- Ferrous chloride (Aldrich, cat. no. 22,029-9)
- Ferrous citrate solution (see Reagent Setup)
- Ficoll 400
- Glucose (Becton, Dickinson, cat. no. 215530)
- Glucose stock solution (see Reagent Setup)
- Growth medium (see Reagent Setup)
- Hydrochloric acid (Fluka, cat. no. 84419)
- Isopropanol (Fluka, cat. no. 34965)
- Isopropanol saturated with CsCl and Tris-EDTA (TE) (see Reagent Setup)
- K-Ac solution (see Reagent Setup)
- λ-Buffer (see Reagent Setup)
- CI (gift from D. Lewis and S. Adhya, Laboratory of Molecular Biology, Center for Cancer Research, National Cancer Institute, US National Institutes of Health)
- Lysozyme (Fluka, cat. no. 62971)
- Lysozyme buffer (see Reagent Setup)
- Magnesium sulfate ($MgSO_4$)
- $MgSO_4$ stock solution (see Reagent Setup)
- PBS buffer (see Reagent Setup)
- PEN buffer (see Reagent Setup)
- PIPES (Fluka, cat. no. 80636)
- Plasmid growth medium (see Reagent Setup)
- PNAs, PNA-1021 (biotin-labeled) and PNA-3593 (digoxigenin-labeled; see Reagent Setup and PROCEDURE)
- Potassium acetate
- Potassium chloride
- Potassium phosphate, dibasic, anhydrous (Sigma-Aldrich, cat. no. 60353)
- Potassium phosphate, monobasic, anhydrous (Fluka, cat. no. 60220)
- Sample buffer (see Reagent Setup)
- Sodium chloride (Sigma-Aldrich, cat. no. S7653)
- NaOH stock solution (see Reagent Setup)
- NaOH-SDS solution (see Reagent Setup)
- Restriction enzyme(s)
- SDS (BDH, cat. no. 436696N)
- SDS stock solution (see Reagent Setup)
- Sodium hydroxide (Riedel-deHaen, cat. no. 30620)
- Sodium phosphate, dibasic
- Sodium phosphate, monobasic
- Streptavidin-coated polystyrene beads (see Reagent Setup; Bangs Laboratories, cat. no. CP01N)
- TAE buffer for agarose gel electrophoresis (see Reagent Setup)
- Tris-EDTA (TE) buffer (see Reagent Setup)
- Trifluoroacetic acid; TFA, Sigma-Aldrich)
- Thiamine-HCl (Sigma-Aldrich, cat. no. T4635)
- Tris base (AppliChem, cat. no. A1086)
- Tris-HCl (Sigma-Aldrich, cat. no. T6666)
- Tris-HCl stock solutions (see Reagent Setup)
- Tryptone (Becton, Dickinson, cat. no. 211705)
- Uracil (Sigma-Aldrich, cat. no. U-0750)
- Yeast extract (Becton, Dickinson, cat. no. 212750)
- Yeast-tryptone (YT)-ampicillin plates (see Reagent Setup)

EQUIPMENT

- Zoom, 1.6× (fits the Leica DMI RB microscope)
- Collimated LED light source, 360 nm (fits the Leica DMI RB microscope)
- Air incubator (37 °C)
- Beakers
- Bransonic ultrasonic cleaner, model 2510 (Fisher Scientific)

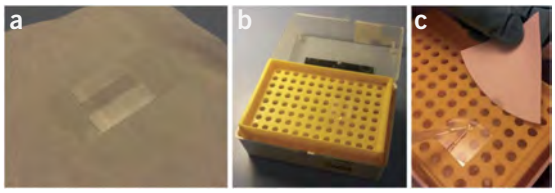

Figure 5 | Preparation of perfusion chamber. (**a**) Construction of chamber. (**b**) The finished perfusion chamber in the evaporation box. (**c**) Example of how to exchange the medium in the perfusion chamber.

- Centrifuge (Sigma-Aldrich 1-13)
- Clear and brown bottles
- Cover glass, 18 mm × 18 mm, no. 1 (Menzel-Gläser, VWR)
- Cover glass, 24 mm × 50 mm, no. 1.5 (Menzel-Gläser, VWR)
- Culture tubes
- Dialysis tubing
- Evaporation box (see PROCEDURE and **Fig. 5**)
- Filter paper (Whatman, Sigma-Aldrich, cat. no. 1001-0155)
- Flasks
- Funnels
- Graduated cylinders
- Graduated, low-binding pipette tips (Sorensen Biosciences, cat. no. 35090)
- High-numerical-aperture (NA, 1.45) 100× oil-immersion objective (Leica)
- High-speed refrigerated centrifuge with rotors and centrifuge tubes
- High-vacuum grease (Dow Corning)
- Inverted microscope (Leica, DMI RB)
- LabView particle tracking software (St. Andrews Tracker, National Instruments; http://www.ni.com/example/25948/en/)
- MATLAB program to perform principal component analysis (PCA)
- Microcentrifuge tubes, RNase/DNase free (Corning, cat. no. 3208/3207)
- Parafilm (VWR)
- ParaSequencer 1.6.3 program to record tethered beads with (Parameter)
- Petri dishes
- Piezo stage (Physik Instrumente, P-517.3CL)
- Plane block heater (Grant Boekel)
- Preparative ultracentrifuge with rotors and centrifuge tubes
- Progressive scan camera (Pike F-100B, Allied Vision Technology)
- Ring stand with clamps
- Standard oil-immersion liquid, $n = 1.518$ (Leica)
- Sterile plastic vials (Nunc and Falcon)
- Stir bars and magnetic stirrer
- Syringes and needles
- Temperature-controlled water bath
- Wooden applicator sticks

REAGENT SETUP

Bis-PNA synthesis The bis-PNA is synthesized by standard solid-phase chemistry[30] or obtained commercially (Panagene). It is important that a PNA containing only one reactive (primary or secondary) amine (e.g., the N terminus) be used. Dry PNA powder is stable for several years at 4 °C. Solutions >1 mg/ml) in water are stable for at least 1 year at −20 °C.

Tris-HCl stock solution, 1 M pH 8.0 (1 liter) Dissolve 42.4 g of Tris base and 102.4 g of Tris-HCl and adjust the volume to l liter; autoclave the solution. This solution is stable for years at RT.

Tris-HCl stock solution, 1 M pH 7.5 (1 liter) Dissolve 18.2 g of Tris base and 134 g of Tris-HCl and adjust the volume to l liter; autoclave the solution. This solution is stable for years at RT.

Tris-HCl stock solution, 1 M pH 7.4 (1 liter) Dissolve 14.2 g of Tris base and 138 g of Tris-HCl and adjust the volume to l liter; autoclave the solution. This solution is stable for years at RT.

EDTA stock solution, 0.5 M, pH 8.0 (1 liter) Suspend 186.12 g of disodium EDTA dihydrate in water. It will dissolve as the pH approaches 8. Adjust the pH with NaOH to 8.0 and the volume to l liter; autoclave the solution and store it in plastic for years at RT.

NaOH stock solution, 1 M Store the solution in plastic; this solution is stable for years if tightly sealed at RT.

SDS stock solution SDS is 10% (wt/vol). This solution is stable for months at RT.

TE buffer TE buffer is 10 mM Tris-HCl (pH 8.0) and 1 mM EDTA. Autoclave the buffer and store it for years at RT.

2× PEN buffer To autoclaved, distilled water, add 0.5 M EDTA to a final concentration of 0.2 mM, 5 M NaCl to a final concentration of 20 mM and PIPES powder to a final concentration of 20 mM. Adjust the pH to 6.5 with NaOH and adjust the volume with autoclaved, distilled water. ▲ **CRITICAL** Do not autoclave the buffer. The buffer can be stored at −20 °C for at least 3 years.

λ Buffer Mix 10 mM Tris-HCl (pH 7.4), 200 mM KCl and 0.1 mM EDTA. Autoclave the buffer and allow it to cool. Remove any particles by filtering through a several-centimeter bed of fine Sephadex. Add DTT to a final concentration of 0.2 mM before use. The buffer can be stored at RT for at least 2 years.

0.1 M DTT Dissolve DTT to a 0.1 M concentration in autoclaved distilled water. ▲ **CRITICAL** Do not heat the solution, and never vortex it, as aeration will speed up oxidation. Divide the solution into small volumes to avoid thawing too many times. Store DTT at −20 °C for years.

PBS buffer Dissolve 1.42 g of Na_2HPO_4 in 10 ml of distilled H_2O to obtain a stock of 1 M Na_2HPO_4. Dissolve 1.19 g of NaH_2PO_4 in 10 ml of distilled H_2O to obtain a stock of 1 M NaH_2PO_4. Mix 5.77 ml of the 1 M Na_2HPO_4 stock with 4.23 ml of the 1 M NaH_2PO_4 stock, and add 90 ml of distilled H_2O. Withdraw 20 ml of this stock (pH 7) and mix it with 0.88 g of NaCl and 80 ml of distilled H_2O. Autoclave and filter the buffer through a several-centimeter bed of fine Sephadex. The buffer can be stored at RT for at least 2 years.

α-Casein solutions (λ buffer and PBS buffer) α-Casein reduces nonspecific binding; it is used to reduce nonspecific interactions between the cover glass surface and the tether complex and prevent the beads from aggregating. Dissolve 2 mg of α-casein in a tube containing 1 ml of λ buffer and in another tube containing 1 ml of PBS buffer. Filter-sterilize both solutions and store them at 4 °C for up to 1 month.

Bead suspension Withdraw 50 µl of polystyrene bead suspension from the stock and dilute it in 950 µl of PBS buffer. Briefly vortex the solution and then centrifuge it at 1,000*g* for 15 min at RT. Remove the supernatant and resuspend the beads with 350 µl of PBS buffer. Store it at 4 °C for up to 6 months. Before use, dilute 5 µl of the bead suspension with 95 µl of 2 mg/ml α-casein solution in PBS buffer, mix it in short pulses five times on a vortex and place it in a sonicator bath for 10 min to separate aggregated beads. ▲ **CRITICAL** We have found that the beads aggregate less if kept in the PBS buffer instead of λ buffer, possibly because of the lower salt concentration.

Anti-digoxigenin solution Dissolve the anti-digoxigenin pellet from Sigma-Aldrich in 1 ml of PBS buffer to a concentration of 200 µg/ml anti-digoxigenin. Distribute 10-µl aliquots of the solution into centrifuge tubes. Store the aliquots at −20 °C for up to 2 years. Before use, thaw the solution, and centrifuge it briefly (100*g* for 10 s at RT) to collect the sample, and then dilute it into 90 µl of PBS buffer to generate a final concentration of 20 µg/ml anti-digoxigenin.

Ferrous citrate solution Dissolve $FeCl_2$ and citric acid in distilled H_2O to a concentration of 20 mM each. Any brown precipitate that fails to dissolve can be removed by filtration through Whatman no. 1 paper. Autoclave the solution in a brown bottle and store it at 4 °C to protect it from light. This solution is stable for years.

5× M63 salts (1 liter) Mix 15 g of KH_2PO_4 (anhydrous), 35 g of K_2HPO_4 (anhydrous) and 10 g of $(NH_4)_2SO_4$. Add 2.5 ml of 20 mM ferrous citrate solution. Adjust the volume to 1 liter with distilled H_2O and autoclave it for storage. Store the salts at RT. If the solution is autoclaved, it should be stable for months. See Pardee *et al.*[34] for details.

$MgSO_4$ solution, 1 M Dissolve $MgSO_4$ to a 1 M concentration in distilled water. Store it at RT. This solution is stable for years.

B1 stock solution, 1 mg/ml Dissolve thiamine-HCl (vitamin B1) to a concentration of 1 mg/ml in distilled water. Filter-sterilize it and store it at 4 °C. This solution is stable for months.

Glucose stock solution, 20% (wt/vol) Filter-sterilize the solution and store it at RT. This solution is stable for years.

PROTOCOL

Decolorized CAA solution Dissolve CAAs to 25% (wt/vol) with distilled H_2O. Add 1 g of activated charcoal powder per 20 g of CAAs. **! CAUTION** Activated charcoal can stain clothes. Stir it at RT for 30 min. Filter the solution through doubled, fluted Whatman no. 1 paper. Measure and record the volume of the filtrate and adjust the pH of the filtrate to 7.0 with NaOH or HCl as appropriate. Adjust the volume of the neutralized CAA filtrate to 20% (wt/vol) CAAs. Distribute the solution into bottles and autoclave them; store the bottles at RT. Unopened bottles remain stable for years. Open the bottles aseptically and store them at 4 °C after opening.

Ampicillin solution, 100 mg/ml Weigh sodium ampicillin and dissolve it with distilled water to a concentration of 100 mg/ml. Filter-sterilize and distribute it into sterile plastic vials. Store it at −20 °C. Unthawed solution is stable for at least 1 year. Thaw and mix the solution before adding it to the medium. This solution can be re-frozen.

YT-amp plates Prepare the medium in a 2-liter Erlenmeyer flask covered with an inverted beaker. **! CAUTION** If mixing after adding antibiotics introduces bubbles, try placing a magnetic stir bar in the flask before autoclaving. To 1 liter of H_2O, add 8 g of tryptone, 5 g of yeast extract, 5 g of NaCl and 15 g of agar. If you have a light touch, you can reduce the concentration of agar. Autoclave the medium for 15–20 min. Mix it well after autoclaving and allow it to cool to 50–60 °C. Aseptically add antibiotic solution to the cooled agar, and mix it without introducing bubbles. Pour it into Petri dishes and allow the agar to solidify overnight. See Miller[35] for details.

YT broth To 1 liter of H_2O add 8 g of tryptone, 5 g of yeast extract and 5 g of NaCl. Mix to dissolve them. Distribute 100-ml aliquots in bottles and sterilize them by autoclaving. Store the aliquots at RT. This medium is stable for months. Aseptically add antibiotic solution before use. See Miller[35] for details.

Plasmid growth medium For 1 liter of medium, autoclave together 200 ml of 5 × M63 salts, 25 ml of 20% decolorized casamino acids, 1 g of uracil and 751 ml of distilled H_2O. Store the medium at RT. Unopened bottles are stable for months. Immediately before use, add aseptically, with mixing after each addition, 1 ml of 1 M $MgSO_4$, 1 ml of 1 mg/ml B1, 20 ml of 20% (wt/vol) glucose and appropriate antibiotic solution (here, 2 ml of 100 mg/ml ampicillin). Distribute it into growth flasks. If you are using Erlenmeyer flasks and aerating by shaker, do not exceed 10% of the flask volume. See Norgard[36] for details.

Lysozyme buffer (100 ml) Mix 1 g of glucose, 2 ml of 0.5 M EDTA (pH 8.0), and 2.5 ml of 1 M Tris-HCl (pH 8.0); add distilled, autoclaved water to 100 ml. Store the buffer at 4 °C for months. Add lysozyme to 2 mg/ml to the amount necessary immediately before use.

NaOH-SDS solution (10 ml) This solution must be prepared daily. To 7 ml of distilled, autoclaved water, add 2 ml of 1 M NaOH and 1 ml of 10% (wt/vol) SDS. Mix it and leave it at RT before use.

K-Ac solution, 5 M, pH 4.8 (500 ml) Dissolve 147 g of KCH_3COO in ~300 ml of H_2O, add glacial acetic acid to pH 4.8 and bring the volume to 500 ml with H_2O. Autoclave the solution and store it at RT. The solution is stable for years.

Ethidium bromide solution, 10 mg/ml Dissolve ethidium bromide with autoclaved, distilled water and store it in a brown bottle at 4 °C. It is stable for years under these conditions. **! CAUTION** Ethidium bromide is mutagenic. Avoid contact with skin. Wear gloves. Avoid breathing the powder when you are preparing the solution. Please note that ethidium bromide is now commercially available in an aqueous suspension; in our laboratory, we will not make it from powder again.

Isopropanol saturated with CsCl and TE Add, in order, CsCl, then isopropanol, and then slowly add TE by shaking after each addition of TE. Add sufficient CsCl and TE so that when the phases resolve you see two liquid phases and some white powder (CsCl) at the bottom of the bottle. The top liquid phase is the organic phase. The solution is stable for years at RT. The bottle can be refilled by adding only isopropanol and TE.

50× TAE (500 ml) Dissolve 121 g of Tris base, 28.5 ml of glacial acetic acid and 50 ml of 0.5 M EDTA (pH 8) in H_2O and adjust the volume to 0.5 liters. Store it at RT. This solution is stable for at least 1 year.

Sample buffer Autoclave 25% (wt/vol) Ficoll 400. After cooling, store the Ficoll solution at −20 °C; it stable for years at this temperature. To prepare the sample buffer, mix 4 ml of 25% (wt/vol) Ficoll 400 with 1 ml of 0.5 M EDTA and add bromophenol blue until the solution is medium blue. The solution is stable for months at 4 °C and for years at −20 °C.

EQUIPMENT SETUP

Microscope In this protocol, we image tethered beads using a high-speed progressive camera mounted on an inverted bright-field microscope with a 100× oil-immersion objective and a 1.6× zoom. For a region of interest of 62 × 62 pixels^2, the frame rate is 225 Hz. The recorded output is obtained with the program ParaSequencer and is an AVI file of the tethered bead, a text file containing the number of recorded frames, frames per second (f.p.s.) and the number of lost frames, which in general is zero. The pixel resolution was determined to be 45.97 nm per pixel by moving a sample with immobilized beads on a cover slide in discrete steps by a piezo stage and taking images of these positions (see PROCEDURE).

Particle tracking algorithm There are several different algorithms for tracking particles, e.g., based on cross-correlation, sum-absolute difference, center of mass or direct Gaussian fits. Here, we used the cross-correlation algorithm, as that approach is suitable for the size of particles used in this work[37]. We used a LabView program based on a normalized cross-correlation algorithm. The program can be downloaded via this link: http://www.ni.com/example/25948/en/. Note that to run the program a licensed version of LabView is required.

PROCEDURE

Preparation of digoxigenin-labeled bis-PNA ● TIMING 20 h

1| Dissolve 1.5 mg of PNA (H-(eg1)$_3$-(diMeLys)$_3$-TJTJTTTJTT-(eg1)$_3$-TTCTTTCTCT-Gly-NH_2) in 400 µl of DMSO (eg1: 8-amino-3,6-dioxaoctanoyl; diMeLys: ε-N,N-dimethyllysine; J: pseudoisocytosine PNA unit).

2| Dissolve digoxigenin-NHS ester (0.5 mg) in 400 µl of DMSO and add it to the PNA solution.

3| Add 25 µl of DIEA in 50 µl of dimethylformamide and incubate the mixture for 16 h at 20 °C.

4| Purify the reaction mixture by reversed-phase HPLC (C18, 5-µm column, 150 × 3.9 mm, eluant: 0–50% acetonitrile in 0.5% (vol/vol) TFA, linear gradient over 30 min with a flow rate of 1 ml/min and UV detection at 260 nm; see HPLC data in **Supplementary Fig. 1a**).

5| Check the identity of the product by performing MALDI-TOF or ESI mass spectrometry on the fractions that appear to contain the product (see MALDI-TOF data in **Supplementary Fig. 1b**). Combine the fractions, lyophilize them and store them at 4 °C for up to several years.

6| Dissolve PNA in pure water for use (store aliquots (~1 mg/ml) at –20 °C; concentrations are determined spetrophotometrically at 260 nm).
! CAUTION The PNA solution is very acidic, as the PNA is isolated as TFA salt.

Preparation of biotin–bis-PNAs conjugates ● TIMING 20 h
7| Prepare biotin–bis-PNAs conjugates. These conjugates can be synthesized as previously reported[20,30], or they can be obtained commercially (Panagene). The conjugates may also be synthesized fully analogously to the digoxigenin conjugates (see Step 2) using biotin-NHS ester (Sigma-Aldrich); to do this, perform Steps 2–6 using 0.5 mg of biotin-NHS ester instead of digoxigenin-NHS ester in Step 2. Handling and stability are as described above (Steps 5–6).
■ PAUSE POINT Lyophilized material can be stored at 4 °C for several years.

Growth schedule for purification of supercoiled plasmid DNA ● TIMING 3 d (after all media are prepared)
8| All DNA preparations begin with a single, well-isolated colony of the transformant harboring the plasmid. Prepare YT agar plates supplemented with the appropriate antibiotic(s). We have used ampicillin as our example of an antibiotic in the descriptions below. Many of our colleagues use LB agar, and both YT and LB are probably comparable.

9| *Revive transformants*. Scrape a small amount of frozen cell suspension from the –80 °C glycerol with sterile wooden applicator stick and inoculate the YT-amp plate.
▲ CRITICAL STEP Do not let the glycerol thaw, but return it to the –80 °C box. Streak the inoculated plate to produce single colonies and incubate it at 37 °C.

10| *Inoculate the starter culture*. On day 2 in the morning, inoculate 5 ml of YT-ampicillin broth and incubate it at 37 °C with aeration, such as on a roller drum.

11| *Large-scale growth of transformants*. At the end of day 2, dilute the YT-ampicillin culture into 0.5 liters of plasmid growth medium and incubate it overnight at 37 °C with shaking.

12| *Plasmid extraction* (modified from Birnboim and Doly[38]). On day 3, transfer the saturated culture to centrifuge bottles.

13| Collect the cells in a refrigerated centrifuge at 4,000*g* for 5 min at 4 °C.

14| Decant the supernatant and resuspend the cells with a 1/20th culture volume of 20 mM Tris-HCl (pH 8.0) and 0.1 M NaCl.

15| Collect the resuspended cells in a refrigerated centrifuge at 4,000*g* for 5 min at 4 °C. Decant and discard the supernatant.

16| Resuspend the washed cells with 4 ml of lysozyme solution (lysozyme buffer with 2 mg/ml lysozyme) per 100 ml of the original culture volume.

17| Incubate the cells with lysozyme for at least 30 min on ice.

18| Per 4 ml of lysozyme solution used, add 8 ml of NaOH-SDS, mix well and incubate the mixture for 5–10 min on ice. Examine the suspension and continue to the next step when the opacity starts to decline.

19| Per 4 ml of lysozyme solution used, add 6 ml of K-Ac, mix well and incubate the mixture for 45 min on ice.

20| Clarify the solution by centrifugation in a refrigerated centrifuge at 7,000*g* for 15 min at 4 °C.

21| Carefully decant the supernatant into a 50-ml conical tube. Note the volume.

22| Distribute the supernatant into the centrifuge tube noting the volume, and add 0.6 volumes of isopropanol (if it is convenient to increase volume of supernatant, e.g., when you are processing more than one sample and you want them all to be the same volume/weight so they can all be centrifuged in a single centrifuge run, use 30 mM Tris-HCl (pH 8.0), 5 mM EDTA and 0.1 M NaCl as diluent). Mix well.

23| Incubate the isopropanol suspension at –20 °C overnight.
■ PAUSE POINT The suspension is stable at –20 °C for at least 1 week.

Plasmid recovery ● TIMING ~0.5 d
24| Collect the precipitate in a refrigerated centrifuge at 6,000*g* for 10 min at 4 °C.

25| Decant and discard the supernatant.

PROTOCOL

26| Resuspend the pellet by vortexing with cold 70% (vol/vol) ethanol.

27| Collect the precipitate in a refrigerated centrifuge at 6,000*g* for 10 min at 4 °C.

28| Decant and discard the supernatant.

29| Centrifuge the pellet briefly (1,000*g* for 30 s at RT) to sediment the residual liquid.

30| Aspirate and discard the residual liquid.

31| Allow the recovered precipitate to dry in air.

32| Re-dissolve the dried pellet with a small volume (about one-half of the centrifuge tube capacity) of 20 mM Tris-HCl (pH 8.0) and 5 mM EDTA.

Plasmid purification ● TIMING ~2 h followed by overnight centrifugation

33| Dissolve 1.05 g of CsCl per ml of plasmid solution and add it to the plasmid solution[39].

34| Transfer the solution to an ultracentrifuge tube and fill it to 95% of the tube volume with Tris-EDTA-CsCl solution.

35| Gently fill the tube with 10 mg/ml ethidium bromide. If you are using quick-seal tubes, this step is easy with a 1-ml syringe with hypodermic needle.
! CAUTION Wear gloves for all manipulations involving the ethidium bromide solution.
▲ CRITICAL STEP DNA–ethidium bromide complexes are light-sensitive. Do not allow the ethidium bromide solution to mix with the DNA solution.

36| Seal the centrifuge tube. Verify that the tube is sealed by squeezing it.
! CAUTION Protect yourself with a gloved hand in case the tube leaks.

37| Mix the ethidium bromide and plasmid solutions thoroughly immediately before placing them in the centrifuge rotor.

38| Centrifuge the solutions using a Beckman Vti65 rotor for 20 h at 42,000 r.p.m. at 15 °C.

Recovery of supercoiled DNA ● TIMING ~2 h followed by overnight centrifugation

39| Remove the tubes one at a time and clamp them in a ring stand over a beaker to collect the waste.

40| Visualize the plasmid band with 366-nm mineral light in a darkened room (a 395-nm lamp from Xenopus Electronix can also be used). The lower of the two central bands will be the plasmid band. The diffuse fluorescent material at the bottom of the centrifuge tube is RNA.
! CAUTION Protect your eyes from UV light.

41| Puncture the tube near the top with a hypodermic needle to provide a vent hole.

42| Insert a fresh hypodermic needle on a syringe above the band with needle pointing downward.
▲ CRITICAL STEP It is prudent to puncture tubes above the desired band so that if the tube leaks you will not lose your sample.

43| Carefully withdraw the band and transfer it to a fresh ultracentrifuge tube wrapped in aluminum foil to protect the DNA-ethidium bromide complexes from excess exposure to light.

44| Fill the tube with Tris-EDTA-CsCl–ethidium bromide solution, seal it and mix. Prepare the balance tube without ethidium bromide and seal it.

45| Repeat the centrifugation and band recovery once (Steps 38–42).

Removal of ethidium bromide ● TIMING 2–3 h followed by overnight incubation

46| Transfer the solution containing the supercoiled plasmid to isopropanol saturated with TE and CsCl, mix it well and let the phases separate. The top phase in the isopropanol/TE/CsCl bottle is the isopropanol phase.

47| Remove and discard the organic phase.

48| Repeat the extraction with isopropanol saturated with TE and CsCl until the organic phase shows no pink color, and extract once more.

49| Dialyze the aqueous phase against 100 volumes of 20 mM Tris-HCl (pH 8), 2 mM EDTA, and 0.1 M NaCl for at least 1 h.

50| Withdraw the dialysate, measure its volume and mix it with two volumes of ethanol. Incubate it at –20 °C overnight.

51| Recover the plasmid DNA by centrifugation at 10,000*g* for 10 min at 4 °C.

52| Discard the supernatant.
▲ **CRITICAL STEP** Be careful not to discard the pellet; it may be small.

53| Gently rinse the tube with –20 °C ethanol and let it dry in air. Dissolve ~200 µl of DNA per liter of original culture with TE.

Characterization of CsCl-purified plasmids ● TIMING 1 d
54| Determine the concentration of the purified plasmid. This can be done by measuring absorbance at 260 nm.

55| *Gel electrophoresis (optional)*. Analyze the samples prepared as described in the in-text table below:

Uncut preparation	To determine the supercoiled fraction (versus relaxed or catenated)
Complete digestion with a restriction endonuclease that cuts the plasmid once	To identify the mobility of the plasmid as linear DNA
Partial digestion with a restriction endonuclease that cuts the plasmid once	To determine if the plasmid is a monomer or multimer

! **CAUTION** Protect eyes from UV light.
▲ **CRITICAL STEP** To quantify relative amounts of the different forms, it is crucial that the gel be stained after electrophoresis. To be sure that the gel is uniformly stained, look at it from the side while it is on the UV transilluminator. If the bands are uniform across the thickness of the gel, the gel is uniformly stained.

Preparation of a chloroquine gel ● TIMING ~4 h of manipulation, plus overnight electrophoresis
56| (Optional) Determine the degree of supercoiling in the plasmid preparation by a chloroquine gel (shown in **Fig. 4a**).
! **CAUTION** Chemicals purchased today are often much purer than those purchased in 1987. Accordingly, start with concentrations as described by Esposito and Sinden[40], but you may have to repeat experiments with a lower concentration of chloroquine. This step is optional, as it is not possible to correlate the bead excursions to the degrees of supercoiling. However, when analyzing the data, it is important to be aware that there will be a spread of overall lengths of the tethered DNA molecules originating from the natural spread in degrees of supercoiling.

57| To determine the diversity of supercoiling in the plasmid preparation, electrophorese serial dilutions of the plasmid on a 1% (wt/vol) agarose gel in 1× TAE buffer supplemented with 2 µg/ml chloroquine-diphosphate. It is important to use low voltage, so the electrophoresis takes ~20 h. After electrophoresis, the gel is stained with 0.5 µg/ml ethidium bromide in 0.25× TAE. The stained gel is then photographed on a UV transilluminator.

Preparation of end-labeled linear DNA ● TIMING 1 d
58| To assess the DNA-PNA coupling conditions in the perfusion chamber, prepare linear DNA with one end labeled with biotin and the other labeled with digoxigenin. End-labeled linear DNA can be prepared by PCR amplification using the protocols provided by the thermophilic DNA polymerase manufacturer.
▲ **CRITICAL STEP** The only changes we made from the standard protocol were to use one primer bearing a 5′ biotin and the other primer bearing a 5′ digoxigenin. Although it is perhaps unnecessary, we removed the unincorporated primers by desalting over Sepharose 2B. The addition of a small amount of bromophenol blue to the sample lets you know when the smallest material has eluted. Fractions containing the desired fragment can be identified by agarose gel electrophoresis and staining with ethidium bromide.

PROTOCOL

Initial identification of PNA-DNA coupling conditions by gel electrophoresis ● TIMING ~2 h on the first day, plus most of the second day

▲ **CRITICAL** Gel electrophoresis allows you to determine the initial concentrations and buffer conditions for PNA-DNA binding. In these experiments, please keep in mind that you are looking for a band that goes missing, not for a single band that appears[41].

59| In a 10-µl reaction, add purified plasmid DNA to 10 nM. Vary the concentration of PNA. For an initial range use 0.1–1 µM PNA. Include a no-PNA control. In addition, prepare samples with the plasmid cut with a restriction enzyme that cuts adjacent to the PNA target, and do not add PNA. The digested plasmid will aid in identifying the target band. We examined two solution conditions: TEN (10 mM Tris-HCl, pH 7.5, 0.1 mM EDTA and 10 mM NaCl) and PEN (10 mM sodium PIPES, pH 6.5, 0.1 mM EDTA and 10 mM NaCl).

60| After mixing the samples, incubate them overnight in a 37 °C air incubator.

61| After incubation, dilute the samples to 30 µl with the high pH restriction enzyme reaction buffer for the diagnostic restriction enzyme.

▲ **CRITICAL** Choose a diagnostic restriction enzyme that cuts the plasmid several times, functions at 37 °C and leaves the diagnostic band well resolved from the other bands.

62| Heat the diluted samples to 65 °C and incubate them for 10 min. Transfer the samples to ice.

63| Add the diagnostic restriction enzyme. Incubate the restriction enzyme reactions at 37 °C.

64| After digestion is calculated to be complete, add 10 µl of sample buffer.

! CAUTION Do not add additional tracking dyes to experimental samples, as xylene cyanol can prevent visualization of ethidium bromide–stained bands that co-electrophorese with xylene cyanol. Electrophorese samples through a polyacrylamide gel in TBE. After electrophoresis, stain the gel with 0.5 µg/ml ethidium bromide. A 1.5-mm thick gel will require ~45 min with agitation for staining to be complete. After staining, visualize the stained DNA with a UV transilluminator and photograph the gel. An example can be seen in **Figure 4b**.

Preparation of PNA and plasmid DNA coupling ● TIMING 15 h

65| Pipette 1 µl of 10 µM PNA-biotin into a low-binding tube, and mix it with 9 µl of PEN buffer. Pipette 1 µl of 10 µM PNA-digoxigenin into another low-binding tube and mix it with 9 µl of PEN buffer. Pipette 1 µl of 200 nM DNA into a third low-binding tube and mix it with 3 µl of PEN buffer. Withdraw 3 µl of each of the three prepared solutions and mix them in a low-binding tube. Incubate the mixture in an air incubator at 37 °C for 14 h.

▲ **CRITICAL STEP** Use low-binding pipette tips and tubes to prevent nonspecific adhesion of the PNA and DNA molecules to the surface of the tubes during preparation.

? TROUBLESHOOTING

■ **PAUSE POINT** After incubation, the solution can be stored at 4 °C for up to 3 d.

66| After incubation, pipette 2 µl of the PNA-DNA solution into a new low-binding tube and dilute it in 48 µl of PEN buffer.

■ **PAUSE POINT** The solution can be stored at 4 °C for up to 3 d.

67| Pipette 4 µl of the diluted PNA-DNA solution into a low-binding tube and mix it with 96 µl of λ buffer. Place this tube in a heat bath at 65 °C for 10 min.

▲ **CRITICAL STEP** The heat bath incubation is important to remove nonspecific binding between PNA and DNA, and it cannot be excluded from the protocol.

■ **PAUSE POINT** The solution can be stored at 4 °C for up to 3 d.

Construction of perfusion chamber ● TIMING 15 min

68| Place two strips of Parafilm on a clean 24 × 50 mm cover slide with a spacing of ~5–7 mm. On top of the Parafilm, place a clean 18 × 18 mm cover slide as a lid (**Fig. 5a**).

69| Heat a plane block heater to ~80 °C, and place the prepared chamber on it to melt the Parafilm. Gently press the two slides together. Remove the chamber from the heat stage, cut off excess Parafilm if necessary and place the chamber in a closed box with a little water in the bottom to prevent evaporation of the open perfusion chamber during sample preparation (**Fig. 5b**).

▲ **CRITICAL STEP** The sample will dry out during preparation if there is not water in the closed box.

Preparation of the PNA-DNA tethered sample ● TIMING 2.5 h

70| Add 20 µl of the 20 µg/ml anti-digoxigenin solution to the perfusion chamber. Incubate it for 30 min at RT. After incubation, wash the chamber with 90 µl of λ buffer.

▲ **CRITICAL STEP** Fluid placed at one end of the channel will be drawn into the chamber by capillary forces and can be withdrawn at the other end of the channel by placing a filter paper to suck up the liquid (**Fig. 5c**). This method is used for all buffer exchanges during the sample preparation. Be careful not to remove more liquid than what is added, as a temporarily dried chamber will acquire air bubbles when new liquid is added and can damage the sample. Preferably always keep an excess of the liquid at the inlet and at the outlet of the flow channel.

71| Add 20 µl of the 2 mg/ml α-casein solution to the perfusion chamber. Incubate it for 30 min at RT. After incubation, wash the chamber with 90 µl of λ buffer.

72| Add 20 µl of the prepared PNA-DNA solution that has been heated in a water bath of 65 °C for 10 min (Steps 65–67) to the perfusion chamber. Incubate it for 60 min at RT. After incubation, wash the chamber with 90 µl of λ buffer.

73| Add 20 µl of the bead suspension containing 2 mg/ml α-casein in PBS buffer (Reagent Setup) to the perfusion chamber. Incubate it for 30 min at RT. After incubation, wash the chamber with 90 µl of λ buffer.

74| Seal the perfusion chamber with high-vacuum grease to prevent evaporation.

▲ **CRITICAL STEP** When you are conducting protein-mediated DNA conformational change studies, add the protein solution before sealing the chamber.

? TROUBLESHOOTING

Identifying noise in the experimental setup ● TIMING ~2 h

▲ **CRITICAL** Before conducting a TPM experiment, it is important to quantify the drift in the system to minimize the level of noise that otherwise can lead to bias in the data. This is especially important for experiments longer than 10 s, in which temperature, stage and microscope drift could be significant factors. In our experiments, we recorded long time series, up to 60 s, in which reduction of drift in the setup was important. Allan variance analysis has proven to be a reliable method to identify low-frequency noise[42,43]. Also, Allan variance is useful to determine the optimal measurement time of an experiment that is subject to low-frequency noise with a possible bias[42,43]. It should be noted, however, that the biological process of interest should also be considered while determining the measurement time. To quantitatively address and to possibly minimize the noise present in a TPM experiment assay, we suggest following Allan variance analysis before the experiments.

75| Sample a long time series of position data of an immobilized bead in the microscope with a sufficiently high acquisition frequency.

76| Import the time series to MATLAB.

77| Calculate the Allan variance, which is defined as

$$\sigma_x^2(\tau) = \frac{1}{2}\left\langle (x_{i+1} - x_i)^2 \right\rangle_\tau$$

of adjacent time series for a set of measurement times τ, where τ is defined as the number of elements in the interval divided by the sampling frequency. A free Allan variance analysis program can be downloaded from http://www.mathworks.com/matlabcentral/fileexchange/26659-allan-v3-0.

78| Determine the optimal measurement time τ where the Allan deviation is minimal, or quantify the drift for a given measurement time.

79| Quantify and possibly minimize noise sources in the setup using the results of the Allan variance calculation.

Imaging condition setup and pixel-to-nm calibration ● TIMING ~1 h

80| Dilute microspheres with diameters of 0.5–3 µm, 1:10,000, in filtered Milli-Q water.

81| Perfuse the diluted microspheres into a perfusion chamber and seal it with vacuum grease to prevent evaporation.

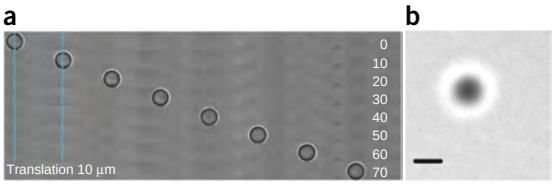

Figure 6 | Image analysis. (**a**) A 3-µm sphere immobilized to a coverslip is moved in 10-µm steps (shown as the distance between the blue vertical lines) by a piezo-stage with nanometer accuracy. The total movement in this figure is 70 µm. In our work, the conversion factor was 45.97 nm/pixel for maximum optical zooming. (**b**) A typical microscope image of the *x*,*y* projected plane of a 0.5-µm tethered bead. Scale bar, 500 nm.

82| Add a droplet of immersion oil on the objective and make sure that no air bubbles are present.

83| Adjust the microscope for bright-field imaging and optimize the illumination and contrast of the sample according to the standard procedure. If the microscope is equipped with differential interference contrast, this mode can be used to enhance the contrast of the beads.

84| Place the perfusion chamber filled with the sample on the microscope stage. Wait until a few microspheres are immobilized to the surface, typically 5–15 min.

85| Find an immobilized microsphere and zoom in using the optical zoom.
▲ **CRITICAL STEP** Digital zooming will not improve the resolution.

86| With a microsphere positioned at one side in the field of view, move the microscopic stage with discreet steps of a few µm (e.g., 5–10 µm) and at each step capture an image. Repeat this step for a few beads.

87| Import the images to an image-processing program (e.g., Gimp or Photoshop) or MATLAB to stitch the images together as shown in **Figure 6a**.

88| Determine the distance-to-pixel conversion factor by measuring the number of pixels between each discreet step (adjacent beads) and dividing that by the known step length (5–10 µm) obtained from the piezo-stage. Repeat Steps 86–88 also for small displacements, i.e., 100-nm steps.

Setup of the sample and image recording preparation ● TIMING ~15 min
89| Add a droplet of immersion oil on the objective; make sure that no air bubbles are present.

90| Place the sample perfusion chamber on the microscope stage.

91| Adjust the microscope for bright-field imaging, and optimize the illumination and contrast of the sample according to the standard procedure. If the microscope is equipped with differential interference contrast, this mode can be used to enhance the contrast of the beads.

92| Optically zoom on a bead that is tethered and that performs Brownian motion.
? TROUBLESHOOTING

93| Set an area of interest/region of interest (AOI/ROI) to minimize the imaging region in order to generate smaller data files and to achieve a faster acquisition rate. If possible, simultaneously image an immobilized object with the bead under investigation to correct for system drifts. In an ROI of 1,000 × 1,000 pixels (ref. 2), there are, on average, one or two tethered beads in a supercoiled sample.
▲ **CRITICAL STEP** Be aware that a small ROI gives a faster acquisition rate compared with a larger ROI, and hence it can capture faster kinetic rates of the DNA conformational changes. However, for investigations in which the time resolution is less important or the transitions occur on time scales on the order of a second, a larger ROI where multiple tethered beads can be imaged simultaneously is a better option as the method is fairly time-consuming.

Acquiring an image of a tethered bead ● TIMING ~5 min
94| Run ParaSequencer and connect to the camera.
▲ **CRITICAL STEP** Make sure that the full bandwidth (maximum package are set) of the camera is used for full-speed image acquisition. We show here the protocol using the frame capture program ParaSequencer 1.6.3 from Parameter Sweden. The same approach can, however, be used for other Institute of Electrical and Electronics Engineers (IEEE)-interface cameras.

95| At the settings dialog, set the number of packages to 7,576 and IEEE speed to 800 Mbps. This allows for 60 f.p.s. at 1,000 × 1,000 pixels^2 (ref. 2).

96| Unclick 'Auto Sequence Numbering', set the 'Video File Path' and name the file. Set a specific number of frames or the acquisition time determined by Allan variance analysis (Steps 75–79).

97| Set the AOI (width and height) and place the marked-up box on the bead under investigation. For higher f.p.s., set an AOI/ROI that minimizes the imaging region; 62 × 62 pixels (ref. 2) will cover a region of 2.85 × 2.85 μm^2 (sufficient for a 0.5-μm bead tethered by an ~7-kbp DNA plasmid performing Brownian fluctuations), and it will allow for 225-Hz recording and thus an exposure time <5 ms. A typical *x*-*y* image plane of a bead in an ROI of 62 × 62 pixels (ref. 2) is shown in **Figure 6b**. Press 'Set AOI' to reset the frame.

98| Press 'Live' to fine-tune the light/contrast and correct the position of the bead to the center of the ROI using the piezo-stage.

99| Press 'Start' and the frames will be recorded and stored in an AVI file format. In addition to the saved AVI file, a .txt file containing the number of recorded frames, the FPS for the sequence and the number of dropped frames is saved.

Particle tracking of a tethered bead ● TIMING ~15 min

100| Import the AVI file into the St. Andrews Tracker program that performs postprocessing of the recorded frames. Choose the .avi file tab and locate the file to be analyzed. Mark the 'SubPixel' accuracy check box. For high-contrast videos, 700 is sufficient for 'Minimum Match Score'. Keep the default settings of the other controllers. Set the ROI by checking the 'New template(s)' box and set the 'End' frame to the number of frames of your AVI file. Start the program.

101| An additional window is opened. Zoom in on the bead and set an ROI around the rim of the bead by clicking and dragging with the mouse in the movie window. An ordered ASCII data file containing the *x* (first column) and *y* (second column) pixels of the bead's center position in each frame is created.

Time series analysis of a TMP data set ● TIMING ~5 min

102| Import the ASCII data file into MATLAB.

103| Subtract the mean of the *x*- and *y*-coordinates $(x(t)-\langle x\rangle)$, $(y(t)-\langle y\rangle)$ from the times series to have the bead positions distributed around the tether point.

104| Plot the *x* and *y* data in a scatterplot and histogram to visually inspect the position data. The data should be centered at position 0.

105| Calculate the time-dependent projected displacement vector ρ, i.e., $\rho^2(t) = (x(t)-\langle x\rangle)^2 + (y(t)-\langle y\rangle)^2$ to quantify the 2D projected displacement. Filter ρ with a sliding window (moving average) (we used a moving average of 20 ms). Plot ρ versus time and inspect the data set.

106| *x* and *y* are random directions, so we perform a principal component analysis (PCA) to determine the principal axes of the positions visited by the bead and interpret the data accordingly to the principal axes. The two principal axes denote the orthogonal axes along which the data have the largest and smallest spread. Use the data from Step 103 to find the principal axes by calculating the covariance matrix as

$$C = \begin{pmatrix} \sigma_{xx} & \sigma_{xy} \\ \sigma_{yx} & \sigma_{yy} \end{pmatrix}$$

where σ_{ij} represents the covariance of the in-plane coordinates (i,j), and where the covariance is defined as

$$\sigma_{ij} = \frac{1}{N}\sum_{k=1}^{N} i^k j^k - \frac{1}{N^2}\left(\sum_{k=1}^{N} i^k\right)\left(\sum_{k=1}^{N} j^k\right)$$

with N representing the number of frames and $k = 1,2,\ldots N$. An example of a PCA analysis on an isotropic and an anisotropic data set is shown in **Figure 7**.

PROTOCOL

107| Transform the *x* and *y* data (defined by the black axes in **Fig. 7a–c**) into the new coordinate system, defined by the principal axes *PA1* (red lines) and *PA2* (green lines), using the minimum and maximum eigenvalues of the eigenvectors from the covariance matrix. In this way, the data are now represented by the axes defining the largest and smallest spread in the data set.

108| Calculate the s.d. of the two transformed data sets along the principal axes std^2_{PA1}, std^2_{PA2}. If the data are not expressed in terms of *PA1* and *PA2*, the spread in an asymmetric data set would be underestimated (compare the black lines in **Fig. 7c** with the red and green lines in **Fig. 7d**).

109| The method of systematically deciding which data sets are qualified and which should be rejected without bias are based on two selection criteria suggested in literature[44–46]. These criteria relate to the size of the r.m.s.d. and the symmetry of the positions visited by the bead and are described in Steps 109–111. The r.m.s.d. gives information of the mean bead displacement and thereby the conformational state of the DNA. The more compacted the molecule, e.g., as a result of supercoiling or protein-mediated looping, the shorter the r.m.s.d. (see ANTICIPATED RESULTS section). The r.m.s.d. value can be found by taking the square root of the added squared s.d. values $\sqrt{std^2_{PA1} + std^2_{PA2}}$. Use this quantity to evaluate whether the bead is correctly tethered and to exclude, e.g., surface-stuck beads that have a low r.m.s.d., ~50 nm or less (**Fig. 8**). We set 60 nm as the lower limit of the r.m.s.d. that could be expected to originate from correctly formed plasmid tethers.

110| From the minimum and maximum eigenvalues, s_1 and s_2 of the covariance matrix, *C*, calculate how symmetric the data set is via the 'symmetry', *s*, defined as the ratio between the two eigenvalues, $s = s_1/s_2$ (where $s_1 \leq s_2$).

111| Set a criterion on the symmetry calculated in Step 110 to assess whether the bead is correctly tethered by a single DNA tether. As the calculations of the covariance matrix gives two values of unit length, the criterion ranges from 0 to 1. As we experience that the data sets originating from the plasmid tethers normally have a high symmetry, we set the symmetry criterion to $s > 0.8$ (compared with 0.5 in Tolic-Norrelykke[44]), thus permitting only data sets similar to **Figure 7a**,**b** in the final analysis (the length of the red and green lines are very close, symbolizing high symmetry). In contrast, a bead tethered by, e.g., multiple tethers or catenated plasmids typically performs an anisotropic motion, as shown in **Figure 7c**,**d**, and is excluded by this criterion (the lengths of the red and green lines are very different). After being subjected to the selection criteria in Steps 109–111, ~50% of the data sets remain from a sample containing a ~7.6-kbp supercoiled DNA molecule[16].

Identification of PNA-DNA coupling conditions in TPM chamber ● TIMING ~1 week (without plasmid preparation)

112| Confirm that the PNAs are binding at their specific targets by TPM analysis. Here we describe the method used in Norregaard *et al.*[16]. Prepare two plasmids lacking either the target for the biotin-labeled PNA or the target for digoxigenin-labeled PNA. Prepare a third plasmid with both targets intact.

113| Perform TPM analysis and subject the data sets to the r.m.s.d. and symmetry criteria. Compare the r.m.s.d. of plasmids lacking a PNA target with the r.m.s.d. of plasmids with both targets intact. Plasmids that are incorrectly tethered will have a very low r.m.s.d.. Hence, if the PNAs bind correctly, only the plasmid with both targets intact should remain after the r.m.s.d. criterion is applied.

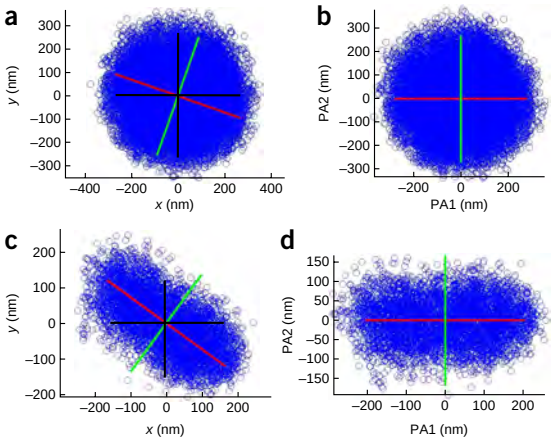

Figure 7 | Example of PCA. The data are rotated so that the maximum variance of the data is along the ordinate axis. (**a**,**b**) A scatter plot of a data set accepted for analysis with r.m.s.d. = 193 nm and $s = 0.95$. The red and green lines represent the principal axes. In **a**, the s.d. of the data set is found along the *x* and *y* (black lines) directions. In **b**, the data set has been transformed and the principal axes *PA1* (red line) and *PA2* (green line) are found. (**c**,**d**) show an example of an anisotropic data set with r.m.s.d. = 132 nm and $s = 0.47$ before (**c**) and after (**d**) the assignment of principal axes. If the s.d. values, which are compared to find *s*, are not calculated along the principal axes (red and green lines) both *s* and the r.m.s.d. of the data set would be underestimated. Because of the low symmetry ($s < 0.8$), the data set shown in **c**,**d** is discarded, and it probably originates from tethering of the bead by multiple tethers.

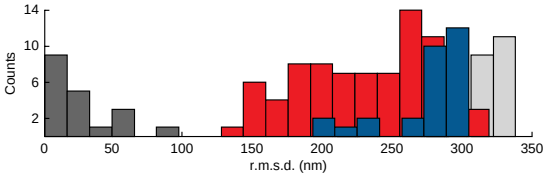

Figure 8 | r.m.s.d. of various plasmid constructs usable for troubleshooting the overall length of the tether. The red bars show the distribution of the r.m.s.d. taken over an entire experiment (not a moving time window as in **Fig. 9**) for a supercoiled plasmid. The r.m.s.d. distribution from a relaxed tether is shown by blue bars, the light gray full bars show the distribution from a linear control DNA and the dark gray bars show the r.m.s.d. from a stuck bead. The linear plasmid has the longest r.m.s.d. with a narrow distribution. The relaxed plasmid (the shortest arc of which has the length of the linear plasmid) has an r.m.s.d. that lies just below the linear plasmid. This is reasonable because it is less flexible than the linear DNA. The supercoiled plasmid has a large distribution of r.m.s.d., which originates from the different number of supercoils that are naturally present in the distribution. As expected, the stuck bead has the lowest r.m.s.d. distribution (with an average value of 36 nm).

? TROUBLESHOOTING

Troubleshooting advice can be found in **Table 1**.

TABLE 1 | Troubleshooting table.

Step	Problem	Possible reason	Solution
65	PNA invasion in relaxed plasmid DNA	PNA binding to the DNA requires opening of the DNA helix, which is less efficient in relaxed DNA compared to the supercoiled state	Identify optimal PNA concentration and/or PNA-DNA incubation time. In our study[16], we increased the concentration of the digoxigenin-labeled PNA to obtain tethers with relaxed plasmid DNA
74	Beads aggregate	Low stability of the beads either from the supplier or possibly because of low functionality of the α-casein	Prepare a new α-casein solution. If this does not help, contact the supplier of the beads to see if the stock solution has an appropriate quality. A cup horn sonicator appears to be more efficient at breaking up aggregates than normal ultrasound
92	No tether formation	Inactive PNA-DNA coupling	Produce a linear DNA molecule to identify the correct PNA-DNA coupling (Step 58). We made a linear DNA molecule with the same length (2.6 kbp) as the shorter of the two arcs in the circular DNA plasmid. If an experiment with PNA tethered circular DNA failed, we could use this linear DNA molecule as a control to examine the reagents involved in the PNA-DNA coupling. This linear DNA molecule could also be used to compare the excursions of the relaxed circular plasmid (see ANTICIPATED RESULTS)

● TIMING

Steps 1–6, preparation of digoxigenin-labeled bis-PNA: 20 h
Step 7, preparation of biotin–bis-PNAs conjugates: 20 h
Steps 8–23, growth schedule for purification of supercoiled plasmid DNA: 3 d in total (20 min on day 1, plus 20 min in the morning and 45 min at the end of day 2)
Steps 24–32, plasmid recovery: ~0.5 d
Steps 33–38, plasmid purification: ~2 h followed by overnight centrifugation
Steps 39–45, recovery of supercoiled DNA: ~2 h followed by overnight centrifugation
Steps 46–53, removal of ethidium bromide: 2–3 h followed by overnight incubation
Steps 54–55, characterization of CsCl-purified plasmids: 1 d
Steps 56–57, preparation of chloroquine gel: ~4 h of manipulation, plus overnight electrophoresis
Step 58, preparation of end-labeled linear DNA: 1 d
Steps 59–64, initial identification of PNA-DNA coupling conditions by gel electrophoresis: ~2 h on the first day, plus most of the second day
Steps 65–67, preparation of PNA and plasmid DNA coupling: 15 h
Steps 68–69, construction of perfusion chamber: 15 min
Steps 70–74, preparation of PNA-DNA tethered sample: 2.5 h
Steps 75–79, identifying noise in the experimental setup: ~2 h

Steps 80–88, imaging condition setup and pixel-to-nm calibration: ~1 h
Steps 89–93, setup of the sample and image recording preparation: ~15 min
Steps 94–99, acquiring an image of a tethered bead: ~5 min (In 2 h, ~50 time series of 60 s can be recorded when the sample search time is included.)
Steps 100–101, particle tracking of a tethered bead: ~15 min
Steps 102–111, time series analysis of a TPM data set: ~5 min
Steps 112–113, identification of PNA-DNA coupling conditions in the TPM chamber: ~1 week (without plasmid preparation)

ANTICIPATED RESULTS

This protocol for specific tethering of circular DNA to surfaces, beads or other markers via PNA handles allows the study of the dynamics of DNA. Circular DNA can either be in its natural supercoiled state or the supercoils can be enzymatically removed, thus leaving the plasmid relaxed. **Figure 9** shows typical data stemming from an experiment where a bead is attached to a naturally supercoiled plasmid DNA incorporating λ bacteriophage operator sites OL and OR (as illustrated in **Fig. 2**). The length of the projected displacement vector, $\sqrt{\langle \rho^2(t) \rangle 20\ \text{ms}}$, of the positions visited by the tethered bead and averaged over a 20-ms time window is shown as a function of time in **Figure 9a**, the corresponding histogram in **Figure 9b**. **Figure 9c** shows $\sqrt{\langle \rho^2(t) \rangle 20\ \text{ms}}$ of a similar supercoiled DNA tether but in the presence of 20 nM (~1/10 of the lysogenic concentration) of the CI. With CI present, DNA looping events are visible as abrupt decreases in $\sqrt{\langle \rho^2(t) \rangle 20\ \text{ms}}$ (for instance, from 700 s). The on and off times can be read off directly from plots such as **Figure 9c**. **Figure 9d** shows the corresponding histogram; the two peaks signifying two distinct distributions represent the looped and unlooped states, respectively. The ratio of the areas of the two distributions gives the probabilities of being in the looped versus unlooped state. In time series stemming from the plasmid alone (**Fig. 9a**), we did not observe changes of $\sqrt{\langle \rho^2(t) \rangle 20\ \text{ms}}$ that would result from a change in writhe. Hence, for a given naturally supercoiled plasmid, both the linking number and the writhe seem to remain constant.

As expected[20], it was more difficult to make the PNA handles attach to DNA if the DNA was enzymatically relaxed. To troubleshoot this problem and to obtain an idea of which r.m.s.d. distribution to expect from the enzymatically relaxed DNA plasmid, we constructed a linear DNA with exactly the same sequence as the arc of the plasmid containing the PNA attachment sites and the λ immunity region (purple part of **Fig. 3a**). The r.m.s.d. distributions from the supercoiled plasmid, the relaxed plasmid and the control linear DNA are shown in **Figure 8**. The linear DNA (light gray bars) has a very narrow distribution of r.m.s.d. The length of the linear control DNA was 2.6 kbp; hence, we know that a r.m.s.d. of ~340 nm corresponds to a tether length of ~870 nm (assuming that each bp is 1/3 nm). The natural distribution of writhe number in the supercoiled plasmids gives rise to a rather large spread of the r.m.s.d. (red bars in **Fig. 8**). This distribution has an r.m.s.d. from 150 nm up to 340 nm, and thus it signifies a large variety of overall tether length among the supercoiled plasmids. The relaxed plasmid gives rise to a narrower r.m.s.d. distribution (blue bars), which is centered at the upper end of the r.m.s.d. distribution from the supercoiled plasmid. This is reasonable because the relaxed plasmid should behave similarly to the fraction of supercoiled DNA with the lowest writhe number. In addition, the center of the r.m.s.d. distribution from the relaxed plasmid lies close to but slightly below the r.m.s.d. distribution from the linear tether. As an arc of the relaxed plasmid is only ~17 times the persistence length of dsDNA and hence not totally flexible, it is expected that the r.m.s.d. distribution of the relaxed plasmid is slightly lower than that of the linear tether. In addition, for a comparison, we show (dark gray bars on **Fig. 8**) the r.m.s.d. distribution for a stuck bead. These types of analyses are recommended if there is doubt about the correctness of the r.m.s.d. values obtained.

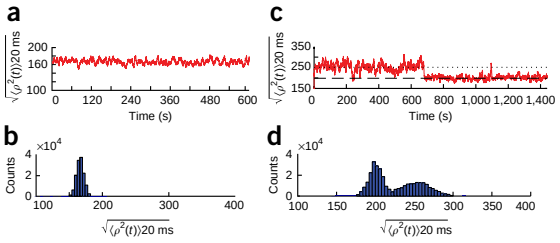

Figure 9 | Typical data resulting from TPM experiments with a supercoiled DNA plasmid. (**a**,**b**) The lateral displacement of a bead tethered to a supercoiled plasmid averaged over a time window of 20 ms as a function of time (**a**) and the corresponding histogram (**b**). (**c**) The lateral displacement of a bead tethered to a supercoiled plasmid, similar to that shown in **a** but in the presence of 20 nM CI, which occasionally clamps the DNA present in the sample (**c**); the corresponding histogram (**d**).

Note: Any Supplementary Information and Source Data files are available in the online version of the paper.

ACKNOWLEDGMENTS The CI protein was a generous gift from D. Lewis and S. Adhya, Laboratory of Molecular Biology, Center for Cancer Research, National Cancer Institute, US National Institutes of Health. We acknowledge financial support from a University of Copenhagen center of excellence and from the Swedish Research Council.

AUTHOR CONTRIBUTIONS P.E.N., S.B. and L.B.O. designed the study; K.N., M.A. and S.B. performed the experiments; P.E.N. and S.B. contributed new reagents; K.N., M.A., S.B. and L.B.O. analyzed data; all authors wrote the paper.

COMPETING FINANCIAL INTERESTS The authors declare no competing financial interests.

1. Bustamante, C., Bryant, Z. & Smith, S.B. Ten years of tension: single-molecule DNA mechanics. *Nature* **421**, 423–427 (2003).
2. Lee, W.M., Reece, P.J., Marchington, R.F., Metzger, N.K. & Dholakia, K. Construction and calibration of an optical trap on a fluorescence optical microscope. *Nat. Protoc.* **2**, 3226–3238 (2007).
3. Strick, T., Allemand, J.F., Croquette, V. & Bensimon, D. Twisting and stretching single DNA molecules. *Prog. Biophys. Mol. Biol.* **74**, 115–140 (2000).
4. Wang, M.D., Yin, H., Landick, R., Gelles, J. & Block, S.M. Stretching DNA with optical tweezers. *Biophys. J.* **72**, 1335–1346 (1997).
5. Gross, P. *et al.* Quantifying how DNA stretches, melts and changes twist under tension. *Nat. Phys.* **7**, 731–736 (2011).
6. Stratmann, S.A. & van Oijen, A.M. DNA replication at the single-molecule level. *Chem. Soc. Rev.* **43**, 1201–1220 (2014).
7. Dulin, D., Lipfert, J., Moolman, M.C. & Dekker, N.H. Studying genomic processes at the single-molecule level: introducing the tools and applications. *Nat. Rev. Genet.* **14**, 9–22 (2013).
8. Herbert, K.M., Greenleaf, W.J. & Block, S.M. Single-molecule studies of RNA polymerase: motoring along. *Annu. Rev. Biochem.* **77**, 149–176 (2008).
9. Chaurasiya, K.R., Geertsema, H., Cristofari, G., Darlix, J.L. & Williams, M.C. A single zinc finger optimizes the DNA interactions of the nucleocapsid protein of the yeast retrotransposon Ty3. *Nucleic Acids Res.* **40**, 751–760 (2012).
10. Paramanathan, T., Vladescu, I., McCauley, M.J., Rouzina, I. & Williams, M.C. Force spectroscopy reveals the DNA structural dynamics that govern the slow binding of actinomycin D. *Nucleic Acids Res.* **40**, 4925–4932 (2012).
11. Forget, A.L., Dombrowski, C.C., Amitani, I. & Kowalczykowski, S.C. Exploring protein-DNA interactions in 3D using *in situ* construction, manipulation and visualization of individual DNA dumbbells with optical traps, microfluidics and fluorescence microscopy. *Nat. Protoc.* **8**, 525–538 (2013).
12. Zurla, C. *et al.* Direct demonstration and quantification of long-range DNA looping by the λ bacteriophage repressor. *Nucleic Acids Res.* **37**, 2789–2795 (2009).
13. Manzo, C., Zurla, C., Dunlap, D.D. & Finzi, L. The effect of nonspecific binding of λ repressor on DNA looping dynamics. *Biophys. J.* **103**, 1753–1761 (2012).
14. Priest, D.G. *et al.* Quantitation of the DNA tethering effect in long-range DNA looping *in vivo* and *in vitro* using the Lac and λ repressors. *Proc. Natl. Acad. Sci. USA* **111**, 349–354 (2014).
15. Normanno, D., Vanzi, F. & Pavone, F.S. Single-molecule manipulation reveals supercoiling-dependent modulation of lac repressor-mediated DNA looping. *Nucleic Acids Res.* **36**, 2505–2513 (2008).
16. Norregaard, K. *et al.* DNA supercoiling enhances cooperativity and efficiency of an epigenetic switch. *Proc. Natl. Acad. Sci. USA* **110**, 17386–17391 (2013).
17. Jian, H.M., Schlick, T. & Vologodskii, A. Internal motion of supercoiled DNA: Brownian dynamics simulations of site juxtaposition. *J. Mol. Biol.* **284**, 287–296 (1998).
18. Bauer, M. & Metzler, R. *In vivo* facilitated diffusion model. *PLoS ONE* **8**, e53956 (2013).
19. Bentin, T. & Nielsen, P.E. *In vitro* transcription of a torsionally constrained template. *Nucleic Acids Res.* **30**, 803–809 (2002).
20. Bentin, T. & Nielsen, P.E. Enhanced peptide nucleic acid binding to supercoiled DNA: possible implications for DNA 'breathing' dynamics. *Biochemistry* **35**, 8863–8869 (1996).
21. Norregaard, K. *et al.* Effect of supercoiling on the λ switch. *Bacteriophage* **4**, e27517 (2014).
22. Lia, G. *et al.* The antiparallel loops in gal DNA. *Nucleic Acids Res.* **36**, 4204–4210 (2008).
23. Lia, G. *et al.* Supercoiling and denaturation in Gal repressor/heat unstable nucleoid protein (HU)-mediated DNA looping. *Proc. Natl. Acad. Sci. USA* **100**, 11373–11377 (2003).
24. Strick, T.R., Croquette, V. & Bensimon, D. Single-molecule analysis of DNA uncoiling by a type II topoisomerase. *Nature* **404**, 901–904 (2000).
25. Lindner, M., Nir, G., Vivante, A., Young, I.T. & Garini, Y. Dynamic analysis of a diffusing particle in a trapping potential. *Phy. Rev. E Stat. Nonlin. Soft Matter Phys.* **87**, 022716 (2013).
26. Mearini, G., Nielsen, P.E. & Fackelmayer, F.O. Localization and dynamics of small circular DNA in live mammalian nuclei. *Nucleic Acids Res.* **32**, 2642–2651 (2004).
27. Norregaard, K., Jauffred, L., Berg-Sørensen, K. & Oddershede, L.B. Optical manipulation of single molecules in the living cell. *Phys. Chem. Chem. Phys.* **16**, 12614–12624 (2014).
28. Nelson, P.C. *et al.* Tethered particle motion as a diagnostic of DNA tether length. *J. Phys. Chem. B* **110**, 17260–17267 (2006).
29. Baek, K., Svenningsen, S., Eisen, H., Sneppen, K. & Brown, S. Single-cell analysis of λ immunity regulation. *J. Mol. Biol.* **334**, 363–372 (2003).
30. Egholm, M. *et al.* Efficient pH-independent sequence-specific DNA binding by pseudoisocytosine-containing bis-PNA. *Nucleic Acids Res.* **23**, 217–222 (1995).
31. Nielsen, P.E. Sequence-selective targeting of duplex DNA by peptide nucleic acids. *Curr. Opin. Mol. Ther.* **12**, 184–191 (2010).
32. Griffith, M.C. *et al.* Single and bis peptide nucleic acids as triplexing agents: binding and stoichiometry. *J. Am. Chem. Soc.* **117**, 831–832 (1995).
33. Yin, H., Landick, R. & Gelles, J. Tethered particle motion method for studying transcript elongation by a single RNA-polymerase molecule. *Biophys. J.* **67**, 2468–2478 (1994).
34. Pardee, A.B., Jacob, F. & Monod, J. Genetic control and cytoplasmic expression of inducibility in the synthesis of β-galactosidase by *E. coli*. *J. Mol. Biol.* **1**, 165–178 (1959).
35. Miller, J.H. *Experiments in Molecular Genetics* (Cold Spring Harbor Laboratory, 1972).
36. Norgard, M.V., Emigholz, K. & Monahan, J.J. Increased amplification of Pbr322 plasmid deoxyribonucleic-acid in *Escherichia coli* K-12 strain-Rr1 and Strain-Chi-1776 grown in the presence of high-concentrations of nucleoside. *J. Bacteriol.* **138**, 270–272 (1979).
37. Cheezum, M.K., Walker, W.F. & Guilford, W.H. Quantitative comparison of algorithms for tracking single fluorescent particles. *Biophys. J.* **81**, 2378–2388 (2001).
38. Birnboim, H.C. & Doly, J. A rapid alkaline extraction procedure for screening recombinant plasmid DNA. *Nucleic Acids Res.* **7**, 1513–1523 (1979).
39. Radloff, R., Bauer, W. & Vinograd, J. A dye-buoyant-density method for the detection and isolation of closed circular duplex DNA: the closed circular DNA in HeLa cells. *Proc. Natl. Acad. Sci. USA* **57**, 1514–1521 (1967).
40. Esposito, F. & Sinden, R.R. Supercoiling in prokaryotic and eukaryotic DNA: changes in response to topological perturbation of plasmids in *E. coli* and SV40 *in vitro*, in nuclei and in CV-1 cells. *Nucleic Acids Res.* **15**, 5105–5124 (1987).
41. Hansen, G.I., Bentin, T., Larsen, H.J. & Nielsen, P.E. Structural isomers of bis-PNA bound to a target in duplex DNA. *J. Mol. Biol.* **307**, 67–74 (2001).
42. Andersson, M., Czerwinski, F. & Oddershede, L.B. Optimizing active and passive calibration of optical tweezers. *J. Opt.* **13**, 044020 (2011).
43. Czaerwinski, F., Richardson, A.C. & Oddershede, L.B. Quantifying noise in optical tweezers by Allan variance. *Opt. Express* **17**, 13255–13269 (2009).
44. Tolic-Norrelykke, S.F., Rasmussen, M.B., Pavone, F.S., Berg-Sorensen, K. & Oddershede, L.B. Stepwise bending of DNA by a single TATA-box binding protein. *Biophys. J.* **90**, 3694–3703 (2006).
45. Blumberg, S., Gajraj, A., Pennington, M.W. & Meiners, J.C. Three-dimensional characterization of tethered microspheres by total internal reflection fluorescence microscopy. *Biophys. J.* **89**, 1272–1281 (2005).
46. Han, L. *et al.* Concentration and length dependence of DNA looping in transcriptional regulation. *PLoS ONE* **4**, e5621 (2009).

IEEE JOURNAL OF SELECTED TOPICS IN QUANTUM ELECTRONICS, VOL. 20, NO. 3, MAY/JUNE 2014 4800112

Optical Trapping of Nanoparticles and Quantum Dots

Poul M. Bendix, Liselotte Jauffred, Kamilla Norregaard, and Lene B. Oddershede

(Invited Paper)

***Abstract*—Optical manipulation of nanostructures offers new exciting possibilities for building new nano-architectures and for exploring the fundamental interactions between light and nanoparticles. The optical properties of nanostructures differ substantially from those of similar bulk material and exhibit an exquisite sensitivity on nanoparticle shape and composition. The plethora of particles available today expands the possibilities of optical manipulation to include control over particle temperature, luminescence, orientation, and even over the rotational optical momentum transferred to the nanoparticle. Here, we summarize recent experimental advances within optical manipulation of individual nanoparticles and quantum dots with a focus on resonant versus non-resonant trapping, optically induced heating, spherical aberration, and orientation control. Also, we present novel quantitative data on the photonic interaction between gold nanoshells and a focused laser beam. Lastly, promising applications of the biophotonical properties of nanoparticles within nanoscience and biophysics are pointed out.**

***Index Terms*—Optical trapping, dielectric nanoparticles, gold nanoparticles, gold nanorods, gold nanoshells, liposomes, plasmonic tweezers, plasmonic heating, quantum dots, spherical aberration, nanosensor, patterning, DNA hybridization.**

I. Introduction

OPTICAL trapping of nanoparticles is a field that is currently being intensely driven by the desire to achieve precise translation and rotational control over nanostructures. An optically mediated contactless control over nanoparticles offers a unique way to do this and to investigate the physics of single or multiple particles in presence of light without any interfering substrate. This, as well as the recent progress within nanostructure architecture and design, has prompted a significant amount of exploration of how individual nanoparticles, or a collection of particles, interact with resonant or off-resonant light [1]–[5].

Optical confinement of Rayleigh particles, whose linear dimensions are significantly smaller than the trapping wavelength, has been challenging because the trapping force scales with the polarizability of the particle. Therefore, effort has been put into testing nanoparticle materials that have enhanced polarizability [6], [7] and to modify the shape of the trapping beam to optimize the trapping potential [8]–[10]. A high polarizability of nanomaterials is also associated with high absorption and consequently the irradiated nanoparticle will emit heat to its surroundings [2], [11]–[14]. Although heating is often undesired, irradiation of nanoparticles does offer a unique way to control temperature at the nanoscale with extremely high temperature gradients, an effect which is anticipated to have great potential in photothermal therapies of, e.g., malignant tissue [15]–[17]. Heating generated from irradiation of plasmonic nanoparticles can also be used, e.g., to tune DNA hybridization between nanoparticles containing complementary single stranded DNA [18]. Novel types of nanostructures, like nanorods or nanoshells, can be readily synthesized with plasmonic resonances that can be tuned by changing the particle's aspect ratio (length divided by width) [15] or core-shell ratio [19], respectively. The exact location of the particle's resonance critically influences its interaction with a trapping laser beam [12], [20].

Dielectric and biological nanoparticles are typically less absorptive in particular at near infrared (NIR) wavelengths and consequently higher powers can be used for trapping without extensive heating of the particle [21]–[25]. Manipulation of nanosized biological constructs such as lipid vesicles [25] offers great potential for probing membrane protein mediated interactions with proteins embedded in their natural environment as is highly relevant, for instance, in the context of SNARE (Soluble NSF Attachment protein Receptor) mediated membrane fusion [26], [27].

Here, we focus on precise optical control and quantitative measurements of individual spherical and rod like nanoparticles made of various materials including metals, semiconductors, and composites. Hence, we mainly focus on optical manipulation by a single tightly focused Gaussian laser beam, but also touch on the exciting progress in development of new optical configurations allowing multiple trapping [28], beam shaping [10], [29], [30] and of plasmonic trapping of nanoparticles [31]–[33].

II. Optical Interactions

A. Relevant Optical Forces

As the wavelength of visible and NIR light is significantly longer than the typical linear dimension of nanoscopic particles the mechanism of trapping can be most conveniently explained by considering the nanoparticle as an induced point dipole moving in an inhomogeneous electromagnetic field. Such a dipole is affected by a force, $\boldsymbol{F}$ (the gradient force):

$$\boldsymbol{F} = \frac{1}{2}|\alpha|\nabla\left\langle \boldsymbol{E}^2 \right\rangle \tag{1}$$

Manuscript received August 1, 2013; revised October 7, 2013; accepted October 15, 2013. This work was supported by Villum Kann Rasmussen Foundation, The Copenhagen University Excellence Program and the Carlsberg Foundation.

The authors are with the Niels Bohr Institute, University of Copenhagen, 2100 Copenhagen, Denmark (e-mail: bendix@nbi.dk; jauffred@nbi.dk; kamilla@nbi.dk; oddershede@nbi.dk).

Color versions of one or more of the figures in this paper are available online at http://ieeexplore.ieee.org.

Digital Object Identifier 10.1109/JSTQE.2013.2287094

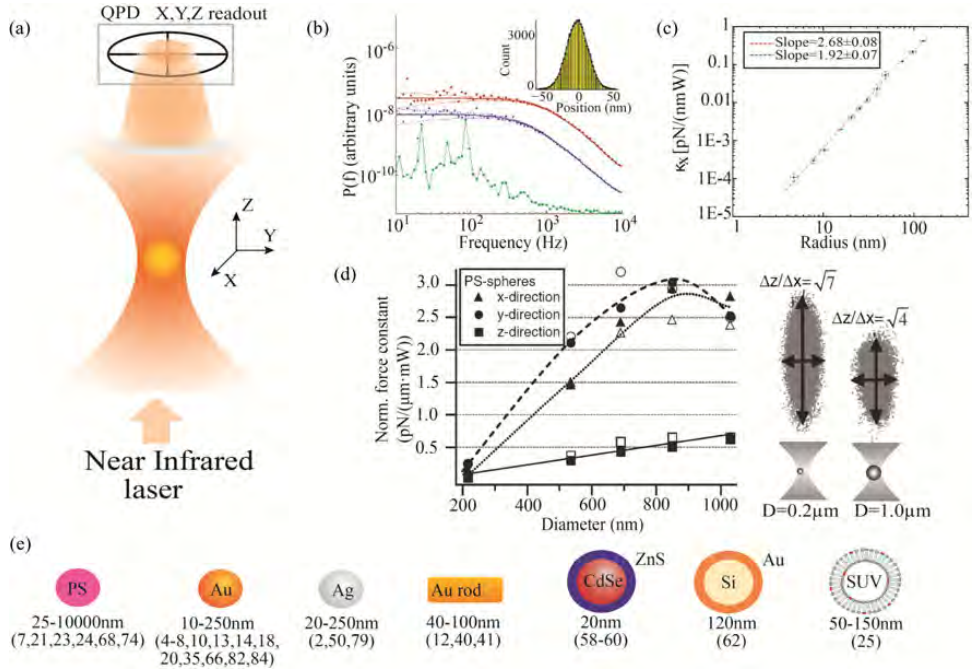

Fig. 1. Optical trapping of nanospheres and quantification of their interaction with the field. (a) Schematic of a single beam optical trap where a NIR laser is focused to a diffraction limited spot. Optical gradient forces attract the nanoparticle to the center of the laser focus. The particle's positions are recorded with nanometer spatial resolution and ∼100 kHz time resolution by using a quadrant photodiode (QPD) to detect the forward scattered light. (b) Power spectra of the time series for two trapped gold nanoparticles with $d = 30$ nm (blue triangles) and $d = 196$ nm (red circles), respectively. The green squares represent the noise from an empty trap. The inset shows the position histogram of the $d = 196$ nm gold nanoparticle, it has a Gaussian shape because the particle moves in a harmonic potential, reproduced with permission from [6]. (c) Spring constants characterizing the lateral strength of the optical trap while trapping gold nanoparticles of various sizes, reproduced with permission from [8]. (d) Spring constants, and their asymmetry for the translational directions, measured for optical trapping of polystyrene nanoparticles, reproduced with permission from [21]. (e) Overview of different types of nanoparticles individually optically trapped in 3-D together with the corresponding references.

where α is the polarizability of the particle, $\boldsymbol{E}$ is the electromagnetic field, and the brackets denote time averaging. $|\boldsymbol{E}^2|$ is proportional to the field intensity and $\boldsymbol{F}$ points along the gradient of the light intensity (toward increasing intensity). Therefore, in a laser beam tightly focused in three dimensions [as sketched in Fig. 1(a)], a point dipole will be attracted toward the focal spot.

Another important optical force, $\boldsymbol{F}_{\mathrm{rad}}$, arises from the radiation pressure on the particle when photons become scattered or absorbed at the incident particle surface [34]:

$$\boldsymbol{F}_{\mathrm{rad}} = \frac{n\langle \boldsymbol{P} \rangle}{c} C_{\mathrm{ext}} \tag{2}$$

where $\langle \boldsymbol{P} \rangle$ is the time average of the Poynting vector, n is the index of refraction of the surrounding liquid, and c is the speed of the light. C_{ext} is the extinction cross section which is a sum of the absorption and scattering cross sections:

$$C_{\mathrm{ext}} = C_{\mathrm{scat}} + C_{\mathrm{abs}} = k^4 |\alpha|^2 / 4\pi + k\alpha'' \tag{3}$$

where k is the wave number, $k = 2\pi n/\lambda$ and α'' denotes the imaginary part of the polarizability. The direction of the resulting radiation pressure points along the axis of the beam and hence acts to destabilize the trap in the axial direction. However, by tightly focusing the light in the axial direction, $\boldsymbol{F}$ can overcome $\boldsymbol{F}_{\mathrm{rad}}$ and stable trapping of nanoparticles can be achieved in three dimensions [6]–[8], [21], [23], [35].

A critical factor for optical trapping is the particle material which has great influence on the trapping stability through the polarizability α [see equations (1) and (2)]. $\boldsymbol{F}$ and $\boldsymbol{F}_{\mathrm{rad}}$ scale linearly and quadratically, respectively, with the polarizability which in turn scales with the polarizable volume, V, of the nanoparticle:

$$\alpha = 3V \frac{\varepsilon_p - \varepsilon_m}{\varepsilon_p + 2\varepsilon_m}. \tag{4}$$

Here, ε_m refers to the dielectric permittivity of the medium and ε_p to that of the particle at the appropriate wavelength [36]. The simple relation in equation (4) is only valid for very small nanoparticles that behave as true dipoles ($d \ll \lambda$). If the particles are coated, the coating will also affect the total polarizability of the particle. The effect of a coating layer was quantified in [37] where they extended equation (4) in order to include a coating layer having a different dielectric constant than the core.

The quadratic scaling of $\boldsymbol{F}_{\mathrm{rad}}$ with α means that the trap becomes destabilized for larger reflective (metallic) particles. The absorption cross section scales with particle volume and absorption leads to heating. This causes dramatic heating of irradiated

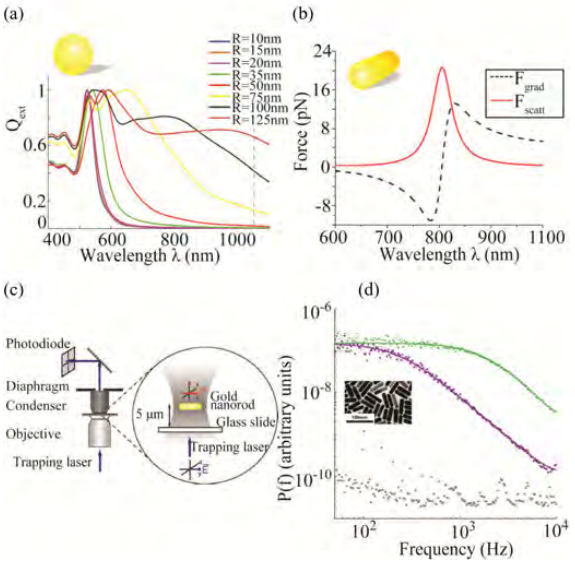

Fig. 2. Resonant versus non-resonant trapping of gold nano-spheres and -rods. (a) Extinction cross section of gold nano-spheres with radii ranging from 10 nm to 125 nm calculated using Mie's equations, the vertical dashed line denotes 1064 nm, the wavelength with which the experiments depicted in Fig. 1 were carried out. (b) Calculated optical forces on a nanorod (15 nm × 60 nm) for wavelengths near the plasmon resonance, reproduced with permission from [45]. (c) Optically trapped single gold nanorods which align with the laser polarization, reproduced with permission from [40]. (d) Power spectra of time series from two trapped nanorods, green: 85.1 ± 7.3 nm × 44.1 ± 6.5 nm, purple: 41.2 ± 8.3 nm x 8.3 ± 1 nm. Lorentzian fits are shown as full lines and black circles represent data from an empty trap. Reproduced with permission from [40].

metallic particles with non-vanishing imaginary polarizability, α'', more details on this are given in Section V.

B. Resonant Versus Non-Resonant Trapping

The particle polarizability, α, in equations (3) and (4) is wavelength dependent and can exhibit a resonance in the optical or NIR spectrum. Therefore, the gradient force, the radiation force, and the particle absorption change dramatically across such a resonance. The gradient force can even become repulsive due to a negative polarizability when the laser wavelength is shorter than the resonant wavelength [10], [20]. Nanoparticles often have a distinct peak in the polarizability spectrum (as shown in Fig. 2(a) where $C_{\rm ext}$ from equation (3) is plotted as function of λ). In the following, trapping at resonance will refer to trapping using a wavelength overlapping with the peak polarizability, whereas off-resonant trapping refers to trapping using a wavelength which is several hundred nanometers away from the peak. For a more elaborate description of the effect of resonance on trapping please see [38].

Plasmonic resonances in metallic particles are due to resonant field induced oscillations of the conduction electrons. At resonance, absorption and scattering are strongly enhanced [39]. Metallic gold nanoparticles have resonances in the middle of the visible spectrum, as plotted in Fig. 2(a). These resonances red shift and broaden with increasing particle size. Gold nanorods can be designed to be resonant with nearly any visible or NIR wavelength by appropriately choosing the aspect ratio [15]. As shown in Fig. 2(b) the forces on a nanorod depend strongly on the proximity of the trapping wavelength to the resonance, in this case the resonance is located just above 800 nm. Gold nanorods can be individually optically trapped by NIR lasers and align with the polarization of the laser [40]–[42], as sketched in Fig 2(c). Tunable resonances are also obtained with composite nanoparticles like gold nanoshells by appropriately choosing the thickness of the gold layer decorating the silica core [19], [43].

III. Quantification of Interactions Between Particle and Optical Trap

A. Dynamics of a Trapped Nanoparticle

An optical trap based on a laser with a Gaussian intensity profile exerts a harmonic force on the trapped object. Hence, the trapping potential has the following form:

$$U = \frac{1}{2}\boldsymbol{\kappa}_x (x - x_{\rm o})^2 \tag{5}$$

where κ_x is the spring constant characterizing the trapping potential along the x-direction (coordinate system as in Fig. 1) and x_0 is the equilibrium position. The corresponding harmonic force on the particle is simply $F_{\rm trap} = -\kappa_x (x - x_o)$. Optically trapped nanoparticles typically undergo significant thermal diffusion within the trapping volume. The characteristic escape time from the trapping potential, $\tau_{\rm esc}$, is given by $\tau_{\rm esc} = \tau_o \exp(U/k_B T)$ [44], where $k_B T$ is the thermal energy and $1/\tau_o$ is the attempt frequency. Therefore, a potential depth of a few times the thermal energy is sufficient for stable trapping of a nanoparticle. Expressions similar to equation (5) apply also in the two other translational directions, however, with different spring constants, κ_y and κ_z. Typically, κ_z is significantly weaker than κ_x and κ_y because it is more difficult to tightly focus the light in the axial direction, resulting in a less steep axial intensity gradient.

The resulting force acting on a nanoparticle in an optical trap is not easily calculated. Therefore, it is common procedure to calibrate the trapping potential in order to quantify the spring constants κ_x, κ_y, and κ_z which then characterize the 3-D trapping potential and can be used for force determination. For a nanoscopic particle which cannot easily be visualized while trapped, calibration is most conveniently and precisely done by passively measuring the Brownian fluctuations of the particle in the trap, see Section III-B.

The distribution of positions visited by a particle exploring a potential U in one dimension, x, is given by Boltzmann's distribution:

$$P(x) = P_o e^{\left(-\frac{U(x)}{k_B T}\right)} \tag{6}$$

where P_o is a normalization constant (the inverse partition function). For a harmonic potential, the standard deviation, σ_x, of this distribution is given by the Equipartition Theorem:

$$\sigma_x = \sqrt{\frac{k_B T}{\kappa_x}}. \tag{7}$$

A measurement of the standard deviation of the particle positions therefore provides κ_x. The expressions in (6) and (7) apply to all translational directions with distinct κ_x, κ_y, and κ_z.

A more popular and robust method (less prone to drift) to determine κ_x, κ_y, and κ_z is to consider the power spectral density of the particle's fluctuations in the trap [46]. The motion of the particle is well described by the Langevin equation, the power spectrum of which yields a Lorentzian function:

$$P(f) = \frac{k_B T}{\gamma} \frac{1}{f^2 + f_c^2}. \tag{8}$$

Here, $f_c = \kappa/2\pi\gamma$ is denoted the corner frequency and is the ratio of the spring constant κ (κ_x, κ_y, or κ_z) and the Stokes drag $\gamma = 6\pi\eta r$. η is the viscosity of the media and r the radius of the particle. Examples of powerspectra recorded with gold nanospheres are shown in Fig. 1(b) [6] and with gold nanorods in Fig. 2(d). From the powerspectrum f_c and consequently κ can be determined, thus fully characterizing the interaction between the nanoparticle and the optical trap. Examples of how κ varies with particle size and material are shown in Figs. 1(c), 1(d), 4(c), and 5(b).

B. Particle Position Detection

As a nano-scopic particle is relatively difficult to visualize and since this visualization becomes even more challenging because of its rapid thermal fluctuations within the trapping volume, the nanoparticle's positions are most conveniently and precisely measured by means of a photodiode. A quadrant photodiode (QPD) can detect the interferometric pattern of the forward scattered laser light, and from this the particle's position can be determined. This approach offers great time resolution (microsecond) as well as nanometer spatial accuracy [47]. Determination of the lateral positions relies on a linear relation between the particle position in the trap and the difference in light intensity incident on four quadrants. The axial position scales linearly with the total intensity incident on all four quadrants, thus allowing for 3-D calibration [47]. Photodiodes are typically fabricated to have optimal performance in the visible spectrum and severe filtering of high frequencies typically takes place while using NIR light [48]. This effect, as well as aliasing, needs to be taken into account in order to perform an accurate calibration [49].

While there exist other ways to detect nanoparticles than QDP detection (see Section VII) it is essential, for accurate calibration, that the particle positions are captured within a short time interval (<1 ms) to minimize position averaging effects. This is particularly important for nanoparticles that diffuse faster than microscopic particles.

IV. Optical Trapping of Nanoparticles

A. Dielectric Particles

Conventional materials used in optical trapping include silica and polystyrene. These materials have indexes of refraction higher than that of water at NIR wavelengths which is a necessary condition for achieving stable optical trapping in water.

Experimental and theoretical quantification of the trapping potentials of polystyrene particles was rigorously performed by Rohrbach [21], see Fig. 1(d). The spring constants increase approximately linearly with particle size for all translational directions up to a particle size of approximately 1 μm at which the particle size starts to exceed the size of the focal spot. At this point the assumption behind equation (1) (that $\lambda >> r$) clearly breaks down and $\boldsymbol{F}$ has to be cast as an integral over the particle volume. Using this approach, very good agreement was found between experimental and calculated values of κ for polystyrene particles [21]. Theoretical calculations of trapping forces have also been carried out for other dielectric constants and particle sizes both in presence and absence of spherical aberration [22], [23], [47], which is treated in more detail in Section VI.

B. Metallic Nanoparticles

Gold nanoparticles have significantly higher polarizability, even when trapped off-resonance, and offer improved trapping stability compared to polystyrene nanoparticles. A direct comparison between polystyrene and gold trapping was performed by Svoboda *et al*. [7] where the maximum force applied to $D = 36.2$ nm gold nanoparticles was found to be $\sim$7 times higher than the maximum force that could be applied to equivalent polystyrene particles. This ratio was found to correlate well with the ratio between the polarizability of the gold and polystyrene nanoparticles thus confirming the importance of a high polarizability in efficient trapping.

Optical trapping of gold and other metallic nanoparticles has now been reported by several groups and focus has been on both quantification of trapping potentials and on characterizing the scaling of the trapping strength with particle size [6], [8], [10], [50]. One obstacle for achieving stable optical trapping of nanoparticles is the spherical aberration inherently present in essentially all focused laser spots, even when using a water immersion objective [51]. Different techniques have been developed to minimize spherical aberration, for instance by correcting the wavefront using an spatial light modulator (SLM) [52] or simply by using special immersion oils for the objective that minimize spherical aberration [9]. This increases the efficiency of the optical trap [see Fig. 7(c)] and is particularly useful for trapping deeper inside the imaging chamber [9]. Employing this technique, gold nanoparticles as small as 9 nm in diameter could be trapped [the results are shown in Fig. 1(c)] [8].

Metallic nanorods are now being intensively explored in optics due to their tunable resonance across the entire optical and NIR spectrum, see Fig. 2(b–d) [20], [40], and their extreme and orientation dependent heating properties [53]. The resonance peak sensitively red shifts with increasing aspect ratio and can be tuned into the NIR region for an aspect ratio of approximately 5. The transparency of biological materials in the NIR spectral window [54] makes such rods extremely interesting candidates in the context of photothermal applications [15].

Interestingly, a trapped nanorod aligns with the polarization of the trapping laser beam, see Fig. 2(c) [40], thus allowing for rotation of the particle by rotation of the laser polarization

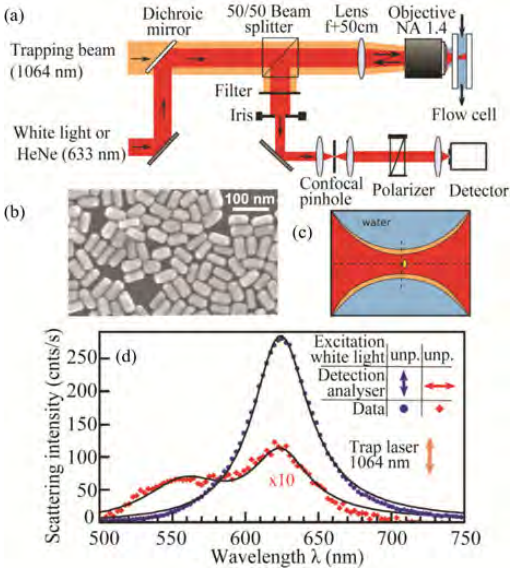

Fig. 3. Trapping and measuring the scattering from individual gold nanorods, reproduced with permission from [12]. (a)–(c) Nanorods, having dimensions 60 nm × 25 nm, align along the transverse laser polarization. (d) Collection of scattered white light polarized parallel or perpendicular to the polarization of the trapping laser. The scattered light with polarization parallel to the trapping polarization (blue circles) shows a peak corresponding to the longitudinal resonance of the rod at ∼630 nm. Scattered light with orthogonal polarization shows a peak corresponding to the transversal resonance at ∼550 nm (red diamonds).

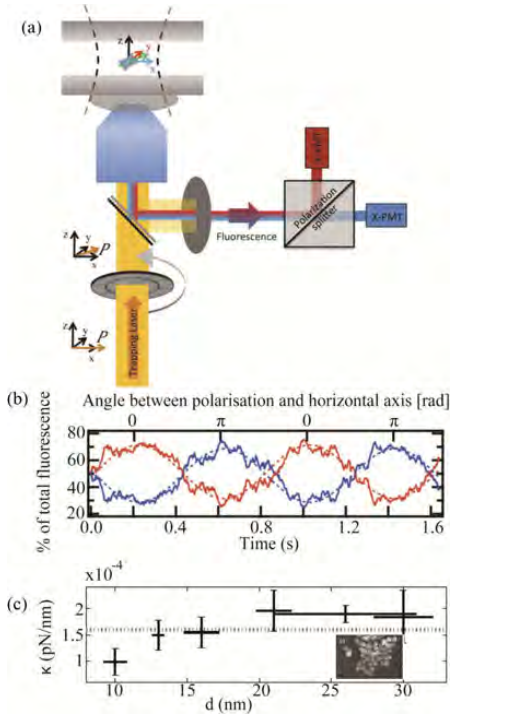

Fig. 4. Optical control of individual quantum dots. (a) Experimental setup to align and spin individual quantum rods in an optical trap. A polarization splitter is used to separate the x and y polarizations of the emitted light from the rod that is aligned with the laser polarization, reproduced with permission from [58]. (b) Polarization spectroscopy of a rod that rotates at a frequency of 50 Hz. Red and blue lines denote x and y polarization, respectively, dashed lines are sinusoidal fits to the data, reproduced with permission from [58]. (c) Quantification of the spring constants characterizing the optical trapping of individual QDs of various sizes, reproduced with permission from [59]. In all experiments trapping is done using a continuous wave (CW) NIR laser.

and for applying an optical torque on the particle [12]. Torques of magnitude around 100 pN·nm have been applied to gold nanorods by an optical trap (setup and results are shown in Fig. 3) [12], this being on the relevant scale for probing the torque of single molecule rotary motors. Related to trapping of nanorods is the optical manipulation of metallic nanowires in 3-D, where optical control of nanowires with lengths between 1 and 100 μm and aspect ratios up to 100 was accomplished [55]. By employing a different beam profile, a Fourier transformed Bessel beam generated with a spatial light modulator, nanowires could be aligned in the image plane along the laser polarization [56].

C. Quantum Dots

Semiconductor nanoparticles, also called quantum dots (QDs), are widely used in biology as photostable substitutes for fluorophores to label single proteins and cellular organelles [57]. The desire to optically control such QDs is motivated by the possibility of simultaneously imaging and performing force spectroscopy of QD conjugated molecules [58]–[60]. The wavelength of the fluorescent light emitted by a QD is inversely proportional to the size of the QD and hence a range of QD sizes exists that emit in the visible spectrum. Off-resonant trapping, using continuous wave NIR light, of a range of conventionally available individual CdSe QDs was reported by Jauffred *et al*. [59], [60]. The resulting spring constants characterizing the interaction between the EM field and the QD were found to be independent of the emission wavelength of the QD, see Fig. 4(c), and of comparable size to the spring constants characterizing metallic nanoparticle trapping.

Interestingly, the relatively weak CW trapping laser light can act as a source for two-photon excitation of the trapped QDs, thus eliminating the demand for an excitation light source for imaging of trapped QDs. This nonlinear effect is, however, only a weak perturbation to the overall trapping which is supported by the finding that the trapping stiffness scales linearly with laser power [59].

Quantum rods have elongated shapes and the polarization of the emitted light from a quantum rod depends on its orientation [experiment shown in Figs. 4(a)]. In Ref. [58] rotation of quantum rods with frequencies up to 320 Hz was achieved. Simultaneously, the rods were two-photon excited by the trapping laser beam and the linearly polarized emitted light measured. By splitting the emitted light in the vertical and horizontal components they found a clear sinusoidal relation between the polarization of the emitted light as a function of the orientation of the rod in the trap, see Fig. 4(b) [58]. These results pave the

way for a QD based system where trapping and visualization is further combined with the ability to measure and transduce torque at nano-scale. Possible further improvements through resonant trapping are theoretically described in [38].

Although a range of different materials are used for commercially available QDs, the material of choice in all reported QD trapping experiments has so far been CdSe whose optical properties were treated in [61]. It is possible that QD trapping efficiency could be improved by choosing QDs made from other semiconductor materials.

D. Hybrid Nanoparticles

Nanoparticles composed of a metallic shell and an inner dielectric core have shifted plasmonic resonances compared to spherical metallic nanoparticles of equal size [19]. The plasmon resonances of gold nanoshells encapsulating a silica core, can be readily tuned across the optical spectrum by changing the ratio between the shell thickness and the diameter of the silica core [19]. NIR resonant gold nanoshells can be designed to produce severe heating upon irradiation with NIR light in the same manner as gold nanorods. Gold nanoshells might be more promising as photothermal absorbers in therapeutic applications, compared to, e.g., gold nanorods, due to their lower cytotoxicity [46].

The possible influence of the resonance in optical trapping of gold nanoshells was recently explored by tuning the wavelength of the laser across a spectral range (from 720 to 850 nm) near the plasmon resonance of the gold nanoshells [62]. The spring constants characterizing the trapping potential were found to be nearly independent of the proximity of the trapping wavelength to the plasmon resonance of the nanoshell. However, the quantification of the exact trapping strength was complicated by heating effects which also depended on the wavelength and consequently changed the effective viscosity [62].

We quantified the trapping potential of gold nanoshells trapped off-resonance at a wavelength of $\lambda = 1064$ nm. The gold nanoshells employed had a broad resonance peak at $\sim$875 nm (see Fig. 5(b), upper left inset) making these nanoshells interesting candidates for biomedical applications due to the transparency of biological material in the NIR region [54]. By using the photodiode detection scheme sketched in Fig. 1 and explained in detail in [48] and the MATLAB procedures from [49] we quantified the trapping potential of gold nanoshells having a silica core of 118 nm and a gold layer of $\sim$15 nm [drawn in the lower right inset in Fig. 5(b)], coated with PEG 5 kD.

The harmonic shape of the position histogram, shown in the inset of Fig. 5(a), as well as the Lorentzian shape of the power spectrum [see Fig. 5(a)], shows that the gold nanoshells were trapped in a harmonic potential.

Fig. 5(b) shows the lateral spring constant as a function of laser power. As shown by the full line there is a linear relation between the spring constant and the laser power, which is a hallmark of optical tweezing and an indication that no significant heating occurs. This observation is consistent with the reportings of Jain *et al*. [63] who showed that nanoshells with dimensions similar to those used in the current study dominantly scatter light whereas only little absorption occurs.

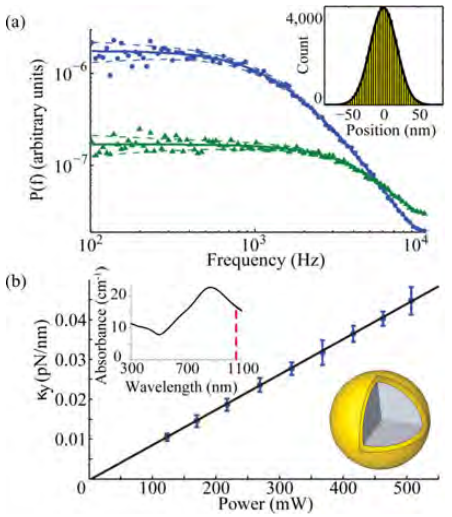

Fig. 5. Quantification of NIR trapping of gold nanoshells. (a) Power spectra of the time series for a trapped gold nanoshell with a $d = 118$ nm silica core and a 15 nm thick gold shell. The laser power at the sample was $P = 508$ mW (green triangles) or $P = 123$ mW (blue circles). Inset shows the position distribution of a gold nanoshell trapped at $P = 123$ mW, full lines denote Lorentzian fits [49]. Inset shows Gaussian position histogram. (b) Spring constant versus laser power measured for gold nanoshells ($n = 12$), the full line denotes a linear fit to data. Upper left inset shows the optical absorbance of the gold nanoshells, dashed red line denotes the 1064 nm trapping laser wavelength. Lower right inset is a drawing of the gold nanoshell.

Interestingly, an extrapolation of the curve down to 50 mW, the laser power used in [62], yields a value for the spring constant which is quite close to the nearly constant value measured in [62] ($\sim$5 pN/μm). This is despite the facts that the shells employed had a different resonance peak and that the trapping lasers had different wavelengths. This supports the finding that the trapping strength is not sensitively dependent on the particle resonance wavelength with respect to the trapping wavelength.

E. Comparing Various Nanoparticles

The optical properties of the nanoparticles reviewed in the preceding sections are summarized in Table I. This table provides the currently available information on the theoretically calculated and experimentally measured polarizabilities, on the measured spring constants, and on the maximum forces exerted. The theoretical values of the polarizability, $\alpha_{\rm calc}$, were found by using equation (4) or, for particles as CdSeZnS and gold nanoshells with a coating/shell, the modified version from [37]. For the composite QD we employed a $d = 5.3$ nm core having $\varepsilon = 6.55$ [64] and a biological coating having $\varepsilon = 2.10$, whereas in [59] the whole QD structure was assumed to be made of CdSe. Experimental values for all $\alpha_{\rm exp}$ were obtained from the reported $\kappa_{\rm exp}$ by using the procedure given in [60].

The discrepancies found between $\alpha_{\rm calc}$, and $\alpha_{\rm exp}$ could be due to several factors. One is that equation (4) is not very accurate for particles larger than $\sim$10 nm. Another source of error is that the red-shifted resonances of the larger metallic nanoparticles are not accounted for by equation (4), this

TABLE I
OPTICAL PROPERTIES FOR VARIOUS NANOSTRUCTURES

Type	α_{calc} [Å^3]	α_{exp} [Å^3]	κ_{exp} [pN/nm/W]	F_{MAX}/P	REF
PS 38nm	2.55×10^{6}	-		0.09 pN/W	[7]
AuNP 36nm	8.2×10^{7}	4.1×10^{10}	5.0×10^{-3}	0.6 pN/W	[7]
AuNP 194nm	1.3×10^{10}	2.2×10^{12}	0.3	38.0 pN/W	[8]
AuNP 254nm	2.8×10^{10}	4.1×10^{12}	0.5	68.0 pN/W	[8]
AgNP 40nm	1.1×10^{8}	7.4×10^{10}	9.0×10^{-3}	-	[50]
QD, CdSe 5/26nm	1.9×10^{6}	2.4×10^{7}	1.6×10^{-3}	-	[59, 60]
SiAuNS 118/15nm	6.3×10^{9}	-	8.0×10^{-2}	-	This work
SUV 50nm	1.2×10^{7}	8.2×10^{9}	1.0×10^{-3}	-	[25]
AuNR (60×25nm)	[a]	[a]	1.5×10^{-2}	100 pNnm [¶]	[12, 40]

All values in the table are obtained using a trapping wavelength λ=1064 nm.
[a] Experimental and calculated polarizabilites for rods can be found in Ref. [40] for a range of aspect ratios and particle volumes. [¶] The maximum torque that could be applied on a rod [12].

could increase the polarizability. Finally, the experimental values, $\alpha_{\rm exp}$, were found by the procedure outlined in [60] which assumes that the intensity distribution is perfectly Gaussian and that the particle is located at the peak of the intensity. In practice, a trapped metallic nanoparticle is most likely displaced from the center [35] and the focal intensity distribution is not perfectly Gaussian [65], these effects lead to an overestimate of $\alpha_{\rm exp}$.

V. Optically Induced Heating

In a typical optical trapping experiment the intensities reach MW/cm^2 at the focus. Potential heating caused by this intense light flux can have detrimental effects on proteins or living cells that might be near or within the laser focus. Of particular concern is the trapping of absorbing nanoparticles like metal particles having plasmon resonances near the trapping wavelength. Such particles can easily reach temperatures near the critical temperature of water and even at much lower temperature elevations radically alter the physical environment, e.g., the viscosity of water. Therefore, it is essential to quantify and take into account the laser induced heating in any application where potential absorption of light takes place.

Several assays have been designed to assess the temperature generated by laser irradiation of nanoparticles fixed to a substrate [53], [66], [67]. However, only few assays have been employed to quantify the heating of nanoparticles that are trapped in 3-D [2], [12]–[14]. One inherent problem complicating trustworthy temperature calculations is that the focal intensity distribution at the nanometer level is unknown and the exact position of the nanoparticle with respect to the focal intensity distribution is difficult to access. For this reason, direct measurements that do not involve a priori assumptions about the position of the particle and focal intensity distributions, are highly desirable.

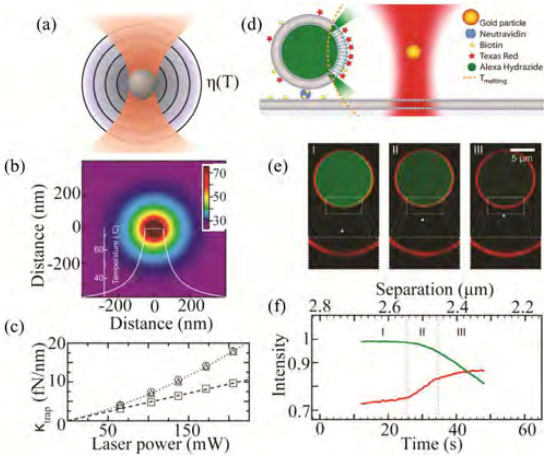

Fig. 6. Different assays to quantify heating of optically trapped nanostructures. (a) Heat radiating from a trapped nanoparticle lowers the viscosity of the nearby solution thus affecting the Brownian motion of the particle. (b) and (c) Heating from an optically trapped gold nanoparticle, $d = 100$ nm, figure reproduced with permission from [14]. A Mie calculation of the temperature profile is plotted in (b), the trapping spring constants found by power spectral analysis (triangles), Stokes drag (circles), and the Equipartition Theorem (rectangles) are plotted in (c). (d)–(f) A gel phase GUV, with melting temperature $T_m = 33\ ^\circ$C, contained a dye in the lumen. The GUV was approached by a trapped gold nanoparticle. By measuring the distance, D, for the onset of GUV leakage the particle temperature was inferred from the simple relation, $T \propto 1/D$, figure reproduced from [13] with permission. Images from the experiment are shown in (e) and time evolution of the membrane and lumen fluorophores in (f).

One of the first quantifications of the heating of optically trapped silica and polystyrene particles ($d \sim 500$ nm) was performed by measuring the changes in the Brownian fluctuations caused by a temperature dependent change of the viscosity of water, as depicted in Fig. 6(a) [68]. The resulting temperature increase during trapping of micron sized polystyrene particles in glycerol and water were found to be on the order of 10 K and 1 K, respectively, at typical trapping laser powers. The temperature increase was attributed to the absorption of NIR light primarily by the solution and not by the dielectric particle [68]. Recent experiments using quantum dot luminescence thermometry have confirmed that heating of an intracellular aqueous environment exposed to NIR wavelengths is indeed on the order of 1 K at typical trapping laser powers [69].

A similar strategy was adopted to quantify the temperature increase of a trapped 100 nm gold nanoparticle [14]. The particle temperature was found through a combination of measurements of the nanoparticle's Brownian motion and Mie calculations, as shown in Fig. 6(b) assuming knowledge of the particle's location within the intensity profile. They found temperature elevations up to $\sim$90 °C at $P = 200$ mW at the surface of the nanoparticle. A linear relation between the spring constant characterizing the optical trapping and the power used is a hallmark of optical trapping. As shown by the triangles in Fig. 6(c), a non-linear relation was found, this being attributed to decreased viscosity of the surrounding liquid caused by the temperature elevation at the surface of the irradiated particle. Correcting the viscosity with a temperature dependent factor returned the expected linear

relation [squares in Fig. 6(c)]. The heating rate for a 100 nm gold nanoparticle was found to be 266 K/W [14].

Other assays designed to measure the heating of irradiated nanoparticles have used a surrounding matrix that can undergo a phase transition at a given temperature as a heat sensor. Such heat sensors have utilized the ice to water phase transition [70] or lipid bilayers undergoing gel to fluid phase transitions [13], [66], [71]. Lipid bilayer phase melting can be visualized by several methods: 1) onset of lipid mobility [71], 2) phase dependent partitioning of certain lipophilic tracer dyes [53], [66], [72], or 3) permeabilization of the lipid bilayer to aqueous fluorophores [13].

The heating of different sizes of gold nanoparticles trapped in three dimensions was recently quantified in an assay schematically shown in Fig. 6(d). A Giant Unilamellar lipid Vesicle (GUV) with a phase transition at $T_m = 33$ °C, was immobilized on a supported lipid bilayer by streptavidin-biotin conjugation. Subsequently, a gold nanoparticle was trapped and brought closer to the GUV at constant velocity. At a certain distance, D_m, the heat radiating from the trapped gold nanoparticle caused the GUV temperature to reach T_m and the GUV became leaky, this being visible by efflux of the encapsulated fluorescent molecules, and an up-concentration of bilayer fluorophores into the fluid membrane phase, see Fig. 6(e) and (f). Since the temperature profile decays as $T(D) \sim 1/D$ away from the nanoscopic particle, knowledge of D_m and T_m renders it possible to deduce the entire temperature profile. One advantage of this method is that it contains no a priori assumptions regarding the focal intensity distribution or the location of the particle.

Surprisingly, the heating of gold nanoparticles trapped in three dimensions did not simply increase monotonically with particle size [13]. For particle diameters exceeding 100 nm the heating was found to decrease implying that the larger particles were stably trapped away from the center of the focus [see Fig. 7(b)] and hence not be exposed to the maximum focal intensity.

Heating is proportional to absorption; hence, it is not so surprising that the heating of irradiated gold nanorods was found to be dependent on rod orientation with respect to laser polarization [53]. Also, compared to their volume, gold nanorods were found to be extremely effective light to heat converters (in the right orientation). In fact, even at 20 mW the heat was sufficient to melt and reshape the rod into a more spherical shape.

While dielectric nanoparticles can be safely trapped at high powers with minimal heating, the heating of irradiated metallic particles is size, shape, and orientation dependent and can easily reach temperatures approaching the critical temperature of water ($T_c = 647$ K) at which the water phase is not stable any longer and explosive heating will occur [73].

VI. Spherical Aberration

To achieve 3-D trapping it is common to use either high NA oil immersion or water immersion objectives to achieve a tight focusing of the laser beam. Focusing of light to a diffraction limited spot of size $\lambda/2$ results in spherical aberration [74].

Additionally, the light must pass water/glass interfaces to enter the aqueous chamber containing the objects to be trapped. Refraction at a water/glass interface significantly changes the shape of the focus intensity distribution of light focused by an oil immersion objective, see Fig. 7(a) [74]. The refraction of light at the water/glass interface causes peripheral rays to converge at different depths inside the chamber relative to rays lying closer to the beam axis, thus resulting in an axially elongated focal volume. Especially for oil immersion objectives, the aberration of the optical trap increases with distance away from the glass surface and often leads to loss of trapping ability at axial depths of tens of micrometers.

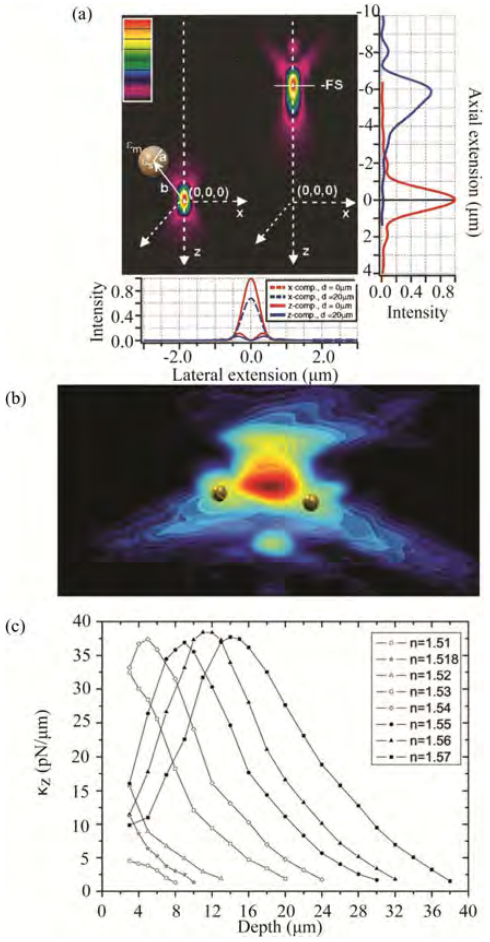

Fig. 7. Effect of spherical aberration in an optical trap. (a) Simulated focal intensity distributions obtained after focusing NIR light ($\lambda = 1064$ nm) by an oil immersion objective through a glass–water interface, reproduced with permission from [74]. (b) Experimentally measured focal intensity distributions within an optical trap focused by a water immersion objective, reproduced with permission from [35], 200 nm gold nanoparticles stably trapped before the focus. (c) Axial spring constants versus distance to the glass–water interface measured for a range of oils having different index of refraction, reproduced with permission from [9].

Since the origin of spherical aberration originates from the refractive index mismatch at the water/glass interface it is possible to compensate these effects by changing the index of refraction of the immersion oil between the glass and the objective. In reference [9] a series of immersion oils with different refractive

indexes was used to trap particles at different heights from the cover glass surface, the measured axial spring constants as function of trapping depth and immersion oil refractive index are shown in Fig. 7(c). An important conclusion is that the axial trapping constant at a depth of 5–10 μm, can be increased almost by a factor of 7 by using an oil with $n_{\mathrm{oil}} = 1.54$ instead of the conventional oil used in microscopy ($n_{\mathrm{oil}} = 1.518$).

Water immersion objectives are typically optimized for visible light and cause spherical aberration of a trapping NIR laser beam. The aberration can, however, be minimized by adjusting the correction collar of the objective [75], and one advantage of the water immersion objective is that the spherical aberration does not change with trapping depth.

Recently, Kyrsting *et al.* mapped the 3-D focal distribution of an optical trap ($\lambda = 1064$ nm) focused by a water immersion objective or oil immersion objective using different immersion oils [13]. As expected, the intensity distributions were strongly sensitive to the immersion medium used and local intensity maxima were observed off-axis and in front of the focal spot as shown in Fig. 7(b). Interestingly, this study also revealed that 200 nm gold nanoparticles stably trap at a position before the intensity maximum [as depicted in Fig. 7(b)] [13]. This is consistent with the heat profile observations [13] implying that larger trapped metallic nanoparticles needed to be displaced from the maximum intensity.

VII. Visualization of Nanoparticles

Köhler illuminated bright field microscopy is often used in conjunction with optical trapping to visualize particles. However, the low contrast makes it difficult to detect even metallic particles. Another modification of transmitted light microscopy yielding better contrast, is Differential Interference Contrast microscopy (DIC) which has been employed to visualize gold nanoparticles of tens of nanometer size [6], [7]. This method depends on the insertion of polarizers and Wollaston prisms in the imaging light path to convert phase contrasts to intensity contrasts in the resulting image.

Confocal microscopy operated in reflection mode can also be used to visualize trapped nanoparticles. This method strongly depends on the reflectance, i.e., the ratio of illumination intensity to reflected intensity. Confocal reflection visualization of very small nanoparticles in the optical trap has been demonstrated [35], [50] and the plasmonic resonances of the particles make them scatter some wavelengths more efficiently than others.

Other methods for visualizing nanoparticles in an NIR optical trap often rely on detection of nanoparticle fluorescence or on elastic scattering of incident light. If the trapped nanostructure incorporates fluorophores, they might become excited by simultaneously absorbing two photons from the trapping NIR beam [59], [76]. This effect is shown for a 200 nm polystyrene nanoparticle (PS) in Fig. 8(a) left. An advantage of the two-photon visualization is that it allows the nanoparticle to be visualized only with a sensitive camera and without the need of additional light sources. Imaging by two-photon excitation by the trapping laser can be implemented in any epifluorescence microscope equipped with a sensitive CCD camera or a photomultiplier tube combined with hot mirrors and color filters to block the trapping laser light from reaching the detector. Also, trapped metallic nanoparticles can be two-photon excited by an additional pulsed and mode-locked laser focused to the same point in space as the trapping laser [5], [41]. One advantage of two-photon fluorescence is that the large frequency difference between the excitation beam and the emission makes it easy to distinguish signal from background illumination.

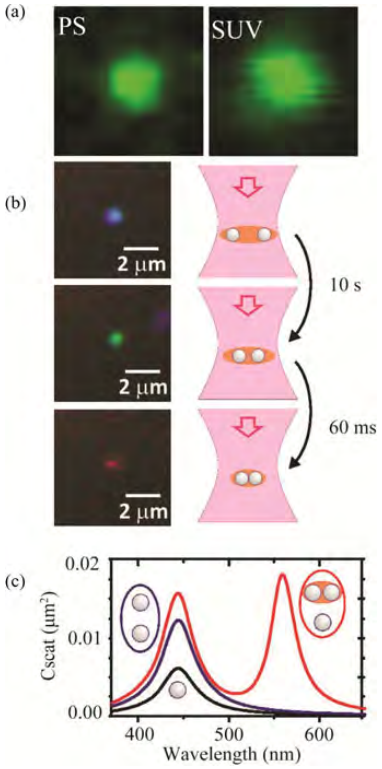

Fig. 8. Imaging of nanoparticles in an optical trap. (a) Left image shows a $d = 200$ nm polystyrene nanoparticle labeled with Alexa Fluo Hydroxide, with absorption maximum at 502 nm, and excited by two-photon absorption of the trapping laser beam. Right image shows the emission from a $\mathrm{DiOC}_{18:2}$ labeled SUV ($d = 70$ nm) held by an optical trap and imaged using confocal scanning microscopy. (b) Color recorded by dark field microscopy of trapped silver nanoparticles, reproduced with permission from [2]. (c) Corresponding simulated scattering spectra for individual and aggregated silver nanoparticles, reproduced with permission from [2].

A combined confocal micoscope and optical trap can also be used to visualize fluorescent trapped nanoparticles, as shown for a trapped Small Unilamellar lipid Vesicle (SUV) in Fig. 8(a) right [25].

Dark field microscopy is a very efficient visualization method for nanoparticles based on elastic scattering of incident light. The dark field method relies on detecting only the light scattered from the nanoparticle and not the illuminating beam. Combining dark field microscopy with optical trapping of nanoparticles is a challenge as it requires a balance between a high NA needed for stable optical trapping (typically NA = 1.3–1.4) and a NA

of the objective that is lower than the NA of the condenser for dark field imaging [77]. Methods for circumventing this strict requirement usually compromise either the trapping stiffness by using a low NA for the objective [78], [79] or the possibility of spectroscopic measurements by using a perpendicular laser for imaging [20], [80]. Recently a method was proposed in which both strong trapping and spectroscopic measurements can be achieved by collecting back-scattered light through an aperture that blocks reflected light from the specimen [81]. Another method demonstrated plasmonic coupling of metallic nanoparticles suspended in an optical trap using dark field microscopy by only constraining the NA in the imaging channel while maintaining a high NA of the trapping laser [see Fig. 8(b) and (c)] [2]. This study revealed a gradual red shift in the observed plasmon resonance because the particles gradually aggregated.

VIII. Future Directions

Nanoparticles can be trapped in relatively weak potentials in which they perform substantial Brownian fluctuations compared to trapped micrometer sized dielectric particles. Therefore, trapped nanoparticles have great potential as ultrasensitive sensors of potentials or for localizing matter at nanoscale. The sensitivity of trapped nanoparticles allows, e.g., for weak acoustic vibrations to be picked up by the trapped nanoparticle as recently demonstrated, see Fig. 9(a) and (b) [82]. This elegant experiment opens up a range of new possibilities to explore the acoustic environment and communication inside and between cells or to measure the dynamics of cellular organelles as, e.g., the rotating bacterial flagellum. Weakly trapped nanoparticles also hold great promise as ultrasensitive force transducers useful, e.g., for measuring thermophoretic effects [83] or for investigating the force properties of molecular motors.

Recently, it was shown that an optical trap could be employed to precisely pattern gold nanoparticles on a substrate [84], and an increased control over individual nanoparticles pave the way for realizing nano-architecture in 3D [see Fig. 9(c)]. We also anticipate that optical trapping will become a useful tool in the rapidly expanding field of plasmonics where multiple optical traps with controllable separation [28] will be very useful for studying collective biophotonical effects such as optical binding [3] without interfering substrates.

The efficiency of optical trapping relies on the size of the focus and hence is limited by the diffraction limit. Recent research is focusing on concentrating light to subdiffraction scales by using plasmonic structures to yield superior localization of the nanoparticles at much laser powers [32], [33]. However, the functionality of such plasmonic traps is compromised due to the necessity of having fixed plasmonic structures nearby and the potential heating effects. Future experiments would aim at quantifying the heat generated by the plasmonic devices and implementing these in biological applications.

In the future, optical trapping of nanoparticles will also contribute with exciting fundamental knowledge regarding light–matter interactions of nanostructures whose optical properties are largely unknown and certainly differ substantially from the corresponding bulk properties. These extraordinary properties giving promise of applications yet beyond imagination.

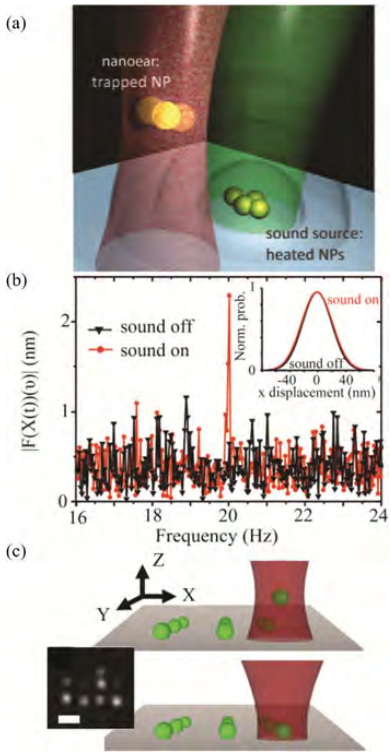

Fig. 9. Future applications of optical trapping of nanoparticles. (a)–(b) A gold nanoparticle, the so-called 'nano-ear,' is optically trapped while an acoustic wave is generated nearby by heating of other nanoparticles. As visible in the power spectrum shown in (b), this weak acoustic wave is picked up by the trapped particle, reproduced with permission from [82]. (c) Optical trap mediated nanopatterning of gold nanoparticles on a glass substrate. The $d = 40$ nm gold nanoparticles were positioned on the surface with a precision of 100 nm and imaged using dark field microscopy, reproduced with permission from [84].

References

[1] L. Tong, H. Wei, S. Zhang, Z. Li, and H. Xu, "Optical properties of single coupled plasmonic nanoparticles," *Phys. Chem. Chem. Phys.*, vol. 15, pp. 4100–4109, Mar. 28, 2013.

[2] A. Ohlinger, S. Nedev, A. A. Lutich, and J. Feldmann, "Optothermal escape of plasmonically coupled silver nanoparticles from a three-dimensional optical trap," *Nano Lett.*, vol. 11, pp. 1770–1774, Apr. 13, 2011.

[3] K. Dholakia and P. Zemánek, "Colloquium: Gripped by light: Optical binding," *Rev. Mod. Phys.*, vol. 82, pp. 1767–1791, 2010.

[4] J. Chen, J. Ng, Z. Lin, and C. T. Chan, "Optical pulling force," *Nat. Photon.*, vol. 5, pp. 531–534, 2011.

[5] Y. Jiang, T. Narushima, and H. Okamoto, "Nonlinear optical effects in trapping nanoparticles with femtosecond pulses," *Nat. Phys.*, vol. 6, pp. 1005–1009, 2010.

[6] P. M. Hansen, V. K. Bhatia, N. Harrit, and L. Oddershede, "Expanding the optical trapping range of gold nanoparticles," *Nano Lett.*, vol. 5, pp. 1937–1942, Oct. 2005.

[7] K. Svoboda and S. M. Block, "Optical trapping of metallic Rayleigh particles," *Opt. Lett.*, vol. 19, pp. 930–932, Jul. 1, 1994.

[8] F. Hajizadeh and S. N. Reihani, "Optimized optical trapping of gold nanoparticles," *Opt. Exp*, vol. 18, pp. 551–559, Jan. 18, 2010.

[9] S. N. Reihani and L. B. Oddershede, "Optimizing immersion media refractive index improves optical trapping by compensating spherical aberrations," *Opt. Lett.*, vol. 32, pp. 1998–2000, Jul. 15, 2007.

[10] M. Dienerowitz, M. Mazilu, P. J. Reece, T. F. Krauss, and K. Dholakia, "Optical vortex trap for resonant confinement of metal nanoparticles," *Opt. Exp.*, vol. 16, pp. 4991–4999, Mar. 31, 2008.

[11] M. Selmke, M. Braun, and F. Cichos, "Photothermal single-particle microscopy: Detection of a nanolens," *ACS Nano*, vol. 6, pp. 2741–2749, Mar. 27, 2012.

[12] P. V. Ruijgrok, N. R. Verhart, P. Zijlstra, A. L. Tchebotareva, and M. Orrit, "Brownian fluctuations and heating of an optically aligned gold nanorod," *Phys. Rev. Lett.*, vol. 107, pp. 037401-1–037401-4, 2011.

[13] A. Kyrsting, P. M. Bendix, D. G. Stamou, and L. B. Oddershede, "Heat profiling of three-dimensionally optically trapped gold nanoparticles using vesicle cargo release," *Nano Lett.*, vol. 11, pp. 888–892, Feb. 9, 2011.

[14] Y. Seol, A. E. Carpenter, and T. T. Perkins, "Gold nanoparticles: Enhanced optical trapping and sensitivity coupled with significant heating," *Opt. Lett.*, vol. 31, pp. 2429–2431, Aug. 15, 2006.

[15] X. Huang, I. H. El-Sayed, W. Qian, and M. A. El-Sayed, "Cancer cell imaging and photothermal therapy in the near-infrared region by using gold nanorods," *J. Amer. Chem. Soc.*, vol. 128, pp. 2115–2120, Feb. 15, 2006.

[16] C. Loo, A. Lowery, N. Halas, J. West, and R. Drezek, "Immunotargeted nanoshells for integrated cancer imaging and therapy," *Nano Lett.*, vol. 5, pp. 709–711, Apr. 2005.

[17] L. R. Hirsch, R. J. Stafford, J. A. Bankson, S. R. Sershen, B. Rivera, R. E. Price, J. D. Hazle, N. J. Halas, and J. L. West, "Nanoshell-mediated near-infrared thermal therapy of tumors under magnetic resonance guidance," *Proc. Natl. Acad. Sci. U S A*, vol. 100, pp. 13549–13554, Nov. 11, 2003.

[18] L. Osinkina, S. Carretero-Palacios, J. Stehr, A. A. Lutich, F. Jackel, and J. Feldmann, "Tuning DNA binding kinetics in an optical trap by plasmonic nanoparticle heating," *Nano Lett.*, vol. 13, pp. 3140–3144, Jun. 24, 2013.

[19] S. Kalele, S. W. Gosavi, J. Urban, and S. K. Kulkarni, "Nanoshell particles: Synthesis, properties and applications," *Curr. Sci.*, vol. 91, pp. 1038–1052, 2006.

[20] K. C. Toussaint, M. Liu, M. Pelton, J. Pesic, M. J. Guffey, P. Guyot-Sionnest, and W. F. Scherer, "Plasmon resonance-based optical trapping of single and multiple Au nanoparticles," *Opt. Exp.*, vol. 15, pp. 12017–12029, Sep. 17, 2007.

[21] A. Rohrbach, "Stiffness of optical traps: Quantitative agreement between experiment and electromagnetic theory," *Phys. Rev. Lett.*, vol. 95, pp. 168102-1–168102-4, Oct. 14, 2005.

[22] A. Rohrbach and E. H. K. Stelzer, "Three-dimensional position detection of optically trapped dielectric particles," *J. Appl. Phys.*, vol. 91, pp. 5474–5488, 2002.

[23] A. Rohrbach and E. H. K. Stelzer, "Optical trapping of dielectric particles in arbitrary fields," *J. Opt. Soc. Amer. A. Opt. Image. Sci. Vis.*, vol. 18, pp. 839–853, Apr. 2001.

[24] A. Ashkin, J. M. Dziedzic, J. E. Bjorkholm, and S. Chu, "Observation of a single-beam gradient force optical trap for dielectric particles," *Opt. Lett.*, vol. 11, pp. 288–290, May 1, 1986.

[25] P. M. Bendix and L. B. Oddershede, "Expanding the optical trapping range of lipid vesicles to the nanoscale," *Nano Lett.*, vol. 11, pp. 5431–5437, Dec. 14, 2011.

[26] D. Min, K. Kim, C. Hyeon, Y. H. Cho, Y. K. Shin, and T. Y. Yoon, "Mechanical unzipping and rezipping of a single SNARE complex reveals hysteresis as a force-generating mechanism," *Nat. Commun.*, vol. 4, pp. 1705-1–1705-10, 2013.

[27] Y. Gao, S. Zorman, G. Gundersen, Z. Xi, L. Ma, G. Sirinakis, J. E. Rothman, and Y. Zhang, "Single reconstituted neuronal SNARE complexes zipper in three distinct stages," *Science*, vol. 337, pp. 1340–1343, Sep. 14, 2012.

[28] K. Visscher, S. P. Gross, and S. M. Block, "Construction of multiple-beam optical traps with nanometer-resolution position sensing," *IEEE J. Sel. Topics Quantum Electron.*, vol. 2, no. 4, pp. 1066–1076, Dec. 1996.

[29] A. Jonas and P. Zemanek, "Light at work: The use of optical forces for particle manipulation, sorting, and analysis," *Electrophoresis*, vol. 29, pp. 4813–4851, Dec. 2008.

[30] M. Dienerowitz, M. Mazilu, and K. Dholakia, "Optical manipulation of nanoparticles: A review," *J. Nanophoton.*, vol. 2, pp. 021875-1–021875-32, 2008.

[31] Y. Pang and R. Gordon, "Optical trapping of 12 nm dielectric spheres using double-nanoholes in a gold film," *Nano Lett.*, vol. 11, pp. 3763–3767, Sep. 14, 2011.

[32] M. L. Juan, M. Righini, and R. Quidant, "Plasmon nano-optical tweezers," *Nat. Photon.*, vol. 5, pp. 349–356, 2011.

[33] P. J. Reece, "Finer optical tweezers," *Nat. Photon.*, vol. 2, pp. 333–334, 2008.

[34] Y. Harada and T. Asakura, "Radiation forces on a dielectric sphere in the Rayleigh scattering regime," *Opt. Commun.*, vol. 124, pp. 529–541, 1996.

[35] A. Kyrsting, P. M. Bendix, and L. B. Oddershede, "Mapping 3D focal intensity exposes the stable trapping positions of single nanoparticles," *Nano Lett.*, vol. 13, pp. 31–35, Jan. 9, 2013.

[36] P. B. Johnson and R. W. Christy, "Optical constants of the noble metals," *Phys. Rev. E.*, vol. 6, pp. 4370–4379, 1972.

[37] C. F. Bohren and D. R. Huffman, *Absorption and Scattering of Light by Small Particles*. Hoboken, NJ, USA: Wiley, 1998, p. 149.

[38] T. Iida and H. Ishihara, "Theoretical study of the optical manipulation of semiconductor nanoparticles under an excitonic resonance condition," *Phys. Rev. Lett.*, vol. 90, pp. 057403-1–057403-4, Feb. 7, 2003.

[39] J. Rodriguez-Fernandez, J. Perez-Juste, F. J. Garcia de Abajo, and L. M. Liz-Marzan, "Seeded growth of submicron Au colloids with quadrupole plasmon resonance modes," *Langmuir*, vol. 22, pp. 7007–7010, Aug. 1, 2006.

[40] C. Selhuber-Unkel, I. Zins, O. Schubert, C. Sonnichsen, and L. B. Oddershede, "Quantitative optical trapping of single gold nanorods," *Nano Lett.*, vol. 8, pp. 2998–3003, Sep. 2008.

[41] M. Pelton, M. Liu, H. Y. Kim, G. Smith, P. Guyot-Sionnest, and N. F. Scherer, "Optical trapping and alignment of single gold nanorods by using plasmon resonances," *Opt. Lett.*, vol. 31, pp. 2075–2077, Jul. 1, 2006.

[42] J. Trojek, L. Chvatal, and P. Zemanek, "Optical alignment and confinement of an ellipsoidal nanorod in optical tweezers: A theoretical study," *J. Opt. Soc. Amer. A Opt. Image Sci. Vis.*, vol. 29, pp. 1224–1236, Jul. 1, 2012.

[43] H. Liu, D. Chen, F. Tang, G. Du, L. Li, X. Meng, W. Liang, Y. Zhang, X. Teng, and Y. Li, "Photothermal therapy of Lewis lung carcinoma in mice using gold nanoshells on carboxylated polystyrene spheres," *Nanotechnology*, vol. 19, pp. 455101-1–455101-7, Nov. 12, 2008.

[44] N. G. Kampen, *Stochastic Processes in Physics and Chemistry*. Amsterdam, The Netherland: North-Holland, 1992.

[45] A. S. Zelenina, R. Quidant, and M. Nieto-Vesperinas, "Enhanced optical forces between coupled resonant metal nanoparticles," *Opt. Lett.*, vol. 32, pp. 1156–1158, 2007.

[46] N. Lewinski, V. Colvin, and R. Drezek, "Cytotoxicity of nanoparticles," *Small*, vol. 4, pp. 26–49, Jan. 2008.

[47] A. Pralle, M. Prummer, E. L. Florin, E. H. Stelzer, and J. K. Horber, "Three-dimensional high-resolution particle tracking for optical tweezers by forward scattered light," *Microsc. Res. Tech.*, vol. 44, pp. 378–386, Mar. 1, 1999.

[48] K. Berg-Sørensen, L. Oddershede, E. L. Florin, and H. Flyvbjerg, "Unintended filtering in typical photo-diode detection system for optical tweezers," *J. Appl. Phys.*, vol. 93, pp. 3167–3176, 2003.

[49] P. M. Hansen, I. M. Tolic-Nørrelykke, H. Flyvbjerg, and K. Berg-Sørensen, "Tweezercalib 2.0: Faster version of a MatLab package for precision calibration of optical tweezers," *Comp. Phys. Commun.*, vol. 174, pp. 518–520, 2006.

[50] L. Bosanac, T. Aabo, P. M. Bendix, and L. B. Oddershede, "Efficient optical trapping and visualization of silver nanoparticles," *Nano Lett.*, vol. 8, pp. 1486–1491, May 2008.

[51] A. Ashkin and J. P. Gordon, "Cooling and trapping of atoms by resonance radiation pressure," *Opt. Lett.*, vol. 4, pp. 161–163, Jun. 1 1979.

[52] T. Čižmár, M. Mazilu, and K. Dholakia, "In situ wavefront correction and its application to micromanipulation," *Nat. Photon.*, vol. 4, pp. 388–394, 2010.

[53] H. Ma, P. M. Bendix, and L. B. Oddershede, "Large-scale orientation dependent heating from a single irradiated gold nanorod," *Nano Lett.*, vol. 12, pp. 3954–3960, Aug. 8, 2012.

[54] R. Weissleder, "A clearer vision for in vivo imaging," *Nat. Biotechnol.*, vol. 19, pp. 316–317, Apr. 2001.

[55] P. J. Pauzauskie, A. Radenovic, E. Trepagnier, H. Shroff, P. Yang, and J. Liphardt, "Optical trapping and integration of semiconductor nanowire assemblies in water," *Nat. Mater.*, vol. 5, pp. 97–101, Feb. 2006.

[56] Z. Yan, J. E. Jureller, J. Sweet, M. J. Guffey, M. Pelton, and N. F. Scherer, "Three-dimensional optical trapping and manipulation of single silver nanowires," *Nano Lett.*, vol. 12, pp. 5155–5161, Oct. 10, 2012.

[57] Y. Shirasaki, G. J. Supran, M. G. Bawendi, and V. Bulović, "Emergence of colloidal quantum-dot light-emitting technologies," *Nat. Photon.*, vol. 7, pp. 13–23, 2013.

[58] C. R. Head, E. Kammann, M. Zanella, L. Manna, and P. G. Lagoudakis, "Spinning nanorods—Active optical manipulation of semiconductor nanorods using polarised light," *Nanoscale*, vol. 4, pp. 3693–3697, Jun. 21, 2012.

[59] L. Jauffred and L. B. Oddershede, "Two-photon quantum dot excitation during optical trapping," *Nano Lett.*, vol. 10, pp. 1927–1930, May 12, 2010.

[60] L. Jauffred, A. C. Richardson, and L. B. Oddershede, "Three-dimensional optical control of individual quantum dots," *Nano Lett.*, vol. 8, pp. 3376–3380, Oct. 2008.
[61] C. Nobile, V. A. Fonoberov, S. Kudera, A. D. Torre, A. Ruffino, G. Chilla, T. Kipp, D. Heitmann, L. Manna, R. Cingolani, A. A. Balandin, and R. Krahne, "Confined optical phonon modes in aligned nanorod arrays detected by resonant inelastic light scattering," *Nano Lett.*, vol. 7, pp. 476–479, Feb. 2007.
[62] B. Hester, G. K. Campbell, C. Lopez-Mariscal, C. L. Filgueira, R. Huschka, N. J. Halas, and K. Helmerson, "Tunable optical tweezers for wavelength-dependent measurements," *Rev. Sci. Instrum.*, vol. 83, pp. 043114-1–043114-8, Apr. 2012.
[63] P. K. Jain, K. S. Lee, I. H. El-Sayed, and M. A. El-Sayed, "Calculated absorption and scattering properties of gold nanoparticles of different size, shape, and composition: Applications in biological imaging and biomedicine," *J. Phys. Chem. B*, vol. 110, pp. 7238–7248, Apr. 13, 2006.
[64] M. Sheik-Bahae, D. C. Hutchings, D. J. Hagan, and E. W. Stryland, "Dispersion of bound electronic nonlinear refraction in solids," *IEEE J. Quantum Electron.*, vol. 27, no. 6, pp. 1296–1309, Jun. 1991.
[65] J. P. Barton and D. R. Alexander, "Fifth-order corrected electromagnetic field components for a fundamental Gaussian beam," *J. Appl. Phys.*, vol. 66, pp. 2800–2802, 1989.
[66] P. M. Bendix, S. N. Reihani, and L. B. Oddershede, "Direct measurements of heating by electromagnetically trapped gold nanoparticles on supported lipid bilayers," *ACS Nano*, vol. 4, pp. 2256–2262, Apr. 27, 2010.
[67] G. Baffou, M. P. Kreuzer, F. Kulzer, and R. Quidant, "Temperature mapping near plasmonic nanostructures using fluorescence polarization anisotropy," *Opt. Exp.*, vol. 17, pp. 3291–3298, Mar. 2, 2009.
[68] E. J. Peterman, F. Gittes, and C. F. Schmidt, "Laser-induced heating in optical traps," *Biophys. J.*, vol. 84, pp. 1308–1316, Feb. 2003.
[69] P. Haro-Gonzalez, W. T. Ramsay, L. Martinez Maestro, B. del Rosal, K. Santacruz-Gomez, C. Iglesias-de la Cruz Mdel, F. Sanz-Rodríguez, J. Y. Chooi, P. Rodriguez Sevilla, M. Bettinelli, D. Choudhuny, A. K. Kar, J. García Solé, D. Jaque, and L. Paterson, "Quantum dot-based thermal spectroscopy and imaging of optically trapped microspheres and single cells," *Small*, vol. 9, pp. 2162–2170, Jun. 24, 2013.
[70] H. H. Richardson, Z. N. Hickman, A. O. Govorov, A. C. Thomas, W. Zhang, and M. E. Kordesch, "Thermooptical properties of gold nanoparticles embedded in ice: Characterization of heat generation and melting," *Nano Lett.*, vol. 6, pp. 783–788, Apr. 2006.
[71] A. S. Urban, M. Fedoruk, M. R. Horton, J. O. Radler, F. D. Stefani, and J. Feldmann, "Controlled nanometric phase transitions of phospholipid membranes by plasmonic heating of single gold nanoparticles," *Nano Lett.*, vol. 9, pp. 2903–2908, Aug. 2009.
[72] T. Baumgart, G. Hunt, E. R. Farkas, W. W. Webb, and G. W. Feigenson, "Fluorescence probe partitioning between Lo/Ld phases in lipid membranes," *Biochim. Biophys. Acta.*, vol. 1768, pp. 2182–2194, Sep. 2007.
[73] V. Kotaidis, C. Dahmen, G. von Plessen, F. Springer, and A. Plech, "Excitation of nanoscale vapor bubbles at the surface of gold nanoparticles in water," *J. Chem. Phys.*, vol. 124, pp. 184702-1–184702-7, May 14, 2006.
[74] A. Rohrbach and E. H. K. Stelzer, "Trapping forces, force constants, and potential depths for dielectric spheres in the presence of spherical aberrations," *Appl. Opt.*, vol. 41, pp. 2494–2507, May 1, 2002.
[75] S. N. S. Reihani, S. A. Mir, A. R. Richardson, and L. B. Oddershede, "Significant improvement of optical traps by tuning standard water immersion objectives," *J. Opt.*, vol. 13, pp. 105301-1–105301-6, 2011.
[76] E. L. Florin, A. Pralle, J. K. Horber, and E. H. Stelzer, "Photonic force microscope based on optical tweezers and two-photon excitation for biological applications," *J. Struct. Biol.*, vol. 119, pp. 202–211, Jul. 1997.
[77] P. Zemanek, A. Jonas, L. Sramek, and M. Liska, "Optical trapping of nanoparticles and microparticles by a Gaussian standing wave," *Opt. Lett.*, vol. 24, pp. 1448–1450, Nov. 1, 1999.
[78] L. Tong, V. D. Miljković, and M. Käll, "Optical manipulation of plasmonic nanoparticles using laser tweezers," *Proc. SPIE*, vol. 7762, pp. 77620O-1–77620O-8, 2010.
[79] J. Prikulis, F. Svedberg, and M. Käll, "Optical spectroscopy of single trapped metal nanoparticles in solution," *Nano Lett.*, vol. 4, pp. 115–118, 2004.
[80] J.-H. Zhou, L.-J. Qu, K. Yao, M.-C. Zhong, and Y.-M. Li, "Observing Nanometre Scale Particles with Light Scattering for Manipulation using optical tweezers," *Chin. Phys. Lett.*, vol. 25, pp. 329–331, 2008.
[81] K. Pearce, F. Wang, and P. J. Reece, "Dark-field optical tweezers for nanometrology of metallic nanoparticles," *Opt. Exp.*, vol. 19, pp. 25559–25569, Dec. 5, 2011.
[82] A. Ohlinger, A. Deak, A. A. Lutich, and J. Feldmann, "Optically trapped gold nanoparticle enables listening at the microscale," *Phys. Rev. Lett.*, vol. 108, pp. 018101-1–018101-5, 2012.
[83] S. Duhr and D. Braun, "Thermophoretic depletion follows Boltzmann distribution," *Phys. Rev. Lett.*, vol. 96, pp. 168301-1–168301-4, Apr. 28, 2006.
[84] M. J. Guffey and N. F. Scherer, "All-optical patterning of Au nanoparticles on surfaces using optical traps," *Nano Lett.*, vol. 10, pp. 4302–4308, Nov. 10, 2010.

Poul M. Bendix received the B.S. degree in mathematics and physics in 2002 and the Cand. Scient degree in physics in 2003 from Niels Bohr Institute (NBI) University of Copenhagen, Copenhagen, Denmark, and the Ph.D. degree in biophysics in 2007 following 6 months a visit at Harvard University, Cambridge, MA, USA. During his postdoc period from 2007 to 2011, he worked at the Nanoscience Center, University of Copenhagen, and at Stanford University, Stanford, CA, USA. Since 2013, he has been an Associate Professor at the NBI. His research interests include interactions between light and nanoparticles with respect to both heating and trapping as well as biophysics of model membrane systems and mechanics of reconstituted cytoskeletal filaments. He received the Young Investigator Award in 2011 from the Villum Foundation.

Liselotte Jauffred received the B.S. degree in mathematics and physics in 2004 and the M.S. degree in physics in 2006 from the University of Copenhagen, Copenhagen, Denmark, and the Ph.D. degree from the Niels Bohr Institute (NBI) in biophysics in 2010. As a Postdoc, she has worked at the FOM Institute AMOLF, Amsterdam, Netherlands, and is currently a Postdoc at NBI. Her research includes interactions between light and quantum dots and she was the first to visualize and quantitate the forces exerted on an optically trapped quantum dot.

Kamilla Nørregaard received her B.S. degree in physics in 2009 and the Cand. Scient degree in physics in 2011 from the University of Copenhagen, Copenhagen, Denmark. Currently she is working toward the Ph.D. degree in biophysics under the guidance of P. M. Bendix and L. B. Oddershede. Her research interests include plasmonic heating and trapping of nanoparticles, nanoparticle mediated photothermal cancer therapy, and nanoparticle delivered gene therapy.

Lene B. Oddershede received the Cand. Scient degree in mathematics and physics and the Ph.D. degree in physics from University of Southern Denmark (SDU), Odense, Denmark, in 1995 and 1998, respectively. She visited the James Frank Institute, University of Chicago 1996–1997. In 1998, she became an Assistant Professor and constructed the optical tweezers laboratory at the Niels Bohr Institute (NBI), University of Copenhagen, Copenhagen, Denmark. In 2003, she was tenured and became an Associate Professor and group leader at the NBI. In 2003, she received the Young Investigator Award from the Danish Optical Society and in 2011 the Silver Medal from the Danish Royal Academy of Sciences. Her research interests include the biophotonical and nanotoxological properties of nanoparticles and their potential use in biological contexts. Also, she is interested in optical manipulation of biological specimen.

PCCP

REVIEW ARTICLE

View Article Online
View Journal | View Issue

Cite this: *Phys. Chem. Chem. Phys.*, 2014, **16**, 12614

Optical manipulation of single molecules in the living cell

Kamilla Norregaard,[a] Liselotte Jauffred,[a] Kirstine Berg-Sørensen[b] and Lene B. Oddershede*[a]

Received 15th January 2014,
Accepted 10th March 2014

DOI: 10.1039/c4cp00208c

www.rsc.org/pccp

Optical tweezers are the only nano-tools capable of manipulating and performing force-measurements on individual molecules and organelles within the living cell without performing destructive penetration through the cell wall and without the need for inserting a non-endogenous probe. Here, we describe how optical tweezers are used to manipulate individual molecules and perform accurate force and distance measurements within the complex cytoplasm of the living cell. Optical tweezers can grab individual molecules or organelles, if their optical contrast to the medium is large enough, as is the case, *e.g.*, for lipid granules or chromosomes. However, often the molecule of interest is specifically attached to a handle manipulated by the optical trap. The most commonly used handles, their insertion into the cytoplasm, and the relevant micro-rheology of the cell are discussed here and we also review recent and exciting results achieved through optical force manipulation of individual molecules *in vivo*.

Introduction

Since the invention of optical trapping[1] and the discovery that living microorganisms could survive while being optically trapped for long periods of time,[2] optical traps have had great success uncovering fundamentals of biological systems at the single molecule level.[3,4] One reason for this success is probably that optical traps are capable of measuring forces and distances in the pico-Newton and nanometer range, which are exactly the forces and distances of interest at the single molecule level of the cellular machinery. Another reason which is particularly important with respect to *in vivo* single molecule measurements is that optical trapping, even inside a living cell, can be performed almost non-invasively,[5] which is in contrast to, *e.g.*, atomic force measurements where the cantilever would need to physically penetrate the cell membrane in order to perform measurements inside a cell. Magnetic tweezers can also operate non-invasively inside living cells, but a magnetic probe particle would need to be inserted into the cytoplasm.

[a] *Niels Bohr Institute, University of Copenhagen, Copenhagen, Denmark. E-mail: oddershede@nbi.dk*
[b] *Department of Physics, Technical University of Denmark, Denmark*

Kamilla Norregaard

Kamilla Nørregaard received her BS degree in physics in 2009 and the Cand Scient degree in physics in 2011 from the University of Copenhagen. Currently she is working on her PhD in biophysics under the guidance of Poul M. Bendix and Lene B. Oddershede. Her research interests include plasmonic heating and trapping of nanoparticles, nanoparticle mediated photothermal cancer therapy, and nanoparticle delivered gene therapy.

Liselotte Jauffred

Liselotte Jauffred received her BS degree in mathematics and physics in 2004 and the Cand Scient degree in physics in 2006 from the University of Copenhagen. She graduated as a PhD from the Niels Bohr Institute (NBI) within biophysics in 2010. As a postdoc she has worked at the FOM Institute AMOLF in Amsterdam and is currently a postdoc at NBI. Her research includes interactions between light and quantum dots and she was the first to visualize and quantitate the forces exerted on an optically trapped quantum dot.

View Article Online
Review Article PCCP

Optical traps belong to the toolbox of techniques capable of observing individual molecules for an extended period of time. Single molecule studies can reveal rare and transient events or dynamical behaviour of single molecules, thus unravelling fundamental properties of bio-molecules that are typically hidden in ensemble studies. In addition to simple video based tracking of individual molecules, which can also be performed with high accuracy, *e.g.*, by the novel super-resolution techniques,[6,7] optical traps are capable of exerting and measuring forces. Force has an important role in driving the fundamental processes of the living cell. For instance, force is known to guide cell motility,[8] be important for cell–environment communication, influence stem cell differentiation,[9] and of course be important for intracellular cargo transportation by molecular motors and cytoskeletal re-organization, also during cell division.

Most biomolecules are controlled in a hierarchical manner by their local environment through signalling pathways, topological constraints, and mechanical forces that all can modulate the biomolecule's function. *In vitro* optical tweezer measurements have successfully uncovered the mechanical and dynamic properties of many molecular motors, for example the run length, step-size, velocity, and load dependence of cytoskeletal motor molecules such as kinesin[10–12] and myosin.[13,14] Also, optical tweezers have been extremely useful in characterizing the mechanical properties of biopolymers such as DNA, microtubules[15] or actin,[16] pinpointing, *e.g.*, DNA's force–extension relation,[17,18] melting,[19,20] and twisting[18] properties as well as its interaction with various proteins.[19,21] *In vitro* single molecule investigations have the distinct advantage of being able to investigate the influence of one well defined parameter at a time, which is important, *e.g.*, for quantifying the coupling between mechanical work and a molecular motor's energy consumption.[11]

In vitro studies have laid the foundation for our understanding of force-dependent and dynamical events of biomolecules. However, purifying and removing a single biomolecule from its natural environment may alter its properties and render *in vitro* results less biologically relevant than observations done within the living cell. Dynein is an example of a molecular motor where *in vivo* observations indicate that the motor is less processive inside a living cell[22] than in a test tube.[23] However the interpretation of such results is not trivial as dynein cannot depart from its cargo as easily *in vivo* as *in vitro* and the number of motors attached to the cargo is not easily determined *in vivo*. Also ribosomes are reported to translate significantly slower *in vitro* than *in vivo*.[5]

Despite the great interest and development of single molecule techniques capable of reaching inside the living cell[5] the results obtained *in vivo* are still limited. This is probably due to the severe challenges associated with bringing single molecule force-measuring techniques into the living cell.[5,24] Here, we focus on optical force manipulation inside living cells, explain how to overcome the *in vivo* challenges, and lay out the methodology for *in vivo* force calibration and measurements. Also we discuss the important issues of internalizing the handle for the optical trap into the living cell and the micro-rheological properties of the cytoplasm. Finally, we review exciting results recently obtained through optical manipulation of single molecules *in vivo*.

Experimental

Optical tweezers are typically formed by tightly focusing a laser beam to a diffraction-limited spot using a high numerical aperture (NA) objective. Fig. 1 shows a setup where an optical trap (the infrared light originating from a 1064 nm Nd:YVO_4 laser)

Kirstine Berg-Sørensen

Kirstine Berg-Sørensen received the Cand Scient degree in chemistry and physics from University of Aarhus (AU) in 1991 and the PhD degree in physics from AU in 1994. She visited the Laboratoire Kastler-Brossel, École Normale Superieure, Paris, in 1992 and was a postdoc at Rowland Institute for Science, Cambridge MA in 1994–1995. In 1998 she established the optical tweezers group at the NBI with funding from the Danish Research Councils. Since 2005, she has been an associate professor at the Dept of Physics, Technical University of Denmark. In her early research years, she investigated optical trapping and condensation of cold atomic gases whereas more recent research interests involve data analysis in connection with optical manipulation in biological specimens and experiments to do so. In addition, she investigates flow in model systems for plants.

Lene B. Oddershede

Lene B. Oddershede, PI of the optical tweezers group at the Niels Bohr Institute (NBI), received the Cand Scient degree in mathematics and physics from University of Southern Denmark (SDU) in 1995 and the PhD degree in physics from SDU in 1998. She visited the James Frank Institute, University of Chicago, in 1996–1997. In 1998 she became an assistant professor and constructed the optical tweezers laboratory at NBI, University of Copenhagen. In 2003 she was tenured as an associate professor at the NBI. In 2003 she received the Young Investigator Award from the Danish Optical Society and in 2011 the Silver Medal from the Danish Royal Academy of Sciences. Her research interests include the biophotonical and nanotoxological properties of nanoparticles and their potential use in biological contexts. She is also interested in optical manipulation of biological specimens.

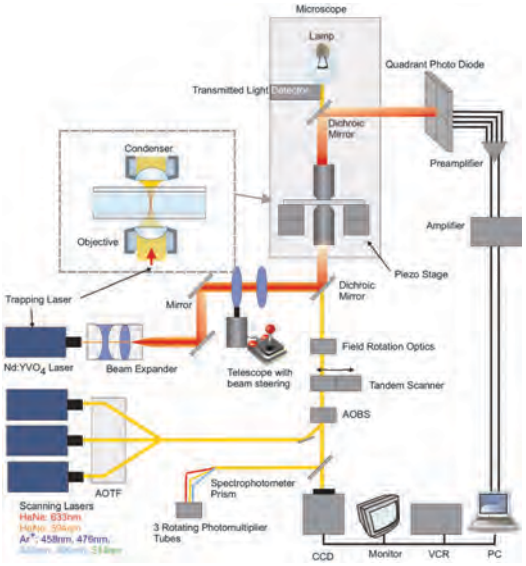

Fig. 1 Illustration of an optical trap implemented in a confocal microscope. This equipment allows for simultaneous fluorescent visualization and force measurements and manipulation. Figure reproduced with permission from Richardson *et al.*[32]

is implemented in a confocal microscope. This type of setup allows for simultaneous force measurements and confocal visualization of fluorescently marked molecules and handles. Equipped with appropriate detection schemes, as for instance photodiodes in the back-focal plane, optical tweezers can measure displacements in three dimensions with a spatial resolution down to 0.2 nm and a temporal resolution on the order of μs. Often the beam profile of the trapping laser is Gaussian because it provides a small well defined focal spot and produces a large intensity gradient, hence a large force. The trapped object experiences a force, F, that is a combination of gradient and scattering forces. The equilibrium position is normally close to the focus of the laser beam, however, it could be displaced somewhat in the axial direction because of the scattering force.[25] For small displacements of the trapped object the force scales linearly with displacement, x. In this regime, the optical trap is well-described as a Hookian spring, $F = -\kappa x$, where κ is the spring constant. κ has a different value in each of the translational directions, is typically weaker in the axial direction than in the lateral directions, and normally has a value of $\sim$0.01–1 pN nm^{-1}, depending on laser power and alignment.

For biological applications, optical tweezers based on near-infrared lasers (850–1064 nm) are preferable because biological tissue and water absorb only very little light at those wavelengths. To create a strong trap based on a single laser beam it is advantageous to use a high NA objective. Oil immersion objectives are available with higher NA than water immersion objectives, however, an oil immersion objective introduces significant spherical aberration in an aqueous sample and the aberration is strongly depth dependent. A water immersion objective introduces less aberration of an infrared laser beam[26] and the aberration is nearly independent of imaging depth (until depths of $\sim$200 μm).

Position detection can be performed either simply using a camera, or by using photodiode based techniques, the latter typically having the advantage of a higher space and time resolution and easier data processing. As depicted in Fig. 1, a photodiode, either a quadrant photodiode detector (QPD) or a position sensitive detector (PSD), can be placed in the back focal plane of the objective. These photodiodes collect the forward scattered light and can easily achieve a spatial resolution down to a few nanometers in 3D[27] and a time resolution of μs.[28,29] For certain purposes it is an advantage to employ a separate laser for position detection, which also allows for implementation of a feedback system with, *e.g.*, acousto-optic[30] or electro-optic[31] deflectors.

Force calibration

In many experimental situations, the laser intensity in the trapping plane is not readily known and as precise calculations of optical forces are quite involved[33] and not necessarily available for complex geometries and handles, the force exerted by the trapping laser is most often found by calibration. A popular choice for precise and fast calibration relevant for *in vitro* experiments relies on recordings of the Brownian motion of an optically trapped dielectric bead. Such recordings are also denoted passive measurements because variations in the position of the trapped particle are caused by thermal fluctuations only and not by any active driving. In the simplest version of passive calibration, the bead radius and the viscosity of the surrounding liquid are assumed to be known. The trapping potential is assumed to be harmonic and by analysis of either the correlation function[34] or the power spectrum[35,36] of the positions visited by the trapped bead, the passive calibration method provides a value for the spring constant κ of the trapping potential. With a value for κ at hand, a precise measurement of the position of a trapped object relative to its equilibrium position, x, will allow extraction of the force, $F = -\kappa x$.

In vivo the task of calibrating the optical trap becomes more complex. Now, the surrounding medium is no longer a liquid with known viscosity but may rather be modelled as a viscoelastic medium. If the trapped object is well characterized and available also outside the cell, one may determine its trapping spring constant in a simple viscous liquid, *e.g.*, through passive calibration. Then, the spring constant in the viscoelastic medium can be approximated by the spring constant found, but modified by accounting properly for the difference in the refractive index between the two media. Another option is to use the limiting behavior at vanishing frequency of the real part of the viscoelastic modulus for the determination of the spring constant of the trap in the viscoelastic medium.[37] Often, however, the size and geometry of the object trapped within the living cell are unknown. In that case, two conceptually different approaches have been applied to determine the force exerted by the optical trap. One relies on the measurement of momentum changes imparted to the trapping laser light – and

requires the ability to detect all the light scattered.[38,39] A completely different approach relies on a combination of active and passive measurements.[40,41] This approach allows for determination both of trap characteristics and of viscoelastic properties of the cytoplasm and does not require that the geometry or optical properties of the handle are known.[42] The procedure involves a series of experiments, as illustrated in Fig. 2: in passive measurements (Fig. 2(a)), time series of the positions visited by the trapped particle are recorded and power spectra, $P(f)$, are calculated. In active measurements (Fig. 2(b)), while oscillating either the sample stage or the trapping laser, time series of the positions of the trapped bead are recorded and compared to the positions of the oscillating trap or stage, and a so-called relaxation spectrum is recorded.

In practice for the active measurements, the stage is oscillated at angular frequency ω, the stage position $x_S(t)$ is described as

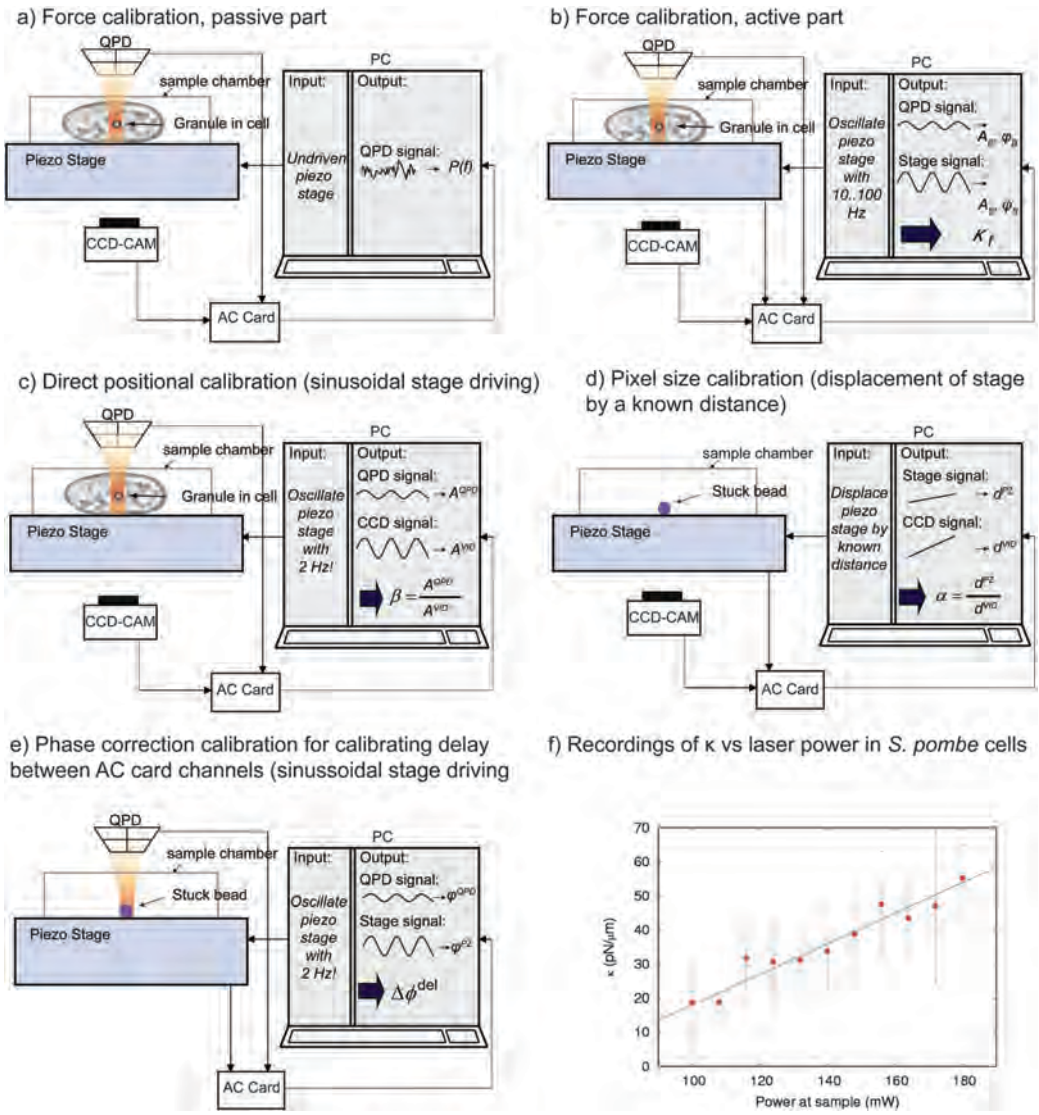

Fig. 2 Illustration of the active–passive calibration method that is applicable in living systems. Sketch is not to scale. In part (a), the passive part of the measurement protocol is illustrated. Recordings of the position of the trapped object inside the cell, here, a lipid granule inside a live *S. pombe* cell, allow for the experimenter to obtain a power spectrum, $P(f)$. In part (b), the active part of the protocol is illustrated, allowing us to obtain values for the amplitude $A_{S/P}$ and phase $\varphi_{S/P}$ of both the stage (subscript S) that is actively driven, and the response of the trapped object (subscript P). In parts (c)–(e), experimental steps to determine parameters of the detection system are illustrated. In panel (f), results obtained with trapped granules in a live *S. pombe* cell demonstrate that the spring constant of the trap, κ, increases linearly with the power of the trapping laser.

View Article Online
PCCP Review Article

$x_S(t) = A_S \sin(\omega t + \varphi_S)$ and the motion of the trapped particle $x_P(t)$, recorded by a QPD, is fitted to the form $x_P(t) = A_P \sin(\omega t + \varphi_P)$. Subsequently, the data both from active and passive spectral measurements are combined to extract the information sought for, namely the spring constant of the trap, κ, and the viscoelastic modulus $G(f)$.

Intermediary steps (described by parts (c)–(e) in Fig. 2) ensure that the final outcome carries the correct physical dimensions. The active–passive method should be applied with a driving frequency chosen in frequency intervals that do not involve active processes, like the action of molecular motors, as the method is based on the assumption that concepts of equilibrium thermodynamics are applicable. Fig. 2(f) demonstrates that the hallmarks of optical traps well-known from *in vitro* also apply *in vivo*: the spring constants characterizing optical trapping of lipid granules inside *S. pombe* yeast cells increase linearly with laser power.[42] This approach was also applied to investigate kinesin and dynein motors in live A549 human epithelial cells and in *Dictyostelium discoideum*.[43]

A slightly different, yet comparable method relies on fitting parameters of a proposed model for the viscoelasticity of the cytoplasm and has provided detailed information on microtubule motors in living cells, using endocytosed latex beads as tracer particles.[44]

What can be trapped?

Individual bio-molecules usually cannot be trapped because the induced dipole moment by the optical trap is not large enough. Therefore, a handle, that can be trapped, is typically specifically and firmly attached to the molecule of interest. Individual polystyrene and silica beads with diameters of several micrometers,[33,45] quantum dots,[46] and various metallic nanoparticles with sizes down to ~10 nm can be optically trapped.[47,48] For *in vivo* studies lipid granules that occur naturally inside most cells are particularly attractive as handles because they need not be internalized and can easily be optically trapped.[49–53] Furthermore, they are often transported by kinesin and dynein, hence these motors are conveniently studied *in vivo* using lipid granules as handles. One shortcoming of optical tweezers is that they lack selectivity and therefore, all dielectric objects with an index of refraction that is larger than the surrounding medium and with an inducible dipole large enough will be trapped. *In vitro* such artefacts can be avoided or brought to a minimum by keeping the concentration of handles in the sample chamber very low. However, in a living cell this is not possible and during the analysis one needs to take into account that maybe more handles are in the trap than aimed for.

Internalizing and conjugating the handle

Unless an endogenously occurring object, such as a lipid granule, is used as a handle for the optical manipulation, the handle needs to be internalized into the cell. Internalizing the handle may distort cellular integrity. The gentlest approach is probably to let the cell endocytose the handle. With many cell types this can be achieved simply by adding particles to the solution containing the cells. An example is given in Fig. 3,

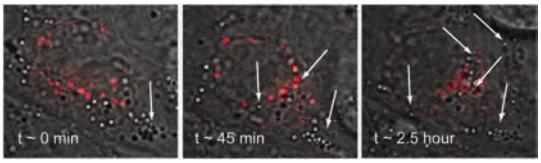

Fig. 3 Endocytosis of 60 nm gold nanoparticles (yellow and marked by a white arrow) by H727 neuroendocrine cancer cells. The lysosomes (marked with Cell light lysosome-RFP; red) are the end destination of the endocytotic pathway and over time it is seen that the fraction of co-localization of the gold nanoparticles with the lysosomes increases.

which shows endocytosis of 60 nm gold nanoparticles by H727 neuroendocrine cancer cells. Conveniently, the size range of endocytotic uptake corresponds well to the size range of handles that can be stably optically trapped.[54] During endocytosis, nanoparticles in contact with the outer cell membrane, either non-specifically or by receptor recognition, are engulfed by large encapsulating lipid compartments called endosomes. Upon internalization, the endosomes are transported, typically along microtubules, to their designated location or the end terminal of the endosomal pathway, the lysosomes. The lysosomes are responsible for degrading the content of the endosomes by means of a highly hostile environment. If, however, one wishes to explore other parts of the cellular machinery than the endocytotic pathway, this approach has the shortcoming that the handle needs to be released from the coating vesicle and actively pulled to the location of interest inside the cell. Another pitfall is that during endocytosis, nanoparticles are typically encapsulated together as multiples (the diameter of the endosome is on the order of ~500 nm) and are therefore unavailable for individual manipulation unless efforts are made to release them from the endosomes.[54,55]

Micropipette injection of particles is an invasive strategy for internalization. Here, the handles are injected into the cytoplasm or nucleus by penetrating the cell wall and membranes with a glass pipette typically with a diameter of 0.2–0.5 μm.[56] An example of this is shown in Fig. 4 where a micropipette was

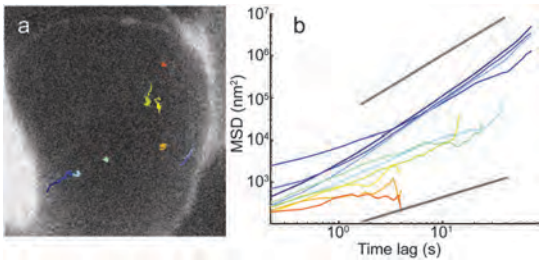

Fig. 4 Diffusion of 125 nm gold nanoparticles that are micropipetted into a neuroendocrine cancer cell. (a) Image of a cell with the extra-cellular space fluorescently marked with Alexa Flour 488 hydrazide. Traces of diffusing gold nanoparticles are overlaid on the image. The traces are obtained from confocal scans (reflection mode). (b) The mean squared displacements (MSD) of the micropipette injected gold nanoparticles, same colour code as in (a). The lower full line has a slope of $\alpha = 0.75$, the upper a slope of $\alpha = 1.5$.

used to perforate a H727 neuroendocrine cancer cell and deliver 125 nm gold nanoparticles into the cytoplasm. Another invasive internalization methodology is to optically inject gold nanoparticles into cells by tightly focussing a laser and burning a hole in the cell membrane (photoporation).[57] Electrophoretic shock has also been used as a delivery strategy, but that causes the cells to become severely stressed by the applied voltage.[58] The advantage of these more invasive approaches is that the handles can be mono-dispersedly internalized into the cell and in principle at any location inside the cell. These 'membrane rupturing approaches', however, have the drawback that they depend on the recovery of the cell membrane after penetration which might not always be possible. Alternative methodologies for internalizing nanoparticles in cells are reviewed in ref. 58 and 59.

It is important that the handle is firmly and specifically attached to the molecule of interest in a one-to-one ratio. One of the main pitfalls of single molecule investigations, in particular *in vivo*, is that the handle, or visualization marker, may not be specifically attached to the molecule of interest or may be attached to multiple of those molecules. Ideally, handle attachment should be specific, strong and not affect the physiological state of the cell. Two successfully used schemes to specifically conjugate single molecules in the living cell are *via* receptor–ligand or antibody–antigen binding. The most commonly used conjugation is the biotin–streptavidin bond, whose strength is nearly the same as that of a covalent bond. Another, but weaker, antibody–antigen-based conjugation is the antidigoxigenin–digoxigenin bond. Other useful schemes include reactive cysteine residues and histidines. Many particles are commercially available with these functionalizations.

Though specific interactions between the biomolecule and the handle are important, reducing unspecific binding is also most crucial. Unspecific interactions between the handle and molecules in the media can easily introduce noise and artefacts. Proteins like bovine serum albumin and α-casein can significantly reduce unspecific interactions; however in the crowded cytoplasm inside the cell it is nearly impossible to prevent unspecific binding completely and clever control measurements must be done instead.

Heating

When performing optical tweezer measurements part of the focused laser light might be absorbed by the living cell or by the handle. Absorbed light is dissipated as heat into the surrounding tissue thus leading to a local temperature elevation. The absorption of infrared light by biological tissue or by silica and polystyrene handles is relatively minor and in aqueous environments typically leads to temperature elevations of 1 °C or less.[60] This value is consistent with a heating of ~1.15 °C per 100 mW found in a cell confined by a 1064 nm trapping laser.[61]

The size range of which metallic nanoparticles can be stably trapped[48] makes them particularly favourable as force transducing handles inside the crowded cytoplasm. Furthermore, the size range is compatible with internalization through the endocytotic pathway. However, due to the plasmonic properties of metallic nanoparticles, they have significant absorption, also in the infrared, and can cause a substantial heating, depending on the particle size,[62] shape,[63] and composition.[64] The temperature elevation at the surface of metallic nanoparticles can easily reach hundreds of degree Celsius, however, if the particle is chosen small enough (*e.g.*, with a diameter of 40 nm) and is irradiated at typical laser powers at the sample (~100 mW) the temperature elevation is too small to be detectable in a sensitive assay based upon the phase-dependent partitioning of fluorophores in a lipid bilayer,[62] that is, it is probably below a couple of degree Celsius.

In conclusion, the temperature increase around optically trapped polystyrene beads, silica beads, or small metallic nanoparticles is probably so low that it would not interfere with physiological processes. Though, it should be noted that most temperature determining assays were carried out in an aqueous environment with larger heat conductivity than inside the cytoplasm; the temperature elevation inside a cell is expected to be larger than in an aqueous sample.

Physiological damage

Since Arthur Ashkin reported the survival of optically trapped microorganisms,[2] it has been a general consensus in the field that upon correct choice of laser wavelength and power, the physiological damage induced by optical traps is minor. Later studies have elaborated on this conjecture: one important effect of the infrared laser beam is that it produces free radicals and singlet oxygen, which has a high reactivity. Membranes and nucleic acids are sensitive to oxygen radicals that can cause oxidative stress and membrane rupture amongst others. Neuman *et al.*[65] addressed the role of oxygen in photodamage in optical trapping of *E. coli* using laser wavelengths from 790 nm to 1064 nm. They measured the rotation rate of the flagella of a trapped *E. coli* under both aerobic and anaerobic conditions[65] and found that the photoinduced damage varied with laser wavelength and that it was significantly higher under aerobic than anaerobic conditions. An effect of photoinduced radicals was also observed in a single molecule assay tethering DNA between two microspheres under both aerobic and anaerobic conditions.[66] Generation of reactive oxygen species has been assessed for mammalian cell lines as well, where exposure to pulsed lasers was shown to be more likely to trigger the formation of reactive oxygen species than exposure to CW lasers.[67]

Trapping of microorganisms such as *E. coli* and *Listeria* has been shown to comprise the ability of the microorganism to maintain a proton gradient across the cell membrane.[68] The physiological damage was dependent on laser power and trapping time, hence, on the integrated power deposited in the organism. However, if trapping powers and exposure times were kept low, no physiological damage was observed.[68]

In conclusion, optical tweezers based on near infrared lasers do impose some degree of physiological damage and probably trigger stressful photochemical reactions.[53,65,69,70] Therefore, for *in vivo* measurements, it is advisable to keep laser exposure time and power to a minimum.

Optical trapping inside the living cell

Objects that are large enough and with high enough optical contrast (mismatch in the index of refraction) to the cytoplasm can be trapped inside the living cell. The trapped objects can be moved around in 3D and, thanks to the development of *in vivo* calibration techniques, the forces acting on the trapped objects can be measured. The biological processes in the cytoplasm are highly complex and many are regulated by mechanical forces, *e.g.*, molecular motor and membrane protein motility, cell differentiation and cellular motility, as visualized in Fig. 5.

The local environment inside a cell may influence or temporarily modulate the function of biomolecule dynamics. Also, in contrast to most *in vitro* studies, a single motor cannot be isolated *in vivo* and many motors probably naturally work in a collective fashion in the living cell. In the subsequent sections we present the progress made using optical tweezers *in vivo*.

Micro-rheology

The first step towards measurements inside the living cell is to internalize and specifically attach the handle to the molecule of interest. As detailed above, there are several ways to do this. If the handles are micropipetted into the cell, some of these will diffuse randomly inside the cell and others will be picked up by molecular motors. An example of this is shown in Fig. 4, where Fig. 4(a) shows an image of H727 neuroendocrine cancer cells. Gold nanoparticles were microinjected into the cell and the traces of the injected particles tracked. Some of the particles hardly moved (red traces), others performed subdiffusive motion (yellow and light blue traces) while others moved in a linear fashion (blue traces). Dynamics within the cytoplasm can be described by different classes of diffusion. These are characterized by the scaling behaviour of the mean squared displacement, $\mathrm{MSD}(\tau) = \langle [r(t+\tau) - r(t)]^2 \rangle$, $r(t)$ being the position of the particle at time t and τ being the time lag. $\mathrm{MSD} = 2Dt^{\alpha}$, where D is the diffusion constant and α is the scaling exponent. The scaling exponent, α, yields information on whether the motion is subdiffusive ($\alpha < 1$), normal diffusion ($\alpha = 1$), or superdiffusive ($\alpha > 1$). In the experiment depicted in Fig. 4, the red traces have $\alpha \sim 0$, thus exhibiting confined diffusion, the yellow and light blue traces have $\alpha \sim 0.75$, hence are subdiffusive, as often observed for passive tracers inside living cells,[42,51,71,72] in accordance with the behavior of semiflexible polymer networks.[73] The blue traces are the result of superdiffusion ($\alpha \sim 1.5$) in accordance with observations of 1–2 μm polystyrene beads in a study of human SV80 cells[74] and micro-injected quantum dots in HeLa cells.[75] If the goal is to study molecular motors inside a living cell, then the super-diffusive particles are the tracers most likely to be bound to active molecular motors.

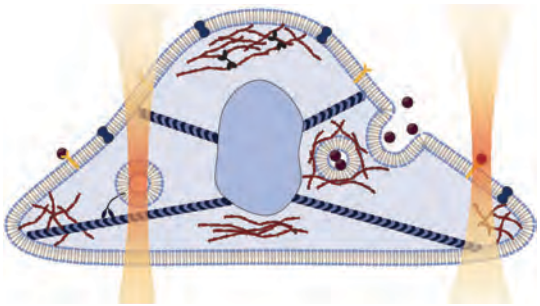

Fig. 5 Illustration of the cellular machinery. Molecular motors such as kinesin and dynein carry cargo along microtubules (blue filaments), whereas the molecular motors in the myosin family move along actin (red filaments). The complex polymer network in the cytoplasm facilitates cellular transport and is also responsible for maintaining cell shape, organelle organization and for cell motility. The membrane contains a large variety of proteins responsible for signal transduction, cell adhesion and recognition, and transport of molecules and nutrients across the membrane. During endocytosis the membrane makes an invagination through which the object is engulfed. Anything with a large enough optical contrast to the cytoplasm can be optically trapped.

Optical tweezers have successfully been used to expand micro-rheology measurements in living cells. The timescales probed with optical tweezers are on the order of (10^{-6}–10^{-3} s),[42,51,71] a regime that is unavailable to standard video based rheology measurements (>0.01 s),[42,51] thus making optical tweezers able to access regimes where interesting dynamics, *e.g.*, weak ergodicity breaking occurs.[52]

Also the impact of the cytoskeletal subcomponents on cellular microrhelogy has been explored. It was found that passive tracers, lipid granules inside *S. pombe*, performed subdiffusional motion at all times during the cell cycle, albeit with a significantly larger scaling exponent during mitosis ($\alpha \sim 0.84$) than during interphase ($\alpha \sim 0.81$).[71] This was attributed to the fact that the network of microtubules are denser, thus making the cytoplasm more elastic during mitosis.[71] Similar lipid granules were also shown to diffuse more freely upon disruption of cellular actin.[51]

The contribution of intermediate filaments to the viscoelasticity of the cytoplasm has recently been assessed using mouse embryonic fibroblasts.[76] Here the influence of vimentin, one of the most common intermediate filaments, was studied using both optical tweezers and video-based particle tracking. The motion of endogenous granules was found to decrease in the presence of vimentin intermediate filaments suggesting that the vimentin network helps localizing cytoplasmic organelles by stiffening the local environment.

As described above, also the viscoelastic modulus $G(f)$ can be extracted from passive and active *in vivo* optical tweezers calibration. This was done using optically trapped granules inside an *S. pombe* cell and showed that the elastic response of the viscoelastic modulus $Re[G]$, also denoted G', increased with an exponent of $\alpha = 0.75$ as a function of frequency,[42] consistent with earlier data.[51] In the narrow frequency window between 5 and 75 Hz G' for *S. pombe* was found to range from $G' \sim 4$ to 30 Pa.[42,51] In mouse embryonic fibroblasts with an intact vimentin network, the elastic response of the viscoelastic modulus was found to be $G' \sim 10$ Pa at 1 Hz with a diffusion exponent of $\alpha = 0.25$ in the frequency range from 1 to 100 Hz.[76] This viscoelastic modulus is significantly larger than the value obtained in *S. pombe* at 1 Hz ($G' \sim 1$ Pa),[42,51] however when

View Article Online
Review Article PCCP

assessed by the diffusion exponent the cytoplasm of the mouse embryonic fibroblasts is also significantly more elastic (α = 0.25)[76] than the cytoplasm of *S. pombe* ($\alpha \sim 0.75$).[42,51] Further, when comparing G' from wild-type mouse embryonic fibroblasts at 1 Hz ($G' \sim 10$ Pa) to G' from vimentin deficient mouse embryonic fibroblasts cells at the same frequency ($G' \sim 5$ Pa) it is clear that the presence of vimentin intermediate filaments stiffens the cytoplasm.[76]

Membrane protein dynamics

The plasma membrane of a cell consists of a phospholipid bilayer that is compartmentalized into many small domains. Embedded into the membrane is a large variety of proteins having essential roles for proper cell function, for instance for communication between the exterior and interior of the cell, transportation across the membrane of ions, nutrients and enzymes, and cell adhesion and recognition.

One of the early applications of optical tweezers *in vivo* was to characterize diffusion of proteins in the membrane of eukaryotic cells.[77,78] Handles composed of 210 nm latex beads or 40 nm colloidal gold particles were in one study attached to a membrane protein and dragged laterally through the plasma membrane of normal rat kidney fibroblastic cells.[78] The force required to drag the protein ranged from 0.05 pN to 0.8 pN, the large range probably signifying the viscoelastic heterogeneity of the plasma membrane which is known to be compartmentalized. In a later study, a method was developed by which the diffusion of the protein in its native location (without dragging it over large distances through the membrane) was studied by optical tweezers.[79] In this study GPI-anchored proteins appeared to localize at a lipid raft for extended periods of time.[79]

Optical tweezers were also used to study the diffusion of proteins in the membrane of prokaryotes. Gram-negative bacteria have several membrane layers in contrast to that of most mammalian cells. In addition to the inner bilayer Gram-negative bacteria also have both an outer membrane consisting of a lipopolysaccharide coat and a peptidoglycan layer separating the plasma membrane from the outer membrane. Using optical tweezers, the local diffusion of a single transmembrane protein, the λ-receptor, in the outer membrane of an *E. coli* was probed by measuring its Brownian motion.[80] It was found that the λ-receptor had a low diffusion constant compared to diffusion in the eukaryotic membranes. Also, the dynamics of the λ-receptor was found to be energy dependent[81] and to correlate with the dynamic reassembly of the peptidoglycan layer.[82] These findings indicated that the λ-receptor is attached to the peptidoglycan layer and that its diffusion is closely linked to the metabolism of the cell, hence it is not a pure thermal diffusion. These results suggest that membrane diffusion studied *in vitro* will be different from *in vivo* studies as the active component linked to cell metabolism is lacking *in vitro*.

Molecular motors

Large molecules, filaments or organelles in the living cell are transported, translocated or rotated actively by motor proteins. These motor proteins use ATP to generate force as they perform their biased motions.

Two classes of motors that transport cargo along microtubules have been identified: the kinesin family that translocates towards the microtubules plus-end and cytoplasmic dynein translocating towards the minus-end. *In vivo* investigations have shown that molecular motors perform saltatory motion in the cellular viscoelastic environment[83,84] and that the stall force, *i.e.*, the minimum force needed to stall a motor pulling on its cargo, for kinesin family is 5–7 pN[43] and for dynein is 1–8 pN.[22,43,44]

The consensus is that *in vivo* several motors are typically involved in cargo transport[85] and, in particular, that cargo is transported along microtubules by complements of kinesin and dynein motors.[86] Furthermore, in a study using endogenously occurring lipid granules as handles in an A549 human cancer cell, the forces exerted by individual motors are found to be additive.[49] Thus, the stall force of *in vivo* active transport allows the identification of the individual motors in the complement.

From a study of phagocytosed latex beads in mouse macrophage cells, the cargo motility along microtubules was found to be the result of a collective motion of a few kinesin molecules moving towards the plus-end, and many dynein moving towards the minus-end.[44] It was also shown that coupled motors at high loads often synchronize their steps to move in the characteristic 8 nm steps along microtubules.[44] Furthermore, in an assay with kinesin-1 and dynein-driven lipid droplets in *Drosophila* embryos, it was found that if the cargo transported in one direction was stalled and detached, it was more prone to be transported in the same direction when resumed.[87]

The stall forces of kinesin and dynein *in vivo* were investigated using endogenous lipid granules in A549 human cancer cells and latex beads in *Dictyostelium discoideum* as optical trapping handles.[43] Stall forces, depicted in Fig. 6(a) and (b) for A549 cells and in Fig. 6(c) and (d) for *Dictyostelium*, were shown to be different in the plus-end and minus-end directions. Interestingly, the plus-end directed (outward) stall force was found to be lower than the *in vitro* value for kinesin, implying that often both kinesins and dyneins attach to the cargo and pull in opposite directions in a tug-of-war manner.[88–90] In the minus-end direction (inwards) the stalling forces were higher than measured for individual dynein *in vitro*, implying that several dyneins (and no kinesins) were acting in a collective fashion during inward motion. Fig. 6(e) shows examples of the dislocation of the cargo, the time traces show regions of linear movement in both directions interrupted by stalls. It has been proposed that even though both dynein and kinesin are bound to the cargo, only motors of one polarity are active at any instant of time, with the activity being reversible with the aid of a co-factor.[22] A candidate co-factor has been identified in a study of kinesin in monkey fibroblasts, where casein kinase 2 is found to regulate kinesins that are attached to their cargo.[91] Also, dyneins are found to team up to generate large forces.[92]

Filopodia dynamics has been shown *via* optical tweezers to be regulated partly by F-actin filament polymerization and depolymerisation,[93] and partly by mechanical work conducted by actin-based myosin molecular motors, inducing a retrograde flow.[94] Using optically trapped IgG-coated polystyrene beads attached to the tip of a filopodium discrete steps during

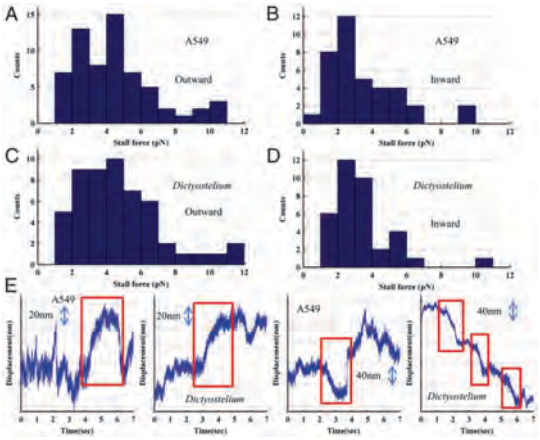

Fig. 6 *In vivo* stall force measurements for lipid granules in A549 human cancer cells (A and B) and for endocytosed latex beads in *Dictyostelium* (C and D). (A and B) Stall force histograms of outward (A) and inward cargo motility (B) in A549 cells. (C and D) Stall force histograms of outward (C) and inward cargo motility (D) in *Dictyostelium*. The distributions for the two cell types are very similar. Both imply significant differences between the stall forces for inward and outward motion. (E) Examples of cargo traces showing periods of active motion in both directions interrupted by stalls. Reproduced with permission from Blehm *et al.*[43]

filopodia retraction were observed, the step sizes were ~36 nm, consistent with myosin being the motor responsible for filopodia retraction.[94] As forces up to 19 pN were measured, most likely several molecular myosin motors work cooperatively to retract filopodia.

The status of the field is that the motors most frequently studied with optical tweezers are kinesin and dynein. Without doubt, this is attributed to the fact that these motors carry endogenously occurring lipid granules that are easily optically trapped and serve as excellent force-transducing handles. However, there are also other endogenously occurring 'objects' in the cell that can be optically manipulated. One such example is the chromosomes that can be trapped to estimate the forces exerted by molecular motors on the mitotic spindle, in this manner the stalling force for chromosome movements in *Mesostoma* spermatocytes was estimated to be 2.3 pN and in crane-fly spermatocytes to be 6–10 pN.[95]

Outlook

Until now optical tweezers have predominantly been used *in vitro*, however, as most of the challenges connected to *in vivo* use of this technique[24] have now been overcome, exciting novel quantitative *in vivo* single molecule results are now beginning to appear.[5,86] Though optical tweezers have themselves very large potential for single molecule *in vivo* investigations, another advantage is that they can easily be combined with other techniques, such as fluorescent imaging,[96] which gives an even larger potential for revealing connections between, *e.g.*, mechanical force and biochemical regulation. Recently, a clever methodology was invented where super-resolution STED microscopy was combined with optical trapping; this equipment was used to reveal protein dynamics on DNA.[97] This type of super-resolution microscopy combined with state-of-the-art force measuring optical traps has huge potential for uncovering fundamental mechanical–biochemical action–reaction schemes inside the living cell.

So far, all reported *in vivo* single molecule optical tweezer investigations were carried out in 2D cell cultures, on single celled microorganisms, or with single cells isolated from multicell organisms or tissue. However, as laser light has the ability to penetrate deep into biological tissue, it is likely that optical traps could be used to investigate also the mechanics within multi-cellular organisms or deep into tissue. Or, as optical tweezers have proven to be able to trap synaptic vesicles,[98] maybe the technique can even shed light on the fundamental mechanism and mechanics governing nerve conduction and development of neuronal diseases.

Acknowledgements

We acknowledge financial support from the Carlsberg Foundation and an excellence grant from the University of Copenhagen.

Notes and references

1 A. Ashkin, K. Schutze, J. M. Dziedzic, U. Euteneuer and M. Schliwa, *Nature*, 1990, **348**, 346–348.
2 A. Ashkin and J. M. Dziedzic, *Science*, 1987, **235**, 1517–1520.
3 K. C. Neuman and A. Nagy, *Nat. Methods*, 2008, **5**, 491–505.
4 C. Veigel and C. F. Schmidt, *Nat. Rev. Mol. Cell Biol.*, 2011, **12**, 163–176.
5 L. B. Oddershede, *Nat. Chem. Biol.*, 2012, **8**, 879–886.
6 M. J. Rust, M. Bates and X. Zhuang, *Nat. Methods*, 2006, **3**, 793–795.
7 T. A. Klar, S. Jakobs, M. Dyba, A. Egner and S. W. Hell, *Proc. Natl. Acad. Sci. U. S. A.*, 2000, **97**, 8206–8210.
8 D. T. Tambe, C. C. Hardin, T. E. Angelini, K. Rajendran, C. Y. Park, X. Serra-Picamal, E. H. Zhou, M. H. Zaman, J. P. Butler, D. A. Weitz, J. J. Fredberg and X. Trepat, *Nat. Mater.*, 2011, **10**, 469–475.
9 R. D. Gonzalez-Cruz, V. C. Fonseca and E. M. Darling, *Proc. Natl. Acad. Sci. U. S. A.*, 2012, **109**, E1523–E1529.
10 K. Svoboda, C. F. Schmidt, B. J. Schnapp and S. M. Block, *Nature*, 1993, **365**, 721–727.
11 K. Visscher, M. J. Schnitzer and S. M. Block, *Nature*, 1999, **400**, 184–189.
12 C. L. Asbury, A. N. Fehr and S. M. Block, *Science*, 2003, **302**, 2130–2134.
13 C. Veigel, L. M. Coluccio, J. D. Jontes, J. C. Sparrow, R. A. Milligan and J. E. Molloy, *Nature*, 1999, **398**, 530–533.
14 C. Veigel, J. E. Molloy, S. Schmitz and J. Kendrick-Jones, *Nat. Cell Biol.*, 2003, **5**, 980–986.
15 L. Laan, J. Husson, E. L. Munteanu, J. W. Kerssemakers and M. Dogterom, *Proc. Natl. Acad. Sci. U. S. A.*, 2008, **105**, 8920–8925.

16 M. J. Footer, J. W. Kerssemakers, J. A. Theriot and M. Dogterom, *Proc. Natl. Acad. Sci. U. S. A.*, 2007, **104**, 2181–2186.
17 M. D. Wang, H. Yin, R. Landick, J. Gelles and S. M. Block, *Biophys. J.*, 1997, **72**, 1335–1346.
18 P. Gross, N. Laurens, L. B. Oddershede, U. Bockelmann, E. J. G. Peterman and G. J. L. Wuite, *Nat. Phys.*, 2011, **7**, 731–736.
19 L. Shokri, B. Marintcheva, M. Eldib, A. Hanke, I. Rouzina and M. C. Williams, *Nucleic Acids Res.*, 2008, **36**, 5668–5677.
20 J. van Mameren, P. Gross, G. Farge, P. Hooijman, M. Modesti, M. Falkenberg, G. J. Wuite and E. J. Peterman, *Proc. Natl. Acad. Sci. U. S. A.*, 2009, **106**, 18231–18236.
21 T. Paramanathan, I. Vladescu, M. J. McCauley, I. Rouzina and M. C. Williams, *Nucleic Acids Res.*, 2012, **40**, 4925–4932.
22 S. P. Gross, M. A. Welte, S. M. Block and E. F. Wieschaus, *J. Cell Biol.*, 2000, **148**, 945–956.
23 Z. Wang, S. Khan and M. P. Sheetz, *Biophys. J.*, 1995, **69**, 2011–2023.
24 Y. F. Dufrene, E. Evans, A. Engel, J. Helenius, H. E. Gaub and D. J. Muller, *Nat. Methods*, 2011, **8**, 123–127.
25 A. Kyrsting, P. M. Bendix and L. B. Oddershede, *Nano Lett.*, 2013, **13**, 31–35.
26 S. N. S. Reihani, S. A. Mir, A. C. Richardson and L. B. Oddershede, *J. Opt.*, 2011, **13**, 105301.
27 A. Rohrbach and E. H. K. Stelzer, *J. Appl. Physiol.*, 2002, **91**, 5474–5488.
28 K. C. Neuman and S. M. Block, *Rev. Sci. Instrum.*, 2004, **75**, 2787–2809.
29 F. Gittes and C. F. Schmidt, *Opt. Lett.*, 1998, **23**, 7–9.
30 K. Visscher and S. M. Block, *Methods Enzymol.*, 1998, **298**, 460–489.
31 M. T. Valentine, N. R. Guydosh, B. Gutierrez-Medina, A. N. Fehr, J. O. Andreasson and S. M. Block, *Opt. Lett.*, 2008, **33**, 599–601.
32 A. C. Richardson, N. Reihani and L. B. Oddershede, *Proc. SPIE*, 2006, **6326**, 632628.
33 A. Rohrbach, *Phys. Rev. Lett.*, 2005, **95**, 168102.
34 A. Pralle, E. L. Florin, E. H. K. Stelzer and J. K. H. Horber, *Appl. Phys. A: Mater. Sci. Process.*, 1998, **66**, S71–S73.
35 F. Gittes and C. F. Schmidt, *Methods Cell Biol.*, 1998, **55**, 129–156.
36 K. Berg-Sørensen and H. Flyvbjerg, *Rev. Sci. Instrum.*, 2004, **75**, 594–612.
37 M. Atakhorrami, J. I. Sulkowska, K. M. Addas, G. H. Koenderink, J. X. Tang, A. J. Levine, F. C. MacKintosh and C. F. Schmidt, *Phys. Rev. E: Stat., Nonlinear, Soft Matter Phys.*, 2006, **73**, 061501.
38 A. Farre and M. Montes-Usategui, *Opt. Express*, 2010, **18**, 11955–11968.
39 S. B. Smith, Y. Cui and C. Bustamante, *Methods Enzymol.*, 2003, **361**, 134–162.
40 M. Fischer and K. Berg-Sørensen, *J. Opt. A: Pure Appl. Opt.*, 2007, **9**, S239.
41 M. Fischer, A. C. Richardson, S. N. Reihani, L. B. Oddershede and K. Berg-Sorensen, *Rev. Sci. Instrum.*, 2010, **81**, 015103.
42 J. Mas, A. C. Richardson, S. N. S. Reihani, L. B. Oddershede and K. Berg-Sørensen, *Phys. Biol.*, 2013, **10**, 046006.
43 B. H. Blehm, T. A. Schroer, K. M. Trybus, Y. R. Chemla and P. R. Selvin, *Proc. Natl. Acad. Sci. U. S. A.*, 2013, **110**, 3381–3386.
44 A. G. Hendricks, E. L. Holzbaur and Y. E. Goldman, *Proc. Natl. Acad. Sci. U. S. A.*, 2012, **109**, 18447–18452.
45 J. R. Moffitt, Y. R. Chemla, S. B. Smith and C. Bustamante, *Annu. Rev. Biochem.*, 2008, **77**, 205–228.
46 L. Jauffred, A. C. Richardson and L. B. Oddershede, *Nano Lett.*, 2008, **8**, 3376–3380.
47 P. M. Hansen, V. K. Bhatia, N. Harrit and L. Oddershede, *Nano Lett.*, 2005, **5**, 1937–1942.
48 P. M. Bendix, L. Jauffred, K. Norregaard and L. B. Oddershede, *IEEE J. Sel. Top. Quantum Electron.*, 2014, **20**, 1–12.
49 P. A. Sims and X. S. Xie, *ChemPhysChem*, 2009, **10**, 1511–1516.
50 G. T. Shubeita, S. L. Tran, J. Xu, M. Vershinin, S. Cermelli, S. L. Cotton, M. A. Welte and S. P. Gross, *Cell*, 2008, **135**, 1098–1107.
51 I. M. Tolic-Norrelykke, E. L. Munteanu, G. Thon, L. Oddershede and K. Berg-Sorensen, *Phys. Rev. Lett.*, 2004, **93**, 078102.
52 J. H. Jeon, V. Tejedor, S. Burov, E. Barkai, C. Selhuber-Unkel, K. Berg-Sorensen, L. Oddershede and R. Metzler, *Phys. Rev. Lett.*, 2011, **106**, 048103.
53 L. Sacconi, I. M. Tolic-Norrelykke, C. Stringari, R. Antolini and F. S. Pavone, *Appl. Opt.*, 2005, **44**, 2001–2007.
54 T.-G. Iversen, T. Skotland and K. Sandvig, *Nano Today*, 2011, **6**, 176–185.
55 S. H. Wang, C. W. Lee, A. Chiou and P. K. Wei, *J. Nanobiotechnol.*, 2010, **8**, 33.
56 Y. Zhang and L.-C. Yu, *BioEssays*, 2008, **30**, 606–610.
57 C. McDougall, D. J. Stevenson, C. T. A. Brown, F. Gunn-Moore and K. Dholakia, *J. Biophotonics*, 2009, **2**, 736–743.
58 J. B. Delehanty, H. Mattoussi and I. L. Medintz, *Anal. Bioanal. Chem.*, 2009, **393**, 1091–1105.
59 R. Levy, U. Shaheen, Y. Cesbron and V. See, *Nano Rev.*, 2010, **1**, 4889.
60 E. J. Peterman, F. Gittes and C. F. Schmidt, *Biophys. J.*, 2003, **84**, 1308–1316.
61 Y. Liu, D. K. Cheng, G. J. Sonek, M. W. Berns, C. F. Chapman and B. J. Tromberg, *Biophys. J.*, 1995, **68**, 2137–2144.
62 P. M. Bendix, S. N. Reihani and L. B. Oddershede, *ACS Nano*, 2010, **4**, 2256–2262.
63 H. Y. Ma, P. M. Bendix and L. B. Oddershede, *Nano Lett.*, 2012, **12**, 3954–3960.
64 H. Ma, P. Tian, J. Pello, P. M. Bendix and L. B. Oddershede, *Nano Lett.*, 2014, **14**, 612–619.
65 K. C. Neuman, E. H. Chadd, G. F. Liou, K. Bergman and S. M. Block, *Biophys. J.*, 1999, **77**, 2856–2863.
66 M. P. Landry, P. M. McCall, Z. Qi and Y. R. Chemla, *Biophys. J.*, 2009, **97**, 2128–2136.
67 S. K. Mohanty, M. Sharma and P. K. Gupta, *Photochem. Photobiol. Sci.*, 2006, **5**, 134–139.
68 M. B. Rasmussen, L. B. Oddershede and H. Siegumfeldt, *Appl. Environ. Microbiol.*, 2008, **74**, 2441–2446.
69 H. Liang, K. T. Vu, P. Krishnan, T. C. Trang, D. Shin, S. Kimel and M. W. Berns, *Biophys. J.*, 1996, **70**, 1529–1533.

70 G. Leitz, E. Fallman, S. Tuck and O. Axner, *Biophys. J.*, 2002, **82**, 2224–2231.

71 C. Selhuber-Unkel, P. Yde, K. Berg-Sorensen and L. B. Oddershede, *Phys. Biol.*, 2009, **6**, 025015.

72 S. Yamada, D. Wirtz and S. C. Kuo, *Biophys. J.*, 2000, **78**, 1736–1747.

73 F. Gittes and F. C. MacKintosh, *Phys. Rev. E: Stat. Phys., Plasmas, Fluids, Relat. Interdiscip. Top.*, 1998, **58**, R1241–R1244.

74 A. Caspi, R. Granek and M. Elbaum, *Phys. Rev. E: Stat., Nonlinear, Soft Matter Phys.*, 2002, **66**, 011916.

75 S. Courty, C. Luccardini, Y. Bellaiche, G. Cappello and M. Dahan, *Nano Lett.*, 2006, **6**, 1491–1495.

76 M. Guo, A. J. Ehrlicher, S. Mahammad, H. Fabich, M. H. Jensen, J. R. Moore, J. J. Fredberg, R. D. Goldman and D. A. Weitz, *Biophys. J.*, 2013, **105**, 1562–1568.

77 M. Edidin, S. C. Kuo and M. P. Sheetz, *Science*, 1991, **254**, 1379–1382.

78 Y. Sako and A. Kusumi, *J. Cell Biol.*, 1995, **129**, 1559–1574.

79 A. Pralle, P. Keller, E. L. Florin, K. Simons and J. K. Horber, *J. Cell Biol.*, 2000, **148**, 997–1008.

80 L. Oddershede, J. K. Dreyer, S. Grego, S. Brown and K. Berg-Sorensen, *Biophys. J.*, 2002, **83**, 3152–3161.

81 T. Winther, L. Xu, K. Berg-Sorensen, S. Brown and L. B. Oddershede, *Biophys. J.*, 2009, **97**, 1305–1312.

82 T. Winther and L. B. Oddershede, *Curr. Pharm. Biotechnol.*, 2009, **10**, 486–493.

83 M. A. Welte, S. P. Gross, M. Postner, S. M. Block and E. F. Wieschaus, *Cell*, 1998, **92**, 547–557.

84 A. L. Jolly, H. Kim, D. Srinivasan, M. Lakonishok, A. G. Larson and V. I. Gelfand, *Proc. Natl. Acad. Sci. U. S. A.*, 2010, **107**, 12151–12156.

85 S. P. Gross, M. Vershinin and G. T. Shubeita, *Curr. Biol.*, 2007, **17**, R478–R486.

86 B. H. a. S. Blehm and P. R. Selvin, *Chem. Rev.*, 2014, DOI: 10.1021/cr4005555.

87 C. Leidel, R. A. Longoria, F. M. Gutierrez and G. T. Shubeita, *Biophys. J.*, 2012, **103**, 492–500.

88 V. Soppina, A. K. Rai, A. J. Ramaiya, P. Barak and R. Mallik, *Proc. Natl. Acad. Sci. U. S. A.*, 2009, **106**, 19381–19386.

89 A. G. Hendricks, E. Perlson, J. L. Ross, H. W. Schroeder, M. Tokito and E. L. F. Holzbaur, *Curr. Biol.*, 2010, **20**, 697–702.

90 A. Kunwar, S. K. Tripathy, J. Xu, M. K. Mattson, P. Anand, R. Sigua, M. Vershinin, R. J. McKenney, C. C. Yu, A. Mogilner and S. P. Gross, *Proc. Natl. Acad. Sci. U. S. A.*, 2011, **108**, 18960–18965.

91 J. Xu, B. J. Reddy, P. Anand, Z. Shu, S. Cermelli, M. K. Mattson, S. K. Tripathy, M. T. Hoss, N. S. James, S. J. King, L. Huang, L. Bardwell and S. P. Gross, *Nat. Commun.*, 2012, **3**, 754.

92 A. K. Rai, A. Rai, A. J. Ramaiya, R. Jha and R. Mallik, *Cell*, 2013, **152**, 172–182.

93 T. Bornschlogl, S. Romero, C. L. Vestergaard, J. F. Joanny, G. T. V. Nhieu and P. Bassereau, *Proc. Natl. Acad. Sci. U. S. A.*, 2013, **110**, 18928–18933.

94 H. Kress, E. H. Stelzer, D. Holzer, F. Buss, G. Griffiths and A. Rohrbach, *Proc. Natl. Acad. Sci. U. S. A.*, 2007, **104**, 11633–11638.

95 J. Ferraro-Gideon, R. Sheykhani, Q. Y. Zhu, M. L. Duquette, M. W. Berns and A. Forer, *Mol. Biol. Cell*, 2013, **24**, 1375–1386.

96 M. J. Lang, P. M. Fordyce, A. M. Engh, K. C. Neuman and S. M. Block, *Nat. Methods*, 2004, **1**, 133–139.

97 I. Heller, G. Sitters, O. D. Broekmans, G. Farge, C. Menges, W. Wende, S. W. Hell, E. J. G. Peterman and G. J. L. Wuite, *Nat. Methods*, 2013, **10**, 910–916.

98 P. M. Bendix and L. Oddershede, *Biophys. J.*, 2012, **102**, 87a.

ARTICLE ADDENDUM

Bacteriophage 4, e27517; January–December 2014; © 2014 Landes Bioscience

Effect of supercoiling on the λ switch

Kamilla Norregaard,[1] Magnus Andersson,[1,†] Kim Sneppen,[1] Peter Eigil Nielsen,[2] Stanley Brown,[1] and Lene B Oddershede[1,*]

[1]The Niels Bohr Institute; University of Copenhagen; Copenhagen, Denmark; [2]Department of Cellular and Molecular Medicine; Faculty of Health and Sciences; Copenhagen, Denmark

[†]Current affiliation: Department of Physics; Umeå University; Umeå, Sweden

The lysogenic state of the λ switch is exceptionally stable, still, it is capable of responding to DNA-damage and rapidly enter the lytic state. We invented an assay where PNA mediated tethering of a plasmid allowed for single molecule investigations of the effect of supercoiling on the efficiency of the epigenetic λ switch. Compared with non-supercoiled DNA, the presence of supercoils enhances the CI-mediated DNA looping probability and renders the transition between the looped and unlooped states steeper, thus increasing the Hill coefficient. Interestingly, the transition occurs exactly at the CI concentration corresponding to the minimum number of CI molecules capable of maintaining the pRM-repressed state. Based on these results we propose that supercoiling maintains the pRM-repressible state as CI concentration decline during induction and thus prevent autoregulation of *cI* from interfering with induction.

Keywords: supercoiling, λ switch, epigenetics, PNA, cooperativity, CI protein, tethered particle motion

Submitted: 11/08/2013

Revised: 12/12/2013

Accepted: 12/12/2013

http://dx.doi.org/10.4161/bact.27517

*Correspondence to: Lene B Oddershede; Email: oddershede@nbi.dk

Addendum to: Norregaard K, Andersson M, Sneppen K, Nielsen PE, Brown S, Oddershede LB. DNA supercoiling enhances cooperativity and efficiency of an epigenetic switch. Proc Natl Acad Sci U S A 2013; 110:17386–91; PMID:24101469; http://dx.doi.org/10.1073/pnas.1215907110

Introduction

The lysis–lysogeny decision by bacteriophage λ was the first genetic switch to be deciphered,[1] this epigenetic switch is now relatively well understood and the most important features are outlined in **Figure 1A and B**. One fascinating feature of this switch is the profound stability of the prophage state. The λ prophage responds to the host (*Escherichia coli*) DNA-damage sensing or SOS system. When the SOS pathway is induced, activated RecA protein catalyzes the self-cleavage of λ repressor protein, CI, causing the prophage to enter lytic development. In strains lacking RecA protein, three quarters of the released phage bear mutations in the *cI* gene.[2] Thus, the prophage state maintained by CI is more stable than the genes encoding components maintaining the repressed state. In fact, two more recent studies found 73 out of a total of 74 apparently wild type phage (*cI*$^+$) released from *recA* lysogens, were mutants in the promoter for repressor maintenance, pRM.[3,4] The rarity of wild type phage released from *recA* lysogens, as pointed out by Little and Michaelowski,[4] may not even be true escapees but may be the result of a mutation in the now dead host. The stability of the prophage state is in part due to the sophisticated regulation of CI synthesis (as detailed in **Fig. 1B**). The intracellular concentration of CI must be carefully fine-tuned such that it is high enough to maintain repression of lytic development but not too high to prevent sufficient degradation by activated RecA.[5] In the lysogenic state, CI activates its own synthesis from pRM.[6] At physiological concentrations CI can repress its own synthesis by binding to the operator, OR3, only if another segment of the prophage genome containing the operator OL3 is clamped next to OR3. The clamp is formed by CI binding as an octamer to the operators OL1-OL2 and OR1-OR2, thus arranging the intervening DNA in a loop (as depicted in **Fig. 1B**).[7] In other words, the OL-CI-OR looped state is necessary for CI repression of pRM.

CI-mediated looping of DNA has been extensively studied in vivo and

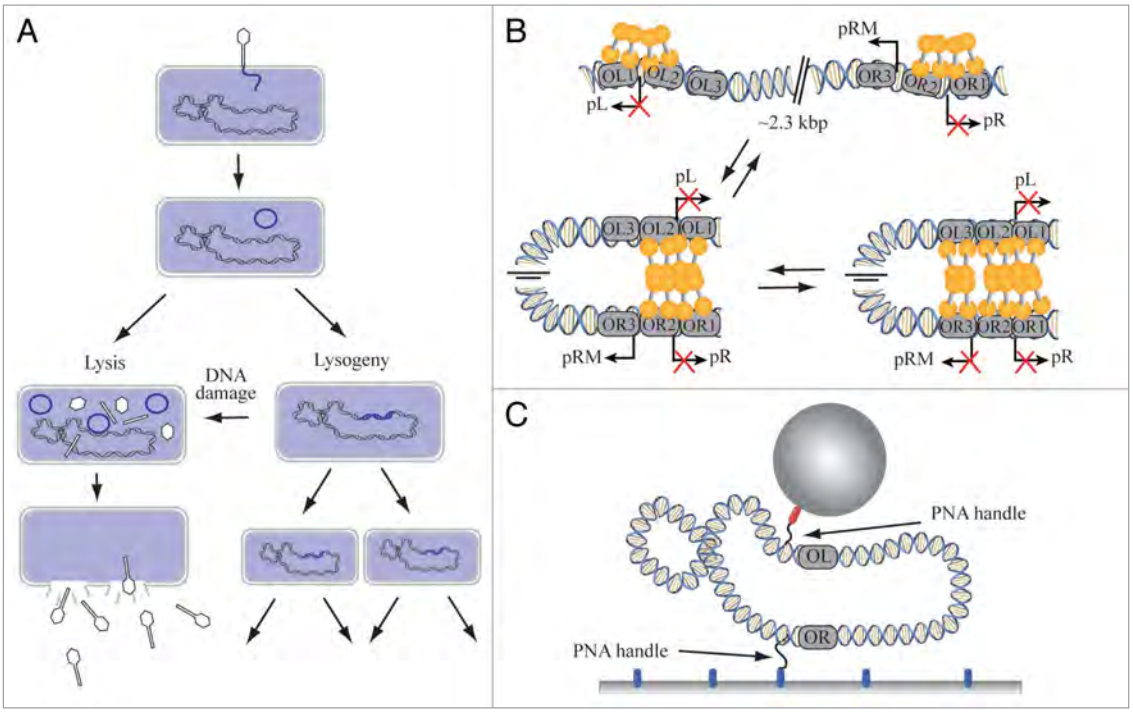

Figure 1. (**A**) λ phage survival strategies after infection of *Escherichia coli*. The phage enters either the lytic pathway (left) or the lysogenic pathway (right). The lytic pathway is irreversible and rapidly produces a crop of phage that is released by lysing the cell. The lysogenic pathway is a dormant state in which the phage DNA is incorporated into the host DNA and passively gets replicated until a signal (e.g., DNA damage) flips the switch and causes entering into the lytic state. (**B**) λ switch regulation. The λ operators, operator right (OR) and operator left (OL), are located ~2.3 kbp apart on the phage DNA overlapping the lysogenic (pRM) and lytic (pR and pL) promoters (marked by bent arrows). Each operator is a constellation of three adjacent sub sites that bind CI (yellow dumbbell) in a hierarchical manner. Cooperative binding between CI dimers bound at OR1 and the adjacent intrinsically weak operator OR2 virtually ensures simultaneously occupancy and is responsible for lytic repression (indicated by red cross) and simultaneously activation of the weak CI promoter pRM located at OR3. Long-range cooperativity affords increased stability to the lysogenic state by a CI octamer clamping OR1-OR2 and OL1-OL2 arranging the intervening DNA in a loop. This complex brings OL3 and OR3 in juxtaposition allowing a CI dimer bound on the intrinsic strong OL3 to assist a CI dimer binding at the weak OR3 resulting in pRM repression (marked by red cross). (**C**) The PNA-based TPM assay. A DNA plasmid is tethered between an anti-digoxigenin coated glass surface and a streptavidin coated polystyrene bead via digoxigenin/biotin PNA handles that form triplex invasion complexes with specific sequences on the DNA. The non-complementary strand is displaced as a small loop. The PNA handles are flanking the λ operators, OR and OL, which limit the λ immunity region.

in vitro. In vitro it was studied both in bulk and single molecule experiments,[8,9] where the most common single molecule approach employed was an assay where a linear DNA was tethered between a coverslip and a submicron sized bead whose Brownian motion was observed and analyzed. The larger the excursions of the particle, the longer the tether and the looped state (yielding an overall shorter DNA tether) could thereby be distinguished from the unlooped state. This type of single molecule assay relying on tethered particle motion (TPM) has confirmed the sites in OL and OR necessary for clamping.[9] Until recently, all TPM studies were performed with linear DNA with no supercoils unless they were mechanically introduced, e.g., by twisting a magnetic bead. Mechanically induced supercoils can be difficult to distinguish from protein-mediated looping events. In this addendum, we describe a novel TPM assay utilizing peptide nucleic acid (PNA) handles to tether natively supercoiled plasmid DNA.[10] We discuss, to our knowledge, the first single molecule evidence of the stability of the pRM repressible state at physiological CI levels and speculate what features of supercoiling may be responsible.

PNA Tethering of Supercoiled DNA

Recently, we developed a novel chemical/biological assay for investigating protein-mediated DNA looping at a single molecule level using naturally supercoiled DNA.[10] Our assay (shown in **Fig. 1C**) consists of a single supercoiled plasmid tethered by sequence specific PNA handles allowing us to tag points on circular DNA without introducing any breaks in the DNA. We attach the PNA handles such that they flank the λ immunity region, tethering the DNA molecule between a glass surface and a

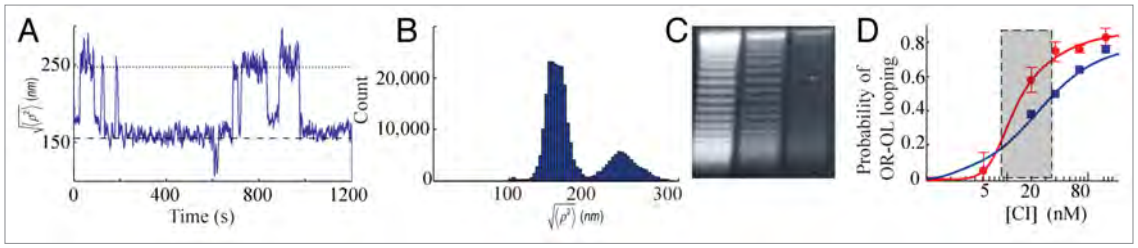

Figure 2. (**A**) The size of the thermal fluctuations of the plasmid tethered bead as function of time in presence of 80 nM CI. The unlooped state causes the bead to exhibit larger fluctuations (indicated by the dotted line) than the looped state (dashed line). (**B**) Histogram corresponding to the time series shown in (**A**), the left peak corresponds to the looped state, the right peak to the unlooped state. (**C**) Chloroquine gel containing 4-fold dilutions of the supercoiled plasmid preparation. The large number of bands confirms that there is a large spread in supercoils (writhe number) in the sample. (**D**) Probability of CI-mediated looping as function of CI concentration for supercoiled DNA (red circles) published in reference 10 and for linear DNA (blue squared) published by Zurla et al.[9] The lines show the corresponding thermodynamical models. Supercoiling enhances the binary response to changes in CI concentration and lowers the CI concentration necessary for pRM repression. The dashed box highlights the narrow sigmoidal transition interval for the supercoiled DNA. Interestingly, 20 nM CI (at the center of the transition interval) corresponds to 12 CI monomers available in the cell and this is exactly the number of CI molecules necessary to form a pRM repressible state. The number of data sets for each concentration is n = 4 for 5 nM CI, n = 7 for 20 nM CI, n = 5 for 40 nM CI, n = 6 for 80 nM CI, and n = 9 for 170 nM CI. Error bars represent one standard deviation.

submicron sized polystyrene bead. TPM experiments confirmed that we could distinguish the dynamics of supercoiled plasmids compared with that of relaxed plasmids and linear relaxed tethers.[10] Using this assay employing naturally supercoiled DNA, CI-mediated looping could be detected directly as a decrease in the Brownian motion of the tethered bead, thus producing a telegraph-like signal over time as shown in **Figure 2A**. We envision this PNA-based assay having numerous applications beyond studies of the λ switch. It could enable studies of protein/enzyme DNA interactions on supercoiled DNA mimicking the native bacterial DNA or eukaryotic chromatin, without the requirement of external interference, e.g., magnetic tweezers.[11-13] We caution interested researchers that in our TPM studies of supercoiled DNA we took great care with the purity of all reagents used: The plasmid DNA was purified through two rounds of isopycnic centrifugation with CsCl and ethidium bromide, the PNA was purified by HPLC and all solutions were filtered through several centimeter beds of fine sephadex to remove particles. We did not examine reagents purified by other methods and therefore cannot comment on their suitability for the supercoiled single molecule assay. We also manipulated all solutions containing PNA/DNA with low-binding and DNAase free plasticware.

Effect of Supercoiling on Looping Probability

Using the PNA-based single molecule assay, the probability of a DNA plasmid being in the looped state is determined by examining the thermal excursions of the tethered bead,

$$\sqrt{\langle \rho^2(t) \rangle_{20ms}}$$

as a function of time (see **Fig. 2A**). The corresponding histogram is shown in **Figure 2B** where the peak centered around 180 nm corresponds to the looped state and the peak around 250 nm to the unlooped state.

Plasmid DNA as recovered from bacteria contains a varying number of supercoils, the writhe number of any single plasmid molecule being constant throughout the looping experiments. To examine the distribution in writhe number, we electrophoresed a sample through a chloroquine gel as shown in **Figure 2C**. The large variety in writhe between plasmids with identical sequence and length posed a challenge to the interpretation of the looping dynamics because the magnitude of the Brownian motion from, say, an unlooped state would vary from one tethered bead to another. Also, this meant that a calibration curve relating sequence length to magnitude of Brownian fluctuation (as routinely done in the linear assays[14]) did not make sense for the supercoiled assay. To overcome this challenge, for each individual time series (as shown in **Fig. 2A**) we calculated the histogram (**Fig. 2B**) and assigned the lower peak to the looped state and the higher peak to the unlooped state. This assignment helped normalize all data sets and collapse them into a single histogram. The ratio of the area under the peak representing the looped state to the total area was then assigned as the probability of looping. This procedure was performed at different CI concentrations, thus establishing the looping probability as function of CI concentration for a supercoiled assay as shown in **Figure 2D** (red circles).

Finzi and coworkers examined CI-mediated looping probabilities using a linear DNA assay in the physiologically relevant CI concentration regime.[9] Their results are shown by blue squares in **Figure 2D**. In the linear assay, the DNA looping probability curve can be described by a low Hill coefficient (h = 1.2). This means the repressible state of pRM is continually responsive to changes in CI concentration and as CI is depleted with activated RecA, pRM will compensate by trying to produce more CI. Considering the sophistication of the prophage maintaining system, such counteraction of CI regulation against lytic induction would be surprising. We speculate that the observed low Hill coefficient was due to the relaxed

nature of linear DNA. This is supported by the results utilizing the supercoiled assay, where we found that the response of supercoiled DNA to varying concentrations of CI was very different from the response of linear or relaxed DNA[10] (compare red circles to blue squares in **Fig. 2D**). Instead of observing a continuous response to CI concentration, the supercoiled assay exhibited a sharp transition between the unlooped and looped state, the narrow transition interval is highlighted by a dashed box in **Figure 2D**. At CI concentrations above approximately 25% of the average lysogenic concentration (~200 nM CI[15]) the operators are nearly always in the looped, pRM-repressible state. Only when the CI concentration falls below approximately 5% of the average lysogenic concentration do the operators spend the majority of their time in the unlooped, pRM-non-repressible state.

The Hill coefficient describing the looping probability of naturally supercoiled DNA as function of CI concentration was estimated to be h = 2.5 (in contrast to h = 1.2 from the linear DNA). Regulatory proteins rarely act alone but instead cooperatively as a multi protein complex. A higher Hill coefficient can be interpreted as a higher degree of cooperativity in a system. Cooperativity helps ensure efficient discrimination between two states and simultaneously enhances a switch-like response to small changes in regulator concentration. Recently it was shown in vivo that DNA looping could be abolished if CI cooperativity was eliminated, supporting the necessity of cooperativity for λ switch efficiency.[16] Therefore, the observed increased Hill coefficient of the supercoiled DNA is in agreement with the binary developmental nature of the λ switch.

Features of Supercoiling Possibly Responsible for Higher Hill Coefficient

DNA supercoiling is an intrinsic property of the circular *Escherichia coli* DNA that helps compact the DNA in a highly condensed form. Because of the topology of supercoiled DNA it can in itself be considered as a regulatory parameter for many cellular processes such as transcription and protein interactions. DNA supercoiling has been found to facilitate protein-protein and enhancer-promoter communication over large distances by increasing the concentration of DNA segments in vicinity to each other.[12,17,18] In addition, changes in the degree of supercoiling induced by a previous RNA polymerase can either help a subsequent RNA polymerase to enter directly into the open complex or impede the movement of a RNA polymerase.[19] Supercoiling is also known to facilitate unwinding of short DNA segments and thereby expose single stranded DNA to which regulatory proteins preferentially bind.[13] Supercoiling is also thought to affect gene regulation by changing the local structure and dynamics of DNA[20] which can influence protein-DNA binding by making the helical structure more or less accessible for the proteins. The possibilities are many and future investigations will be necessary to determine what aspect of supercoiled DNA is responsible for the higher Hill coefficient.

Thermodynamic Parameters

By analyzing our data in the light of a thermodynamic model put forward in refs.[7,21,22] we estimated the cooperative binding energies associated with loop formation. The model including the free energies for the supercoiled system is shown as the red curve in **Figure 2D**. In the model, ΔG_{oct} represents the net free energy change due to octamerization of CI bound across OL-OR together with the cost of formation of a DNA loop, this was set to 0 kcal/mol. ΔG_{tetr} which represents the cooperative free energy due to tetramerization of CI bound across OL3-OR3 was set to -1.0 kcal/mol. By setting ΔG_{oct} to 0 kcal/mol we require that supercoiling together with octamerization of CI balances the cost of bending the DNA into a loop. This is in accordance with the facts that octamer-mediated looping has been established to be biologically relevant[7] and that the bacterial DNA has in vivo been shown to be highly condensed even in the absence of nonspecifically bound CIs to help facilitate the DNA looping.[16] This value of ΔG_{oct} is also in agreement with in vivo observations.[7, 16] ΔG_{tetr} differs somewhat from values estimated in vivo, however in vitro experiments lack parts of the machinery of a living cell and hence some processes may be more favorable in vivo, thus displaying a higher free energy. In comparison to the parameters describing the linear assay,[9] we modeled the observed increased cooperativity by lowering the intrinsic binding energies between CI and each operator site by 1.5 kcal/mol, thus making multiple CI binding energetically more favorable than monomeric CI binding. In total, with these parameters we thermodynamically allowed the biologically relevant octamer-mediated loop to be formed and the negative total free energy change associated with DNA looping, i.e., the sum of the two cooperative terms, indicated that looping on supercoiled DNA is thermodynamically favorable.

Supercoiling Tunes λ Immunity

Most interestingly, the minimum number of CI molecules in the cell necessary to form the pRM-repressible state (12 CI molecules) corresponds to a cellular concentration of 20 nM. Our results on the looping probability of supercoiled DNA (**Fig. 2D**) show that this minimum cellular concentration corresponds to looping the DNA between the operators 58% of time. Below 20 nM of CI, the probability of the operators being in the looped state drops rapidly. Thus, during induction by the SOS pathway, pRM remains in the repressible state until all of the free CI has been degraded with activated RecA. We propose that below this minimum threshold, the CIs abruptly vacate OR and OL and lytic repression collapses. Despite the low copy number of CIs in the cell, the pRM repressible state is robust to both perturbations in gene expression that can vary dramatically from cell to cell, and to CI nonspecific DNA binding that would otherwise lead to spontaneous transition to lytic development. Based on our findings we propose that supercoiling plays a role in stabilizing the pRM-repressible state such that CI synthesis from pRM does not impede induction.

Concluding Remarks

By using PNA as handles, we tethered supercoiled DNA plasmids and utilized

the assay for a single molecule study of the λ switch in a naturally supercoiled system. This assay has potential to examine how DNA in its natural supercoiled state interacts with proteins, enzymes, histones in nucleosomes, and the transcription and replication machinery. Interestingly, our results show that the λ switch is finely tuned to have an optimal, fast and efficient response to the cellular SOS system exactly at the cellular concentration corresponding to the minimum number of CI molecules capable of maintaining the CI repressible state.

Disclosure of Potential Conflicts of Interest

No potential conflicts of interest were disclosed.

Acknowledgment

We acknowledge financial support from the University of Copenhagen excellence program.

References

1. Ptashne M. A Genetic Switch: Lambda Phage Revisited. Cold Spring Harbor, NY: Cold Spring Harbor Lab Press, 2004
2. Brooks K, Clark AJ. Behavior of lambda bacteriophage in a recombination deficient strain of Escherichia coli. J Virol 1967; 1:283-93; PMID:4918235
3. Baek K, Svenningsen S, Eisen H, Sneppen K, Brown S. Single-cell analysis of lambda immunity regulation. J Mol Biol 2003; 334:363-72; PMID:14623180; http://dx.doi.org/10.1016/j.jmb.2003.09.037
4. Little JW, Michalowski CB. Stability and instability in the lysogenic state of phage lambda. J Bacteriol 2010; 192:6064-76; PMID:20870769; http://dx.doi.org/10.1128/JB.00726-10
5. Bailone A, Levine A, Devoret R. Inactivation of prophage lambda repressor in vivo. J Mol Biol 1979; 131:553-72; PMID:159955; http://dx.doi.org/10.1016/0022-2836(79)90007-X
6. Meyer BJ, Ptashne M. Gene regulation at the right operator (OR) of bacteriophage lambda. III. lambda repressor directly activates gene transcription. J Mol Biol 1980; 139:195-205; PMID:6447796; http://dx.doi.org/10.1016/0022-2836(80)90304-6
7. Dodd IB, Shearwin KE, Perkins AJ, Burr T, Hochschild A, Egan JB. Cooperativity in long-range gene regulation by the lambda CI repressor. Genes Dev 2004; 18:344-54; PMID:14871931; http://dx.doi.org/10.1101/gad.1167904
8. Lewis D, Le P, Zurla C, Finzi L, Adhya S. Multilevel autoregulation of λ repressor protein CI by DNA looping in vitro. Proc Natl Acad Sci U S A 2011; 108:14807-12; PMID:21873207; http://dx.doi.org/10.1073/pnas.1111221108
9. Zurla C, Manzo C, Dunlap D, Lewis DE, Adhya S, Finzi L. Direct demonstration and quantification of long-range DNA looping by the lambda bacteriophage repressor. Nucleic Acids Res 2009; 37:2789-95; PMID:19276206; http://dx.doi.org/10.1093/nar/gkp134
10. Norregaard K, Andersson M, Sneppen K, Nielsen PE, Brown S, Oddershede LB. DNA supercoiling enhances cooperativity and efficiency of an epigenetic switch. Proc Natl Acad Sci U S A 2013; 110:17386-91; PMID:24101469; http://dx.doi.org/10.1073/pnas.1215907110
11. Lia G, Semsey S, Lewis DE, Adhya S, Bensimon D, Dunlap D, Finzi L. The antiparallel loops in gal DNA. Nucleic Acids Res 2008; 36:4204-10; PMID:18573800; http://dx.doi.org/10.1093/nar/gkn389
12. Normanno D, Vanzi F, Pavone FS. Single-molecule manipulation reveals supercoiling-dependent modulation of lac repressor-mediated DNA looping. Nucleic Acids Res 2008; 36:2505-13; PMID:18310101; http://dx.doi.org/10.1093/nar/gkn071
13. Lia G, Bensimon D, Croquette V, Allemand JF, Dunlap D, Lewis DE, Adhya S, Finzi L. Supercoiling and denaturation in Gal repressor/heat unstable nucleoid protein (HU)-mediated DNA looping. Proc Natl Acad Sci U S A 2003; 100:11373-7; PMID:14500788; http://dx.doi.org/10.1073/pnas.2034851100
14. Nelson PC, Zurla C, Brogioli D, Beausang JF, Finzi L, Dunlap D. Tethered particle motion as a diagnostic of DNA tether length. J Phys Chem B 2006; 110:17260-7; PMID:16928025; http://dx.doi.org/10.1021/jp0630673
15. Reichardt L, Kaiser AD. Control of lambda repressor synthesis. Proc Natl Acad Sci U S A 1971; 68:2185-9; PMID:4943790; http://dx.doi.org/10.1073/pnas.68.9.2185
16. Hensel Z, Weng X, Lagda AC, Xiao J. Transcription-factor-mediated DNA looping probed by high-resolution, single-molecule imaging in live E. coli cells. PLoS Biol 2013; 11:e1001591; PMID:23853547; http://dx.doi.org/10.1371/journal.pbio.1001591
17. Polikanov YS, Bondarenko VA, Tchernaenko V, Jiang YI, Lutter LC, Vologodskii A, Studitsky VM. Probability of the site juxtaposition determines the rate of protein-mediated DNA looping. Biophys J 2007; 93:2726-31; PMID:17573434; http://dx.doi.org/10.1529/biophysj.107.111245
18. Liu Y, Bondarenko V, Ninfa A, Studitsky VM. DNA supercoiling allows enhancer action over a large distance. Proc Natl Acad Sci U S A 2001; 98:14883-8; PMID:11742093; http://dx.doi.org/10.1073/pnas.261477898
19. Liu LF, Wang JC. Supercoiling of the DNA template during transcription. Proc Natl Acad Sci U S A 1987; 84:7024-7; PMID:2823250; http://dx.doi.org/10.1073/pnas.84.20.7024
20. DiNardo S, Voelkel KA, Sternglanz R, Reynolds AE, Wright A. Escherichia coli DNA topoisomerase I mutants have compensatory mutations in DNA gyrase genes. Cell 1982; 31:43-51; PMID:6297752; http://dx.doi.org/10.1016/0092-8674(82)90403-2
21. Anderson LM, Yang H. DNA looping can enhance lysogenic CI transcription in phage lambda. Proc Natl Acad Sci U S A 2008; 105:5827-32; PMID:18391225; http://dx.doi.org/10.1073/pnas.0705570105
22. Ackers GK, Johnson AD, Shea MA. Quantitative model for gene regulation by lambda phage repressor. Proc Natl Acad Sci U S A 1982; 79:1129-33; PMID:6461856; http://dx.doi.org/10.1073/pnas.79.4.1129

DNA supercoiling enhances cooperativity and efficiency of an epigenetic switch

Kamilla Norregaard[a], Magnus Andersson[a,b], Kim Sneppen[a], Peter Eigil Nielsen[c], Stanley Brown[d], and Lene B. Oddershede[a,1]

[a]The Niels Bohr Institute, University of Copenhagen, 2100 Copenhagen, Denmark; [b]Department of Physics, Umeå University, SE-901 87 Umeå, Sweden; and [c]Department of Cellular and Molecular Medicine, Faculty of Health and Sciences and [d]Department of Biology, University of Copenhagen, 2200 Copenhagen, Denmark

Edited by Sankar Adhya, National Institutes of Health, National Cancer Institute, Bethesda, MD, and approved July 8, 2013 (received for review September 12, 2012)

Bacteriophage λ stably maintains its dormant prophage state but efficiently enters lytic development in response to DNA damage. The mediator of these processes is the λ repressor protein, CI, and its interactions with λ operator DNA. This λ switch is a model on the basis of which epigenetic switch regulation is understood. Using single molecule analysis, we directly examined the stability of the CI-operator structure in its natural, supercoiled state. We marked positions adjacent to the λ operators with peptide nucleic acids and monitored their movement by tethered particle tracking. Compared with relaxed DNA, the presence of supercoils greatly enhances juxtaposition probability. Also, the efficiency and cooperativity of the λ switch is significantly increased in the supercoiled system compared with a linear assay, increasing the Hill coefficient.

epigentic switch | autoregulation | repression | kinetics | gene regulation

Developmental programs are decision-making processes, primarily controlled by epigenetic switches. Once a cell differentiates, its daughter cells continue the developmental program. The decision between the dormant state (the lysogenic state) and the vegetative state (the lytic state) made by bacteriophage λ upon infection of an *Escherichia coli* was the first epigenetic switch to be deciphered (1) and continues to provide insights into biological processes (2, 3). Once the lysogenic state is established, it is exceptionally stable and departure in the absence of the DNA damage sensing system is nearly always caused by mutation (4–6). Maintenance of lysogeny is mediated by the λ repressor protein, CI, and its formation of a complex with phage DNA. The CI protein binds at two regulatory regions called operator right (OR) and operator left (OL), located about 2.3 kbp apart on the phage genome. Each operator is a constellation of three adjacent subsites that each bind dimers of CI in a hierarchical manner (1, 7). In a lysogenic cell, CI prevents lytic growth by directly repressing the lytic promoters pR and pL. This repression is enhanced by long-range cooperative interactions between CI dimers bound to the OL1–OL2 and OR1–OR2 regions, thus looping the DNA that lies between them (8) (Fig. 1 *A* and *B*). CI-mediated DNA looping brings OR3 in proximity to OL3. This juxtaposition allows a CI dimer bound to the strong OL3 to facilitate another CI dimer to bind to the intrinsically weak OR3, thus reducing the concentration of CI necessary to occupy OR3. In this manner CI can autoregulate its own expression by binding to OR2 (activation) or by binding to OR3 (repression). This autoregulation is crucial for the phage to maintain repression while preventing excessive accumulation of CI. When DNA in the lysogen is damaged, the bacterial DNA-damage–sensing system is triggered, leading to CI inactivation by self-cleavage (9) and to an efficient switch to the lytic state, eventually leading to production of progeny phage and cell death (1).

The switch from the lysogenic to the lytic state must be decisive. Partial entry into vegetative growth may kill the host without producing a full burst of progeny phage. Because the in vivo state of DNA is supercoiled (10), we sought to examine protein-mediated DNA looping on native, supercoiled DNA. In vitro single molecule experiments addressing looping have revealed important information regarding looping dynamics (11–14). However, previous experiments all used linear nonsupercoiled DNA or linear DNA where supercoils were mechanically introduced—for example, by twisting a bead attached to the end of a DNA tether (15–17). We developed a unique peptide nucleic acid (PNA)-based assay by which the long-range CI-mediated DNA looping can be measured directly in vitro on a naturally supercoiled DNA plasmid (sketched in Fig. 1*C*). For each plasmid molecule the degree of supercoiling is constant, hence, the change in overall length between the operator sites is due to CI-mediated looping only and not due to the introduction of additional supercoils.

After CI binding to the operators, loop formation can be divided into two steps: juxtaposition of the λ operators and closing the loop by protein interactions. As protein–protein binding is a fast process, site juxtaposition is believed to be the rate-limiting step (18). Supercoiled DNA is a compacted state; thus, many pairs of sites, although separated along the DNA contour, are positioned in close vicinity to each other. In comparison, a relaxed DNA of the same size is less compact and bears a much smaller number of juxtaposed sites. Brownian dynamics simulations scrutinizing the thermal motion of relaxed and supercoiled DNA suggest a dynamic difference between the two (19). The simulations predicted that site juxtaposition is in general a slow process, which is accelerated by supercoiling. Thus, supercoiling is expected to enhance loop formation. Using our naturally supercoiled plasmid system, we found the juxtaposition probability is greatly enhanced in a supercoiled plasmid in comparison with a

Significance

Bacteriophage λ was the first epigenetic switch to be deciphered and continues to contribute to our understanding of gene regulation. Its dormant state is exceptionally stable. In spite of this stability, viral development is efficiently activated in response to DNA damage. This ability to respond efficiently is due to a long-range protein-mediated DNA looping. We developed a single molecule assay based on peptide nucleic acid tethering of a naturally supercoiled DNA plasmid. The internal kinetics of the supercoiled plasmid was monitored, and the dynamics and stability of regulatory protein-mediated DNA looping investigated. We found that the DNA loop becomes tolerant to reductions in the regulator when DNA is supercoiled, thus helping explain the bistable nature of the lambda switch.

Author contributions: P.E.N., S.B., and L.B.O. designed research; K.N., M.A., and S.B. performed research; K.S., P.E.N., and S.B. contributed new reagents/analytic tools; K.N., M.A., and L.B.O. analyzed data; and K.N., M.A., S.B., and L.B.O. wrote the paper.

The authors declare no conflict of interest.

This article is a PNAS Direct Submission.

[1]To whom correspondence should be addressed. E-mail: oddershede@nbi.dk.

This article contains supporting information online at www.pnas.org/lookup/suppl/doi:10.1073/pnas.1215907110/-/DCSupplemental.

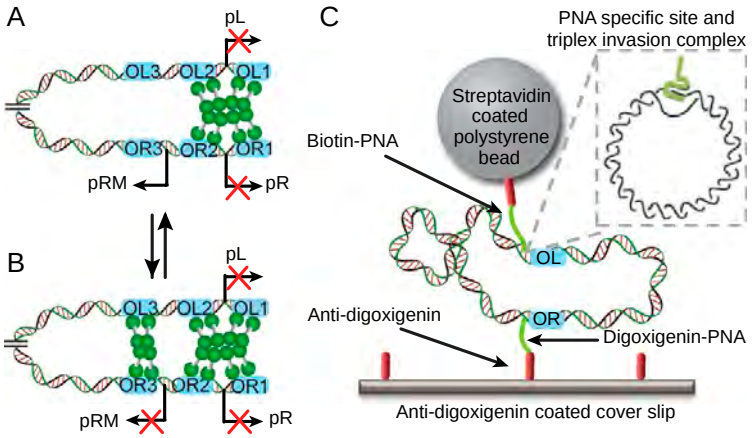

Fig. 1. A schematic of CI autoregulation by DNA looping and the experimental assay. Protein complex formation between the λ operator sites displaces the intervening DNA in a loop. The in vivo distance between the operators is ~2.3 kbp. The bent arrows show the transcription start points of the lytic promoters pL and pR and the lysogenic promoter pRM. The blue rectangles show the adjacent operator subsites OL1, OL2, OL3 and OR1, OR2, OR3. Red X signifies that the promoter is turned off in the shown configuration. CI dimers are shown as green dumbbell structures. (*A*) Octamer-mediated DNA looping by CI tetramers binding to OL1–OL2 and OR1–OR2. The lytic promoters, pL and pR, are repressed while CI transcription is activated by CI bound to OR2. (*B*) After octamer-mediated loop formation, an additional CI tetramer can bind cooperatively between OL3 and OR3, thus forming the octamer+tetramer complex. This represses both lytic genes and CI synthesis. (*C*) A plasmid DNA is tethered to an antidigoxigenin-coated cover slide via a digoxigenin–PNA and a streptavidin-coated μm-sized polystyrene bead via a biotin–PNA. The plasmids contain the entire λ immunity region and the two λ operators, OL and OR, flanked by the PNA-specific sites. CI dimers binding at OL and OR introduce loop formation and cause a detected decrease in the distance between the bead and the surface. (*C, Inset*) The PNA binds with sequence specificity to a DNA target and forms a triplex invasion complex while displacing the noncomplementary DNA strand in a loop.

relaxed plasmid. A supercoiled plasmid DNA has fewer accessible states and all available states are more rapidly explored than for a relaxed plasmid DNA.

Furthermore, we found that the presence of supercoils on DNA greatly enhances the looping probability at all investigated CI concentrations until saturation, in comparison with the looping probability of linear DNA (14). In particular at low concentrations (~20–40 nM) of CI monomers, the probability of being in the looped state is significantly higher for the supercoiled DNA, and the concentration interval where both the looped and unlooped states occur with significant probability is decreased. Hence, supercoiling facilitates looping at low CI concentrations and causes the switch between the looped and unlooped states to be sharper. Our findings are in accordance with an existing thermodynamic model (14, 20, 21), and we identified thermodynamic parameters that needed revision to make the model more compatible with in vivo observations (21, 22). The Hill coefficient characterizing the supercoiled assay ($h = 2.5$) is significantly higher than for the linear assay ($h = 1.2$), thus rendering the transition between states in a supercoiled system more robust to biological noise.

Results

PNA-Plasmid Assay. To examine binding of CI protein to DNA in its native, supercoiled state, we used two "handles" to monitor the dynamics of DNA at designated positions. The handles were made of bis-PNA, one bearing a biotin and the other a digoxigenin at its N terminus (Fig. 1*C*). Triplex invasion complexes formed between the homopyrimidine bis-PNA and DNA and resulted in an internal PNA–DNA–PNA triplex in which two PNA strands hybridized to the complementary DNA strand by combined Watson Crick and Hoogsteen base pairing (23) (Fig. 1*C*, *Inset*). Consequently, the noncomplementary DNA strand was displaced as a small, single stranded loop (24). A plasmid was constructed that contained the λ immunity region including the λ operators, OL and OR. On each side of the immunity region, unique PNA binding sites were engineered. Via a biotin-conjugated PNA, the plasmid was attached to a streptavidin-coated bead and via a digoxigenin-conjugated PNA to an antidigoxigenin-coated surface. The bound plasmid was torsionally constrained because the streptavidin bead was too large to rotate through the DNA plasmid circle.

A series of experiments was performed to determine the specificity and stability of the triplex invasion complexes. First, electrophoretic mobility shift experiments were conducted to identify initial solution conditions for accurate and efficient binding of both PNAs to their target sites (*SI Text* and Fig. S1). Next, two plasmids were prepared, one lacking the digoxigenin–PNA target (pSB4293) and another lacking the biotin–PNA target (pSB4300). Tethers were only expected to form with the plasmid bearing both PNA targets, pSB4312, and we used particle tracking to follow the motion of individual beads possibly tethered by each of the three plasmids. The excursions of the bead were analyzed by a principal component analysis as detailed in ref. 25 and in *SI Text*. Fig. S2 shows the 2D projected positions visited by the tethered bead, a typical time series, and a position histogram. The analysis yielded a number for the root mean square deviation (RMSD) of the bead from the center of its excursions, presumably the anchoring point. The larger the RMSD, the longer the overall length of the DNA tether. The RMSDs for each of the control plasmids as well as for pSB4312 are shown in Fig. S3. We found that the RMSD distribution from a sample with pSB4312 containing both PNA targets showed a bimodal distribution, the two peaks being separated by a large value. We attributed the peak representing the long excursions (RMSD > 150 nm) as stemming from correctly formed DNA–PNA tethers. The other peak representing short or no excursions of the bead (RMSD < 100 nm) was interpreted as originating from nonspecifically tethered beads. The presence of this lower peak is consistent with the RMSD distribution obtained from a control sample containing only beads and no DNA. The two control plasmids each lacking one PNA target only had the lower peak corresponding to unspecific bead attachments. The percentage of tethers with an RMSD above 150 nm out of the total number of tethers was 48% for pSB4312, whereas it was 4% and 8% for pSB4300 and pSB4293, respectively. A Student *t* test showed that the likelihood that the distribution observed with plasmids bearing both PNA targets is the same as the distribution observed with plasmids bearing only one of the PNA targets is $<6\times10^{-8}$. Hence, correct PNA targets were a prerequisite for formation of DNA tethers and the PNAs were binding to their designated target sites.

Juxtaposition Kinetics of Relaxed and Supercoiled DNA. First, we investigated the dynamics of supercoiled plasmids versus that of relaxed plasmids. For this purpose we prepared a smaller plasmid (pSB4357) containing 5,546 base pairs; 2.6 kbp containing the λ

DEVELOPMENTAL BIOLOGY

immunity region was on one of the arcs connecting the bead and the surface and 2.9 kbp was on the other arc. Two types of experiments were carried out, one with the plasmid in its native supercoiled state and the other using a plasmid that was relaxed by nicking with the single strand endonuclease Nt.BspQI (pSB4357-R). PNA–DNA binding has a 2 order of magnitude higher binding rate to negatively supercoiled DNA compared with relaxed DNA (26). This is because PNA binding to DNA requires opening of the DNA helix and therefore PNA strand invasion is more efficient (faster) in the negatively supercoiled state in which strand separation is facilitated. For this reason higher PNA concentrations are needed for binding PNA handles to the relaxed tether. Also, by PCR we constructed a linear control DNA molecule with the same length (2.6 kbp) as the short of the arcs on pSB4357. All DNA constructs were examined in tethering experiments.

Inspired by the literature (25, 27) and the results from Fig. S3, we imposed the following selection criteria to minimize the occurrence of unspecific tethers in the analyzed datasets: (*i*) Results from beads that probably were attached directly to the surface, or by unspecific tethers, and hence had a small RMSD were discarded, and (*ii*) if the positions visited by the bead displayed a low degree of symmetry (s) as defined in *SI Text*, the bead might be attached to the surface by more than one DNA tether and the time series was discarded. More specifically, we set the RMSD threshold to RMSD > 60 nm and symmetry threshold to $s > 0.8$.

The RMSD of 83 beads tethered to the supercoiled plasmid pSB4357 and of 31 beads tethered by the relaxed plasmid pSB4357-R are plotted in the histograms shown in Fig. 2*A* and *B*. The two RMSD histograms have mean values of 242 ± 46 nm (mean ± SD) for the supercoiled plasmid and 276 ± 39 nm for the relaxed plasmid, respectively. A Student t test on the two distributions returned a P value of 2.1×10^{-4}; therefore, the two distributions are significantly different. The RMSD of the relaxed pSB4357-R plasmid was compared with the RMSD of the linear control DNA molecule, 315 ± 26 nm. As the length of the linear control DNA molecule is identical to that of the short arc of pSB4357, it is reasonable that the means of the two RMSDs within the error bars are identical. Due to the semistiff nature of the DNA and the fact that the length of the arc is only around 17 DNA persistence lengths, it is, however, also reasonable that the excursions of the relaxed plasmid on average are a little smaller than those of the linear tether.

The broad distribution of RMSD observed for supercoiled DNA may be due to the broad distribution of supercoiled states in our plasmids as extracted from the bacteria. Due to the geometrical constraints on the system, once extracted, the degree of supercoiling (the writhe number) of each plasmid remained constant. Of all the plasmids, 99% contained at least one supercoil. To quantify the in vivo spread in writhe, we performed a chloroquine gel analysis, and the result is shown in Fig. 2*C* (the entire gel is shown in Fig. S4). For a particular plasmid preparation, the appearance of at least 10 distinct bands indicated that at least 10 different writhe numbers were present. The broad distribution of supercoiled states also gave rise to a broad distribution of tether lengths in the presence of CI protein.

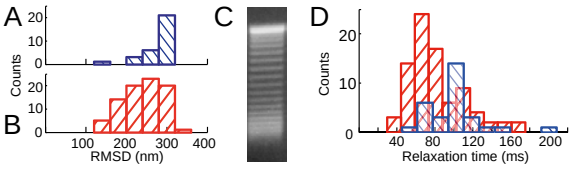

Fig. 2. Juxtaposition kinetics of supercoiled versus relaxed DNA. Histograms of the RMSD for the relaxed plasmid pSB4357-R (*A*) and for the naturally supercoiled plasmid pSB4357 (*B*). (*C*) Portion of chloroquine gel showing distribution of supercoils in the pSB4357 preparation. Entire electrophoretic gel shown is in Fig. S4. (*D*) Histogram of the relaxation time for all used datasets of pSB4357 (supercoiled plasmid; red) and pSB4357-R (relaxed plasmid; blue).

To investigate the intrinsic dynamics of supercoiled plasmids compared with that of relaxed plasmids, the autocorrelation between the positions in the time series was calculated: $C(\tau) \propto x(t+\tau)x(t) \propto \exp(\frac{-t}{\tau})$. The relaxation time, τ, describes how long a system retains prior information and was extracted from fitting the latter expression to the time series. The autocorrelation of supercoiled DNA falls off faster than for relaxed DNA (Fig. S5). The calculated relaxation times were plotted in histograms (Fig. 2*D*) and the mean values (±1 SD) of τ for supercoiled and relaxed plasmids were found to be 81 ± 30 ms and 100 ± 30 ms, respectively. A Student t test comparing relaxation times between pSB4357 and pSB4357-R returned a P value $<3.1\times10^{-3}$, thus showing that the correlation times characterizing the two plasmids were significantly different. The supercoiled plasmid has a shorter relaxation time than the relaxed plasmid, representing faster internal motion of the supercoiled plasmid and thus a more rapid exploration of all available states. The relaxation time of the linear DNA molecule corresponding to the shorter arc of pSB4357 was 129 ± 49 ms. This value is significantly larger than that of the relaxed plasmid ($P = 8.0\times10^{-3}$) and reflects the influence of the geometrical constraints on the plasmid compared with the linear tether. These findings support the idea, consistent with previously proposed models (19), that juxtaposition kinetics are dependent on supercoiling as the internal motion of a DNA molecule is accelerated when the DNA is supercoiled. This is important as the frequency of site juxtaposition, in this case operator site juxtaposition, is believed to be a key factor in the occurrence of DNA looping (16, 18, 28).

CI-Mediated DNA Looping of Supercoiled Plasmids. In our assay, DNA looping mediated by CI proteins could be directly measured by a decrease in the overall length of the plasmid tether. To quantify protein clamping, we used a time-dependent measure, $\rho(t)$, to quantify the 2D projected length of the plasmid tether at time t. Whereas RMSD gives an average tether length during the entire time series, $\rho(t)$ measures the plasmid extension at time t. More precisely, we defined $\rho^2(t) = (x(t) - \langle x\rangle)^2 + (y(t) - \langle y\rangle)^2$, where the averages $\langle x\rangle$ and $\langle y\rangle$ were taken over the entire time series and hence designate the anchor point. To obtain the average value of ρ in a narrow window around t, $\rho(t)$ was filtered by a sliding window of 20 ms. The 2D projected physical distance between the tethering point and the position of the bead around time t is denoted $\sqrt{\langle\rho^2(t)\rangle_{20ms}}$ and is the quantity plotted in Fig. 3. As in the RMSD analysis we invoked a criterion on the projected length set to $\rho > 60$ nm. We often observed a decrease in the symmetry upon the CI clamping. Therefore, the criterion for s previously stated ($s > 0.8$) was used to select tethers before adding CI; however, after adding CI, the symmetry criterion was relaxed to $s > 0.6$.

To compare our data to single molecule studies on linear DNA tethers (14), we varied the CI concentrations from 5 to 170 nM (close to the estimated physiological concentration of CI monomers in a lysogenic cell, which is ~ 200 nM) (29, 30). The same bead tethered by pSB4357 was monitored up to 20 min after CI protein was added.

Typical $\sqrt{\langle\rho^2(t)\rangle_{20ms}}$ time series for different CI concentrations and their corresponding histograms are shown in Fig. 3 *A* and *B*. The histogram of the control experiments without CI is shown in Fig. 2*B* and additional time series for all tested concentrations of CI are shown in Fig. S6. All tethers had maximum excursions smaller than the 2.6 kbp linear DNA molecule; however, as the individual tethers displayed a relatively large distribution of degree of supercoiling (as shown in Fig. 2*C*), the overall length

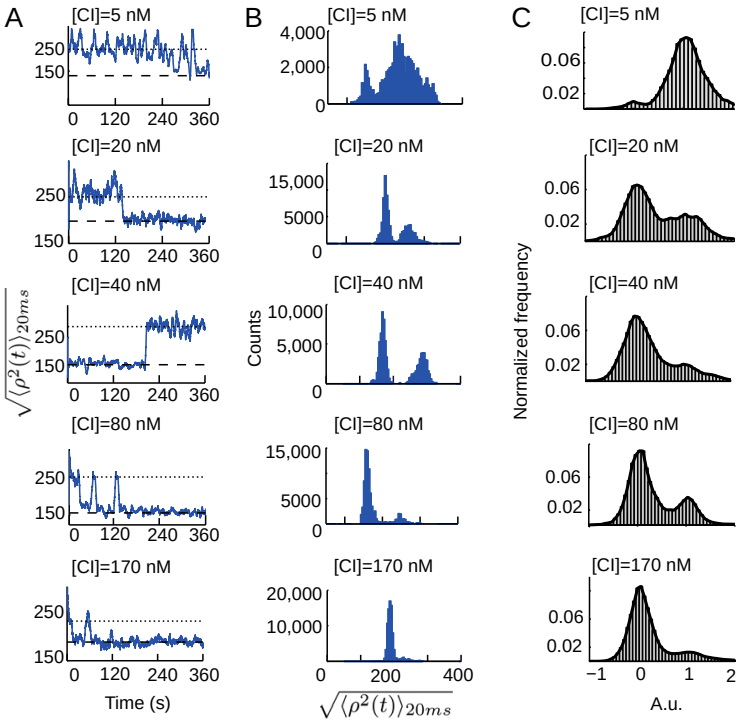

Fig. 3. Tethered particle motion time series signal and histograms of the looped and unlooped state for different CI concentrations using the pSB4357 plasmid. (*A*) Effective length of tether, $\sqrt{\langle \rho^2(t) \rangle_{20ms}}$, plotted as a function of time for beads tethered by a supercoiled plasmid. The plotted lines in the trajectory indicate the average excursions for unlooped (dotted line) and looped (dashed line). (*B*) Histograms of the time series shown in *A* (same abscissa for all concentrations). (*C*) Normalized collapsed histograms of looped and unlooped states, represented by the values 0 and 1, respectively, from all obtained datasets (same abscissa for all concentrations). The number of datasets for each concentration is $n = 4$ for 5 nM CI, $n = 7$ for 20 nM CI, $n = 5$ for 40 nM CI, $n = 6$ for 80 nM CI, and $n = 9$ for 170 nM CI, and significantly longer time series were used for the analysis than here shown. The looping probability increases as a function of CI concentration.

of the tether varied accordingly and the absolute value of $\sqrt{\langle \rho^2(t) \rangle_{20ms}}$ did not carry information on whether the plasmid was looped or not. However, a typical time series would show two distinct states (assigned to the looped and the unlooped form) and transitions between these two states. Therefore, we used the characteristic two-states shown in the time series to identify the looped and unlooped states. If no transitions were observed, the time series was not analyzed with respect to CI-mediated looping (which might give rise to an underestimation of looping at [CI] = 170 nM, where the plasmid could remain constantly looped during the entire observation period). To collapse all time series into a single histogram, we performed a linear transformation of the position histograms by designating a value of 0 to the peak of the distribution originating from the looped state (on histograms as shown in Fig. 3*B*) and a value of 1 to the peak of the unlooped state. The result of the data collapse for each CI concentration is shown in Fig. 3*C*. The data were fitted by two Gaussian distributions, one for the looped and one for the unlooped state. The looping probabilities were calculated as the ratio between the area under the Gaussian curve representing the looped state and the total area of the histogram. The uncertainties of the measured loop probabilities were determined by error propagation of the 95% confidence interval of the Gaussian fitting parameters as detailed in *SI Text*.

From Fig. 3*C* it is seen that the probability of looping increased as the concentration of CI increased. The observation that loop formation was negligible at low CI concentrations was expected because it was unlikely that the two operators, OL and OR, would be occupied simultaneously by CI. As CI concentration increased, octamer/octamer+tetramer complexes stabilized the loop configuration until saturation of the operator sites occurred and there was only little effect of increasing the concentration further (from 80 nM to 170 nM CI). The experiment depicted in Fig. 3*C* found the equilibrium between looped and unlooped states shifts toward more plasmids being in the looped state as CI concentration was increased.

The result of quantifying looping probabilities as function of CI concentration is shown in Fig. 4*A*, where the solid red circles denote data from CI-mediated looping of supercoiled plasmids. For comparison, we also plotted data on looping probability of linear DNA (solid blue squares) reported by Zurla et al. (14). Clearly, supercoiled DNA responded differently to CI concentration than linear DNA responded. In particular, the CI concentration interval where both the looped and unlooped states were significantly populated became narrower with supercoiled DNA than with linear DNA. A sharp response to changing CI concentration is expected for a regulatory network displaying a binary response. This is in contrast to metabolic pathways whose expression scales with nutrient availability as in the case of lactose utilization (31).

To investigate whether the difference in CI-mediated looping was due to the circular nature of the supercoiled plasmid, we examined looping in the relaxed form, pSB4357-R. To this end we chose the concentrations of CI that lead to the greatest difference in looping probability between linear and supercoiled DNA, 40 nM and 80 nM CI, and the results of looping probability are shown as open black triangles in Fig. 4*A*. The looping probability of relaxed pSB4357-R appeared similar to that reported for linear DNA (14). This observation suggests the difference between looping probability of supercoiled DNA and linear DNA is due to supercoiling rather than the circular nature of the supercoiled plasmid.

Thermodynamic Model. To further investigate the stability of the λ switch in a supercoiled system, we analyzed our data in the light of a thermodynamic model first put forward in ref. 20 and later modified to account for DNA looping (21, 22). The model relates the probability of each operator configuration to a given measure of the free CI monomer concentration. Details of the model can

DEVELOPMENTAL BIOLOGY

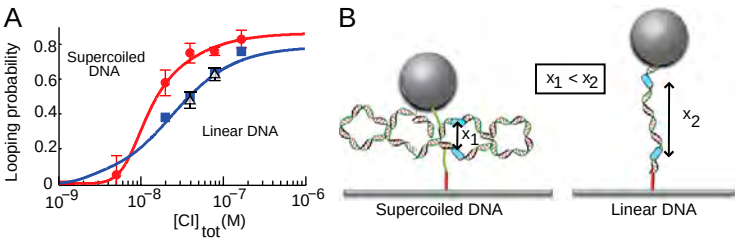

Fig. 4. Looping probability as a function of CI concentration for supercoiled DNA and linear relaxed DNA. (*A*) Data obtained from CI-mediated looping of supercoiled DNA plasmids are shown as solid red circles. Data from CI-mediated looping of linear DNA (solid blue squares) were published by Zurla et al. (14). The hollow black triangles denote data from the relaxed plasmid pSB4357-R, which coincide with the results from linear DNA. Lines show fits of the modified thermodynamic model to data from the supercoiled assay (red) and of the original model to the linear assay (14) (blue), respectively. Error bars represent SD. (*B*) Illustration of difference between supercoiled and linear assay, on average the effective distance between the two operator sites, OL and OR (marked by blue rectangles), is significantly shorter in the supercoiled configuration (x_1) than in the linear configuration (x_2). The relaxed pSB4357-R is identical to the structure shown on the left but without supercoils.

be found in ref. 14 and in *SI Text*; the blue line in Fig. 4*A* shows a fit of the model to looping data of linear DNA using the parameters found in ref. 14. Protein-mediated looping introduces two cooperative free energy terms: ΔG_{oct} and ΔG_{tetr}. ΔG_{oct} reflects the net free energy change due to octamerization of CI bound across OL1–OR1–OL2–OR2, together with the cost of formation of a DNA loop: $\Delta G_{oct} = \Delta G_{oct}^{(P)} - RT \ln(\Delta S_{loop})$. Here $\Delta G_{oct}^{(P)}$ is the cooperative free energy associated with octamer interactions and $-RT \ln(\Delta S_{loop})$ the entropic part of the free energy associated with DNA looping. ΔG_{tetr} reflects the cooperative free energy due to tetramerization of CI bound across OL3–OR3 and is only added if a loop is present and CI binds to the two remaining operators, thus forming an octamer–tetramer complex. As the previous model (14) (blue line in Fig. 4*A*) was optimized to fit a linear DNA, a modification was needed to adapt the model to our data collected with supercoiled DNA. In the supercoiled state, fewer conformations are available than for the linear state and all states are more rapidly explored. Hence, OR and OL are more frequently in proximity (as illustrated in Fig. 4*B*) and supercoiling enhances loop probability by lowering entropy costs. Therefore, ΔG_{oct} was decreased from 1.7 kcal/mol to 0 kcal/mol and ΔG_{tetr} was set to –1.0 kcal/mol instead of –2.4 kcal/mol. $\Delta G_{oct} = 0$ kcal/mol is in good agreement with free energies reported in vivo (~ -0.5 kcal/mol) (21, 22). The sum of the free energies $\Delta G_{complex} = \Delta G_{oct} + \Delta G_{tetr} = -1.0$ kcal/mol indicates that looping on supercoiled DNA is energetically more favorable than on linear DNA ($\Delta G_{complex} = -0.3$ kcal/mol); a comparison of the values of ΔG_{oct} and ΔG_{tetr} from the literature is given in Table 1. A second modification of the thermodynamic parameters entering the model was that we decreased the binding energies for all operator sites while keeping the cooperative parameters constant; the reasoning behind this is that gene regulation is commonly found to be sensitive to supercoiling (32), as it can change the local structure of DNA and influence protein DNA binding. In practice we weakened all binding energies between CI dimers and operator sites by 1.5 kcal/mol.

A fit of the model adopted to include supercoiling is shown as a red line in Fig. 4*A*. Another way of quantifying the cooperativity is to fit the Hill function to the data. This yields a Hill coefficient of 2.5 for the supercoiled data compared with 1.2 for the linear data (14). Cooperativity is a consequence of the binding of multiple proteins simultaneously and is essential for switch efficiency, as it steepens the transition.

Table 1. Comparison of free energies

Reference	ΔG_{oct}, kcal/mol	ΔG_{tetr}, kcal/mol
Current study	0	−1.0
Zurla et al. (14)	1.7	−2.4
Dodd et al. (22)	−0.5	−3

This pronounced bistable nature of the supercoiled system is in accordance with the nature of the λ phage: Once the λ phage has committed to enter either the lysogenic or the lytic state, the commitment is complete. Not only is the lysogenic state extremely stable in the supercoiled system, but when the host is exposed to inducing factors, switching to the lytic state can be efficiently done upon only a small change in CI concentration. In conclusion, our data show that natively supercoiled DNA provides an efficient and stable λ switch.

Discussion

We developed a PNA-based assay that allowed us to tether supercoiled plasmids between cover slides and beads. We investigated the internal dynamics of individual DNA tethers, both supercoiled plasmids, relaxed plasmids, and linear tethers, as well as protein-mediated DNA looping in a supercoiled system.

The RMSDs of supercoiled, relaxed, and linear DNA were compared, and it was found that the RMSD of the entangled supercoiled plasmid was significantly smaller than those of the relaxed plasmid and linear tether, which were comparable. Further, we found that the supercoiled plasmid exhibited a much faster relaxation time than the relaxed plasmid and the linear tether, which is analogous to enhanced site juxtaposition in the supercoiled state. These findings support previously published molecular dynamics simulations (19) and in vitro transcription assays (18).

The thermodynamic parameters of DNA looping have previously been studied in vivo (21, 22) and by single molecule experiments using linear DNA (14). In the latter study using linear DNA, the results showed that DNA looping involving six operators and six CI dimers was relative stable, whereas looping involving only four dimers (without OR3 and OL3 being occupied) was less stable. It appears that supercoiling of DNA enhances loop stability in comparison with looping of a linear DNA tether. The experimental result is supported by the fact that the thermodynamic model provided an excellent fit to the in vitro supercoiled DNA experimental data, yielding parameters consistent with in vivo observations (21, 22). A more recent in vitro study using supercoiled templates in a transcription assay has confirmed the enhancement of pRM activation by the octamer-mediated loop and the cooperative role of OL3 and OR3 in pRM repression (12). These findings indicate supercoiling increases the loop stability as directly observed here.

In summary, we have developed a single molecule assay using natively supercoiled DNA. We investigated the looping probabilities as a function of CI concentration and found a sharper transition between looped and unlooped states than observed with linear DNA (14). This sharper transition is expected for the regulatory network deciding between lytic and lysogenic states. By fitting a thermodynamic model to our data, we obtained values for the free energies associated with loop formation that were consistent with values reported for in vivo natively supercoiled DNA. Our work provides crucial insight into how supercoiling changes the dynamics of the lambda switch, the first epigenetic switch to

be deciphered and the switch that has become a paradigm for transcriptional regulation.

Materials and Methods

DNA. All plasmids were prepared as monomers in the recombination-deficient strain, SS74 (5). pSB4293, pSB4300, and pSB4312 all bear the BamHI to EcoRI fragment of λ (nucleotides 34,500–39,168) containing the immunity region and the early phage terminators replacing the BamHI–EcoRI fragment of pBluescriptKS(–) (Stratagene). The target for PNA1021, 5′-AAGAAGAAAA-3′, was placed adjacent to λ nucleotide 34,500 in pSB4293 and pSB4312. The target of PNA3593, 5′-AGAGAAAGAA-3′, was placed adjacent to λ nucleotide 39,168 in pSB4300 and pSB43412. pSB4357 is similar to pSB4312 but bears λ DNA from 35,517–38,126, placing OL and OR closer to the PNA targets. The 2.6 kbp linear DNA was prepared by PCR amplification of λ DNA representing nucleotides 35,501–38,140, with primers bearing 5′-biotin and 5′-digoxygenin. Oligonucleotides and methods are described in *SI Text*.

PNA. The bis-PNAs PNA1021 [Biotin-(eg1)$_3$-TTJ TTJ TTTTLys-aha-Lys-aha-Lys-TTTT CTT CTT-Lys-NH$_2$] (23) and PNA3593 [Dig-(eg1)$_3$-(DMLys)$_3$-TJT JTT TJT T-(eg1)$_3$-TTC TTT CTC T-Gly-NH$_2$ (DMLys = ε-N,*N*-dimethyl lysine; aha = 6-aminohaxanoic acid, eg1 = 8-amino-3,6-oxaoctanoic acid)] were synthesized using solid phase Boc chemistry according to published procedures (23, 33, 34). Digoxigenin was conjugated to the bis-PNA in solution using Digoxigenin NHS-ester. PNAs were purified by HPLC and characterized by MALDI-TOF mass spectrometry.

Chloroquine Gel Analysis of Supercoiling. Samples were electrophoresed through 1% agarose in Tris-acetate EDTA buffer supplemented with 3 μg/mL chloroquine-diphosphate as described by ref. 35 and stained with ethidium bromide (Fig. 2*C* and Fig. S4).

Preparation of DNA–PNA-Bead Complex and Flow Chambers. Triplex invasion of PNA and DNA was executed by incubating a 20-fold excess of PNA, 17 nM DNA with 0.33 μM PNA1021 (biotin labeled) and 0.33 μM PNA3593 (digoxigenin labeled), in (PEN buffer) 10 mM sodium Pipes pH 6.5, 0.1 mM EDTA, and 10 mM NaCl for 14–15 h at 37 °C in an air incubator (23). After incubation the DNA–PNA complex was diluted 25-fold in PEN buffer and stored at 5 °C until use. Before use, the DNA–PNA complex was further diluted (25-fold) in λ buffer (10 mM Tris·HCl pH 7.4, 200 mM KCl, 0.1 mM EDTA, 0.2 mM DTT). To remove nonspecifically formed triplex invasion complexes, the samples were incubated at 65 °C for 10 min in a water bath (23). A rectangular perfusion chamber (~15 μL) was created by joining two cover slides by two melted strips of parafilm. We perfused 20 μL of 20 μg/mL antidigoxigenin dissolved in PBS buffer into the chamber and incubated it for 30 min at room temperature. Then, the chamber was incubated with 20 μL of 2 mg/mL α-casein in λ buffer for 30 min at room temperature to passivate the surface. Hereafter, it was incubated with 20 μL of the prepared DNA–PNA complex for 60 min at room temperature, allowing the digoxigenin-labeled PNA to bind to the antidigoxigenin-coated surface. Finally, the chamber was incubated with 20 μL containing an excess of streptavidin-coated beads in 2 mg/mL α-casein dissolved in PBS for 30 min at room temperature. This allowed the biotin-labeled PNA end to bind to a streptavidin-coated bead. Between each exchange the chamber was washed with 90 μL of λ buffer. In looping experiments, the chamber was filled with 20 of μL CI diluted to the required concentration before sealing the chamber. Experiments were initiated after 10 min of incubation.

CI Protein. The λ repressor protein (CI) used in this work was expressed, purified, and generously provided by Dale Lewis and Sankar Adhya (Laboratory of Molecular Biology, Center for Cancer Research, National Cancer Institute, National Institutes of Health, Bethesda, MD). CI was stored in λ buffer at –20 °C in small aliquots and only thawed and diluted immediately before use.

Single Particle Tracking Experiments and Analysis Method. Images of the tethered beads were recorded via a progressive scan camera mounted on an inverted microscope equipped with a 100× oil immersion objective. Movement of the tethered particle was examined by Principal Component Analysis (PCA) to calculate the RMSD of a bead and its excursion symmetry (*s*) as detailed in *SI Text*.

ACKNOWLEDGMENTS. The CI protein was generously provided by Dale Lewis and Sankar Adhya (Laboratory of Molecular Biology, Center for Cancer Research, National Cancer Institute, National Institutes of Health, Bethesda, MD). The MatLab-based thermodynamic model was generously provided by Carlo Manzo (Single Molecule Biophotonics, The Institute of Photonic Sciences, Barcelona, Spain) and Laura Finzi (Department of Physics, Computational and Life Science Core Faculty, Emory University, Atlanta, GA). We also thank Thomas Bentin for advice on handling PNAs. This research was funded by the Excellence Program at the University of Copenhagen.

1. Ptashne M (2004) *A Genetic Switch: Phage Lambda Revisited* (Cold Spring Harbor Lab Press, Cold Spring Harbor, NY), 3rd Ed.
2. Ptashne M (2011) Principles of a switch. *Nat Chem Biol* 7(8):484–487.
3. Thompson JN (2012) Evolution. The role of coevolution. *Science* 335(6067):410–411.
4. Brooks K, Clark AJ (1967) Behavior of λ bacteriophage in a recombination deficienct strain of Escherichia coli. *J Virol* 1(2):283–293.
5. Baek K, Svenningsen S, Eisen H, Sneppen K, Brown S (2003) Single-cell analysis of lambda immunity regulation. *J Mol Biol* 334(3):363–372.
6. Little JW, Michalowski CB (2010) Stability and instability in the lysogenic state of phage lambda. *J Bacteriol* 192(22):6064–6076.
7. Wang H, Finzi L, Lewis DE, Dunlap D (2009) AFM studies of lambda repressor oligomers securing DNA loops. *Curr Pharm Biotechnol* 10(5):494–501.
8. Révet B, von Wilcken-Bergmann B, Bessert H, Barker A, Müller-Hill B (1999) Four dimers of lambda repressor bound to two suitably spaced pairs of lambda operators form octamers and DNA loops over large distances. *Curr Biol* 9(3):151–154.
9. Kim B, Little JW (1993) LexA and lambda CI repressors as enzymes: Specific cleavage in an intermolecular reaction. *Cell* 73(6):1165–1173.
10. Espejo RT, Canelo ES, Sinsheimer RL (1969) DNA of bacteriophage PM2: A closed circular double-stranded molecule. *Proc Natl Acad Sci USA* 63(4):1164–1168.
11. Manzo C, Zurla C, Dunlap DD, Finzi L (2012) The effect of nonspecific binding of lambda repressor on DNA looping dynamics. *Biophys J* 103(8):1753–1761.
12. Lewis D, Le P, Zurla C, Finzi L, Adhya S (2011) Multilevel autoregulation of λ repressor protein CI by DNA looping in vitro. *Proc Natl Acad Sci USA* 108(36):14807–14812.
13. Zurla C, et al. (2006) Novel tethered particle motion analysis of CI protein-mediated DNA looping in the regulation of bacteriophage lambda. *J Phys Condens Matter* 18(14):S225–S234.
14. Zurla C, et al. (2009) Direct demonstration and quantification of long-range DNA looping by the lambda bacteriophage repressor. *Nucleic Acids Res* 37(9):2789–2795.
15. Lia G, et al. (2008) The antiparallel loops in gal DNA. *Nucleic Acids Res* 36(12):4204–4210.
16. Normanno D, Vanzi F, Pavone FS (2008) Single-molecule manipulation reveals supercoiling-dependent modulation of lac repressor-mediated DNA looping. *Nucleic Acids Res* 36(8):2505–2513.
17. Lia G, et al. (2003) Supercoiling and denaturation in Gal repressor/heat unstable nucleoid protein (HU)-mediated DNA looping. *Proc Natl Acad Sci USA* 100(20):11373–11377.
18. Polikanov YS, et al. (2007) Probability of the site juxtaposition determines the rate of protein-mediated DNA looping. *Biophys J* 93(8):2726–2731.
19. Jian H, Schlick T, Vologodskii A (1998) Internal motion of supercoiled DNA: Brownian dynamics simulations of site juxtaposition. *J Mol Biol* 284(2):287–296.
20. Ackers GK, Johnson AD, Shea MA (1982) Quantitative model for gene regulation by lambda phage repressor. *Proc Natl Acad Sci USA* 79(4):1129–1133.
21. Anderson LM, Yang H (2008) DNA looping can enhance lysogenic CI transcription in phage lambda. *Proc Natl Acad Sci USA* 105(15):5827–5832.
22. Dodd IB, et al. (2004) Cooperativity in long-range gene regulation by the lambda CI repressor. *Genes Dev* 18(3):344–354.
23. Bentin T, Nielsen PE (2002) In vitro transcription of a torsionally constrained template. *Nucleic Acids Res* 30(3):803–809.
24. Nielsen PE, Egholm M, Berg RH, Buchardt O (1991) Sequence-selective recognition of DNA by strand displacement with a thymine-substituted polyamide. *Science* 254(5037): 1497–1500.
25. Tolić-Nørrelykke SF, Rasmussen MB, Pavone FS, Berg-Sørensen K, Oddershede LB (2006) Stepwise bending of DNA by a single TATA-box binding protein. *Biophys J* 90(10):3694–3703.
26. Bentin T, Nielsen PE (1996) Enhanced peptide nucleic acid binding to supercoiled DNA: Possible implications for DNA "breathing" dynamics. *Biochemistry* 35(27):8863–8869.
27. Blumberg S, Gajraj A, Pennington MW, Meiners JC (2005) Three-dimensional characterization of tethered microspheres by total internal reflection fluorescence microscopy. *Biophys J* 89(2):1272–1281.
28. Liu Y, Bondarenko V, Ninfa A, Studitsky VM (2001) DNA supercoiling allows enhancer action over a large distance. *Proc Natl Acad Sci USA* 98(26):14883–14888.
29. Reichardt L, Kaiser AD (1971) Control of lambda repressor synthesis. *Proc Natl Acad Sci USA* 68(9):2185–2189.
30. Aurell E, Brown S, Johanson J, Sneppen K (2002) Stability puzzles in phage lambda. *Phys Rev E Stat Nonlin Soft Matter Phys* 65(5 Pt 1):051914.
31. Clark DJ, Marr AG (1964) Studies on the repression of beta-galactosidase in escherichia coli. *Biochim Biophys Acta* 92:85–94.
32. DiNardo S, Voelkel KA, Sternglanz R, Reynolds AE, Wright A (1982) Escherichia coli DNA topoisomerase I mutants have compensatory mutations in DNA gyrase genes. *Cell* 31(1):43–51.
33. Christensen L, et al. (1995) Solid-phase synthesis of peptide nucleic acids. *J Pept Sci* 1(3):175–183.
34. Egholm M, et al. (1995) Efficient pH-independent sequence-specific DNA binding by pseudoisocytosine-containing bis-PNA. *Nucleic Acids Res* 23(2):217–222.
35. Esposito F, Sinden RR (1987) Supercoiling in prokaryotic and eukaryotic DNA: Changes in response to topological perturbation of plasmids in E. coli and SV40 in vitro, in nuclei and in CV-1 cells. *Nucleic Acids Res* 15(13):5105–5124.